Molecular mechanisms underlying leaf dorsiventrality: Prepatterns and Small RNA Morphogens

Dissertation

der Mathematisch-Naturwissenschaftlichen Fakultät

der Eberhard Karls Universität Tübingen

zur Erlangung des Grades eines

Doktors der Naturwissenschaften

(Dr. rer. nat.)

vorgelegt von

Shreyas Meda

aus Bangalore, Indien

Tübingen

2023

Gedruckt mit Genehmigung der Mathematisch-Naturwissenschaftlichen Fakultät der Eberhard Karls Universität Tübingen.

Tag der mündlichen Prüfung:	30.01.2024
Dekan:	Prof. Dr. Thilo Stehle
1. Berichterstatter:	Prof. Dr. Marja Timmermans
2. Berichterstatter:	Prof. Dr. Gerd Jürgens
3. Berichterstatter:	Prof. Dr. Catherine Kidner

Contents

List of Abbreviations

A. lyrata	*Arabidopsis lyrata*
A. thaliana	*Arabidopsis thaliana*
ab	Abaxial
ACR	Accessible chromatin region
ad	Adaxial
AG	AGAMOUS
AGO	ARGONAUTE
AM	Axillary meristem
AP2/EREBP	APETALA2/ETHYLENE-RESPONSIVE ELEMENT BINDING PROTEIN TF family
ARF	AUXIN RESPONSE FACTOR
AS1/2	ASYMMETRIC LEAVES 1/2
AS2	GENE
AS2	PROTEIN
ATAC-seq	Assay for transposase-accessible chromatin sequencing
AUX-RE	Auxin Response Element
B. rapa	*Brassica rapa FPsc*
B. stricta	*Boechera stricta*
BMP	BONE MORPHOGENETIC PROTEIN
C. grandiflora	*Capsella grandiflora*
C. rubella	*Capsella rubella*

CAS9	CASCADE 9
CLV3	CLAVATA 3
CNA	CORONA
CNS	Conserved non-coding sequences
Col-0	Columbia-0
cr-1/2	CRISPR allele-1/2
CRISPR	Clustered regularly interspaced short palindromic repeats
CRM	*cis*-regulatory modules
CUC3	CUP-SHAPED COTYLEDON 3
CZ	central zone
D2/DII	Aux/IAA auxin-interaction domain 2
DAP-seq	DNA affinity purification sequencing
DCL1	DICER-LIKE 1
DOF	DNA-BINDING ONE ZINC FINGER
dsRNA	double stranded RNA
E. salsugineum	*Eutrema salsugineum*
EC1.1	EGG CELL SPECIFIC PROMOTER
EIL	EIN3-like TF family
erGFP	endoplasmic reticulum localised GFP
FIL	FILAMENTOUS FLOWER
FT	FLOWERING LOCUS T
GFP	GREEN FLUORESCENT PROTEIN
GO	Gene Ontology

GRAS	GAI, RGA, SCR TF family
GRN	Gene Regulatory Network
gRNA	guide RNA
HDZIPIII	CLASS III HOMEODOMAIN-LEUCINE ZIPPER
HIS3	Encodes imidazoleglycerol-phosphate dehydratase – (Histidine biosynthesis gene)
HYL1	HYPONASTIC LEAVES 1
IAA	Indole -3-acetic acid
jba-1D	*Jabba-1D* (miR166g overexpressor)
KAN1	KANADI 1
Lac Z	β-galactosidase
LAT52	Pollen-specific gene
LOB/AS2	ASYMMETRIC LEAVES2/LATERAL ORGAN BOUNDARIES TF family
MADS	MCM1, AGAMOUS, DEFICIENS, and SRF TF family
mD2/mDII	Mutated Aux/IAA Auxin-interaction domain 2
men1	*meristem enlargement 1* (miR166a overexpressors)
miR165/166	mature miRNA 165/166
mirarf	artificial miRNA targeting ARF 2, 3 and 4
miRNA	microRNA
MP	MONOPTEROS
mRNA	messenger RNA
mutTFBS	mutated Transcription Factor Binding Site

MYB	MYELOBLASTOSIS TF family
N7	Nuclear localised sequence
NAC	NAM, ATAF1, ATAF2 and CUC2 TF family
NPA	N-1-naphthylphthalamic acid
NPH4	NON-PHOTOTROPIC HYPOCOTYL 4
p 1	primordium 1
p -1	incipient primordium 2
PHAN	PHANTASTICA
PHB	PHABULOSA
PHV	PHAVOLUTA
PIN1	PIN-FORMED 1
pMIR166A	promoter MIR166A
pre-miRNA	precursor miRNA
pri-miRNA	primary miRNA
PZ	Peripheral Zone
R2D2	Ratiometric version of two D2s
RAM	Root Apical Meristem
RDR6	RNA-DEPENDENT RNA POLYMERASE 6
REV	REVOLUTA
RISC	RNA-INDUCED SILENCED COMPLEX
SAM	Shoot Apical Meristem
SCR	SCARECROW
scRNA-seq	single-cell RNA sequencing

SE	SERRATE
SGS3	SUPPRESSOR OF GENE SILENCING 3
SHR	SHORT ROOT
siRNA	short interfering RNAs
SRDX	EAR repression domain
ssRNA	Single stranded RNA
tasiARF	TAS3-derived trans-acting short interfering RNAs targeting ARFs
tasiRNA	Trans-acting siRNAs
TCP	TEOSINTEBRANCHED1, CYCLOIDEA, PROLIFERATING CELL FACTOR TF family
TDH3	Encodes Glyceraldehyde 3-phosphate dehydrogenase
TF	Transcription Factor
TFBS	Transcription Factor Binding Sites
TIR/AFB	TRANSPORT INHIBITOR RESPONSE 1/AUXIN SIGNALING F-BOX
TSS	Transcription start site
UMAP	Uniform Manifold Approximation and Projection
WOX9	WUSCHEL-RELATED HOMEOBOX 9
WT	Wild type
WUS	WUSCHEL
Y1H	Yeast one-hybrid
ZFHD	ZINC FINGER HOMEODOMAIN TF FAMILY

Publications

Published papers

Burian, A., G. Paszkiewicz, K. T. Nguyen, **S. Meda**, M. Raczyńska-Szajgin and M. C. P. Timmermans (2022). "Specification of leaf dorsiventrality via a prepatterned binary readout of a uniform auxin input." Nature Plants **8**(3): 269-280.

Submitted Manuscripts

Scacchi E, G. Paszkiewicz, K. T. Nguyen, **S. Meda**, Burian, A., W. de Back, and M. C. P. Timmermans (2023)." A Diffusible Small-RNA-based Turing System Dynamically Coordinates Organ Polarity " Nature Plants (In revision).

Manuscripts

Meda, S., M.I. Tauber , W. Xi, G. Paszkiewicz , A. Burian, M. Bauer and M. C. P. Timmermans (2023). "Multi-layered genetic redundancy buffers miR165/166 morphogen levels to ensure robust organ polarity."

Meda, S., G. Paszkiewicz, M.I. Tauber, W. Xi, K. T. Nguyen., P. Solansky P**, T.** Denyer, and M. C. P. Timmermans (2023). "A Multifaceted Transcriptional Landscape Governs Morphogen dynamics in Organ Polarity."

Zusammenfassung

Die flache Architektur des Blattes ist eine wichtige evolutionäre Anpassung. Sie gewährleistet den effizienten Austausch von Gasen und maximiert die Photosynthese. Sie erfordert eine komplizierte Regulierung der adaxialen-abaxialen (ad-ab) Musterung, die genau spezifiziert und über die Länge und Breite des Blattes verbreitet werden muss, um die Flachheit während des gesamten Wachstums zu erhalten. Außerdem muss das ad-ab-Muster aufgrund der sessilen Natur der Pflanzen robust gegenüber Störungen durch die Umwelt bleiben. Daher ist es interessant, die molekularen Mechanismen zu verstehen, die für die Etablierung der ad-ab-Polarität verantwortlich sind, damit diese robust und dennoch flexibel ist. In diesem Zusammenhang wurden verschiedene Modelle mit gegensätzlichen Ansichten über die Bedeutung von Auxin und dem Blattrand postuliert. Eine große Herausforderung, die zu der Diskrepanz zwischen den Modellen führt, ist die Schwierigkeit, die Blattgründerzellen in der sehr kleinen Sprossspitze zu identifizieren, in der sich die Genexpression schnell und vorübergehend ändert. In dieser Arbeit überwinden wir die oben genannten Herausforderungen. Durch die Kombination von Zeitrafferaufnahmen, Zelllinienverfolgung und molekularer Analyse zeigen wir, dass die Expression von AS2 und KAN1, die adaxiale bzw. abaxiale Determinanten sind, die Meristemperipherie vorstrukturiert. Dieses Vormuster überführt den gleichmäßigen Auxin-Input, der die Organogenese fördert, in eine polare Auxin-Reaktion, die über ARF3 ausgelesen wird, um ad- und ab-Blattgründerzellen zu unterscheiden. Darüber hinaus zeigen wir, dass sich die Expression von miR165/166, einem Morphogen, von dem berichtet wird, dass es bei der Aufrechterhaltung der ad-ab-Polarität eine Rolle spielt, mit der von KAN1 an der Meristemperipherie überschneidet. Als solches strukturiert miR165/166 seine Ziel-HDZIPIII-Transkriptions Faktoren (TF), um die Meristemhomöostase und das adaxiale Zellschicksal zu regulieren. Wir vermuten, dass die Aktivität von miR165/166 die richtige räumlich-zeitliche Entstehung und ad-ab-Polarisierung des Blattes gewährleistet, indem sie die HDZIPIII-Funktion am Meristem von der im Blatt trennt. Quantitative Analysen zeigten außerdem, dass miR165/166 in einer schwellenwertabhängigen Weise wirkt, wobei Pflanzen nur dann ein normales SAM und ein flaches Blatt entwickeln, wenn die miR165/166-Spiegel innerhalb eines optimalen Fensters liegen.

Nach der Etablierung wird die ad-ab-Polarität durch ein kompliziertes genregulatorisches Netzwerk (GRN) aus TF und kleinen RNAs aufrechterhalten. Antagonistische TF-Interaktionen fördern ad-ab-Zellschicksale, während die kleinen RNAs miR165/166 und tasiARF als Morphogene fungieren und die notwendigen Positionsinformationen liefern, um eine scharfe Grenze auf Domänenebene zu bilden. Die Organisationsprinzipien des GRN waren jedoch nicht bekannt. In dieser Arbeit wird durch eingehende theoretische und rechnerische Modellierung gezeigt, dass das GRN den Organisationsprinzipien eines Turing-Systems folgt, das sich dynamisch anpasst, um die ad-ab-Grenze robust gegenüber Störungen zu halten. Das modellierte Netzwerk sagt auch neuartige Eigenschaften wie die Mobilität von AS2 und die Aktivierung von miR165/166 durch den KAN-ARF-Komplex voraus, die für die ad-ab-Polarität notwendig sind und die wir *in planta* nachgewiesen haben. Wichtig ist, dass die Turing-Dynamik die oft kontraintuitiven Phänotypen von Polaritätsmutanten erklärt und die für die Erzeugung der Vielfalt von Blattformen erforderliche Flexibilität berücksichtigt.

Die Ad-ab-Polarität ist nicht nur ein Schlüsselmechanismus für die Blattmorphologie, sondern auch ein elegantes Modell zum Verständnis grundlegender Konzepte der Musterbildung. In dieser Hinsicht haben genregulatorische Netzwerke zwangsläufig empfindliche/fragile Komponenten, die berücksichtigt werden müssen. Die molekularen Mechanismen, die dies steuern, sind jedoch nicht gut verstanden. Ebenso müssen die Morphogene, die die Musterbildung vorantreiben, sowohl auf räumlich-zeitlicher als auch auf quantitativer Ebene genau reguliert werden, aber die transkriptionellen Regulationsmechanismen, die ihre robuste Expression gewährleisten, sind nicht bekannt. Unter Verwendung der ad-ab-Polarität als Paradigma wurde in dieser Arbeit versucht, neue Erkenntnisse zu den oben genannten Konzepten zu gewinnen. Umfassende molekulare und genetische Analysen zeigten, dass miR165/166 einen empfindlichen Knoten im GRN der Polarität bildet. Wir stellen fest, dass die genetische Redundanz auf der Ebene der MIR165/166-Familie und die überschüssige Produktion kleiner RNAs Mechanismen sind, die Pflanzen einsetzen, um diese empfindliche Komponente zu schützen und die Robustheit der Musterbildung zu gewährleisten. Darüber hinaus organisieren sich auf der Ebene der einzelnen Gene redundante cis-regulatorische Module (CRMs) innerhalb des MIR166A-Promotors, dem dominanten Faktor für miR165/166, wie Schattenverstärker bei Tieren, um die Expression stabil zu halten. Dies führt auch zu phänotypischer Robustheit auf Organebene. Bei der Analyse der regulatorischen Logik von MIR166A identifizieren wir ein

komplexes Netzwerk von TF, sowohl Aktivatoren als auch Repressoren mit gewebespezifischer oder breiter Expression. Die Verteilung ihrer Bindungsstellen über den MIR166A-Promotor erhöht die Komplexität der Regulierung und lässt auf eine Enhancerpleiotropie schließen. Redundante cis- und trans-Mechanismen sorgen gemeinsam für die Gewebespezifität von MIR166A und die Regulierung seiner quantitativen Ausprägung und weisen auf mögliche allgemeine Phänomene bei der Regulierung von Morphogenen hin.

Insgesamt bietet diese Arbeit Einblicke in die Etablierung und Aufrechterhaltung der ad-ab-Polarität, die die Bildung eines flachen Blattes sowie eines breiten Spektrums anderer Blattformen ermöglicht. Darüber hinaus identifizieren wir am Beispiel der ad-ab-Musterung molekulare Mechanismen, die die Expression empfindlicher Netzwerkkomponenten sicherstellen und die Gewebespezifität wichtiger Morphogene etablieren, um die Robustheit der Musterung zu gewährleisten.

Summary

The flat architecture of the leaf is a vital evolutionary adaptation. It ensures the efficient exchange of gases and maximizes photosynthesis. The flat leaf architecture requires intricate regulation of adaxial-abaxial (ad-ab) patterning, which must be precisely specified and propagated across the length and width of the leaf to maintain flatness throughout growth. Further, due to the sessile nature of plants, the ad-ab pattern must remain robust to environmental perturbations. As such, it is intriguing to understand the molecular mechanisms that govern ad-ab polarity establishment, allowing it to be robust yet flexible. In this regard, different models with contrasting views on particularly the importance of auxin and the leaf margin have been postulated. A major challenge that leads to the discrepancy among the models is the difficulty of identifying leaf founder cells within the very small shoot apex, within which gene expression changes are rapid and transient. In this work, we overcome the above challenges. Combining time-lapse imaging, cell lineage tracing, and molecular analysis, we show that the expression of AS2 and KAN1, which are adaxial and abaxial determinants, respectively, prepatterns the meristem periphery. This prepattern, coverts the uniform auxin input that promotes organogenesis into a polar auxin response readout via ARF3 to distinguish ad- and ab leaf founder cells. Further, we show that the expression of miR165/166, a morphogen with reported roles in ad-ab polarity maintenance, overlaps that of KAN1 at the meristem periphery. As such, miR165/166 patterns its target HDZIPIII TFs, to regulate meristem homeostasis and adaxial cell fate. We propose that miR165/166 activity ensures proper spatiotemporal emergence and ad-ab polarization of the leaf by separating HDZIPIII function at the meristem to that in the leaf. Quantitative analysis further demonstrated that miR165/166 acts in a threshold-dependent manner, wherein plants develop a normal SAM and a flat leaf only when miR165/166 levels are within an optimal window.

Post establishment, ad-ab polarity is maintained by an intricate Gene Regulatory Network (GRN) of TFs and small RNAs. Antagonistic TF interactions promote ad-ab cell fates while the small RNAs, miR165/166 and tasiARF, act as morphogens providing the necessary positional information to form a sharp boundary at the domain level. However, the organizing principles of the GRN were not known. In this work, in-depth theoretical and computational modelling demonstrates that the GRN follows the organizing principles of a Turing system that dynamically adapts to keep the ad-ab boundary robust to perturbations. The modelled network

also predicts novel features such as mobility of AS2 and activation of miR165/166 by the KAN-ARF complex necessary for ad-ab polarity, which we demonstrated in planta. Importantly, the Turing dynamics explains the often-counterintuitive phenotypes of polarity mutants and accommodates the flexibility needed for generating diversity in leaf shapes.

Ad-ab polarity, along with being a key patterning mechanism for leaf morphology, serves as an elegant model to understand fundamental concepts underlying pattern formation. In this regard, gene regulatory networks inevitably have sensitive/fragile components that need to be accommodated. However, the molecular mechanisms that govern this are not well understood. Similarly, morphogens driving the pattern formation need to be precisely regulated, both at spatiotemporal and quantitative level but transcriptional regulatory mechanisms that ensure their robust expression are not known. As such, using ad-ab polarity as a paradigm this work sought to provide new insights into the above concepts. Extensive molecular and genetic analysis showed that miR165/166 forms a sensitive node in the polarity GRN. We identify that genetic redundancy at the MIR165/166 family level and excess small RNA production as mechanisms that plants employ to safeguard this fragile component and to ensure patterning robustness. In addition, at the individual gene level, redundant *cis*-regulatory modules (CRMs) within the *MIR166A* promoter, the dominant contributor to miR165/166, organize like shadow enhancers in animals to keep its expression robust. This further translates into phenotypic robustness at the organ level. Analyzing the regulatory logic of *MIR166A* we identify a complex network of TFs, both activators and repressors with tissue-specific or broad expression. Their binding site distributions across the *MIR166A* promoter enhance the complexity of regulation and suggest enhancer pleiotropy. As such, redundant *cis* and *trans* mechanisms collectively generate tissue specificity of *MIR166A* and regulate its quantitative level and highlight potential general phenomena regulating morphogens.

Taken together, this thesis provides insights into the establishment and maintenance of ad-ab polarity accommodating the formation of a flat leaf, as well as a wide range of other leaf shapes. Further, using ad-ab patterning as a model we identify molecular mechanisms that safeguard the expression of sensitive network components as well as establish tissue specificity of key morphogens, to ensure robustness in patterning.

Introduction

Pattern Formation

The development of multicellular organisms is a highly complex process, orchestrated by the formation and intersection of multiple patterns. During pattern formation, gene expression, signalling cues and other cellular behaviours are coordinated at the spatiotemporal level, to organize cells into distinct domains (Wolpert et al., 2015). Key fundamental questions in developmental biology are how patterns are established and regulated. Decades of research have provided valuable insights into mechanisms involved in pattern formation during development. In both plants and animals, despite the diversity among patterns, certain conceptual parallels tend to underline them. Patterning mechanisms exhibit different classes influenced by the presence or absence of cell–cell communication. Furthermore, the communication between cells can be through signalling molecules or mechanical interactions. Among the different classes, inductive mechanisms are widely studied and rely on cell-cell communication via mobile signals. These mobile signals further lead to differential expression of genes and spatial positioning of cells to generate patterns (Reviewed in (Salazar-Ciudad, 2017; Salazar-Ciudad et al., 2003). Different models in this regard have been postulated over the years. The first was the Reaction-Diffusion model where two diffusible mobile signals termed morphogens with specific interactions among them break organ symmetry giving rise to patterns such as spots, labyrinths, and stripes (Gierer & Meinhardt, 1972; Turing, 1952). Such patterns now termed Turing patterns are self-organizing and remain stable and yet provide flexibility throughout development (Turing, 1952). Another proposed theory was the positional information model where morphogens diffuse from their fixed source generating a concentration gradient. Based on the concentration of mobile signals perceived by the cells, these cells evaluate their position on a spatial level. This results in the activation of subsequent downstream gene regulatory networks leading to distinct cell fates and thereby forming patterns (Wolpert, 1969).

In both plants and animals, much of development occurs during embryogenesis (Ingham, 1988; Jurgens, 2003). However, plants show post-embryonic development of new organs to form their final adult phenotype. Shoot and root apical meristems, initiated during embryogenesis, contain pluripotent stem cells and are responsible for producing new organs post-embryonically

throughout the plant's lifetime. (Stahl & Simon, 2010). The root apical meristem (RAM) is necessary for the growth and development of adult root architecture (Perilli et al., 2012). The stem cell niche of the RAM consists of slow-dividing cells that form the quiescent centre (QC), which acts as a reservoir and maintains the surrounding stem cell population. The latter are mitotically active and acquire specific tissue identity based on their spatial positions subsequently giving rise to differentiated tissues such as the vasculature, columella, endodermis, cortex, etc. (Dolan et al., 1993). On the other hand, the shoot apical meristem (SAM) is more complex and generates the aerial tissues of the plant such as the leaves, shoots, and flowers (Carles & Fletcher, 2003). It is a dome-shaped structure consisting of pluripotent stem cells at its apex, forming the central zone (CZ). Below this lies the organizing centre, which functions like the QC in the RAM, maintaining the stem cell population and the organization of the niche. However, in contrast to the RAM, stem cells of SAM do not have a specified tissue identity. In the SAM, stem cell daughters are displaced toward the flanking region, the SAM peripheral zone (PZ), where at regular intervals lateral organs initiate (Braybrook & Kuhlemeier, 2010; Fletcher, 2002).

Formation of a Flat Leaf

Leaves are the primary source of energy for a plant, acting as photosynthetic units and sites for gaseous exchange during respiration. They develop during the vegetative growth phase of the SAM before it transitions to flowering. Auxin, a hormone that has roles in almost every part of plant development, plays a pivotal role during leaf initiation (Reinhardt et al., 2000). Micro application of auxin inhibitor N-1-naphthylphthalamic acid (NPA) on tomato shoot apex prevented leaf formation. Further, leaf initiation was restored on the application of auxin Indole-3-acetic acid (IAA) on these meristems, demonstrating the necessity of auxin during leaf organogenesis (Reinhardt et al., 2000). During leaf initiation, auxin is transported from the epidermis of the SAM, mediated by the efflux carrier, PIN-FORMED 1 (PIN1) and converges at the SAM periphery, forming an auxin maxima and thereby distinguishing the leaf founder cells from the meristem (Heisler et al., 2005; Reinhardt et al., 2000; Reinhardt et al., 2003). Further, the polar auxin transport is also necessary for phyllotaxis, the arrangement of leaves around the SAM. Here, the existing primordium acts as a sink for auxin which leads to an auxin-depleted

area surrounding the primordium which prevents a new leaf initiation within its vicinity. As a result, the future leaf is initiated at the meristem periphery away from the existing primordia, thereby generating a distinct phyllotactic arrangement of leaves (Reinhardt et al., 2003).

At a molecular level, cells respond to auxin signalling via Transcription Factors (TF) called AUXIN RESPONSE FACTORS (ARF). These ARFs bind to specific *cis*-elements called Auxin Response Elements (AUX-RE) in the promoter of responsive genes thereby either activating or repressing a multitude of genes. During low auxin levels, the ARFs are inhibited by hetero-dimerisation with AUX/IAA proteins. Once the auxin level increases, auxin forms a complex with AUX/IAA and TIR/AFB proteins that undergoes degradation, thereby making ARFs free to perform their function on auxin-responsive genes during developmental processes (Gomes & Scortecci, 2021). Two redundant ARFs, MONOPTEROS (MP) and NON-PHOTOTROPIC HYPOCOTYL (NPH4) are necessary for leaf inhiation, as shown in the *mp nph4* double mutants that fail to develop lateral organs (Hardtke et al., 2004). However, downstream components of ARFs that participate in leaf initiation are not well understood.

Post initiation, these founder cells emerge as bud-like structures at the peripheral region of the meristem. Simultaneously, it develops along three different axes - the proximal-distal, adaxial(ad)-abaxial(ab), and mediolateral, to give rise to a functional leaf and acquire a distinct leaf shape. During leaf growth and development, the flexibility within these three axes which are influenced by both internal and external cues, leads to the diversity of leaf shapes and sizes seen in nature (Bar & Ori, 2014; Waites & Hudson, 1995). Among the diverse leaf shapes, flat leaf architecture is observed in most flowering plants and is a vital adaptation during evolution that maximizes the leaf activity concerning photosynthesis and respiration (Husbands et al., 2009).

Flat leaves contain two sides i.e., the adaxial (upper) and abaxial (lower) sides. It was shown that the juxtaposition of the adaxial-abaxial (ad-ab) domains is necessary for leaf blade outgrowth which leads to a flat leaf (Waites & Hudson, 1995). Further, the adaxial surface comprises tightly packed palisade mesophyll cells that optimize light capture, maximizing photosynthesis. Conversely, the abaxial side has spongy mesophyll cells with stomata, which ensures the efficient exchange of gases during respiration. In addition, vascular tissues are distinct in the ad/ab domains. The adaxial side contains xylem tissue, whereas the phloem is on the abaxial side. Similarly, at the molecular level, distinct genes determining ad/ab cell fates have been

identified, and these are discussed later (Husbands et al., 2009). As such, the formation of a flat leaf by ad-ab patterning serves as an elegant model to gain more insight into general patterning mechanisms. Multiple phases are proposed during ad-ab polarity starting from its establishment to its maintenance throughout plant growth and development (Husbands et al., 2009). Although much has been discovered on this front, many questions remain yet to be resolved, which are discussed in detail in the following sections.

Establishment of Adaxial-Abaxial Polarity

A fundamental question during leaf development is how ad-ab polarity is established. Multiple models have been proposed in this regard. The earliest model on polarity establishment was based on classical surgical experiments in potatoes, which proposed that a signal from the meristem prompts adaxial cell fate, thus breaking organ symmetry. This was determined by a surgical incision between the meristem and the incipient primordia that was found to lead to a radialised leaf, as opposed to a flat leaf. Further surgical incisions blocking the contact of incipient primordia with the adjacent older primordia, but not the meristem, led to a normal leaf shape. Collectively, these surgical experiments suggest that a meristem-derived signal, the so-called "SUSSEX signal", is necessary for ad-ab polarity establishment (Sussex, 1951, 1954) (Kuhlemeier & Timmermans, 2016). A study on tomato meristems reinforced the above model through both surgical dissection and laser ablation of cells between the meristem and the incipient primordia (Reinhardt et al., 2005). In addition, ablating the L1 epidermal layer of the apex was sufficient to disturb ad-ab polarity, suggesting that the L1 epidermis is necessary to transport the meristem-borne Sussex signal to pattern the primordia (Reinhardt et al., 2005).

In the hunt for the so-called SUSSEX signal, an exciting study in 2014 identified auxin as a signal that patterns ad-ab polarity (Qi et al., 2014). Here, the authors identified a low auxin concentration in the adaxial side of the young primordia when compared to the abaxial side by imaging the distribution of DII-venus, an auxin sensor (Brunoud et al., 2012; Qi et al., 2014). On ectopic manipulation of auxin on the adaxial side of the young primordia by application of IAA led to the conversion of adaxial cell identity to abaxial cell identity. A similar ad to ab transition of cell fates was obtained when a mutated version of MP that acts independent of auxin-mediated regulation was induced on the adaxial side of the young primordia (Qi et al., 2014). Further, it was shown that

the low auxin state of the adaxial side was due to its depletion from the adaxial side of the leaf to the meristem via PIN1. Accordingly, this asymmetric auxin distribution between the primordia leads to the specification of ad-ab polarity (Qi et al., 2014). In contrast to the proposed Sussex signal derived from meristems, this model suggests auxin as an opposite, a "reverse SUSSEX signal" (Qi et al., 2014).

However, the necessity of the hypothetical Sussex signal and its role in ad-ab polarity specification are contended by other studies. Laser ablation of cells between the incipient primordium and the meristem in *Arabidopsis* did not lead to any radialised leaves. Further, performing these ablations 2-3 plastochrons (time of interval between two successive leaves), before primordia emerge, also showed similar effects, suggesting that the information for ad-ab establishment is not dependent on a meristem-borne signal, at least in *Arabidopsis* (Zhao & Traas, 2021). However, the authors suggest that the differences in mechanisms establishing ad-ab polarity between *Arabidopsis* and *Solanum* could be a probable explanation for the absence of radialised leaves after laser ablation in *Arabidopsis*, but not in *Solanum* apices (Zhao & Traas, 2021).

Another proposed concept independent of the meristem-derived signal is that the ad-ab domains could be pre-patterned in the incipient primordium (Husbands et al., 2009). Based on this, another model for ad-ab polarity specification has been proposed. Interestingly, this model also depends on the distribution of auxin within the young primordia (Caggiano et al., 2017). Accordingly, the ad-ab polarity is established on a pre-patterned high auxin middle domain. This middle domain further ensures the polarized expression of the adaxial determinant REVOLUTA (REV) and the abaxial determinant KANADI 1 (KAN1) TFs to their respective domains in very young primordia. In the sites between these expression domains, when auxin response is maximum, the future ad- ab pre-patterned primordia emerge (Caggiano et al., 2017). The same authors in another study using the ratio-metric auxin sensor R2D2, which has two components, DII-Venus, and mDII-tomato (mutated DII) and allows for performing a quantitative assessment of Auxin signalling (Liao et al., 2015) reanalysed the distribution of auxin in the primordia (Bhatia et al., 2019). In this regard, a low DII/mDII ratio indicates a high auxin level while a high DII/mDII ratio indicates a low auxin level. Visualizing this reporter in the young primordia, displayed no differences in auxin levels between the adaxial and abaxial side of the leaf, but high auxin levels were observed in distal regions at the tip of the primordia, thereby refuting the

previous model of the necessity of auxin depletion from the adaxial side for polarity establishment (Bhatia et al., 2019; Qi et al., 2014).

However, the key cause for the differences between the hypotheses could be due to the complexity of the shoot apex. It is small in size with continuous growth and rapid cell fate changes. As such it makes it challenging to precisely identify the few leaf founder cells and study ad-ab polarity establishment. In this regard, it is plausible that all the models explained above, although seemingly contradicting each other, could be correct in their own ways and occur at distinct temporal windows during different stages of ad-ab development. However, this still needs to be scrutinized further.

Maintenance of Adaxial-Abaxial leaf polarity

The flat leaf architecture is not the default state of the plant. This is evident from perturbations in either adaxial or abaxial cell identity leading to defects in leaf shape that no longer remain flat (Eshed et al., 2001; Waites & Hudson, 1995). As such, ad-ab polarity must be maintained throughout the leaf growth and development. Further, this sharp ad-ab boundary must be robust enough to withstand the external perturbations to which the plant is exposed. In addition, a recent study in *Utricularia gibba* shows that changes in the ad-ab domain of expression or its effect on growth lead to cup-shaped leaf development as opposed to a planar leaf (Whitewoods et al., 2020). As such the ad-ab polarity must also be flexible to allow leaf shape variations.

To maintain a sharp boundary, it is necessary either to transfer the patterning information from the meristem continuously to the growing primordium, or post polarity establishment the primordium becomes organ autonomous and self-sufficient to maintain the boundary throughout its development. Surgical experiments suggest the latter hypothesis, whereby an incision between meristem and younger primordia beyond a specific stage does not make them radial but continues to develop a flat shape (Reinhardt et al., 2005; Sussex, 1951). In this regard, studies over the years have identified an intricate network of TFs and small RNAs that play key roles in the maintenance of ad-ab polarity which are discussed in detail in the next sections.

Molecular Determinants of Adaxial-Abaxial Cell Fate: A Transcription Factor Saga

Mutants in *Antirrhinum majus* of a MYB TF, *Phantastica* (*Phan*), provided the first molecular insights into the role of TFs in ad-ab polarity (Waites & Hudson, 1995; Waites et al., 1998). Here strong *phan* mutants showed completely radialised leaves, while the weaker mutants showed small switches from adaxial to abaxial identity. An in-depth analysis of these mutants demonstrated the necessity of juxtaposed ad-ab domains for a flat leaf formation (Waites & Hudson, 1995). Consequently, this study formed the basis of a new research avenue which led to the identification of many TFs that act as adaxial or abaxial determinants. In *Arabidopsis*, ASYMMETRIC LEAVES 1 and 2 (AS1-AS2) and CLASS III HOMEODOMAIN-LEUCINE ZIPPER (HDZIPIII) family of TFs act as major adaxial determinants (Lin et al., 2003; McConnell & Barton, 1998). AS2 forms a complex with AS1 (the ortholog of PHAN) and promotes adaxial cell fate (Husbands et al., 2015; Iwakawa et al., 2007; Lin et al., 2003; Phelps-Durr et al., 2005). PHABULOSA (PHB), PHAVOLUTA (PHV), and REVOLUTA (REV), which belong to the class of HDZIPIII TFs are expressed on the adaxial side of the leaf and act as adaxial determinants. Gain-of-function mutants with uniform HDZIPIII expression develop adaxialised leaves that are radial and needle-shaped (Emery et al., 2003; McConnell & Barton, 1998; McConnell et al., 2001). Along with adaxial determinants, multiple genes that ensure the abaxial identity of the cell have been studied. Members of the YABBY family of TFs FILAMENTOUS FLOWER (FIL) YABBY2, YABBY3 and YABBY5 were some of the earliest abaxial determinants identified (Sarojam et al., 2010; Siegfried et al., 1999). Further, KANADI (KAN) TFs, members of the G2-like family promote abaxial cell fate where *kan1 kan2* double mutants have cup-shaped cotyledons with leaves developing outgrowths on the abaxial side (Eshed et al., 2001; Kerstetter et al., 2001). In addition, to the above TFs, select ARFs also contribute to ad- ab polarity. In this regard, mutational analysis of MP which is expressed on the adaxial side of the growing primordia promotes adaxial cell fate (Guan et al., 2017; Krogan & Berleth, 2012; Qi et al., 2014). On the other hand, ARF2, 3 and 4 redundantly act as abaxial determinants (Guan et al., 2017; Pekker et al., 2005).

Interestingly, studies over the years have shown that the ad and ab determinants act antagonistically to one another in promoting respective cell identities. This might be necessary to make the ad and ab cell fates mutually exclusive. In this regard, the AS1-AS2 complex directly

represses abaxial determinants such as YABBY5 and ARF3 TFs (Husbands et al., 2015). AS2 also either directly- or indirectly restricts the abaxial determinant TF KAN1 to the abaxial side (Wu et al., 2008). On the other hand, KAN1 promotes abaxial cell fate by directly repressing AS2 and restricting it to the adaxial side of the leaf (Wu et al., 2008). In summary, all the above TFs collectively form an intricate gene regulatory network that promotes adaxial or abaxial cell fate by mutual antagonism.

Mobile Small RNAs Pattern Adaxial-Abaxial polarity in the leaf

Although an intricate network of TFs maintains ad-ab cell fates, they are insufficient to maintain the boundary at a tissue or domain level. For pattern formation, a fundamental necessity is for the cells to assess their relative position within the tissue or organ relayed by mobile signals (Wolpert, 1969). TFs in the ad-ab networks are immobile or their mobility is not known. As such other mobile signals are necessary to define ad-ab domains. This is provided by small RNAs (Chitwood et al., 2009; Skopelitis et al., 2017).

Small RNAs are key players in regulating plant growth and development as well as stress and immune responses (D'Ario et al., 2017; Huang et al., 2016). They are divided into two major classes, microRNAs (miRNA) and short interfering RNAs (siRNA), based on their mode of biogenesis. In brief, miRNAs are initially transcribed as long primary transcripts (pri-miRNA) that fold to form an imperfect hairpin-like structure. These pri-miRNAs are first processed into small precursor miRNA (pre-miRNAs) and then into a mature miRNA duplex of usually 21nt, by DICER-LIKE 1 (DCL1), an RNase endonuclease and its associated proteins HYPONASTIC LEAVES 1 (HYL1) and SERRATE (SE). The single-stranded mature miRNA is then assembled with ARGONAUTE (AGO) proteins to form the RNA-induced silenced complex (RISC). This RISC complex is guided by the miRNA sequence to specifically bind to the complementary sequence of its target transcripts. The AGO component of the complex then cleaves the mRNA, which is subsequently degraded. In addition, the RISC complex can also lead to translational inhibition of the target gene (reviewed in (Wang et al., 2019; Zhan & Meyers, 2023).

On the other hand, siRNAs are derived from long double-stranded RNA sequences. These are processed by other DCL proteins to produce 21-24nt siRNAs. Further, siRNAs show transitivity,

where the siRNA population is amplified. Here, the initially generated primary siRNA binds to ssRNA transcripts and acts as a priming sequence, to form dsRNA by RNA-dependent RNA polymerase (RDR6). DCL proteins further process them to form more secondary siRNA molecules. Based on the origin of the dsRNA and the processing proteins, multiple subclasses of siRNA exist. Relevant here are the Trans-acting siRNAs (tasiRNA). Here, the *TAS* loci produce noncoding RNA transcripts that are transcriptionally cleaved by miRNAs. These cleaved products further act as templates and form dsRNA, mediated by RDR6 and SUPPRESSOR OF GENE SILENCING 3 (SGS3). DCL4 then processes the dsRNA to form 21nt tasiRNAs, which are loaded into specific AGO for further activity (Allen & Howell, 2010; Sanan-Mishra et al., 2021).

In the scenario of ad-ab polarity maintenance, two small RNAs, miR165/166 and tasiARF, act as morphogens and provide the positional information needed for the sharp boundary across the leaf (Chitwood et al., 2009; Juarez et al., 2004; Skopelitis et al., 2017). *MIR165/166* gene family plays key roles in distinct developmental programs of the root, shoot apical meristem, leaf, and flower, as well as various abiotic and biotic stress responses (Carlsbecker et al., 2010; Jung & Park, 2007; Rhoades et al., 2002; Yadav et al., 2021). In the leaf, miR165/166 are expressed on the abaxial epidermis and act as morphogens and move across the leaf, generating a concentration gradient (Nogueira et al., 2009; Yao et al., 2009). This concentration gradient leads to a threshold-based response, resulting in a binary readout of HDZIPIII expression restricting it to the adaxial side of the leaf (Juarez et al., 2004; Nogueira et al., 2009; Skopelitis et al., 2017). The second small RNA involved in ad-ab polarity is tasiARF. These are generated from the cleavage of *TAS3* transcripts by miR390. They are then incorporated into AGO7 and target *ARF3* and *ARF4* transcripts (Allen et al., 2005; Axtell et al., 2006; Montgomery et al., 2008). Contrary to miR165/166, tasiARF is expressed on the adaxial side of the leaf. They move across the leaf from its source, forming a concentration gradient opposite to that of miR165/166. Furthermore, the tasiARF gradient also in a threshold-based manner leads to a binary expression of its target ARF3 restricting it to the abaxial side of the leaf (Chitwood et al., 2009; Skopelitis et al., 2017). As such the morphogen-like behaviour of these two small RNAs with opposing gradients restricting the expression of its targets to defined domains, generates a uniform and stable ad-ab boundary (Skopelitis et al., 2017). Further, the antagonistic interaction exists also among the polarity-determining TFs and small RNAs. The adaxial determinant REV (HDZIPIII) in combination with HDZIPII TFs (HAT3, ATHB4) directly repress *MIR166A* on the adaxial side

(Merelo et al., 2016). Similarly, the AS1-AS2 complex, also represses *MIR166A* on the adaxial side, restricting its expression to the abaxial side of the leaf (Husbands et al., 2015).

Overall, the mutual repression among adaxial and abaxial determining TFs, and positional information derived by small RNAs, maintain a sharp and defined ad-ab polarity of the leaf across its growth and development. However, the organizing principles behind the self-sufficiency and flexibility within the network to accommodate different leaf shapes are not understood.

Aim and objectives.

In plants, adaxial-abaxial (ad-ab) patterning is vital for flat-leaf architecture. It must be precisely specified and stably propagated to ensure the leaf acquires and retains flat morphology throughout growth (Waites & Hudson, 1995). How the ad-ab polarity of the leaf is acquired is a pivotal question in plant developmental biology. Research over the years has proposed different models offering opposing hypotheses to explain ad-ab polarity establishment (Caggiano et al., 2017; Qi et al., 2014; Sussex, 1951). A major reason for this lies in the complexity and dynamics of the shoot apex. The Shoot Apical Meristem (SAM) is continuously growing, causing very rapid and transient changes in patterns of gene expression. Further, given the small size of the SAM, identifying cells that specifically mark the leaf founder cells remained challenging. In Chapter One, we address these caveats by combining time-lapse imaging with cell lineage tracing to link changes in gene expression to cell fate acquisition, during polarity establishment.

Along with the establishment of ad-ab polarity, maintenance of the sharp ad-ab boundary throughout primordium growth and development is critical to keep the leaf flat. Decades of research have so far identified an intricate Gene Regulatory Network (GRN) of TFs acting via mutually antagonistic interactions to promote ad-ab cell identity (Husbands et al., 2009). In addition, small RNAs act as morphogens and provide the positional information needed to ensure a sharp ad-ab boundary at the tissue/domain level (Skopelitis et al., 2017). However, the organizing principles that keep the polarity GRN robust leading to a flat leaf, remain unknown. As such, in Chapter Two, using theoretical and computational modelling approaches, we aim to understand the principles that tune the intricate ad-ab polarity network and provide the required flexibility to accommodate shifts in ad-ab gene expression associated with leaves of different shapes (Kim et al., 2003; Whitewoods et al., 2020).

Ad-ab patterning with its intricate network of TFs and small RNAs serves as an elegant model to understand general concepts during pattern formation which remain to be resolved. In this regard, GRNs often contain sensitive components that impact patterning outputs and, as a result, these components must be safeguarded to ensure the robustness of the pattern (Lempe et al., 2013; Whitacre, 2012). The molecular underpinnings offering this robustness are not well understood. Similarly, morphogens are critical for providing positional information during

patterning (Turing, 1952; Wolpert, 1969). However, despite a good understanding of the mode of action of these morphogens as well as their targets, the spatiotemporal and quantitative regulation of these morphogens at the transcriptional level is less well understood (Kicheva & Briscoe, 2023; Klesen et al., 2020; Skopelitis et al., 2017). In chapter Three, using leaf ad-ab patterning as a framework we aim to understand the molecular mechanisms that organisms have developed to cope with sensitive components. Further, in chapter Four, specifically focusing on miR165/166, a morphogen that determines abaxial cell fate, we aim to decipher general principles that may play a role in the transcriptional regulation of morphogens by analyzing the regulatory logic of miR165/166.

Taken together, this study focuses on understanding the molecular principles governing the establishment and maintenance of ad-ab polarity. Further, using leaf polarity as a paradigm, we aim to understand molecular underpinnings of general mechanisms during pattern formation such as sensitive nodes and the regulation of morphogens.

Chapter One: Specification of leaf dorsiventrality via a prepatterned binary readout of a uniform auxin input

Agata Burian*, Gael Paszkiewicz*, Khoa Thi Nguyen, Shreyas Meda, Magdalena Raczyńska-Szajgin & Marja C. P. Timmermans

Abstract

Developmental boundaries play an important role in coordinating the growth and patterning of lateral organs. In plants, specification of dorsiventrality is critical to leaf morphogenesis. Despite its central importance, the mechanism by which leaf primordia acquire adaxial versus abaxial cell fates to establish dorsiventrality remains a topic of much debate. Here, by combining time-lapse confocal imaging, cell lineage tracing and molecular genetic analyses, we demonstrate that a stable boundary between adaxial and abaxial cell fates is specified several plastochrons before primordium emergence when high auxin levels accumulate on a meristem prepattern formed by the AS2 and KAN1 transcription factors. This occurrence triggers a transient induction of ARF3 and an auxin transcriptional response in AS2-marked progenitors that distinguishes adaxial from abaxial identity. As the primordium emerges, dynamic shifts in auxin distribution and auxin-related gene expression gradually resolve this initial polarity into the stable regulatory network known to maintain adaxial–abaxial polarity within the developing organ. Our data show that spatial information from an AS2–KAN1 meristem prepattern governs the conversion of a uniform auxin input into an ARF-dependent binary auxin response output to specify adaxial–abaxial polarity. Auxin thus serves as a single morphogenic signal that orchestrates distinct, spatially separated responses to coordinate the positioning and emergence of a new organ with its patterning.

Contributions

A.B., G.P. and M.T. designed the project and experiments. S.M. performed the transient expression assays for investigating interactions among polarity determinants. K.N. performed the ChIP assays. A.B. and G.P. performed all the other experiments and analysed the data with help from M.R.S. A.B., G.P. and M.T. wrote the manuscript.

*These authors contributed equally

For details, see Appendix I

Chapter Two: A Diffusible Small-RNA-based Turing System Dynamically Coordinates Organ Polarity

Emanuele Scacchi*, Gael Paszkiewicz*, Khoa Thi Nguyen*, Shreyas Meda, Agata Burian, Walter de Back, and Marja C. P. Timmermans

Abstract

The formation of a flat and thin leaf presents a developmentally challenging problem, requiring intricate regulation of adaxial-abaxial (top-bottom) polarity. The patterning principles controlling the spatial arrangement of these domains during organ growth have remained unclear. Here, we show that this regulation is achieved by an organ-autonomous Turing reaction-diffusion system centered on mobile small RNAs. The data illustrates how Turing dynamics transiently instructed by pre-patterned information is sufficient to self-sustain properly oriented polarity in a dynamic, growing organ, presenting intriguing parallels to left-right patterning in the vertebrate embryo. Computational modelling demonstrates that this self-organising system continuously adapts to coordinate the robust planar polarity of a flat leaf while affording flexibility to generate the tissue patterns of evolutionarily diverse organ shapes. Our findings identify a small-RNA-based Turing network as a dynamic regulator of organ polarity that accounts for leaf shape diversity at the level of the individual organ, plant, or species.

Contributions

Functional analysis of AS2 mobility via complementation analysis and transient expression assays. Verification of specific interactions within the polarity gene regulatory network. Aided in the design, assembly and editing of figures; helped with writing and editing the paper.

*These authors contributed equally

For details, see Appendix II.

Chapter Three: Multi-layered genetic redundancy buffers miR165/166 morphogen levels to ensure robust organ polarity

Shreyas Meda, Meike Irene Tauber, Wanyan Xi, Gael Paszkiewicz, Agata Burian, Martha Bauer, and Marja C. P. Timmermans

Abstract

Developmental patterning in multicellular organisms is governed by intricate molecular networks that keep the pattern reproducible and robust to perturbations. Within these networks are fragile components that require safeguarding to ensure robustness. However, the molecular mechanisms leading to this are not well understood. In plants, a complex network of Transcription factors (TF) and small RNAs orchestrate adaxial-abaxial (ad-ab) patterning, crucial for a flat leaf geometry. MicroRNA 165/166 is part of a sensitive component of this network and acts as a morphogen ensuring a sharp ad-ab boundary at domain level. Here, by extensive molecular and genetic analysis, we demonstrate the necessity of miR165/166 during ad-ab specification and meristem homeostasis. Its unperturbed activity is ensured by virtue of genetic redundancy within the *MIR165/166* family. At individual gene loci, *MIR166A*, the major contributor of miR165/166, generates the required minimal level for its function. Further, the *MIR166A* promoter harbors redundant *cis* architecture, leading to a robust gene expression that, at a phenotypic level, translates into robust ad-ab patterning, and maintenance of a flat leaf shape. Our data thus provides insights into different mechanisms by which sensitive components are buffered to keep the pattern robust to genetic and environmental perturbations.

Contributions

S.M. and M.T. designed the project and experiments. All experiments and analyses were performed by S.M. with contributions from W.X to quantitative gene expression analysis, M.I.T to CRISPR screening of *pMIR166A* deletions, and G.P and A.B to confocal imaging. M.B. performed preliminary stress experiments.

The CRISPR screening of *pMIR166A* was also a part of the bachelor thesis of Meike Irene Tauber (2021) *"*Identification of *CIS* regulatory elements and diverse transcription factors regulating *MIR166A* expression during leaf polarity establishment in *Arabidopsis thaliana."*

Acknowledgements

We thank Diana Vranjkovic and Richard Gavidia for all the technical help.

Introduction

The development of complex, multicellular organisms depends upon the coordination of countless developmental patterns at cell-, tissue- and organ levels. These patterns must be highly reproducible and fundamentally robust to intrinsic noise, genetic perturbations, and environmental variations. The proper formation of these patterns is governed by the precise spatiotemporal orchestration of complex molecular networks (Wolpert et al., 2015). Here, the arrangement of the network components into specific regulatory motifs and the occurrence of genetic redundancy whereby duplicate genes compensate for aberrant gene function, provide this robustness (Abley et al., 2016; Lachowiec et al., 2015). However, intricate networks often contain fragile, critical hubs and nodes that form sensitive components, the perturbation of which can lead to loss of or changes to patterning (Lempe et al., 2013; Whitacre, 2012). As such, organisms must safeguard these components to keep developmental patterns robust. However, the mechanistic underpinnings for this are poorly understood.

In plants, their sessile nature, and the ability to develop organs post-embryonically, make it particularly vital to have these complex developmental patterns robust over the course of its lifetime. Adaxial (ad)- abaxial (ab) patterning of leaves is one such complex process necessary for the formation of a flat leaf and provides a tractable paradigm to approach this problem (Waites & Hudson, 1995). However, a flat leaf is not a default state but instead requires a stable propagation of a precise ad-ab boundary across the leaf during growth. As such, failure of ad-ab polarity specification and maintenance affects leaf shape, leading to radial leaves that impact the normal functioning and health of the plant (Husbands et al., 2009; Kuhlemeier & Timmermans, 2016; Waites & Hudson, 1995).

The progression of ad-ab patterning involves a network of Transcription factors (TF) and small RNAs (sRNA) which can be divided into three phases: establishment, resolution, and maintenance (Husbands et al., 2009; Kuhlemeier & Timmermans, 2016). Leaves are initiated at the flanking regions of the shoot apical meristem (SAM) periphery; marked by an auxin maximum (Reinhardt et al., 2000). The TFs, ASYMMETRIC LEAVES 2 (AS2) and KANADI 1 (KAN1) form concentric rings of expression at the meristem periphery and mark the adaxial- and abaxial cell fates, respectively. Their early expression contributes to polarity establishment by converting the uniform auxin input into a binary auxin response (Chapter 1- (Burian et al.,

2022)). This is mediated by AUXIN RESPONSE FACTOR 3 (ARF3) (Chapter 1- (Burian et al., 2022)). As the primordia grow, the pre-patterned information must be resolved. The pre-patterned information then gets fine-tuned from an externally derived pattern to an internal autonomous process. During resolution, other TFs, such as those from the Class III Homeodomain-Leucine Zipper (HDZIPIII) family, emerge (Chapter 1- (Burian et al., 2022; Caggiano et al., 2017). During the maintenance phase, ad-ab patterning is maintained by an intricate network of TFs and sRNAs that promote adaxial and abaxial cell fates (Kuhlemeier & Timmermans, 2016). The HDZIPIII family members, PHB (PHB), PHAVOLUTA (PHV) & REVOLUTA (REV), and ASYMMETRIC LEAVES 1 (AS1) & AS2 family members promote adaxial cell fates. Conversely, the abaxial side is promoted by KANADI 1 (KAN1), KAN2, AUXIN RESPONSE FACTOR 3 (ARF3) and ARF4 (Eshed et al., 2001; Lin et al., 2003; McConnell & Barton, 1998; Pekker et al., 2005). However, these TFs alone are unable to create a sharp boundary at the domain level. Mobile signals are necessary to provide the positional information required to form a sharp boundary across the leaf. The sRNAs microRNA165/166 (miR165/166) and TAS3-derived trans-acting short interfering RNAs (tasiRNAs – specifically, tasiARF) in this regard act as morphogens providing the necessary positional information (Chitwood et al., 2009; Skopelitis et al., 2017). miR165/166 is expressed on the abaxial side but moves from its source across the leaf generating a concertation gradient, across the leaf (Skopelitis et al., 2017; Yao et al., 2009). Conversely, tasiARF is expressed on the adaxial side and generates an opposing gradient to that of miR165/166 (Chitwood et al., 2009). These opposing gradients of miR165/166 and tasiARF are assessed by the cells and through a threshold-based readout lead to binary expression of their respective targets, HDZIPIII and ARF3. This leads to the positioning of a sharp and stable ad-ab boundary along the leaf (Skopelitis et al., 2017).

Recently, we have shown that this network of TFs and sRNAs is self-organizing and follows the principles of a Turing system (Chapter 2- Scacchi et al., 2023). This network dynamically adapts to coordinate the spatial distribution of the network components, stably maintaining ad-ab polarity during primordium growth to allow the formation of a flat leaf (Chapter 2- Scacchi et al., 2023). Although the leaf polarity network is generally robust, modelling shows that miR165/166 is part of a sensitive node. In addition, changing its levels alters the wavelength of the Turing dynamics, which leads to a shift of the ad-ab boundary (Chapter 2- Scacchi et al., 2023). As

such, miR165/166 function during ad-ab polarity must be guarded, and its sensitivity attributes could significantly impact ad-ab patterning. Deciphering further the mechanisms behind the regulation of miR165/166 during ad-ab polarity will unravel systems that are in place that organisms utilize to ensure that the sensitive/fragile nodes are protected.

In this study, we show miR165/166's spatiotemporal and quantitative necessity during ad-ab polarity specification, in addition to its known role in maintenance which re-emphasizes its sensitivity during ad-ab polarity. Our data shows that plants have developed diverse mechanisms to buffer miR165/166 activity, ensuring that ab-ad patterning remains robust to genetic and environmental perturbations. Redundancy within *MIR165/166* family members ensures its spatiotemporal activity remains unperturbed upon genetic aberrations. This further protects the miR165/166 function by generating excess miR165/166 beyond the required minimal level. Further, at the individual gene level, the redundant *cis*-regulatory architecture of the *MIR166A* promoter, the dominant contributor of miR165/166, ensures its expression is robust to perturbations. These mechanisms further translate into the phenotypic robustness of ad-ab patterning, guaranteeing a flat leaf under different genetic or environmental variations.

Results

Redundant and Specific Roles of Individual *MIR165/166* Genes Ensure Proper Leaf Development

As a first step, to unravel the mechanisms that safeguard sensitive components we investigated the genetic redundancy within the *MIR165/166* family. Previously we have reported that among all nine *MIR165/166* family members *MIR165A*, *MIR166A*, and *MIR166B* share expression on the abaxial domain of young leaf primordia (Chapter 2-Scacchi et al., 2023). Post primordia emergence, both *MIR166A* and *MIR166B* expression is re-established at the meristem organ boundary where new organs initiate, resulting in a narrow ribbon of expression around the meristem periphery (Chapter -Scacchi et al., 2023). Indeed, cell lineage tracing shows that *MIR166A* expression in the incipient primordium (p-2) marks the abaxial founder cells in the same manner as KAN1 (Chapter-Scacchi et al., 2023). Overall, these observations reveal a dynamic spatiotemporal pattern of *MIR165/166* expression in the shoot apex. Their early expression pattern, in turn, can contribute to the prepatterning of abaxial identity in the leaf (Chapter 2-Scacchi et al., 2023). Multiple active *MIR165/166* loci in the shoot apex with partial overlapping expression patterns point to redundancy among the family members. Analyzing loss-of-function mutants is essential to further decipher how these loci contribute to ad-ab polarity. However, at the time, no loss-of-function mutants were available for *MIR165*/166. Although mutants that quench miR165/166 via short tandem target mimicry (STTM) exist, these cannot clarify the specific contributions of individual *MIR165/166* loci (Yan et al., 2012). To overcome this, knockout mutants of the three *MIR165*/166 loci that are expressed predominantly in the shoot apex, were generated using the CRISPR/Cas9 approach. Two gene-specific guide RNAs were designed to create deletions within the precursors of *MIR165A*, *MIR166A*, and *MIR166B*. For *MIR166A,* a 138 bp deletion was achieved, removing most of the miRNA hairpin (Fig 1A). For *MIR166B,* a 266 bp deletion was obtained, removing over half of the hairpin and its upstream region (Fig 1A). For *MIR165A*, two deletions of 198 (*cr-1*) and 207bp (*cr-2*) were identified, leading to a complete removal of the hairpin (Fig 1A). These allelic changes will likely result in loss-of-function mutants (Lian et al., 2021; Ó'Maoiléidigh et al., 2021).

Phenotypic analysis of the single knockout mutants *mir165a*$^{cr-1}$, *mir166a,* and *mir166b* did not reveal any visible leaf shape or plant architecture defects (Fig 1A, Sfig 1A). Likewise, the double

mutant combination *mir165a*$^{cr-1}$ *mir166b* displayed an almost wild type (WT) phenotype with only occasional mild upward leaf curling (Fig 1B). However, the triple mutant *mir165a*$^{cr-1}$ *mir166a mir166b* showed growth defects with reduced size and severe developmental phenotypes at the shoot apex, with fewer leaf primordia, severely reduced size, and adaxialised cotyledons (Fig 1B). In addition, confocal imaging of the seven-day-old shoot apex identified an enlarged and fasciated meristem structure with a non-spiral phyllotaxy of primordia (Fig 1G). Double mutant combinations containing *mir166a* (*mir166a mir166b* and *mir165a*$^{cr-2}$ *mir166a*) show similar early defects (Fig 1B). These phenotypes reinforce the early role of *MIR165/166* loci at the shoot apex and the existing functional redundancy among them. Although all these mutants share developmental phenotypes such as adaxialisation of the leaf and alteration of the SAM architecture, their morphological changes during subsequent development varied, giving insights into the individual contributions of each locus. (Fig 1C, D). In *mir166a mir166b,* the early phyllotactic defect persists as the plants grow, with leaf positions deviating from the typical spiral arrangement (Fig 1C, D). Confocal microscopy imaging of the *mir166a mir166b* shoot apex revealed that this phyllotactic defect was due to an enlarged and fasciated meristem (Fig 1F). However, the young, mildly upward-curled leaves eventually recover into a WT-like flattened shape (Fig 1D).

Conversely, in *mir165a*$^{cr-2}$ *mir166a* the delayed primordia continues to exhibit growth and morphological defects with increased serration in older leaves (Fig 1C, D). They occasionally also show strong upward curled leaves, consistent with a partial adaxialisation. Indeed, confocal imaging of the older *mir165a*$^{cr-2}$ *mir166a* meristem shows primordia with leaf blade defects and ectopic growth on the abaxial side (Fig 1F). However, the initial phyllotactic defect partially recovers later in development, evident from both visualizations of *mir165a*$^{cr-2}$ *mir166a* meristem and the overall rosette structure in older plants (Fig 1D, F). However, the triple mutant *mir165a*$^{cr-1}$ *mir166a mir166b* shows a combination of both sets of phenotypes, as expected (Fig 1C, D).

These phenotypic analyses collectively reveal that *MIR165/166* loci share functionally redundant roles in the meristem and the leaf. The observed meristematic defects corroborate with the known role of HDZIPIII TFs for meristem homeostasis. Similarly, the leaf developmental defects with adaxialized leaves are in line with a role in ad-ab polarity (McConnell & Barton,

1998; Prigge et al., 2005). The analysis also reveals that consistent with the observed expression patterns, *MIR166B* contributes more to meristem architecture and early leaf development, while *MIR165A* contributes to ad-ab polarity (Fig 1E). In addition, these data suggest that *MIR166A* is the predominant player among *MIR165/166* loci with pleiotropic roles in both meristem homeostasis and ad-ab polarity (Fig 1E).

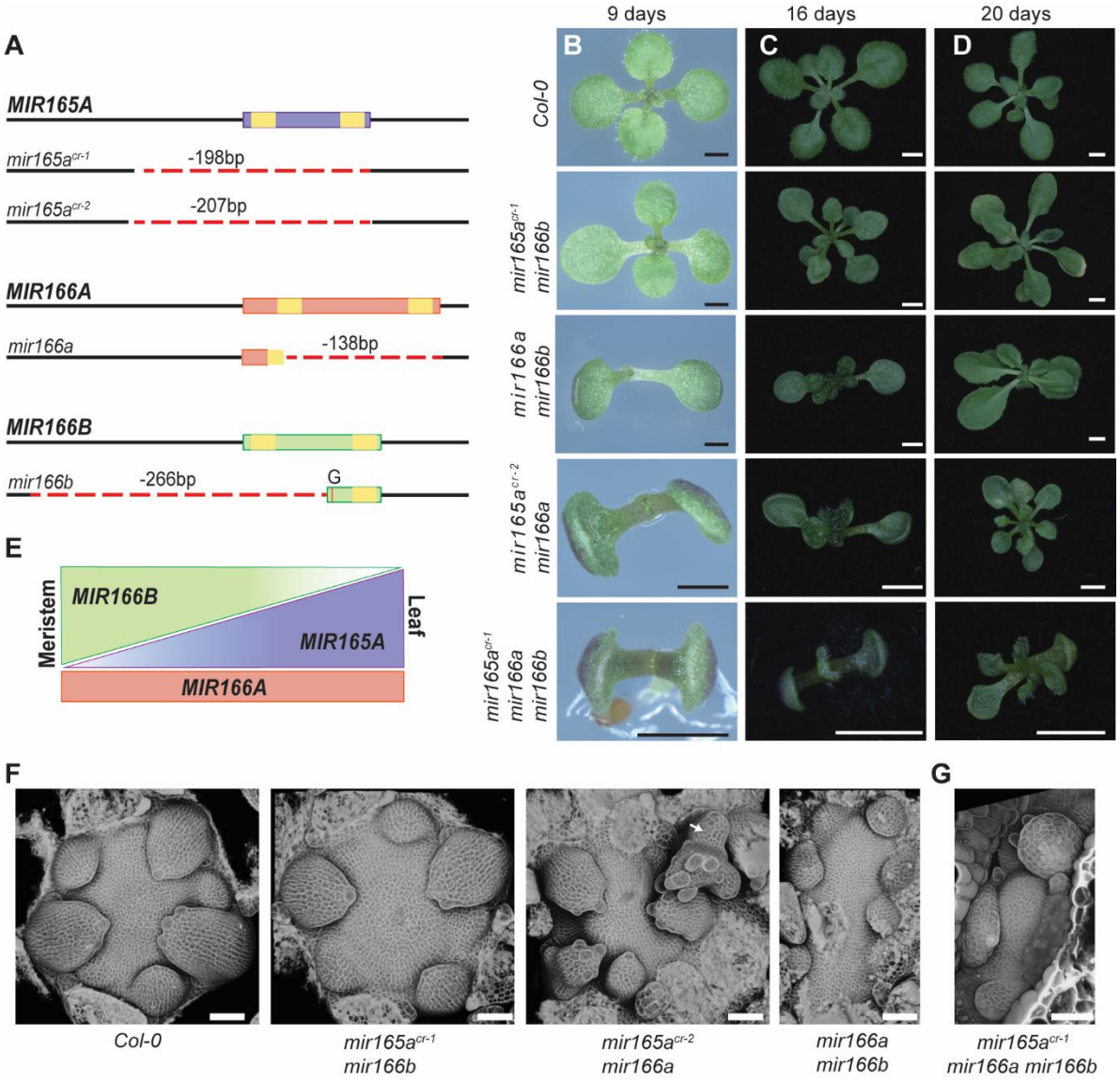

Fig1: **Redundant and specific action of the *MIR165/166* gene family is necessary for meristem homeostasis and leaf ad-ab polarity.** A) Pictorial representation of *MIR165A*, *MIR166A* and *MIR166B* gene around the miRNA stem-loop in wild type (WT, Col-0), and respective CRISPR/CAS9 knock-out alleles. Purple, red, green boxes - stem-loop, yellow boxes-mature/star miRNA, dashed lines (red)- deletions. Base substitution in *mir166b* indicated by the

substituted nucleotide (B) Top view of 9-day-old seedlings of *mir165a^{cr-1} mir166a mir166b* triple and double mutants containing *mir166a* (*mir166a mir166b* and *mir165a^{cr-2} mir166a*), showing severe phenotypic defects with no developed flat leaves and adaxialised cotyledons, contrary to WT and *mir165a^{cr-1} mir166b*. Scale bar: 0.1cm. (C-D) 16- and 20-day old *mir165/166* mutants showing contributions of individual *MIR165/166* loci between *MIR165A*, *MIR166A* and *MIR166B* in SAM architecture and ad-ab leaf patterning. Scale bar: 0.25cm. Note: Recovery of upward curled leaves into flat WT-like shape in *mir166a mir166b*, and recovery of phyllotactic defects in *mir165a^{cr-2} mir166a*, but not in *mir166a mir166b*. (E) Schematic representation showing the role of *MIR166A* in both the SAM and leaf and the predominant role of *MIR166B* and *MIR165A* only in the meristem and leaf, respectively. (F) Top view of >30-day-old shoot apices showing elongated and fasciated meristems in *mir166a mir166b*, while *mir165a^{cr-2} mir166a* show outgrowth of older primordia (white arrow), in comparison to WT and *mir165a^{cr-1} mir166b* (no meristem or leaf defects). (G) Top view of 7-day-old *mir165a^{cr-1} mir166a mir166b* meristem displaying an enlarged and fasciated meristem and non-spiral phyllotaxy. (F, G) Scale bar:50µM.

miR165/166 Generates a Threshold-Based Phenotypic Readout at the Shoot Apex

The morphogen-like role of miR165/166 suggests that quantitative levels might be important for proper activity, as well as its spatiotemporal expression pattern. Indeed, *MIR166A,* the predominant player among *MIR165/166* loci, accumulated higher precursor transcript levels at the shoot apex, as quantified by qRT-PCR, than *MIR166B* or *MIR165A* (Fig 2A). Further, *mir166a (+/-) mir165a^{cr-1} mir166b* mutants with a single copy of *MIR166A* showed an intermediate phenotype, with no noticeable phyllotaxy defects but mild upward curling of leaves, suggesting a dose-dependent effect on its activity (Fig 2B). These results suggest that the miR165/166 level may be vital for its normal activity at the shoot apex.

To further investigate the quantitative role of miR165/166 at the shoot apex, transcript levels of miR165/166 and its target, *PHB*, were measured by qRT-PCR in shoot apices from all single-, double- and triple *mir165/166* mutants (Fig 2C, D). All mutants display a significant reduction in *miR165/166* levels compared to Col-0 (Fig 2C). Moreover, *PHB* levels are significantly increased in all mutant variants except for *mir165a^{cr-1}* (Fig 2D). Interestingly, *mir165a^{cr-1}mir166b* mutants, which display a WT-like phenotype, produced only 33% of WT miR165/166 levels, suggesting excess production by the plant. However, a slight drop in its level to 29% of WT, as observed in *mir165a^{cr-2} mir166a* mutants, leads to phenotypic defects in the shoot apex (Fig 1B, 2C). Further, *mir165a^{cr-2} mir166a, mir166a mir166b* and *mir165a^{cr-1}mir166a mir166b,* which exhibit phenotypic defects at the shoot apex and during leaf development show

significantly different *PHB* levels compared to *mir165a*$^{cr\text{-}1}$ *mir166b* mutants, which display a WT phenotype (Fig 1B, 2D). A key observation here was the necessity of a critical level of miR165/166, where slight changes in its levels as seen between *mir165a*$^{cr\text{-}1}$ *mir166b* and *mir165a*$^{cr\text{-}2}$ *mir166a* lead to significant changes in *PHB* levels, and subsequently plant phenotype (Fig 2C, D). In addition, reinforcing the dominant contribution of *MIR166A* observed from the phenotypic analysis, mutants lacking *MIR166A* loci showed the most significant reduction in miR165/166 and an increase in *PHB* level (Fig 2C, D). Taken together, these results indicate that *miR165/166* regulates its target PHB in a dose-dependent manner at the shoot apex, probably generating a threshold on its activity to ensure proper leaf development (Fig 2E). Further, they reveal the necessity of minimal miR165/166 levels to maintain meristem structure and ad-ab polarity. At the same time, plants produce an excess of miR165/166, which probably contributes towards the robustness of its activity.

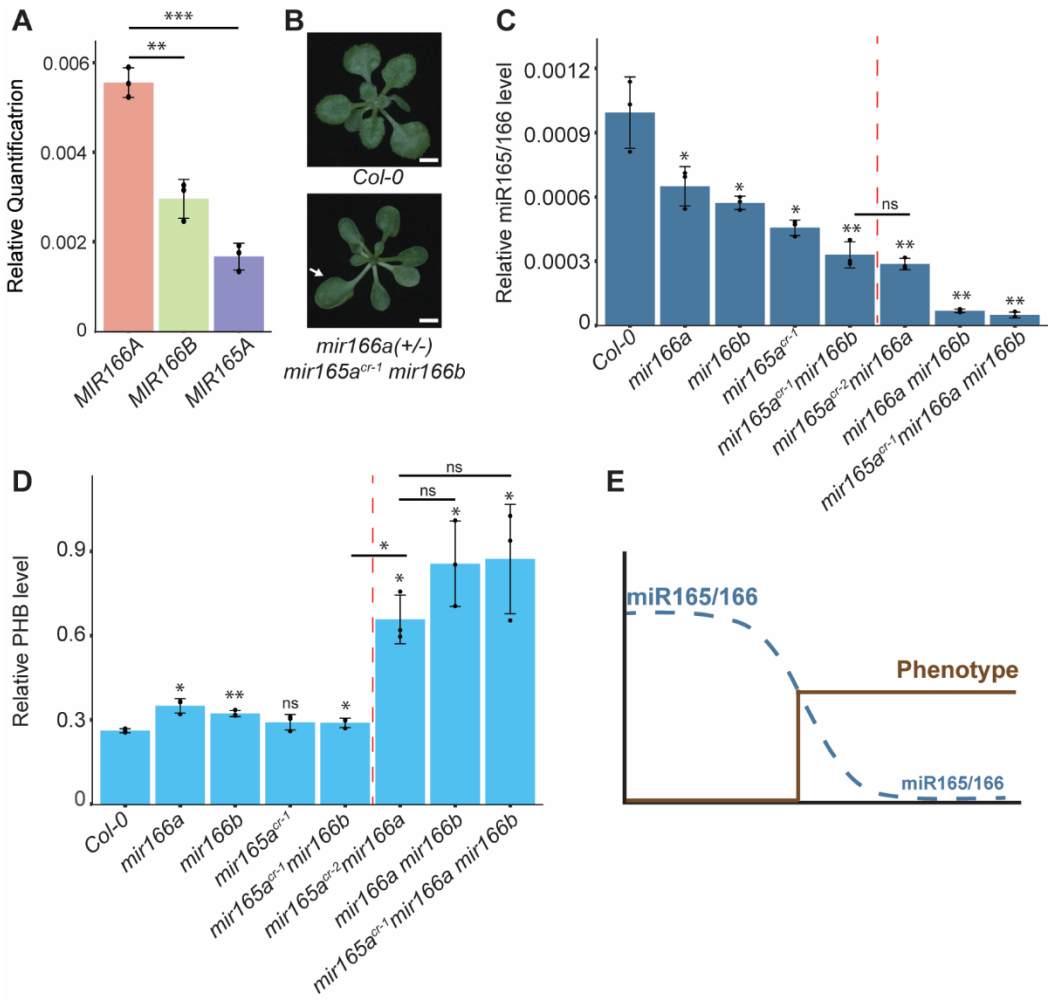

Fig2: **miR165/166 generates a threshold-based phenotypic readout at the shoot apex** (A) Bar plots showing higher relative expression of *MIR166A* than *MIR166B* and *MIR165A* at the shoot apex. Values (mean ±SD, n=3 biological replicates) relative to *PP2A*. Two-tailed Student's t-test: **p <0.01, *** p<0.001 (B) Top view of 16-day old *mir166a(+/-) mir165a*$^{cr-1}$ *mir166b* seedlings showing mild upward curled leaves (white arrow) in comparison to the flat leaves of WT (Col-0). Scale bar: 0.25cm. (C-D) Bar plots showing miR165/166 and *PHB* transcript levels across different *mir165/166* knock-out mutants compared to WT where a small reduction in miR165/166 (C) between *mir165a*$^{cr-1}$ *mir166b* and *mir165a*$^{cr-2}$ *mir166a* mutants leads to a threshold-based phenotypic defect in the plant with significant change in *PHB* level (D). Values (mean ±SD, n=3 biological replicates) relative to *U6* for miR165/166 and *PP2A* for *PHB*. Two-tailed Student's t-test compared to Col-0 unless indicated otherwise: *p <0.05**p <0.01, *** p<0.001. ns- Not significant. The dashed line (red) indicates the thresholding point/level that leads to the phenotypic switch. (E) Schematic representation of dose-dependent activity of miR165/166 leading to a threshold-based binary readout of the phenotype.

Redundant Regulation of *MIR166A* Ensures a Minimal miR165/166 Level at the Shoot Apex

The integrated phenotypic and quantitative analyses of *mir165/166* mutants demonstrate that *MIR166A* is the dominant contributor of miR165/166 at the shoot apex, pivotal to meristem homeostasis and ad-ab polarity. At a quantitative level, *mir165a*$^{cr\text{-}1}$ *mir166b* mutants that carry functional *MIR166A* produce sufficient miR165/166 levels to be above the threshold and have a WT phenotype, suggesting that *MIR166A* ensures a minimal level of miR165/166. Further, *mir165a*$^{cr\text{-}1}$ *mir166b* mutant phenotypes remain robust under mild stress conditions suggesting that *MIR166A* expression is robust (Sfig 2A). This in turn predicts that *MIR166A* expression must be precisely regulated to ensure that the spatiotemporal and quantitative activity of miR165/166 is not perturbed.

Cis-regulatory modules are vital components of transcriptional regulation that ensure precise gene expression (Biłas et al., 2016; Priest et al., 2009). We therefore next sought to dissect the *cis*-regulatory landscape to gain further insights into the regulatory mechanisms governing *MIR166A* accumulation and its pleiotropic effects. Recent studies in *Solanaceae* have successfully dissected the role of *cis*-regulatory modules (CRM) regulating quantitative and pleiotropic gene functions using CRISPR/Cas9 (Hendelman et al., 2021; Rodríguez-Leal et al., 2017). Similarly, taking advantage of the *mir165a*$^{cr\text{-}1}$ *mir166b* mutant with a WT phenotype, the *MIR166A* promoter (*pMIR166*A) was targeted in this background using CRISPR/Cas9, and a phenotypic screen was performed (Fig 3A). This sensitized mutant background enabled the study of the specific contribution of *MIR166A*. A genomic fragment 2.4kb in length upstream of the *MIR166A* hairpin which is sufficient for its function in a complementation assay (Skopelitis et al., 2017), was as such selected as the *MIR166A* promoter.

As a first step, the accessible chromatin regions (ACRs) and conserved non-coding sequences (CNSs) on *pMIR166A* were analyzed. These are two key features of the *cis*-regulatory landscape that serve as a guide to identify CRMs that have gene regulatory roles (Hendelman et al., 2021; Schmitz et al., 2021). Recently, a computational tool developed based on the above and other features of CRMs has been successfully shown to effectively identify *cis* regions that are essential in gene regulation (Zhou et al., 2023). At first, the available *Arabidopsis* leaf ATAC-seq dataset was examined to identify ACRs on *pMIR166A* (Lu et al., 2019). Although peaks that

correspond to ACR close to the proximal end of the promoter were identified, the rest of the promoter was noisy with smaller peaks, the significance of which was unclear (Sfig 3A). Next, to analyze if *pMIR166A* harbors any CNSs with cis-regulatory functions, phylogenetic footprinting was performed on *pMIR166A* across select *Brassicaceae* species. As a result, five conserved non-coding sequences distributed across *pMIR166A* were identified (CNS A, CNS B, CNS C, CNS D, CNS E) (Fig 3C).

Furthermore, CNS D, CNS E and part of CNS C regions were also found to be conserved between *pMIR166A* and *pMIR166B*, genes sharing similar expression patterns at the shoot apex (Sfig 3B). However, no conserved regions were obtained with other members of the family (not shown). Also, CNS D and CNS E overlap with the ATAC-seq peaks (Sfig 3A). Based on this analysis, multiple *cis* regions across the entire promoter could have a functional role. As such, CRISPR/Cas9 guides were designed to target different regions encompassing the entire *pMIR166A* (Fig 3A).

Altogether, 54 *pMIR166A cis* alleles were generated, primarily consisting of deletions and occasionally other modifications such as insertions and inversions across *pMIR166A* (Fig 3B, Sfig 4A). Intriguingly, none of the *pMIR166A cis* mutants display the *mir165a*$^{cr\text{-}1}$ *mir166a mir166b* phenotype (Fig 3D). In addition, some of these *cis* mutants had a deletion of either the entire or significant portions of the CNS A, B, C, and D (#5,19,26,34) but showed no phenotypic difference compared to *mir165a*$^{cr\text{-}1}$ *mir166b* (Fig 3D, Sfig 4B). These results suggest either these multiple CRMs are redundant or have an impact on *pMIR166A* regulation.

A mild phenotype, with rolled and partial adaxialized leaves, was observed when ~250 bp encompassing the transcription start site (TSS) that overlaps with CNS E was deleted (#76) (Fig 3D). In addition, a similar phenotype was obtained when a part of CNS D was deleted along with this 250bp fragment (#42) (Fig 3D). Using our large *cis* mutant collection, we tried to identify if smaller *cis* regions exist within this 250 bp that contribute to the observed phenotype. Two *cis* mutants #41 and #74 partially overlap with the CRM of #76. However, no phenotype was seen upon a smaller deletion of 93 bp (#41) on *pMIR166A*, partially overlapping with ~250 bp, which also deleted the TSS (Sfig 4C). A phenotype milder than #76 with slightly upward curled leaves presented when ~326 bp was deleted (#74) (Fig 3D). In this case, 176 bp overlapped with CNS D and the remaining 150 bp of the deletion overlapped with the ~250 bp, but not the TSS (Fig

3B). All these results show that the entire 250 bp overlapping with CNS E of *pMIR166A* encompassing the TSS plays a role in *MIR166A* regulation.

Further, visualizing 3xVenus_N7 driven by *pMIR166A* lacking CNS E show comparable expression to the *pMIR166A* (WT) reporter line at the shoot apex (Fig4 A). To assess whether CNS E is sufficient to drive *MIR166A* function, *mir166a mir166b* mutant was complemented with 276bp comprising CNS E fragment driving miR166A. However, this construct fails to complement the *mir166a mir166b* mutant phenotype (Fig 4B). These results reveal that the first 250 bp of *pMIR166A*, possibly containing its minimal promoter, only partially contributes to its function and that multiple additional *cis*-regulatory regions spanning *pMIR166A* redundantly contribute to *MIR166A* activity.

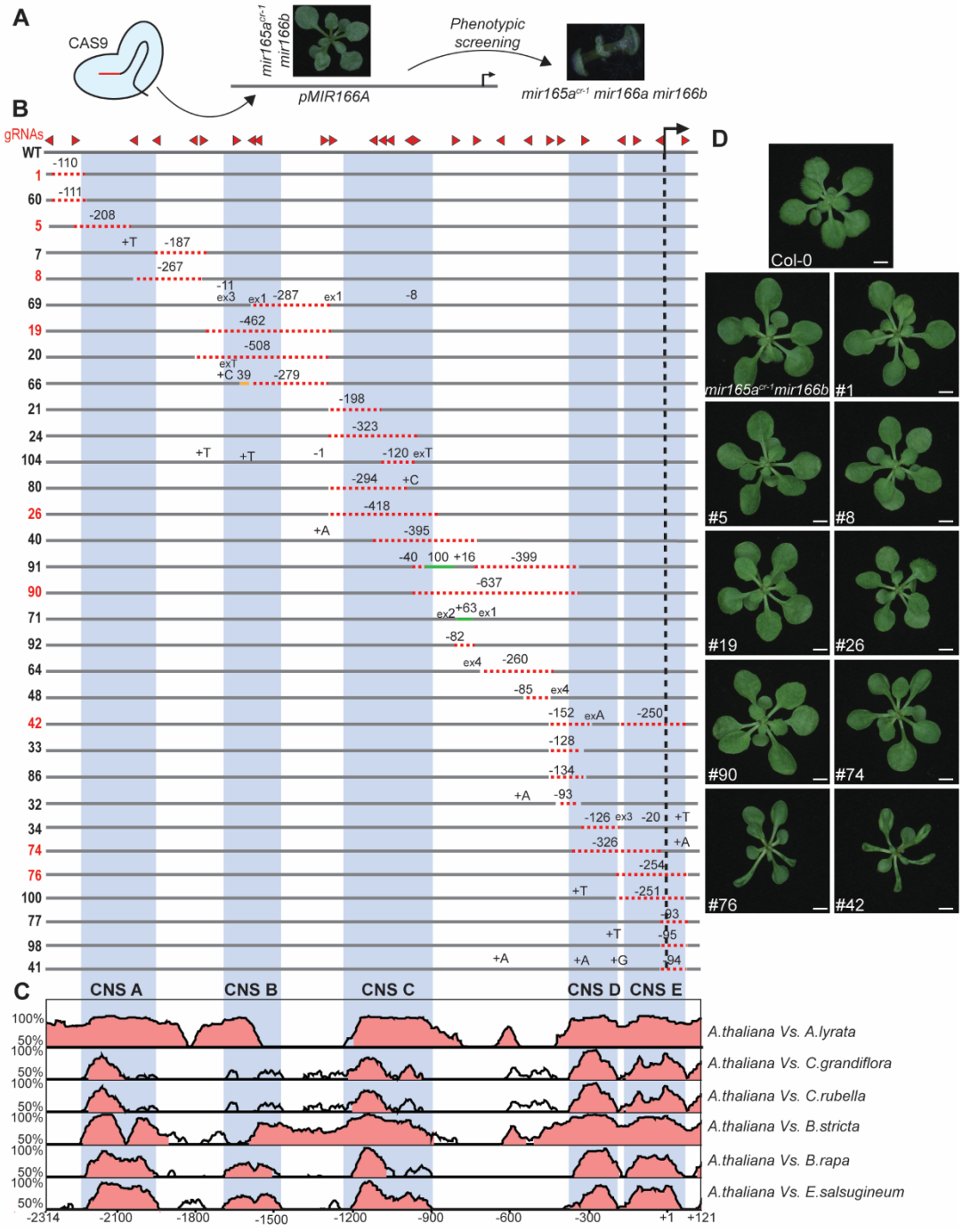

Fig3: **Multiple redundant *cis*-regulatory modules regulate *MIR166A* at the shoot apex.** (A) CRISPR-CAS9 mediated *cis* mutants were generated across the *MIR166A* promoter (*pMIR166A*) in the *mir165a*$^{cr\text{-}1}$ *mir166b* background to screen for *mir165a*$^{cr\text{-}1}$ *mir166a mir166b*-like phenotype. (B) Schematic representation of 32/54 *cis pMIR166A* alleles are shown. Smaller deletions (-), insertions (+), and substitutions (ex) are marked with numbers and letters. Red (dashed), yellow, and green lines indicate large deletions, inversions, and insertions, respectively. Red arrowheads, gRNAs. Grey boxes indicate the *pMIR166A* and the black dashed line with the arrow indicates the TSS. (C) Phylogenetic footprinting of *pMIR166A* between *A.*

thaliana and 5 select species of *Brassicaceae* depicted by sequence alignments using mVISTA showing CNS. Pink regions of the mVISTA plot showing >70% similarity over a 100bp window. CNS are shaded blue. (D) Top view rosettes of 18-day-old *cis* mutants spanning *pMIR166A,* showing no *mir165a*$^{cr-1}$ *mir166a mir166b*-like phenotype. The 9 *cis* alleles are numbered in red in panel B. Note the mild phenotypes observed only when harboring *cis* deletions at the proximal end of *pMIR166A* encompassing the TSS (#76 and #42). Scale bar: 0.25cm.

We have shown that the optimal miR165/166 amount is essential for normal ad-ab polarity and flat leaf architecture, and hence, to understand if these *cis* mutants alter its level, the miR165/166 levels in nine *cis* mutants that together span the whole *pMIR166A* were quantified (Fig 4C). Six *cis* alleles (#1,5,8,19,26,90) with no phenotype showed no significant changes in miR165/166 levels compared to *mir165a*$^{cr-1}$ *mir166b* (Fig 4C). However, the two *cis* alleles (#42,76) with adaxialized leaves indeed exhibited a reduced miR165/166 level (Fig 4C). In addition, the *cis* mutant (#74), which displayed a milder polarity phenotype having slightly upward curled leaves, appears to have a miR165/166 level between the *cis* mutants with no phenotype (#1,5,8,19,26,90) and with adaxialised leaves phenotype (#42,76). These quantitative studies are reminiscent of the dosage-dependent miR165/166 activity described before.

This CRISPR screening for CRMs of *pMIR166A* demonstrates that the pleiotropic function of *MIR166A* in the shoot apex is not driven by a discrete single CRM, but rather by multiple *cis*-regulatory modules in a redundant manner. This involves multiple- or redundant enhancers. Further, the quantitative analysis of miR165/166 in these mutants demonstrates that this redundant regulation ensures a minimal miR165/166 level needed for its thresholding activity at the shoot apex.

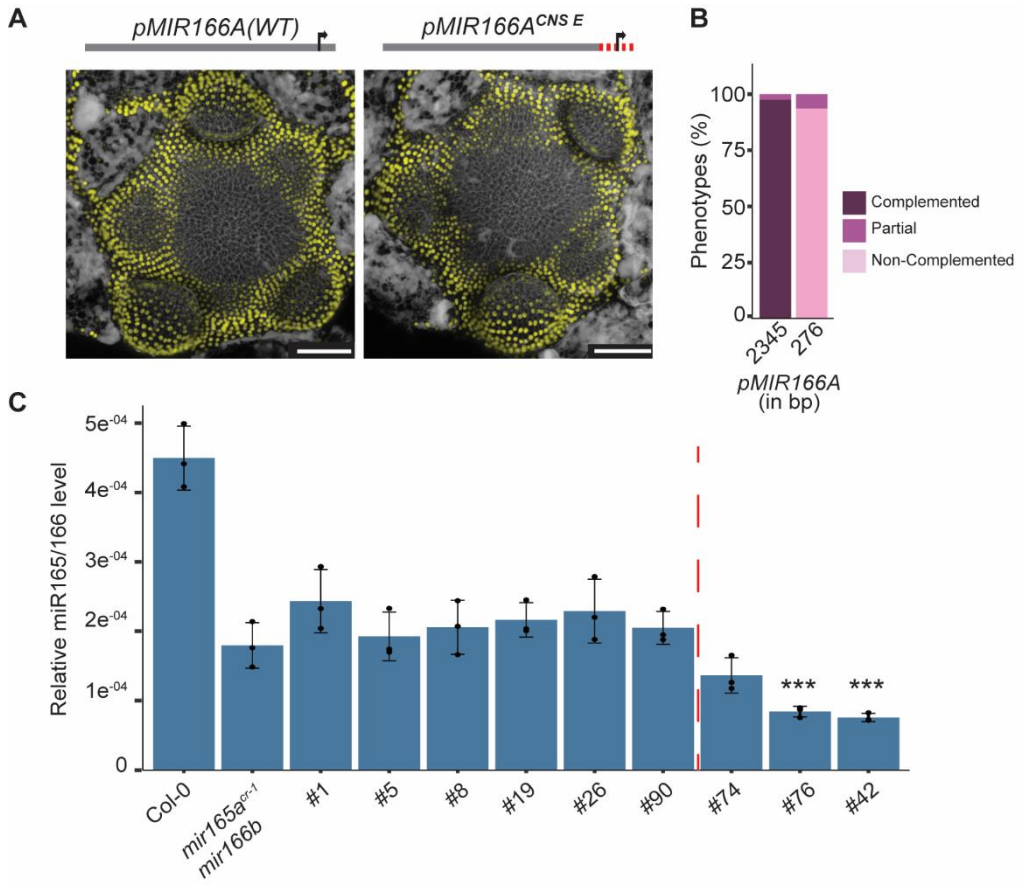

Fig4: **Quantitative, redundant activity of *MIR166A* CRMs ensures a minimal level of miR165/166 at the shoot apex.** (A) Top view of shoot apices of transcriptional reporters for *pMIR166A* lacking CNS E, showing a similar pattern of expression like full-length WT *pMIR166A*. Scale bar: 50µM. (B) Stacked bar plots showing successful complementation of *mir166a mir166b* phenotype with full-length *pMIR166A* of 2435 bp but not with 276 bp of *pMIR166A* comprising only CNS E. (C) Bar plot showing reduced miR165/166 level in *cis* mutants #42 and #76 that display a phenotype compared to *miR165a*$^{cr-1}$ *miR166b*, but not the other *cis* mutants that lack a phenotype. Values (mean ±SD, n=3 biological replicates) relative to U6. Two-tailed Student's t-test compared to *miR165a*$^{cr-1}$ *miR166b*: *** p <0.001. The dashed line (red) indicates the thresholding point that leads to the phenotypic switch.

Complex *MIR166A* Transcriptional Regulation Orchestrates miR165/166 Activity Robust to External- and Internal Perturbations

The involvement of multiple CRMs ensures transcriptional regulation of *MIR166A* is tolerant to mutational perturbations. They also ensure that the minimal level of miR165/166 is produced, such that it remains within the optimum range for proper activity. However, often gene expression is perturbed under non-ideal or stress conditions and plants/organisms have developed buffering mechanisms to keep them robust to perturbations (Lachowiec et al., 2015; Lempe et al., 2013). In animals, the importance of redundant *cis* regions to buffer gene expression is exposed under non-optimal conditions (Perry et al., 2010). To further investigate if the regulation of *pMIR166A* is tolerant to environmental perturbations, six *cis* mutants spanning *pMIR166A* #1,5,8,19,26,90, with no phenotypes under standard long-day conditions, were subjected to moderate heat and light stress conditions. These are primary factors affecting leaf growth and development (Li et al., 2021) (Fig 5A-F). Under low light conditions (60 µmol m^{-2} s^{-1} UML), neither *mir165a*$^{cr-1}$ *mir166b* nor any of the six *cis* mutants display a discernible phenotypic effect on overall plant morphology when compared to standard light conditions (120 UML, Fig 5A, B). Likewise, no phenotypic change is observed under constant light (120 UML, 24 hours, Fig 5D). Although growing plants under high light of 300 UML decreased the rosette size of all the plants, none of the mutants showed a difference in leaf curling or ad-ab polarity (Fig 5C).

Next, plants were subjected to heat stress (28 °C and 30 °C). At 28 °C, irrespective of the genotype or the *cis* mutant analyzed, there were always variable numbers of stressed plants. However, all other plants showed no change in leaf flatness or polarity compared to *mir165a*$^{cr-1}$ *mir166b* (Fig 5E). Similarly, under heat stress of 30 °C, none of the *cis* mutants showed any leaf defects compared to *mir165a*$^{cr-1}$ *mir166b*. Interestingly, at 30 °C, all the Col-0 plants were severely stressed (Fig 5F). The lack of leaf morphology defects in the *pMIR166A cis* mutants under stress conditions suggests that the miR165/166 level might be within the optimal range necessary for its activity. Further, analysis of *cis* mutants (#42,74,76), that already have a mild adaxialized leaf phenotype under standard conditions, revealed no phenotypic enhancement under the above light and heat stresses (Fig 5A-F, Sfig 5A). Instead, *cis* mutant #74, displayed much weaker leaf phenotypes under low light, high light, and heat stress conditions (Fig 5A, C,

E, F) while *cis* mutants #42 and 76 displayed weaker phenotypes specifically under low and high light conditions (Sfig 5A).

Collectively, these results show that regulation of *MIR166A* by multiple CRMs ensures optimal miR165/166 activity robust to mutational and environmental perturbations. This precise *MIR166A* regulation translates further into the phenotypic robustness to develop a flat leaf at the organ level.

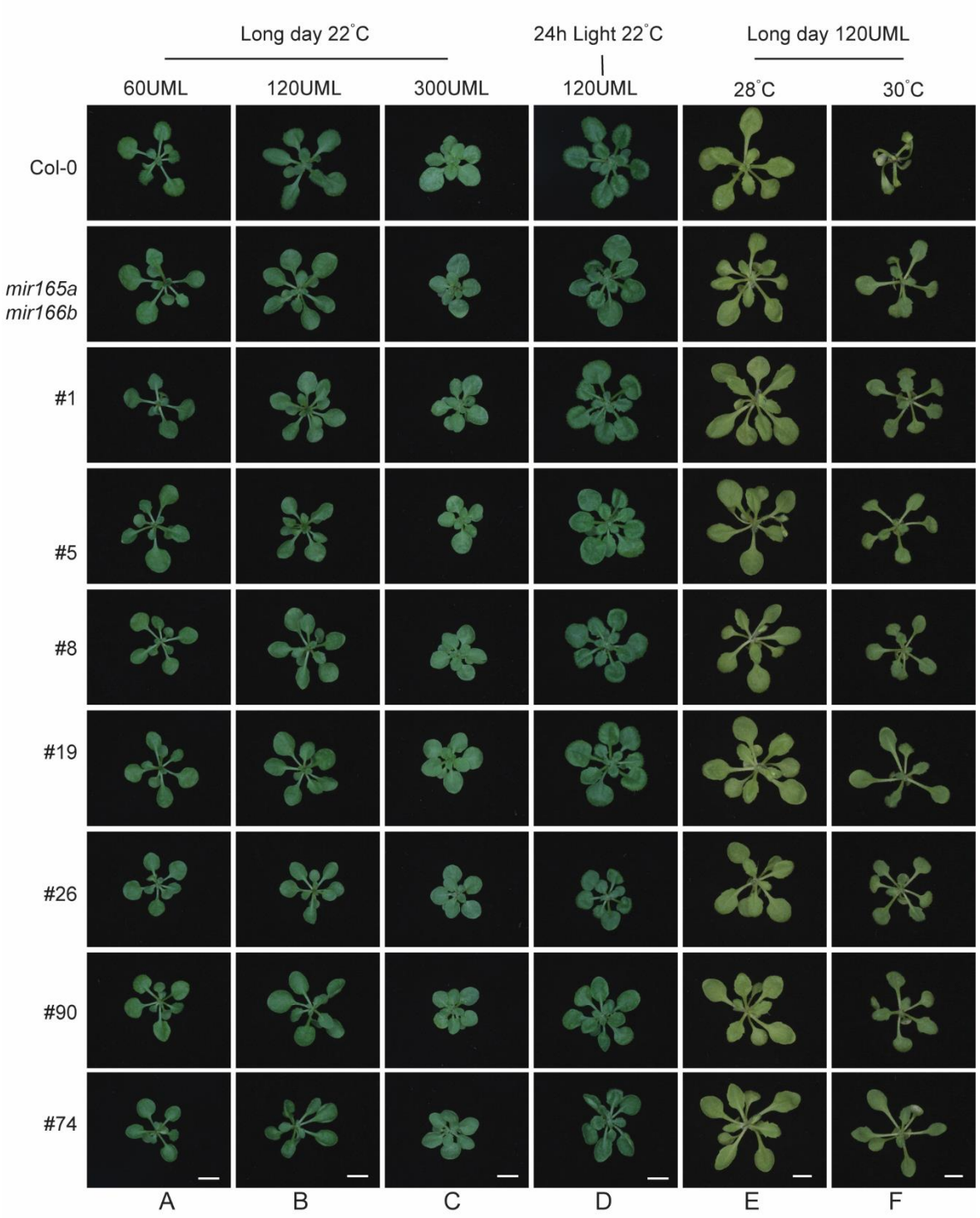

Fig5: **Redundant *MIR166A cis*-regulation ensures robust miR165/166 activity upon environmental perturbations.** (A-F) Top view of 18-day-old rosette of *cis* mutants of *pMIR166A,* subjected to various light and heat stress conditions. *Cis* mutants (#1,5,8,19,26,90) show no phenotypic changes compared to *mir165a*$^{cr\text{-}1}$*mir166b* in leaf shape or phyllotaxy under low light (A), high light (C), or continuous light (D), and standard light conditions (B). Similarly, no discernable phenotypes were observed under heat stress at 28°C (E) and 30°C (F). *Cis*

mutants #74 show weaker phenotypes under low light (A), high light (C), and heat stress at 28°C (E) and 30°C (F) conditions compared to standard conditions (B). Note that plants under high light show smaller rosette sizes while under 30°C petioles are elongated but the flat leaf shape remains robust. Under 30°C only Col-0 shows a severely stressed phenotype. Scale bar: 0.5cm

Discussion

Sensitive components within developmental networks must be safeguarded to ensure the developmental patterning remains robust even in the presence of diverse perturbations (Whitacre, 2012). However, mechanisms of how plants cope with sensitive nodes are poorly understood. Adaxial-abaxial (ad-ab) polarity, necessary for flat leaf formation is an example to study mechanisms of robustness, where flat leaf shape is sensitive to changes (reviewed in (Husbands et al., 2009)) (Chapter 2- Scacchi et al., 2023). The ad-ab patterning is controlled by an intricate network of TFs and sRNAs, among which miR165/166 is part of a sensitive node (Chapter 2- Scacchi et al., 2023). In this study, we show the spatiotemporal and quantitative requirement of miR165/166 early on during ad-ab polarity specification, highlighting its necessity to be safeguarded by the plant. In this study, in-depth analysis using miR165/166 function as a tractable paradigm, we show diverse mechanisms plants have developed to ensure unperturbed activity of miR165/166 during leaf flattening. Further, we show that miR165/166 activity is regulated in a complex and redundant manner both at the family- and individual gene levels. We define these complex regulatory underpinnings to be mechanisms by which plants safeguard miR165/166 function, thereby ensuring a flat leaf, robust to perturbations.

Spatiotemporal and Quantitative miR165/166 Activity Necessary at the Shoot Apex

This study shows that miR165/166 mediated repression of HDZIPIII TFs is necessary for structuring SAM architecture and ad-ab polarity specification. The in-depth molecular and genetic analyses highlight that spatiotemporal and dose-dependent effects of miR165/166 activity are necessary for their proper functioning at the shoot apex.

miR165/166 loss-of-function mutants display a fasciated meristem with phyllotaxy defects. These phenotypes are reminiscent of HDZIPIII gain-of-function mutants, reemphasizing miR65/166 role for SAM homeostasis (McConnell & Barton, 1998). It is well known that the *WUS-CLV3* pathway controls for stem cell homeostasis (reviewed in (Fletcher, 2018)). Genetic analysis on HDZIPIII mutants and *MIR165/166* overexpression lines in combination with *wus* mutants has shown that the miR165/166-*HDZIPIII* module regulates an independent pathway parallel to that of *WUS-CLV3* and limits stem cell specification (Jung & Park, 2007; Lee & Clark, 2015). However, this pathway's precise mechanism and downstream players are poorly

understood. The collection of *miR165/166* mutants generated in this study provides an ideal toolbox to further understand the molecular players downstream of the miR165/166-*HDZIPIII* pathway and its overlap with the *WUS-CLV* pathway governing SAM homeostasis.

In addition to its role in stem cell homeostasis, miR165/166 restricts HDZIPIII expression to the adaxial side during the maintenance phase of ad-ab polarity (Skopelitis et al., 2017). However, our findings suggest a much earlier role during polarity establishment. This is apparent by the early *MIR165/166* expression at the meristem periphery that marks the abaxial founder cells (p-2) and the phenotypes displayed by the miR165/166 mutants (Chapter 2- Scacchi et al., 2023).

Interestingly, at the meristem periphery, REV (HDZIPIII) is not expressed in the entire incipient primordium (p-2), as opposed to expected polarized adaxial expression like in the later stages of leaf development (Chapter 1- (Burian et al., 2022)). This raises an intriguing question, why HDZIPIII expression is inhibited at the meristem periphery, during initial polarity establishment? Our data suggests that this might be to separate the function of HDZIPIII between the stem cells and the leaf. As the SAM develops and undergoes cell fate changes, the meristematic function of HDZIPIII must be confined to prevent ectopic meristematic cell fate, thereby ensuring proper spatiotemporal leaf development and ad-ab polarity specification. Indeed, loss of *MIR165/166* mutants leads to an enlarged and fasciated meristem with phyllotactic defects and delayed leaf growth.

Besides the spatiotemporal gene expression, our data shows that the dosage of miR165/166 is critical for its activity. Quantitative analysis in *MIR165/166* loss-of-function mutants show that the dose-dependent miR165/166 activity on HDZIPIII in the shoot apex is essential for developing a flat leaf. Intriguingly, this dosage effect generates a threshold-based phenotypic readout. This effect at the phenotypic level is plausibly a translation of its morphogenic behaviour shown before at a cellular level during ad-ab polarity (Skopelitis et al., 2017). In the leaves at a cellular level, miR165/166 follows a rheostat-clearance mode of thresholding behaviour leading to a binary readout of HDZIPIII. Accordingly, when the level of the miR166/HDZIPIII (small RNA/target) ratio is above a certain threshold, it entirely turns off HDZIPIII gene expression on the abaxial side (clearance mode). In contrast, when the miR166/HDZIPIII ratio is below the threshold, the expression of the HDZIPIII is less variable on the adaxial side of the leaf (rheostat mode) (Skopelitis et al., 2017). However, at the meristem

periphery, miR165/166 activity leads to no expression of the HDZIPIII, suggesting exclusively a clearance mode of thresholding behaviour. Indeed, in the leaf increasing the concentration of an artificial miRNA at its source in an inducible manner shifts the thresholding behaviour from a rheostat-clearance mode exclusively to a clearance mode (Skopelitis et al., 2017). As such, it is plausible that at incipient primordium (p-2), abaxially expressed miR165/166 shows only clearance mode, thereby inhibiting HDZIPIII completely across the incipient primordia (p-2). Further, as the primordia develop (from p0), either reduced expression of the miR165/166 at its source or induction of HDZIPIII could change the small RNAs/target ratio, shifting the behaviour towards the rheostat-clearance model and leading to a polarized HDZIPIII expression like in leaf polarity maintenance (Skopelitis et al., 2017). In addition, primordia growth and development lead to changes in cell number between the ad and ab sites of the primordia, which could plausibly alter the diffusion and concentration gradient of the morphogen. This could be an alternative explanation for the shift in the thresholding behaviour to a rheostat-clearance model in older primordia. However, time-lapse imaging and quantification of miR165/166 and HDZIPIII activity in the meristem periphery (p-2) would be essential to support this hypothesis.

Further, adding more insights into the quantitative function of miR165/166 was the enlarged and fasciated meristem in *MIR165/166* loss-of-function mutants reminiscent of *men1 and Jabba-1D (jba-1D)* mutants that overexpress miR166a and miR166g, respectively (Kim et al., 2005; Williams et al., 2005). These phenotypic defects raise an intriguing hypothesis about whether the miR165/166 buffering range is capped by a second threshold, suggesting an optimal window of expression level for its activity. Analyzing and quantifying miR165/166 levels in vegetative shoot apices of miR165/166 overexpression lines will aid in further understanding the double threshold effect. Interestingly, the phenotypic defect of the SAM when outside the optimal window is similar with enlarged meristems, while in the leaf, both *men1/+ and jba-1D mutants* have downward curled leaves, converse to those of *MIR165/166* mutants (Kim et al., 2005; Williams et al., 2005). The phenotypic similarity at the meristem periphery could be due to antagonistic contributions from different HD-ZIPIII family members in this context, as has been noted previously for REV, PHB and CORONA (CNA) (Prigge et al., 2005).

This study resolves the early roles of *MIR165/166* at meristem and different stages of ad-ab polarity, from inception to its maintenance. The early functions of *MIR165/166* can be divided

into two roles: firstly, at the PZ to maintain stem cell homeostasis, and secondly to separate the functions of HDZIPIII between the stem cell and the leaf. This ensures proper spatiotemporal positioning of the leaf at the shoot apex. miR165/166 later roles during ad-ab patterning ensure that the developing leaf remains flat throughout growth and development. Further, we demonstrate the necessity of optimum levels of miR165/166 for its activity on HDZIPIII to ensure these functions. In this regard, studying the other small RNA involved in ad-ab polarity, tasiARF (Chitwood et al., 2009), would be the natural next step in gaining further insights into the role of small RNAs during different stages of ad-ab polarity.

Genetic Redundancy of the *MIR165/166* Family Orchestrates Robustness of Flat Leaf

Having demonstrated a vital role for miR165/166 across the different stages of ad-ab patterning and its sensitivity towards optimum levels, we next examined what mechanisms exist to safeguard miR165/166 function during leaf development. Genetic redundancy is a common mechanism in this regard, whereby the organism compensates for the loss of gene function through the action of other genes. This entails either the occurrence of multiple gene copies sharing overlapping functions resulting post multiple rounds of whole genome duplication during evolution or non-homologous genes in independent pathways driving similar mechanisms (Diss et al., 2014; Kitano, 2004; Wagner, 2008). *Arabidopsis thaliana* has undergone three rounds of whole genome duplication, increasing redundancy complexity (Simillion et al., 2002). Here, we demonstrate, the robust spatiotemporal and quantitative activity of miR165/166 via genetic redundancy, at the gene family level. In addition, the genetic redundancy also leads to other molecular mechanisms to keep the miR165/166 activity robust at the shoot apex.

At a spatiotemporal level, overlapping expression patterns between *MIR166A* and *MIR165A* in the abaxial primordia (from p1), and between *MIR166A* and *MIR166B* at the meristem organ boundary suggest redundancy. Individual *MIR165/166* loci are dispensable, but the *mir165a*$^{cr\text{-}1}$ *mir166a mir166b* triple mutant displays defects in the shoot apex, indicating functional redundancy. Although there are specific differences in phenotypic strength and temporal effects, the double mutant combinations *mir165a*$^{cr\text{-}2}$ *mir166a* and *mir166a mir166b* affect similar aspects of meristem homeostasis and ad-ab polarity. Similar functional redundancy among members of

the *MIR164* and *MIR172* families, regulating shoot development and flowering time, respectively, are known (Lian et al., 2021; Ó'Maoiléidigh et al., 2021; Sieber et al., 2007). In the *MIR172* family, three members, *MIR172A, MIR172B*, and *MIR172D*, are predominant in controlling flowering time, while the other two, *MIR172C* and *MIR172E*, are only minor contributors (Lian et al., 2021; Ó'Maoiléidigh et al., 2021). Similarly, the necessity of *MIR166A* and its dominant contribution to the shoot apex is evident from both its spatiotemporal expression and mutational analysis. Phenotypic and quantitative analysis of knockout mutants reinforces its dominant role, with only double mutants lacking *MIR166A* dropping the miR165/166 levels below the threshold and displaying phenotypic defects. Further, *MIR166A* being the dominant player at the shoot apex showed a higher expression level than its counterparts. Similarly, the predominant contributors of the *MIR172* family also have a higher expression level than the minor contributors as similarly seen with (Ó'Maoiléidigh et al., 2021). On the other hand, genetic analysis reveals specific contributions of the induvial miR165/166 loci during flat leaf development. *MIR166B* and *MIR165A* show predominant roles in stem cell homeostasis and ad-ab polarity in the primordia, respectively. Their contributions correlate with their spatiotemporal expression patterns at the shoot apex (Chapter 2-Scacchi et al.,2023). The partial redundancy among the members explains the initial leaf patterning defects in double mutants, which are corrected during the later stages of development. Although *MIR166A* is the dominant contributor at the shoot apex, single *mir166a* mutants showed no discernible phenotype. It is known that redundant genes compensate for the loss-of-function of their counterparts (Diss et al., 2014). Similarly, it is plausible that in the absence of *MIR166A*, other *MIR165/166* genes compensate for its loss, keeping the miR165/166 function robust.

Investigation into the evolution of *MIR165/166* members provides further insights into their function. In the early land plants, *Marchantia polymorpha*, only *MIR166A* and *MIR166B* are identified, with *MIR166A* substantially higher expressed, plausibly reemphasizing its dominant contribution (Tsuzuki et al., 2015). However, whether the *MIR166A* across species are orthologous and show similar dominant functions is not known. It is known that during gene duplication events, genes may retain their ancestral function, or diverge from this, retaining only part of the function (sub-functionalization) or develop novel functions (neo-functionalization) (Birchler & Yang, 2022; Ma et al., 2021; Maher et al., 2006). Phylogenetic analysis demonstrates that *MIR166A* and *MIR166B* evolved from a large duplication and belong to the same clade,

while *MIR165A* forms a distinct clade (Hashimoto et al., 2018; Maher et al., 2006). The redundant and specific roles of *MIR165/166* members suggest that during evolution, *MIR166A* plausibly retained the ancestral gene function. At the same time, *MIR166B* and *MIR165A* may have undergone sub-functionalization with roles related to meristem homeostasis and ad-ab polarity, respectively. Interestingly, *MIR165A* expression in the centre of the meristem-lateral organ boundary overlaps where the future axillary meristem (AM) originates, suggesting neofunctionalization (Chapter 2- Scacchi et al.,2023). Indeed, AGO10 sequesters miR165/166, promoting REV expression and leading to axillary meristem development (Zhang et al., 2020). As such, it is plausible that *MIR165A* prevents premature axillary meristem formation during the vegetative phase by repressing HDZIPIII. Imaging of *pMIR165A* reporter lines in shoot apices during the transition to flowering will provide greater insights into the role of *MIR165A* in AM formation.

The key finding in this study was that the functional redundancy of *MIR165/166* members at a quantitative level safeguards its function at the shoot apex by excess production of miR165/166. The excess production is evident from the absence of phenotypes in all *MIR165/166* single mutants and *mir165a*$^{cr\text{-}1}$ *mir166b* double mutant despite producing significantly reduced miR165/166 levels than in Wild Type. Such excess production of miRNA is also observed in the *MIR159* family, whereby miR159a and miR159b are fully redundant and single mutants show no phenotypic change (Allen et al., 2007). However, unlike *MIR159* single mutants that show no change in level or phenotype, the *MIR165/166* single mutants alter the level of their targets but still lack a phenotype (Allen et al., 2007). This further suggests the presence of an extensive buffering range for optimal miR165/166 morphogen-like function, leading to phenotypic robustness in forming a flat leaf.

However, increased concentration of the small *RNA* can shift the boundary position and affect patterning (Skopelitis et al., 2017). As such, the morphogen gradient must also remain robust. Different mechanisms in animal studies have been identified, demonstrating how morphogen gradients are robust to gene dosage (Barkai & Shilo, 2009). For example, in the case of the BMP (Bone Morphogenic Protein) morphogen gradient in *Drosophila,* excess morphogen is buffered by storing it in a restricted space lacking its inhibitor, ensuring the gradient is not altered (Eldar et al., 2002). However, such mechanisms in modulating miR165/166 gradients are not known. In

the miR165/166 scenario, post-transcriptional mechanisms such as the activity of AGO10 that sequesters miR165/166 in the SAM could buffer excess levels, which needs to be analyzed (Zhu et al., 2011).

miR165/166 quantification data in the mutants lacks the resolution of spatiotemporal changes in the meristem periphery and primordia, which is essential for understanding the robustness of these morphogen gradients. Going forward, using an inducible system, the spatiotemporal and quantitative levels of miR165/166 can be manipulated in a controlled manner to understand further the robustness of its morphogen activity and to decipher mechanisms that translate its function from tissue- to organ levels.

Overall, this work shows in part that plants via genetic redundancy at the family level ensure robust activity of miR165/166 at spatiotemporal and quantitative levels. Further, the redundancy compensates for the loss of miR165/166 level by generating excess miR165/166, ensuring its levels remain within the thresholding activity. These mechanisms ensure miR165/166 function is not perturbed and in turn, translate to phenotypic robustness, ensuring the formation of a flat leaf. Analysis of *MIR165/166* loss-of-function mutants under diverse environmental stresses would provide further insights into this robustness.

Redundant *cis*-Regulation of *MIR166A* Confers Phenotypic Robustness at the Shoot Apex

Besides genetic redundancy at the family level, this work unravels mechanisms also at the individual gene level that help plants cope with sensitive components of a network. It is demonstrated that redundant *cis*-regulatory modules (CRMs) regulate *MIR166A*, the dominant contributor at the shoot apex, ensuring the minimal level of miR165/166 expression necessary for its function at the shoot apex. This robust *MIR166A* expression further confers phenotypic robustness in the plant. CRMs are vital components of transcriptional regulation and, spatiotemporally fine-tune gene expression in developmental programs (Hendelman et al., 2021; Marand et al., 2023; Priest et al., 2009). Recent studies in tomato, rice, and maize demonstrate the importance of understanding CRMs for improving crop yield traits (Liu et al., 2021; Rodríguez-Leal et al., 2017; Zhou et al., 2023). Similarly in this study, analyzing the *pMIR166A*

cis-regulatory allelic collection generated by CRISPR/CAS9 demonstrated that multiple CRMs contribute to *MIR166A* function at the shoot apex. The loss of CRMs that contain conserved non-coding sequences (CNS) that serve as a proxy for *cis*-regulation also does not lead to any phenotypic or quantitative change, highlighting the requirement for multiple CRMs (Hendelman et al., 2021; Nelson & Wardle, 2013; Wang et al., 2021).

However, the loss of CNS E, a CRM of 250 bp at the proximal end of the promoter encompassing the transcriptional start site (TSS) region, alters the quantitative *pMIR166A* activity. Core promoter regions encompassing the TSS, around 50-100 bp in plants, are crucial *cis*-regulation components for initiating transcription (Marand et al., 2023; Schmitz et al., 2021). Indeed, this CRM of 250 bp or part of it appears to be the core promoter for *MIR166A*. Further, the failure of this putative core promoter region to complement the *miR166a miR166b* phenotype reemphasizes the necessity of additional *cis*-regulatory activity to drive proper *MIR166A* expression.

Besides core promoters, enhancers are a vital part of the *cis*-regulation of genes. Enhancers are distally located from the gene and increase the transcription rate in a tissue-specific manner (Schmitz et al., 2021). As described in animals, enhancers identified in plants are also present at distal regions located at accessible chromatin regions (ACRs) and associated with specific histone marks (Lu et al., 2019; Weber et al., 2016). However, given the compact genome of *Arabidopsis*, it is plausible that *cis*-regions regulating *MIR166A* with enhancer-like functions are not always distal from one another but also adjacent and closer to the target gene. Indeed, several studies have shown that the location and distribution of CRMs correlate with genome size (Schmitz et al., 2021)). Although the enhancer function of *MIR166A* CRMs has not been fully assessed, these CRMs have been conserved over evolution, overlap with ACRs, partly fulfilling enhancer properties (Schmitz et al., 2021). Further analysis of epigenetic signature marks- and expression of CRMs is necessary to confirm their enhancer-like function.

The *cis*-regulation of *MIR166A* in the shoot apex varies compared to the regulation of other developmental genes, such as *WOX9*. Here, single-defined CRMs explain the pleiotropic role of *WOX9* during vegetative and reproductive development in *Solanaceae* (Hendelman et al., 2021). On the other hand, *cis*-regulation of *MIR166A* is like regulation of *WUS* in *Solanaceae*, where the loss of CRMs is tolerated and does not lead to any phenotypic changes, even though some of

the *cis* regions are highly conserved in evolution (Wang et al., 2021). The insufficiency of CRMs individually to regulate *MIR166A* activity strongly favours the idea that these CRMs are redundant in function.

The redundant regulation by CRMs seems reminiscent of shadow enhancers extensively studied in animal development (reviewed in (Kvon et al., 2021)). These redundant enhancers individually drive similar expression patterns of their target gene. However, often redundant enhancers with partial spatial overlap have also been identified (Cannavò et al., 2016). They collectively fine-tune gene expression, either acting additively, synergistically, sub-additively or repressively (Kvon et al., 2021). Although not termed shadow enhancers in plants, early studies in pollen development have identified two *cis* regions redundantly enhancing the expression of LAT52, a pollen-specific gene (Twell et al., 1991). Other examples in plants/*Arabidopsis* are AGAMOUS (AG), the floral homeotic gene and FLOWERING LOCUS T (FT), vital for the floral transition that are regulated by redundant enhancers (Bomblies et al., 1999; Zicola et al., 2019). Similarly, in *Solanaceae,* interaction between multiple *cis* regions regulate *CLV3*, leading to a quantitative change in fruit locule number (Wang et al., 2021). Although the spatiotemporal expression contributed by individual CRMs of *pMIR166A* has not been analyzed here, the *cis*-regulation of *MIR166A* appears to follow the characteristics of such shadow enhancers. However, compared to the above studies in plants with two redundant CRMs, it is plausible, based on these results, that more than two CRMs are redundantly involved in *MIR166A* activity. In a similar manner, *shaven baby,* an essential gene in *Drosophila* necessary for developing hair-like projections (trichomes) of epidermal cells, is driven by seven redundant enhancers (Frankel et al., 2010; Stern & Frankel, 2013). Overall, this study and those mentioned above demonstrate that the presence of shadow enhancers may be a common feature in plant developmental programs, like in animals, waiting to be identified.

Redundant CRMs of *MIR166A* can ensure mutational robustness at a quantitative level by keeping miR165/166 within optimum levels. Similarly, in yeast, *cis* regions of the *TDH3* promoter involved in cell growth have also been shown to be robust to mutational perturbations (Duveau et al., 2017). As such robust *MIR166A* gene regulation by redundant CRMs translates into phenotypic robustness. In addition, the redundant CRMs of *MIR166A* also confer phenotypic robustness to miR165/166 activity to counter environmental perturbations. This is supported by

cis mutants displaying unaltered plants with flat leaves under sub-optimal light and heat conditions. Further, *cis* mutants that produce reduced levels of miR165/166, partially recover their leaf phenotype under select stress conditions compared to the standard conditions. It would be interesting to quantify the miR165/166 levels under these conditions to better understand the observed effects. In addition, deeper analysis in the *cis* mutants with quantitative measurements of the leaf area and curvature would be necessary. Studies in the animal field have documented multiple examples of shadow enhancers conferring robustness in gene expression and phenotypic robustness in a similar manner (Osterwalder et al., 2018). During *Drosophila* embryo development, redundant enhancers for the *snail* gene are dispensable under normal conditions, but at higher temperatures, their expression pattern is perturbed, affecting gastrulation (Perry et al., 2010). Similarly, deleting two of the seven enhancers for s*haven baby* increase trichome loss in *Drosophila* embryos when developed under sub-optimal temperatures (Frankel et al., 2010). As *MIR166A* has more than two redundant regions, analyzing the plant phenotypes with deletions of multiple CRMs will be essential to confirm its requirement for conferring environmental robustness. Although some redundant enhancers have been identified in plants, this study, for the first time, addresses the role of redundant CRMs in conferring robustness to gene expression and, subsequently its function as well.

Overall, this study demonstrates that plants have multiple mechanisms to cope with sensitive components of a network, during development. Extensive analysis of miR165/166 during the establishment and maintenance of ad-ab polarity demonstrates that multifaceted redundant mechanisms orchestrate robust activity, thereby ensuring a flat leaf. At the organ level, redundancy among different *MIR165/166* family members ensures that genetic mutations do not perturb spatiotemporal activity. Further, redundancy leads to excess miR165/166 production, conferring quantitative robustness that translates to phenotypic robustness. In addition, at an individual gene level, a redundant and complex *cis* regulome ensures the precise activity of *MIR166A*, the dominant contributor of miR165/166 at the shoot apex. This complex transcriptional regulatory architecture keeps *MIR166A* robust to mutational and environmental perturbations, guaranteeing a flat leaf at the organ level.

Supplementary Figures

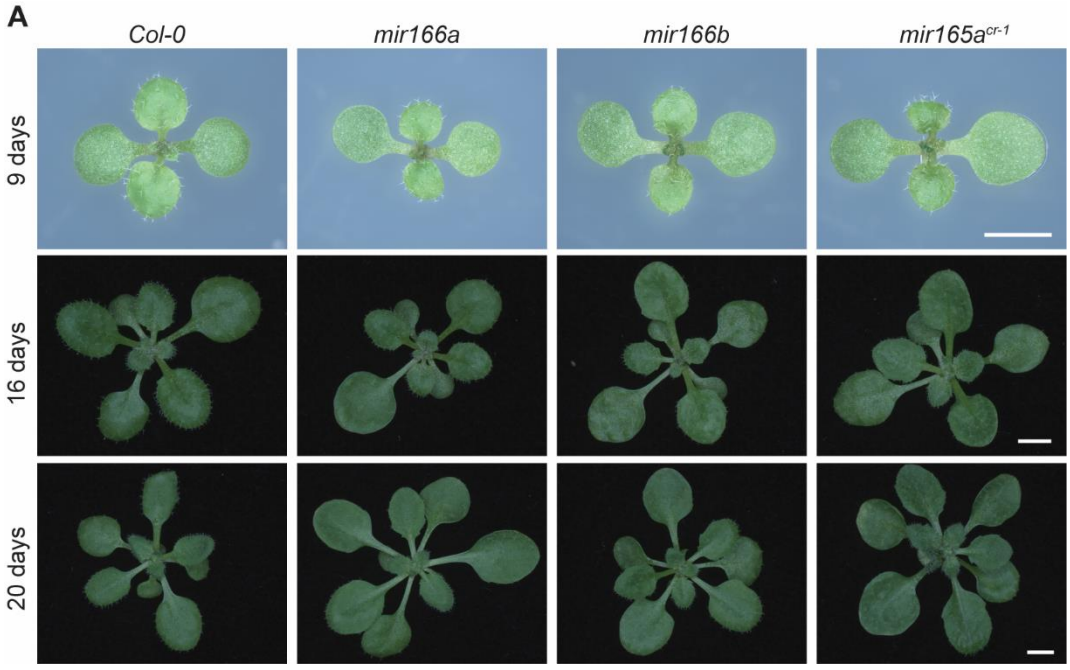

Sfig1: Phenotypic analysis of miR165/166 CRISPR KO. (A) Top view of 9-, 16- and 20-day-old *mir166a*, *mir166b* and *mir165a*$^{cr-1}$ knock-out mutants showing no phenotypic defects compared to WT (Col-0). Scale bar: 0.5 cm.

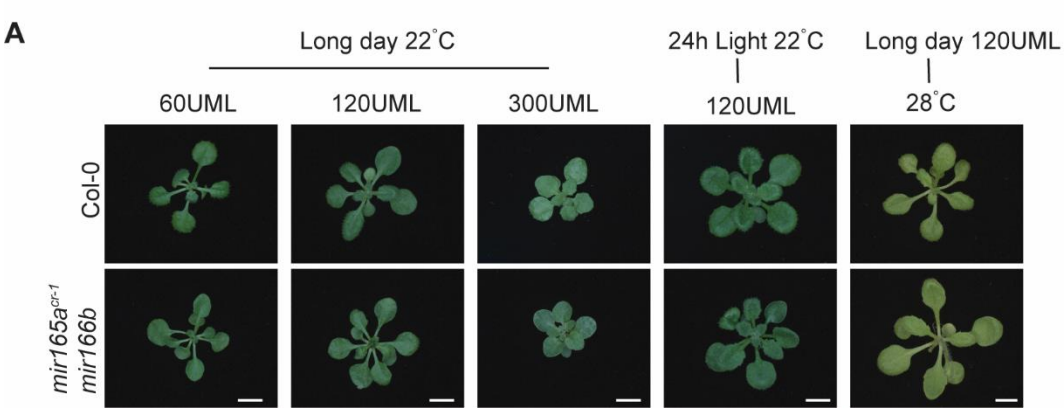

Sfig2: ***MIR166A*** **activity is robust under environmental stress conditions** (A) Top view of 18-day-old rosettes of *mir165a*$^{cr-1}$ *mir166b*, subjected to various light- and heat stress conditions, remain robust with no alterations in the leaf morphology compared to Col-0 under these conditions. Scale bar: 0.5cm

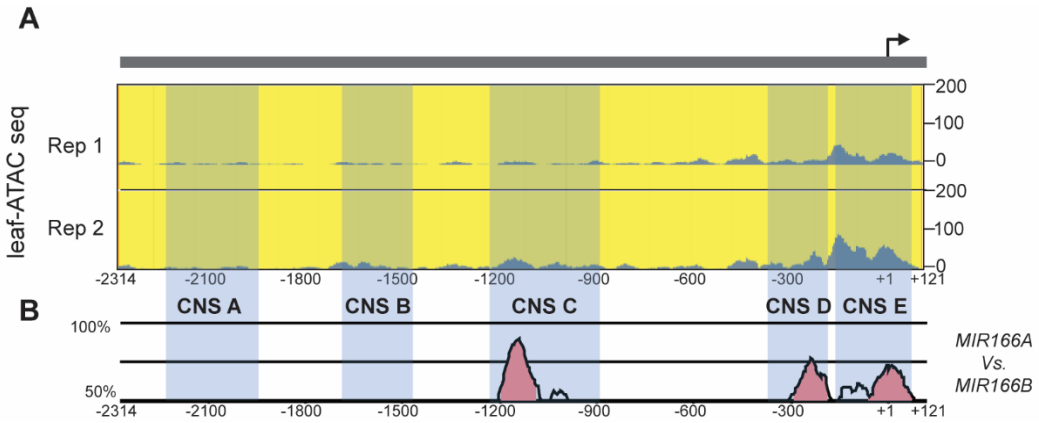

Sfig3: ***cis*-regulatory modules of *pMIR166A*.** (A) Leaf ATAC-seq coverage (grey) of 2 replicates across *pMIR166A* showing chromatin accessibility at the proximal end of the *pMIR166A* including the TSS (Lu et al., 2019). (B) Conserved sequences between *pMIR166A* and *pMIR166B* in *A. thaliana* depicted by sequence alignments using mVISTA. Pink regions - mVISTA plot showing >70% similarity over 100 bp window. Grey box- *pMIR166A*; black right bent/curved arrowhead - TSS. CNS of *pMIR166A* across *Brassicaceae* are shaded in blue.

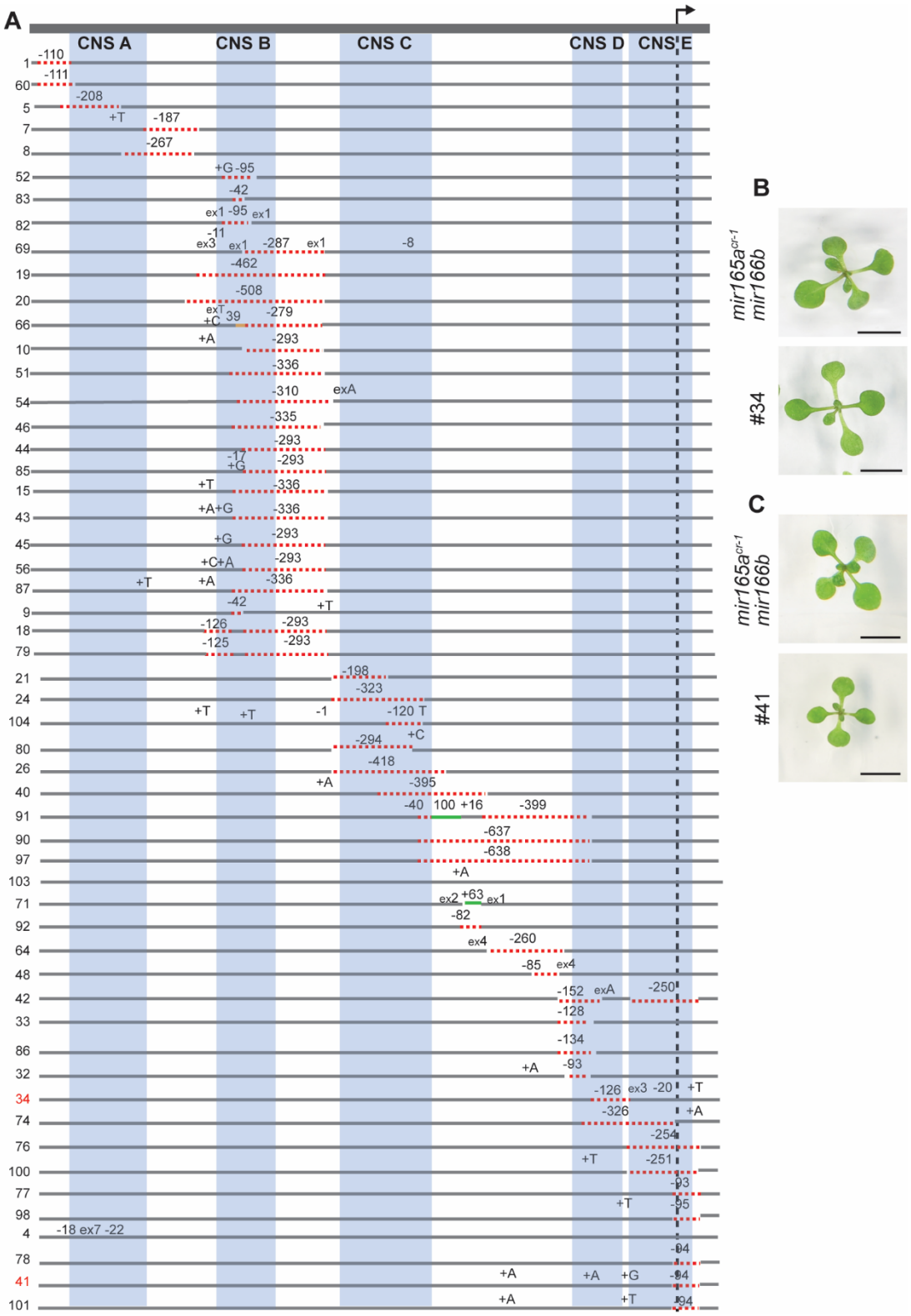

Sfig4: **Multiple CRMs Regulate *pMIR166A* at the Shoot Apex**. (A) Schematic representation showing all 54 *cis pMIR166A* alleles. Smaller deletions (-), insertions (+), and substitutions (ex) are marked with numbers and letters. Red (dashed), yellow, and green lines indicate large

deletions, inversions, and insertions, respectively. Red arrowheads, gRNAs. Grey boxes indicate the *pMIR166A* and the black dashed line with an arrow indicates the TSS. (B-C) Representative of top view rosettes of *cis* mutants #34 (10 days) and #41 (11 days) show no phenotypic differences compared to *mir165a*$^{cr-1}$ *mir166b*. Scale bar: 0.5 cm

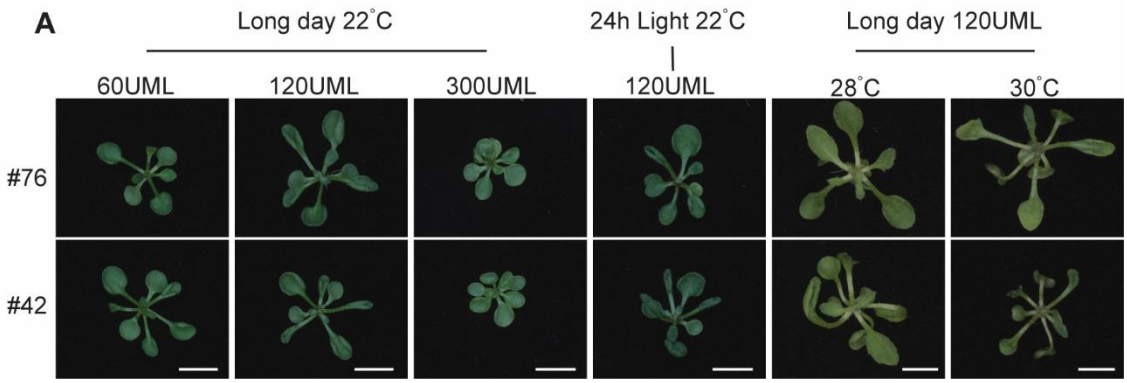

Sfig5: **Redundant *MIR166A cis*-regulation ensures robust miR165/166 activity upon environmental perturbations** (A) Top view of 18-day-old rosettes of *pMIR166A cis* mutants lacking CNS E (#76 and #42), showing no enhancement of their phenotypes when subjected to various light and heat stress conditions, rather show milder phenotypes under low light (60 UML) and high light (300 UML). Scale bar: 0.5cm.

Chapter Four: A Multifaceted Transcriptional Landscape Governs Morphogen Dynamics in Organ Polarity.

Shreyas Meda, Gael Paszkiewicz, Pavel Solansky, Wanyan Xi, Meike Irene Tauber, Khoa Thi Nguyen, Tom Denyer and Marja C. P. Timmermans

Abstract

Positional cues are vital for coordinating spatiotemporal cell fate decisions and thereby ensuring the proper development of an organism. Mobile signals such as morphogens provide the necessary positional information. They move from their source, generating a concentration gradient. This regulates target gene expression in a threshold-based manner, which cells interpret to acquire distinct cell fates. As such, morphogens need to be regulated with precision at the spatiotemporal and quantitative level. However, the molecular basis for such regulation is not well known. In plants, miR165/166 is one such morphogen, vital for adaxial-abaxial patterning of the leaf, and studying its regulatory architecture will aid in understanding general mechanisms underlying morphogen regulation. Here, using in-depth molecular-, genetic-, and genomic analysis, we demonstrate that *MIR166A* is regulated at the shoot apex by a complex network of Transcription factors (TF) belonging to 30 TF subtypes, interacting at both intra- and inter-family levels. They include activating and repressing TFs with tissue-specific as well as broad/pleiotropic expression patterns across the shoot apex. These TFs further have multiple TF binding sites distributed across the *MIR166A* promoter and collectively they fine-tune *MIR166A* expression at spatiotemporal and quantitative levels. Overall, through this work, we show that a complex TF network collectively regulates miR165/166 activity, which could be an underlying mechanism that orchestrates tissue specificity in morphogens, as well as other critical genes during plant development.

Contributions

S.M. and M.T. designed the project and experiments. Experiments and analyses were performed by S.M. with contributions from W.X to quantitative gene expression analysis, M.I.T to the complementation analysis, and G.P. to confocal imaging. T.D. generated the scRNA-seq libraries. P.S. performed the scRNA seq analysis. K.N. cloned the Y1H plasmids.

The complementation analysis of TFBS mutants was also a part of the bachelor thesis of Meike Irene Tauber (2021) *"*Identification of *CIS* regulatory elements and diverse transcription factors regulating *MIR166A* expression during leaf polarity establishment in *Arabidopsis thaliana."*

Acknowledgements
We thank Diana Vranjkovic and Richard Gavidia for all the technical help.

Introduction

The development of multicellular organisms relies on the complex organization of multiple patterns at molecular-, cellular-, tissue-, and organ levels. During pattern formation, spatiotemporal specification of diverse cell types takes place, necessary for normal development in both plants and animals (Willemsen & Scheres, 2004). A key aspect underpinning precise pattern formation is the positional information that a cell acquires during growth via mobile signals (Wolpert, 1969). Among the mobile signals are morphogens, which move from their origin/source and generate a concentration gradient which is interpreted by the cell as a threshold-based readout leading to precise cellular differentiation at the spatial level (Wolpert, 1969). In the scenario of morphogens, along with their tissue-specific expression, their levels must also be precisely regulated (Skopelitis et al., 2017). Although the role of morphogens is well studied, the regulatory network that ensures spatiotemporal and quantitative levels of morphogens during developmental patterning is not well understood.

Over the years extensive research in animals has identified several morphogens involved in different aspects of development be it *Drosophila* embryo development or limb development in vertebrates (Driever & Nüsslein-Volhard, 1988; Ferguson & Anderson, 1992; Tabata & Takei, 2004). In plants, small RNAs act like morphogens during adaxial-abaxial (ad-ab) patterning (Skopelitis et al., 2017). During ad-ab patterning, mutual antagonistic interaction among the TFs promotes either the ad or ab cell fates (Husbands et al., 2009). However, the morphogen function of small RNAs, miR165/166 and tasiARF, provide the necessary positional information at the domain level. Abaxially expressed miR165/166 and adaxially expressed tasiARF move from their source generating opposing concentration gradients which are interpreted as a threshold-based binary readout of their targets HDZIPIII and ARF3, respectively. This, in turn, leads to a precise and stable ad-ab boundary along the leaf (Chitwood et al., 2009; Skopelitis et al., 2017). At the meristem periphery, miR165/166's function is likewise postulated to generate a threshold-based response necessary to repress HDZIPIII in the peripheral zone (PZ), thereby separating the function of HDZIPIII between the stem cells and the leaf (Chapter 3). Indeed, given the functional attributes of miR165/166, its spatio-temporal and quantitative levels are vital for normal shoot development (Chapter 3). miR165/166 is encoded by 9 different loci (Xie et al., 2005). Among them, *MIR166A* is the dominant contributor of miR165/166 as the shoot apex (Chapter 3). It is expressed on the abaxial side of the primordia and is re-established at the

meristem organ boundary where new leaves are initiated, thereby showing a dynamic expression across the shoot apex (Chapter 2- Scacchi et al.,2023). As such, understanding the molecular mechanisms that ensure tissue specificity and optimal levels of *MIR166A* as a model, would provide insights into the regulatory logic of morphogens during pattern formation.

Previously, we showed multiple redundant *cis*-regulatory modules (CRMs) generate robustness in *MIR166A* expression (Chapter 3). This, however, does not fully explain *MIR166A* regulation as CRMs partially function through distinct TFs that bind on specific TF Binding Sites (TFBS) distributed across them (Spitz & Furlong, 2012). As such, understanding which TFs and their TFBS are associated with *MIR166A* will aid in further understanding how its spatiotemporal and quantitative expression is regulated.

In plants, combinatorial TF regulation is often envisioned as a simple network of TFs that regulate gene expression during development. A classical example of this is the ABC model, which regulates floral identity/architecture by five gene functions acting in different combinations (Bowman et al., 1991). Similarly, in sepals, giant cell-specific expression mediated by an enhancer was identified to be controlled by the combinatorial activity of TCP, HDZIPIV and DOF TFs (Hong et al., 2023). Conversely, in this work we show that *MIR166A* is regulated by a complex TF network that comprises an unexpectedly large number of distinct TFs belonging to diverse TF families that are redundant at both intra and inter-family levels. This TF network including tissue-specific and pleiotropic/broad expressed TFs functioning as activating, and repressive TFs collectively fine-tune the spatiotemporal and quantitative *MIR166A* expression. Further, we show that this TF network is controlled in part by the pleiotropic TCPs that plausibly, in a tissue-dependent manner, interact with distinct TFs and, in a combinatorial manner, regulate *MIR166A* expression. The complexity in *MIR166A* regulation is enhanced by the vast number of TFBS distributed across *MIR166A* promoter providing the mechanistic underpinning for the redundant *cis*-regulatory activity. This work reenforces the emerging idea that during plant development, combinatorial TF activity involving a large number of TFs regulate gene expression (Sparks et al., 2016; Truskina et al., 2021). Overall, the work here shows that a complex *trans*-regulatory architecture in coordination with redundant cis-regulatory components regulates *MIR166A*, thereby providing insights into mechanisms that generate optimum levels and tissue specificity in morphogens.

Results

Diverse Transcription Factors with Multiple Transcription Factors Binding Sites Regulate *MIR166A* Expression

TFs such as the AS1/AS2 complex repress *MIR166A* expression on the adaxial side of the leaf (Husbands et al., 2015). Complexes of, the HDZIPII (ATHB4, HAT3)/HDZIPIII (REV) TFs share this function (Merelo et al., 2016). Conversely, we have demonstrated that the KAN1/ARF3 complex activates *MIR166A* expression on the abaxial side of the growing primordia (Chapter 2- Scacchi et al.,2023). However, *kan1 kan2 mirarf* mutants lead to a loss of *pMIR166A:erGFP* expression only on the abaxial side of the growing primordia, whereas the reactivation of *MIR166A* at the meristem-organ boundary post primordia emergence remains unperturbed (Chapter 2- Scacchi et al.,2023). These observations suggest that additional TFs must regulate *MIR166A* expression pattern and levels at the meristem periphery; necessary to separate the roles of HDZIPIIIs in meristem homeostasis and during ad-ab polarity.

To gain insights into the global TF regulatory network driving tissue-specific *MIR166A* expression at the shoot apex, we performed an enhanced yeast one-hybrid (eY1H) screen as a first step. Such Y1H screens are extensively used as they are reliable, sensitive, and efficient in identifying and studying genome-wide TF networks (Sparks et al., 2016; Truskina et al., 2021). The *MIR166A* promoter (*pMIR166A*) was used as bait and an arrayed library of 2,033 TFs as prey. The previously described genomic fragment, 2.4 kb in length upstream of the *MIR166A* hairpin, functional in a complementation assay was selected as *pMIR166A* (Skopelitis et al., 2017). The analysis identified 127 TFs belonging to 32 TF families that could activate *pMIR166A* in yeast (Fig 1A, Table S1), revealing the convergence of multiple TFs and TF families on *pMIR166A*. These TFs were grouped into 48 subtypes based on the DNA binding motifs they bind and phylogenetic analysis (Fig 1A, Table S1,2). This suggests that a wide array of DNA binding motifs from different TF families are involved in *MIR166A* regulation (Table S1). Among them, demonstrating the sensitivity of the screen, we recovered known regulators of *MIR166A*, including AS2 and TFs in the KAN, and ARF, subtypes (Husbands et al., 2015)(Chapter 2- Scacchi et al.,2023).

To corroborate the binding of the 48 subtypes obtained from Y1H analysis, the interaction of TFs belonging to these subtype classes was tested using a dual luciferase assay in *Arabidopsis* protoplasts. Here, the TF of interest was transiently overexpressed (*2xp35S:TF*) in protoplasts alongside *pMIR166A*: *firefly_ luciferase,* and *2xp35S: Renilla_luciferase* (Lau et al., 2011). The binding of TFs was confirmed by subsequent analysis of changes in firefly luciferase activity in the presence and absence of the TFs, with Renilla luciferase as an internal control. 37/48 motif subtypes were successfully cloned and tested, and the binding of 23 subtypes on *pMIR166A* was validated (Fig 1B, C). Additionally, by mining the available DNA affinity purification sequencing (DAP-seq) data (O'Malley et al., 2016), interactions of TFs from 11 subtypes were verified, four of which were also validated with the dual luciferase assay, and 7 validated anew (Fig 1B,). In total, 30/48 motif subtypes (62.5%) were demonstrated to bind and regulate *pMIR166A*. This percentage is consistent with data from other large-scale Y1H screens (Sparks et al., 2016; Truskina et al., 2021). These results confirm that diverse TF motifs belonging to multiple TF families regulate *MIR166A*.

To understand the organization of these multiple TFs on *pMIR166A* and to determine if they form hubs/clusters by binding on specific CRMs of the promoter, their TFBS distribution was analyzed. The binding position of TFs on *pMIR166A* was predicted using FIMO software (https://meme-suite.org/meme/tools/fimo). This showed that TFs regulating *MIR166A* have multiple binding sites (average nine), whereby 21/30 validated motif subtypes had >4 TFBS distributed across the *MIR166A* promoter (Fig 1D, E, Table S3). No TF hubs specific to a single CRM could be identified since the high number of TFBS are not localized to a specific CRM on *pMIR166A* but are rather distributed throughout the promoter (Fig 1E). Further, the distribution of TFBS across multiple CRMs of *pMIR166A* may explain why the loss of single *pMIR166A cis* mutants does not alter its activity (Chapter 3).

These results collectively demonstrate that *MIR166A* transcriptional regulation involves multiple TFs having multiple TFBS that bind across the *pMIR166A,* which points to redundant mechanisms to ensure the tissue-specific activity of *MIR166A*. However, it remains open whether these TFs, in a combinatorial manner, regulate *MIR166A* specifically at the shoot apex, or are necessary for its regulation in different plant tissues such as the root and embryo, where *MIR166A* is active (Carlsbecker et al., 2010; Miyashima et al., 2013).

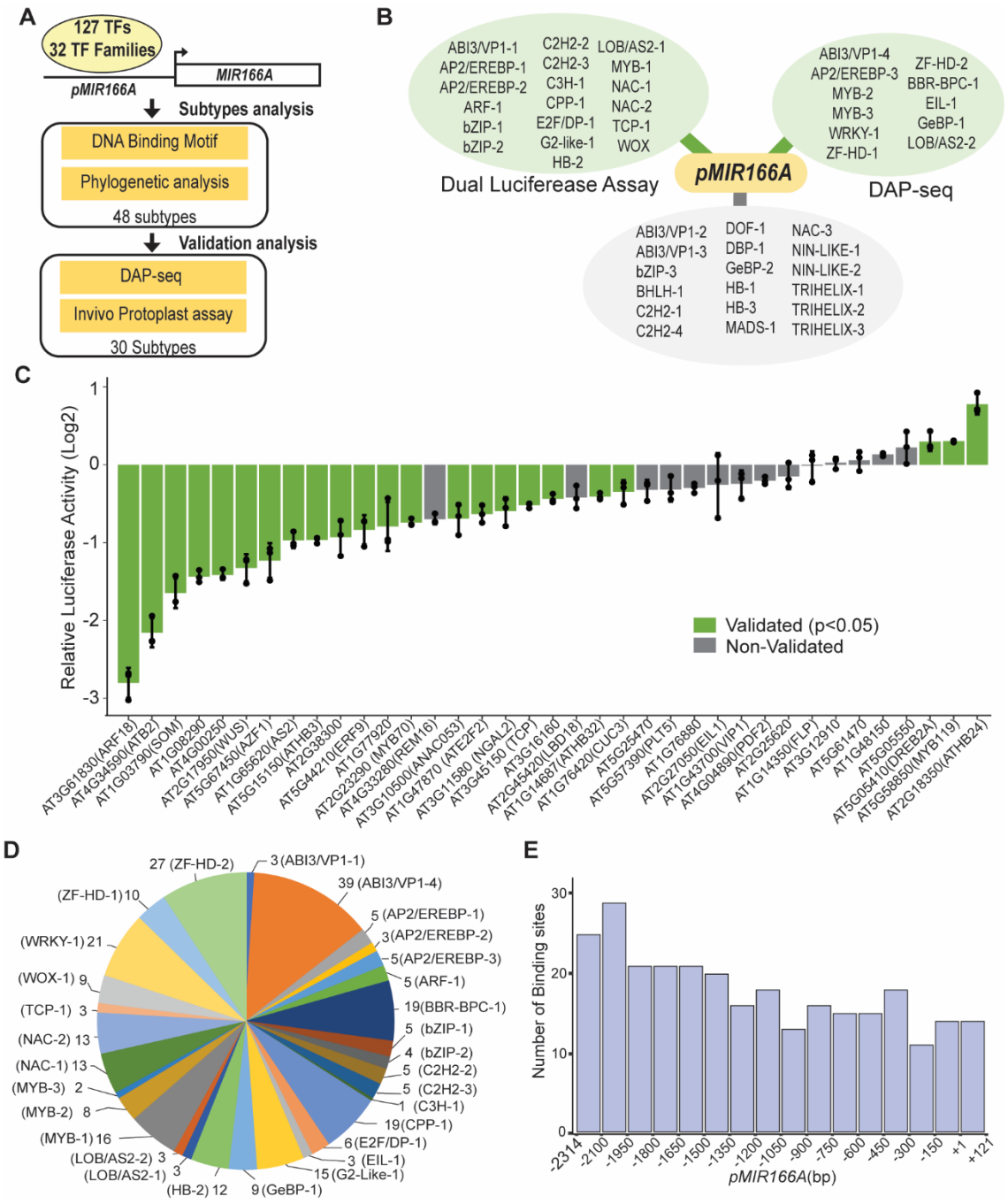

Fig1: ***MIR166A* is regulated by Transcription Factors (TFs) representing multiple distinct classes.** (A) Schematic design of eY1H and TF validation analyses where 127 TFs across 32 TF families identified to bind on *pMIR166A*, grouped into 48 subtypes of which 30 are validated. (B) Schematic of the *pMIR166A*–TF interaction network showing 30/48 motif subtypes (62.5%) validated as binding and regulating *pMIR166A*, either by transient luciferase assay in *Arabidopsis* protoplasts, or available DNA affinity purification sequencing (DAP-seq) data (O'Malley et al., 2016). Green Bubbles: Validated, Grey Bubbles: Non-Validated. (C) Bar plots of relative *luciferase* activity calculated as Firefly over Renilla *luciferase* showing validated TF

subtypes (green bars) that significantly alter *pMIR166A* activity. Grey bars are non-validated TF subtypes. Values: Mean ± SD, n=3 biological replicates. Two-tailed Student's t-test: $p < 0.05$. (D) Pie chart showing the presence of multiple TF binding sites (TFBS) for each TF subtype on *pMIR166A*. Total Binding sites are indicated by the number next to the TF subtype. (D) Bar plots showing the distribution of TFBS across segments of *pMIR166A*.

Tissue-Specific & Broad Expressed TFs Work in a Combinatorial Manner to Establish *MIR166A* expression at the Shoot Apex

While the Y1H analysis identified multiple TFs regulating *MIR166A*, information regarding the developmental context(s) within which they exert their activity is lacking. Considering the known roles of *MIR166A* in root and embryo development (Carlsbecker et al., 2010; Miyashima et al., 2013), further dissecting TF activity in a tissue-specific manner is pivotal to resolving *MIR166A* regulation at the shoot apex. It will also provide insights into specific contributions of multiple TFs to ensure dynamic expression patterns and optimal levels of *MIR166A* in distinct tissues of the shoot apex, i.e., meristem-organ boundary and the abaxial side of primordia.

As a first step, the expression of the regulators of *MIR166A* was examined in available bulk transcriptomic data of the shoot apex. Although most TFs detected by Y1H analysis were expressed at the shoot apex, datasets of this nature lack the resolution to resolve expression within different tissues of the shoot apex, specifically (Schmid et al., 2005). To address this issue, a SAM TRAP-seq (Targeted purification of polysomal mRNA-Seq) data-set was analyzed (Tian et al., 2019). To an extent, this method circumvents the problem of tissue heterogeneity, but they lack data from small RNAs. To overcome these caveats, a scRNA-seq atlas of shoot apex cells was generated from transgenic plants carrying the *pMIR166A:erGFP* reporter. In this way, GFP transcripts served as a proxy for *MIR166A* expression (Denyer et al., 2019).

The resulting atlas was of high quality and comprised 12439 cells with a median of 4286 genes detected per cell. These were arranged in 25 distinct clusters (c), and 21/25 of these clusters were assigned cell identities using established cell type-specific marker genes (Burian et al., 2022; Byrne et al., 2000; Kim et al., 2021; Lopez-Anido et al., 2021; Shi et al., 2020; Tenorio Berrío et al., 2021; Tian et al., 2019; Yamada et al., 2010; Zhang et al., 2021) (Fig 2A, Sfig 1A). The single cell atlas delineated cells of the epidermis (c0,12) from subepidermal - meristem (c1,6), organ boundaries (c16), leaf primordia (c6,7,11,14,19), and vasculature (c3,4,

13,15,17,18,20,21,22,24). The latter separates xylem and phloem cell types and subtypes (Fig 2A, Sfig 1A). Interestingly, 85% of TFs belonging to 28/30 validated subtypes were found to express within the shoot apex. Furthermore, when phylogenetically closely related TFs belonging to the same subtype were included (Table S2), TFs belonging to all 30 subtypes were detected. These results reveal that the high number of TFs validated from Y1H is not due to the *MIR166A*'s role in other plant tissues but, indeed, is necessary for regulating *MIR166A* in a combinatorial manner at the shoot apex.

To further understand the dynamics of these TFs on *MIR166A* regulation, *MIR166A* positive clusters were identified based on the proportion of *GFP* transcripts across each cluster. 5/25 (c0,1,6,14,16) clusters with cells from the apex epidermis, Rib zone, organ boundary, leaf primordia and mesophyll positive for *MIR166A* expression were considered (Fig 2D, Sfig 1B, Table S4). Since analysing the vasculature and the hypocotyl was beyond the scope of the study, cells of clusters 10,18,21 that predominantly mark the cortex and shoot endodermis were not considered, despite displaying high GFP-positive transcripts. To further resolve tissue heterogeneity within these principal clusters, sub-clustering was performed. This resulted in 13 subclusters (Fig 2B, C). A cluster comprising apex epidermal cells (c0) separated into those of meristem (s3), organ boundary (s12), adaxial- (s11), abaxial- (s9) primordia and a 5th cluster of unidentified cells (s5). Similarly, the mesophyll cluster (c14) separated into two subclusters, both marking abaxial mesophyll cells (s7,8). Cluster 6 (c6), containing sub-epidermal SAM and leaf primordia cells, resolved into those of the meristem and very early primordia (s2), and leaf primordia (s4). Cluster one (c1) defines the rib zone and is separated into three subclusters (s0,1,10), which could not be resolved into specific sub-tissue types using available markers. The sub-epidermal organ boundary cluster (c16) did not separate into further distinct subclusters (s6) (Fig 2B, C). Tables S4 and S5 summarize all clusters, subclusters, and markers used to define tissue types. Within these 13 subclusters, seven were enriched for *GFP* (*MIR166A*) transcripts (s0,3,6,7,8,9,12, Fig 2E, F, Table S5). Consistent with our imaging analysis (Chapter 3), the GFP-enriched subclusters represent tissues at the organ boundary (s6,12) and abaxial primordia (s7,8,9), from both epidermal and sub-epidermal layers. On the other hand, subclusters lacking GFP expression comprise cells such as adaxial primordia (s11), that do not express *MIR166A*. These results also validate using *pMIR166A:erGFP* as a proxy for *MIR166A* expression.

Analyzing the expression patterns of *MIR166A* regulators identified regulators that co-express with *MIR166A* and like GFP show expression in a subset of cell types/subclusters (Fig 2G). Further, we observed that many TFs appeared with broad expression across the subclusters while a few with tissue specific expression (Fig 2G). As such, we calculated Shannon entropy which acts as a measure to assess the degree of tissue specificity in gene expression where high entropy specificity values indicate tissue-specific gene expression while low entropy specificity indicates genes with broader expression (Ameri & Lewis, 2021). This analysis revealed that 27% of TFs have high entropy specificity (>1) and as such are limited to distinct tissues belonging either to*MIR166A*-enriched- or non-enriched subclusters, and might act as activators and repressors of *MIR166A,* respectively. The vast majority of TFs (72%) displayed low entropy specificity (<1) and are expressed broadly across all or multiple subclusters (Fig 2G, Table S6). These results suggest that tissue-specific TFs intersect with TFs that are expressed broadly across the shoot apex, to bring about the correct spatial, temporal and quantitative expression of *MIR166A*. Repetition of the same analysis, including phylogenetically closely related TFs for the given subtype, supported this notion (Sfig 1C, Table S7).

This single-cell resolution analysis provides a valuable resource to analyze the regulators of *MIR166A* in depth within specific tissue types of the shoot apex. Moreover, it predominantly shows that the regulators of *MIR166A* have diverse expression patterns, and exhibit redundancy at inter- and intra-TF family levels. The combined results from the Y1H and scRNA-Seq studies show that *MIR166A* regulation is more complex than the classical examples of transcriptional regulation studied in plants. This seems of the essence given that *MIR166A*, encodes a morphogen vital for ad-ab patterning.

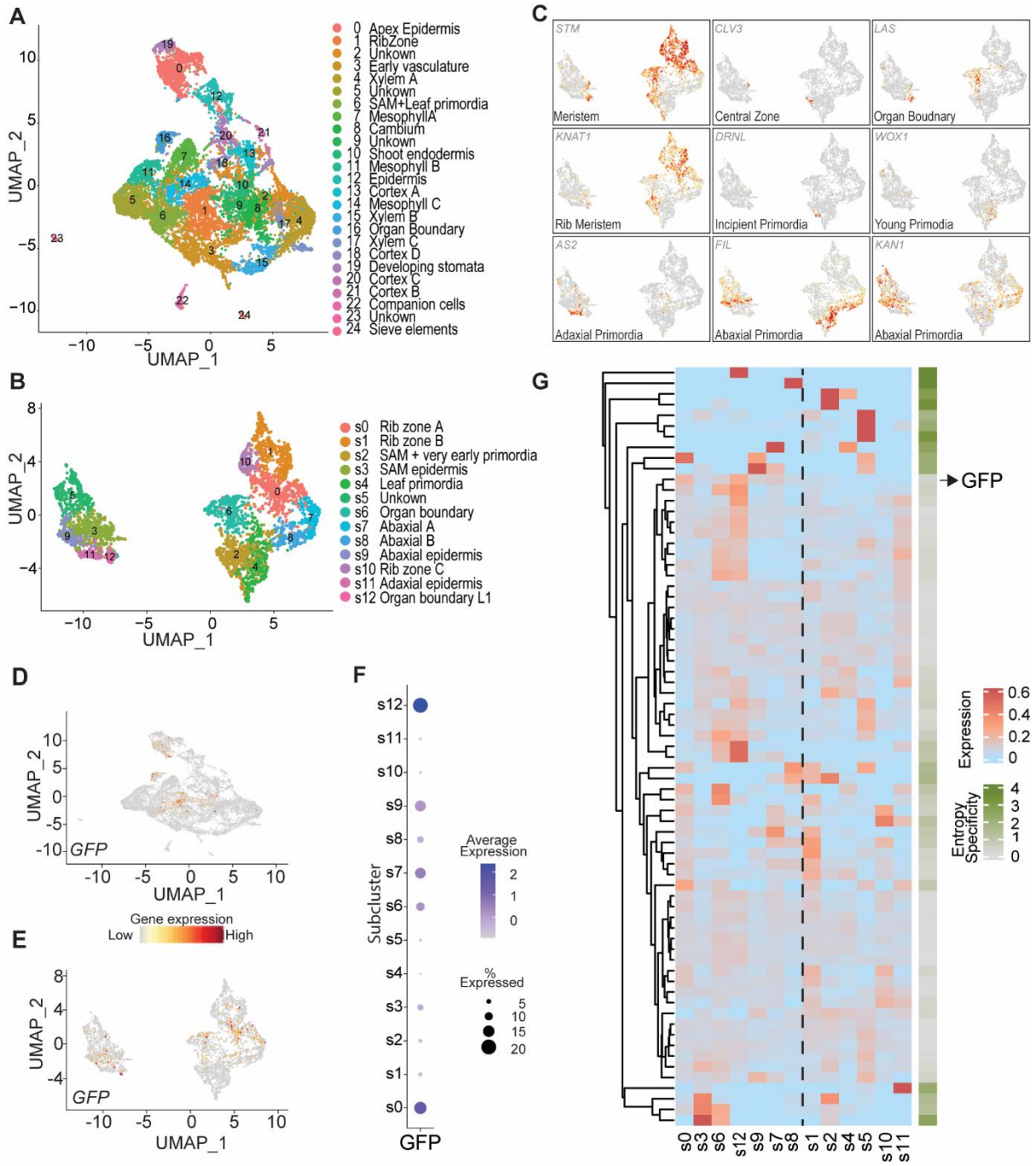

Fig2: **Tissue-specific and broad contributions of diverse TF subtypes in *MIR166A* regulation.** (A) UMAP plot showing 25 cell clusters of Arabidopsis *pMIR166A: erGFP* vegetative shoot apices, resolved by scRNA seq. (B) UMAP visualization of subclusters derived from GFP (*MIR166A*) positive clusters. Dots-individual cells; colour-cell clusters/subclusters. (C) UMAP plot of representative marker genes for different tissue types in the subclusters. (D, E) UMAP plot showing the expression profile of *MIR166A* (GFP), in clusters (D) and subclusters (E). (F) Dot plot showing the expression of *MIR166A* (GFP) in subclusters and identification of *MIR166A* enriched subclusters. Dot diameter-proportion of cluster cells

expressing GFP; colour-mean expression across cells in that subcluster. (G) Heatmap of *MIR166A* regulators, validated by Y1H, showing tissue-specific and broad patterns of expression across *MIR166A* enriched- (s0,3,6,12,9,7,8) and non-enriched (s1,2,4,5,10,11) subclusters, separated by dashed (black) line. Colour, scaled mean expression across cells in that subcluster. Heat map (green) showing entropy specificity of the TFs across the sub-clusters.

Extensive Inter- and Intra-TF Family Redundancy Regulates *MIR166A* During Leaf Development

Single-cell resolution analysis identified diverse expression dynamics of TFs regulating *MIR166A* expression. They variably show tissue-specific as well as broad expression. In addition, many TFs co-express with *MIR166A*. As levels of *MIR166A* are vital for its proper activity, it is plausible that activating- and repressive TFs share expression patterns and modulate *MIR166A* expression levels. As such, to analyze these diverse TF dynamics in *MIR166A* regulation and their combinatorial role *in planta,* a collection of *pMIR166A* variants with mutated TFBS ($pMIR166A^{mutTFBS}$) were generated for select TFs. Mutating TFBS on *pMIR166A* allows us to analyze direct effects on *pMIR166A* expression, overcoming potential redundancy within TF families and avoiding the necessity to create higher-order TF knockout mutants.

For this analysis, we selected nine subtypes whose TFBS are dispersed across different CRMs of *pMIR166A*. This was an essential criterion, as we know that single *cis*-regulatory module (CRM) deletion does not necessarily affect its activity (Chapter 3). As such, the subtypes AP2/EREBP-1, AP2/EREBP-2, AP2/EREBP-3, LOB/AS2-2, MYB-1, NAC-2, TCP-1, ZFHD-1, and ZFHD-2 were selected (Fig 3A).Expression of these $pMIR166A^{mutTFBS}$ variants at the shoot apex was determined by confocal imaging. For this, $pMIR166A^{mutTFBS}$ were cloned upstream of the *3xVenus_N7* reporter. Expression analysis at the shoot apex of $pMIR166A^{mutTFBS}$*:3xVenus_N7* reassured the role of multiple TFs and TF families in *MIR166A* regulation and revealed their mode of action (Fig 3B). For qualitative analysis of the spatio-temporal *pMIR166A* expression pattern, SAMs with good VENUS signal were considered. We identified TF subtypes that activated *MIR166A* in the organ boundary. Mutation of ZFHD-2 TFBS revealed a partial loss of expression in the organ boundary (Fig 3B). Similarly, mutating NAC-2 TFBS led to delayed onset of *MIR166A* expression at the meristem-organ boundary. Here expression at the organ boundary showed expression post p3/p4 stage, while *pMIR166A* (WT) displayed expression at

the meristem organ boundary early on at p2 (Fig 3B). On the other hand, repressor subtypes such as ZFHD-1 and MYB-1 were identified whose TFBS mutation on *pMIR166A* led to misexpression of *MIR166A* more apical towards the meristem, when compared to expression of the wild type promoter (*pMIR166A^{WT}:3xVenus_N7*, Fig 3B). However, *pMIR166A* variants mutated for the TFBSs of AP2/EREBP-1, AP2/EREBP-2, AP2/EREBP-3, LOB/AS2-2 showed no change in *MIR166A* expression patterns (Fig 3B). Likewise, the expression of *pMIR166A* with mutations in TFBS of the TCP-1 remained comparable to the wild-type *pMIR166A* (Fig 3B). However, almost twice the number of *pMIR166A_mutTCP* SAMs (n=6/12) showed a global reduction in *MIR166A* expression, than the ones carrying *pMIR166A^{WT} :3xVenus_N7* (n=3/11), suggesting TCPs may act as a global activator of *pMIR166A*.

To test this idea and to analyze whether these TFs subtypes have a potential quantitative impact on its regulation, we measured the transcript levels of *3xVENUS_N7* (a proxy for *MIR166A*) by qRT-PCR in the shoot apices of pools of independent T1 lines carrying the above indicated *pMIR166A* variant. Firstly, corroborating our imaging analysis mutation of TCP-1 TFBS showed a reduction in *MIR166A* promoter activity (Fig 3C). Similarly, mutation of NAC-2 showed reduced *pMIR166A* activity. Conversely, mutating AP2/EREBP-3 and LOB/AS2-2 TFBS which showed no change in expression pattern increased *pMIR166A* activity, thereby acting as repressors of *pMIR166A*, possibly tuning its level in its expression domains (Fig 3C). However, no change in *MIR166A* promoter activity was observed in apices carrying *pMIR166A^{mutTFBS}* for ZFHD-1 and MYB-1 which led to misexpression of *MIR166A* into the peripheral zone (PZ). Similarly, no change in *MIR166A* levels was observed in *pMIR166A^{mutTFBS}* for ZFHD-2 SAMs which led to a partial loss of expression in the boundary (Fig 3C). AP2/EREBP-1 and AP2/EREBP-2 TFBS mutated *pMIR166A* that did not alter the expression pattern, resulted in no change in *MIR166A* promoter activity (Fig 3C).

Overall, from the above experiments, seven of nine TF subtypes were found to impact either *MIR166A* expression patterns or levels, reinforcing the role of multiple TFs in *MIR166A* regulation in the shoot apex. As TFs within each subtype share similar DNA binding motifs, any of these could be responsible for regulating *MIR166A* in these tissues. Further analysis of expression patterns of the member TFs of each subtype from the single cell atlas, in both

MIR166A-enriched and not-enriched tissue, would aid in narrowing down TF or TFs that likely regulate *MIR166A*.

To further investigate the functional role of these subtypes in *MIR166A* regulation, complementation analysis of *mir166a mir166b* mutants was performed using *pMIR166A*^{mutTFBS} variants for seven subtypes that either affect its expression pattern or levels: AP2/EREBP-3, LOB/AS2-2, MYB-1, NAC-2, TCP-1, ZFHD-1, and ZFHD-2. Introducing *pMIR166A*^{WT}*:miR166A* fully rescues the *mir166a mir166b* phenotype, resulting in a wild-type-like phenotype (Fig 3D, E, Chapter 3). Conversely, introducing *pMIR166A*^{mutTFBS}*:miR166A* into *mir166a mir166b,* either fully or partially complements the mutant phenotype (Fig 3D, E). Upon thorough phenotypic analysis, plants carrying *pMIR166A*^{mutTFBS}*:miR166A* of TCP-1 TFBS that activated *MIR166A* level across the shoot apex showed the weakest complementation rate with over 50% of the plants having either *mir166a mir166b,* or only partially complemented phenotypes leading to delayed growth or defects in the leaf (Fig 3D, E). Furthermore, mutating NAC-2 TFBS resulted in partial complementation whereby seedlings had delayed leaf development that recovered over time, correlating with their delayed *MIR166A* expression at the organ boundary (Fig 3D, E). Conversely, *pMIR166A*^{mutTFBS}*:miR166A* lines of AP2/EREBP-3 and LOB/AS2-2 TFBS, repressors of *MIR166A* expression levels, showed a complementation equivalent to *pMIR166A*^{WT}. (Fig 3D, E). Although these TF subtypes act as repressors on *pMIR166A* based on our quantitative analysis (Fig 3C), their ability to complement in a similar manner to *pMIR166A*^{WT}, and not lead to any overexpression-like phenotypes, suggests that the increased miR165/166 level is within the optimal window necessary for its activity (chapter3). Interestingly, ZFHD-1 and MYB-1, which misexpress *MIR166A* at the meristem periphery, and ZFHD-2 which generate variable expression in the organ boundary, also complemented like the *pMIR166A*^{WT} (Fig 3D, E). This suggests that plants tolerate misexpression of *MIR166A* at the meristem boundary, probably due to its inherent function of moving from the meristem periphery towards the CZ (Skopelitis et al., 2018).

These *in planta* experiments demonstrate that *MIR166A* is regulated by both activating- and repressing TF subtypes. Furthermore, these results reveal that distinct, tissue-specific TFs from diverse subtypes, activate *MIR166A* in the organ boundary and repress it in the peripheral zone, confining its expression within the meristem-organ boundary. In addition, TF subtypes,

AP2/EREBP-3 and LOB/AS2-2, tune *MIR166A* probably in multiple tissues at the shoot apex. On the other hand, TFs from the TCP-1 subtype activate *MIR166A* pleiotropically in both primordia and at the meristem-organ boundary. These multiple, redundant TF subtypes collectively ensure the correct spatiotemporal, and quantitative positioning of *MIR166A,* and ensure tissue specificity.

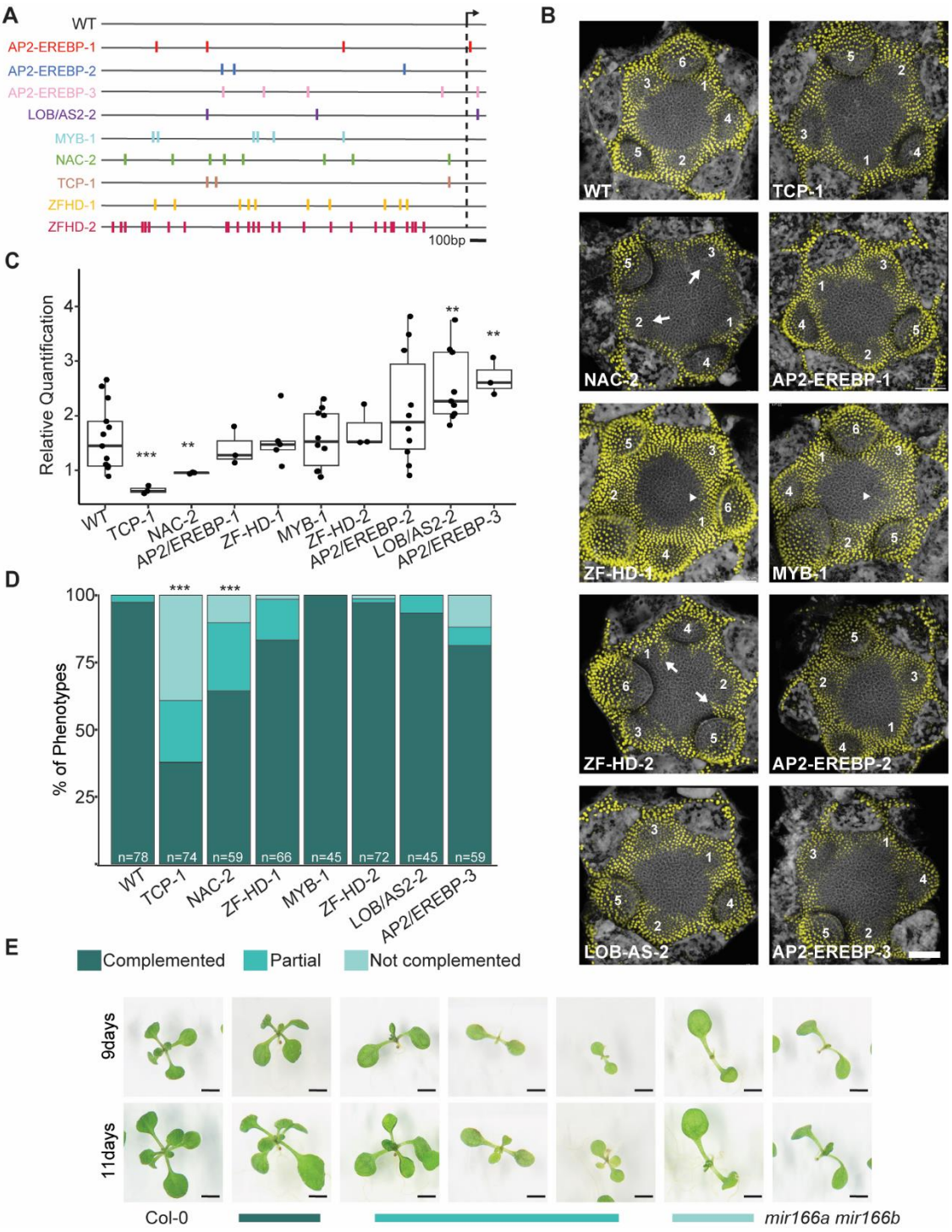

Fig 3: **Inter- and Intra TF family regulates *MIR166A* at the shoot apex.** (A) Schematic representation of mutated TFBS of *in planta* analyzed TF subtypes, distributed across *pMIR166A*. Grey line: *pMIR166A*; colour vertical lines- TFBS; Black dashed line with arrow: TSS position. (B) Effects of specific TFBS mutations on *pMIR166A* (mutTFBS) expression compared to wild type *pMIR166A* (WT), showing partial loss (white arrow), misexpression (white arrowhead), or no change in expression, highlighting complex combinatorial contributions

of TFs in *MIR166A* regulation. Scale bar: 50µM. Note: Images are representative of the pattern and do not reflect the level of expression. (C) Box plots showing reduced, a gain of- or no change in *3x_Venus_N7* levels (a proxy for *pMIR166A*), relative to *PP2A* in *pMIR166A* (mutTFBS) for specific TF subtype in comparison to *pMIR166A* (WT). Boxes, 25th to 75th percentile; whiskers, 5^{th} to 95^{th} percentile; n≥3 biological replicates; Two tailed Student's t-test: **p <0.01, *** p<0.001. (D) Quantification of phenotypic defects on complementation of *mir166a mir166b* with *pMIR166A* (mutTFBS) in comparison to *pMIR166A*(WT). Mann-Whitney-U test: *** p<0.001 (E) Phenotypes seen in 9- and 11-day-old T1 seedlings upon complementation of *mir166a mir166b* mutants with *pMIR166A* (WT) or *pMIR166A*(mutTFBS) grouped into 3 classes: complemented-WT like; partial-delayed leaf development; not complemented- *mir166a mir166b* like phenotypes. Scale bar: 0.25cm. Note: *pMIR166A* (WT) complementation data from Chapter 3 is shown.

Discussion

In this work to understand the regulatory logic controlling the activity of morphogens, we used *MIR166A* as a model, which is a dominant contributor of miR165/166, a morphogen vital for meristem homeostasis and ad-ab leaf polarity determination (Chapter 3). Our data provides evidence that the *trans*-regulatory architecture driven by broad and tissue-specific TF networks involving activators and repressors regulates *MIR166A*. This in coordination with the *cis*-regulation ensures spatio-temporal and quantitative *MIR166A* expression at the shoot apex.

In this study, we show that diverse TFs belonging to 30 TF subtypes collectively regulate *MIR166A*. Here, repression of *MIR166A* at the meristem peripheral zone by MYB-1 and ZF-HD-1 subtype TFs and activation of *MIR166A* in the meristem organ boundary by NAC-2, ZF-HD-2 and TCP-1 subtype TFs reemphasize the presence of inter-TF family dependency. Indeed, in recent years, cross-family TF interactions during plant growth and development have been documented (Bemer et al., 2017). Cross-TF interactions play a crucial role in transcriptional responses either by impacting the nuclear import of the TF or the TF-TF complex, the affinity, or stability of the TF-TF complex, and/or by influencing their cooperative binding on DNA (Bemer et al., 2017). However, further analysis is required to understand the extent of interaction across these TF families. Further, TFBS mutagenesis reveals the inability of TFs to individually obliterate *MIR166A* expression or lead to 100% non-complementation of the *mir166a mir166b* mutants, reinforcing the role of combinatorial activity. Our *in planta* analysis showed that mutation of TFBS for LOF1(MYB-1) and CUC3 (NAC-2) leads to misexpression and loss of expression in incipient primordia, respectively, suggesting their prominent role in *MIR166A* regulation.

Although this study does not identify the explicit TFs for every TF subtype involved in *MIR166A* regulation, the data proposes a model of combinatorial regulation necessary for generating tissue specificity of *MIR166A* at the shoot apex. Accordingly, TFs belonging to TF subtypes NAC-2 and ZF-HD-2 activate *MIR166A* expression at the organ boundary, while the KAN1-ARF3 complex maintains the expression in abaxial cells of primordia (Chapter 2- Scacchi et al., 2023). In addition, pleiotropic TCPs of the TCP-1 subtype, activate *MIR166A* pleiotropically in both primordia and at the meristem-organ boundary. On the other hand, repressors TFs belonging to MYB-1 and ZF-HD-1 subtypes inhibit *MIR166A* expression at meristematic PZ while AS2 TF

represses it on the adaxial side of the leaf (Husbands et al., 2015). Finally, broad expressed TFs both activators and repressors fine-tune *MIR166A* expression at the shoot apex.

Although the above-described model captures the probable combinatorial TF mechanism, given the role of multiple regulators, it does not reflect the entire network but rather a key portion involved in *MIR166A* regulation at the shoot apex. It is plausible that additional combinatorial mechanisms are involved in *MIR166A* regulation. Most TF subtypes have member TFs that show tissue specificity as well as pleiotropic expression at the shoot apex. Thus, it is plausible that not just the pleiotropic TFs, but also tissue-specific TFs within the same subtype could regulate *MIR166A* in different tissues of the shoot apex. It is also plausible that pleiotropically expressed TFs could have different effects on *MIR166A* activity based on tissue type, availability of the right partner, and environmental cues/conditions (Strader et al., 2022).

Among the inplanta analyzed TF subtypes, AP2/EREBP-2 subtype validated in vivo assays, did not spatiotemporally alter *MIR166A* expression in planta. Interestingly, GO term enrichment analysis of the members within these subtypes shows that they are primarily enriched in response to abiotic stresses such as heat (Thomas et al., 2022). Similarly, AP2/EREBP-1 GO term enrichment analysis revealed predominant enrichment for ethylene activated signalling pathway, which plays a vital role in various abiotic stress responses (Chen et al., 2022; Thomas et al., 2022). Further, we have shown that *MIR166A* expression is robust to environmental perturbations (Chapter 3). As such, it is plausible that the role of the above TF subtypes is revealed under stress conditions, probably necessary to keep *MIR166A* expression robust. However, this would require further analysis. We know that ARF3, involved in mediating an auxin response, forms a complex with KAN1 and activates *MIR166A* on the abaxial side of the leaf (Chapter 2- Scacchi et al., 2023). Along with the ARF TF subtype, we obtained TFs belonging to EIL-1 subtypes involved in ethylene signalling from Y1H analysis (Chao et al., 1997; Ju & Chang, 2015). This suggests a probable role of cross-hormone signalling inputs in *MIR166A* regulation at the shoot apex. Indeed, the crosstalk between auxin and ethylene during different aspects of seedling growth is well documented (Hu et al., 2017). All the evidence above collectively shows that the regulation of *MIR166A* involves a complex network of TFs that could act at different spatiotemporal contexts of the shoot apex. In addition, a subset of TFs within the

network may be essential for conveying different signalling inputs under variable environmental conditions.

Among the multiple regulators of *MIR166A*, the TCP TF subtype plays a predominant role, pleiotropically regulating *MIR166A* in the meristem organ boundary and the abaxial side of primordia. TCPs belong to a small family of TFs comprising 24 members subdivided into two classes based on sequence homology and have diverse roles in plant growth and development (Li, 2015; Viola et al., 2023). Notably, they redundantly alter leaf shape by regulating cell proliferation (Kieffer et al., 2011). Further, altering the activity of a subset of Class II TCPs targeted by miR319 leads to serrated and non-flat leaves, emphasizing their role in leaf margin development (Koyama et al., 2017; Palatnik et al., 2003). Although a Class I TCP was detected in our Y1H assay as a *MIR166A* regulator, the binding sites of both TCP classes are remarkably similar and have common targets (Danisman et al., 2012; Kosugi & Ohashi, 2002; Li et al., 2005). As such, it is plausible that TFs from both classes of TCP participate in *MIR166A* regulation. Interestingly, seedlings expressing dominant negative variants of class I TCP show upward curled cotyledons and leaves, reminiscent of leaf phenotypes observed in miR165/166 KO mutants (Aguilar Martinez & Sinha, 2013; Uberti-Manassero et al., 2011). Further, recently, the Class II TCP subfamily was shown to activate an enhancer region, resulting in broad epidermal expression in all cell types of the sepal, like the pleiotropic activation of *MIR166A* by TCPs at meristem organ boundary and the abaxial primordia (Hong et al., 2023). All, these observations reemphasize the involvement of TCPs in the broad/pleiotropic activation of *MIR166A* at the shoot apex.

These TCPs have multiple long Intrinsic Disordered Regions (IDR) that provide higher structural flexibility, allowing them to interact with multiple proteins dynamically (Sun et al., 2013; Valsecchi et al., 2013). In addition, along with self-dimerization, cross-TF interactions of TCPs with members from diverse TF families such as NAC, LOB-AS2, MYB, GRAS, and MADS have been reported (Bemer et al., 2017; Dhaka et al., 2017). The presence of IDRs and interactions with multiple TFs by TCP suggest their importance in controlling regulatory networks. In addition, given their role in different aspects of plant growth and development, they are suggested to act as hubs interconnecting these regulatory networks (Bemer et al., 2017). These properties of TCPs suggest that the observed effect on *MIR166A* expression upon

mutation of TCP-1 TFBS is not solely due to TCPs, but rather a combinatorial effect where they interact with multiple TFs and regulate *MIR166A*. Indeed, on the abaxial side of the leaf along with TCPs, the KAN1-ARF3 complex activates *MIR166A* (Chapter 2- Scaachi et al., 2023). Similarly, NAC-2 and ZF-HD-2, along with TCPs, regulate *MIR166A* in the meristem organ boundary. Further, the BioGRID database (https://thebiogrid.org/) shows that KAN1, ARF3 and CUCs (NAC-2) interact with TCPs. Therefore, during *MIR166A* regulation, TCPs appear to partner with distinct TFs and form distinct regulatory networks. As such, inhibiting the binding of TCP leads to the non-functioning of TCPs along with its multiple TF interactors, plausibly affecting the synergistic activity or cooperativity of these TFs on *pMIR166A* and subsequently affecting precise *MIR166A* expression.

In this work, we validate *in planta* 7 new regulators of *MIR166A* at the shoot apex. However, a key finding of this work is that other than these 7, there exist 23 additional subtypes validated in our in vivo assays that regulate *MIR166A* at the shoot apex. This clearly shows that the regulation of *MIR166A* is far more complex contrary to the simple gene regulation models in plants like the ABC model during floral organ development or recently shown tissue-specific giant cell expression collectively regulated by TCP, DOF and HDZIPIII TFs (Bowman et al., 1991; Hong et al., 2023). As such, the regulation of *MIR166A* also differs from the regulatory mechanism of class A ARFs, which largely repress and modulate their activity (Truskina et al., 2021). Instead, *MIR166A* regulation involves activators and repressors acting in partly opposing domains, like in SHORTROOT (SHR) regulation, necessary for ground tissue development (Sparks et al., 2016). However, in the case of *MIR166A*, these activator and repressor TFs also have overlapping expressions across multiple tissues, which might be necessary to fine-tune *MIR166A* quantitatively. Further, an interesting outcome of this study is the multiple TFBS of these TFs that are distributed across *pMIR166A*, adding another layer of complexity to its regulation. Their distribution explains why the loss of single *pMIR166A cis* mutants does not alter its activity thereby providing a molecular basis that ensures the redundant function of CRMs of *MIR166A* (Chapter 3). It suggests that every CRM has equal prominence and that the redundancy within the CRMs is not confined to a single tissue at the shoot apex but is rather pleiotropic across multiple tissues at the shoot apex. This differs from WOX9 regulation in tomatoes, where specific CRMs are necessary to regulate its function in distinct tissue types (Hendelman et al., 2021). In animals, this is termed enhancer pleiotropy (Laiker & Frankel, 2022;

Sabarís et al., 2019). A comparable example is the *shaven baby* (*svb*) in *Drosophila*, whose redundant enhancers show enhancer pleiotropy by driving *svb* expression in multiple tissues across development (Preger-Ben Noon et al., 2018). Analyzing the spatiotemporal expression of *MIR166A* CRMs at the shoot apex will provide further insights into this concept.

All these findings raise an intriguing question; what is the necessity of such complex *cis* and trans-regulatory activity during *MIR166A* regulation? The answer lies in the function of miR165/166. Along with being a sensitive component, its morphogenic function requires its expression to be spatiotemporal and quantitatively maintained (Chapter 3). As such, the complex regulatory architecture ensures robust *MIR166A* expression as well as the necessary minimal level of miR165/166, thereby guaranteeing its unperturbed function at the shoot apex. Overall, our in-depth analysis of *MIR166A* regulation provides insights into the regulation of morphogens. Further, in line with recent studies, the work here shows that in plants, the combinatorial activity of diverse TFs during development may be a common feature in generating tissue specificity (Knauer et al., 2019; Sparks et al., 2016; Truskina et al., 2021).

Supplementary Figures

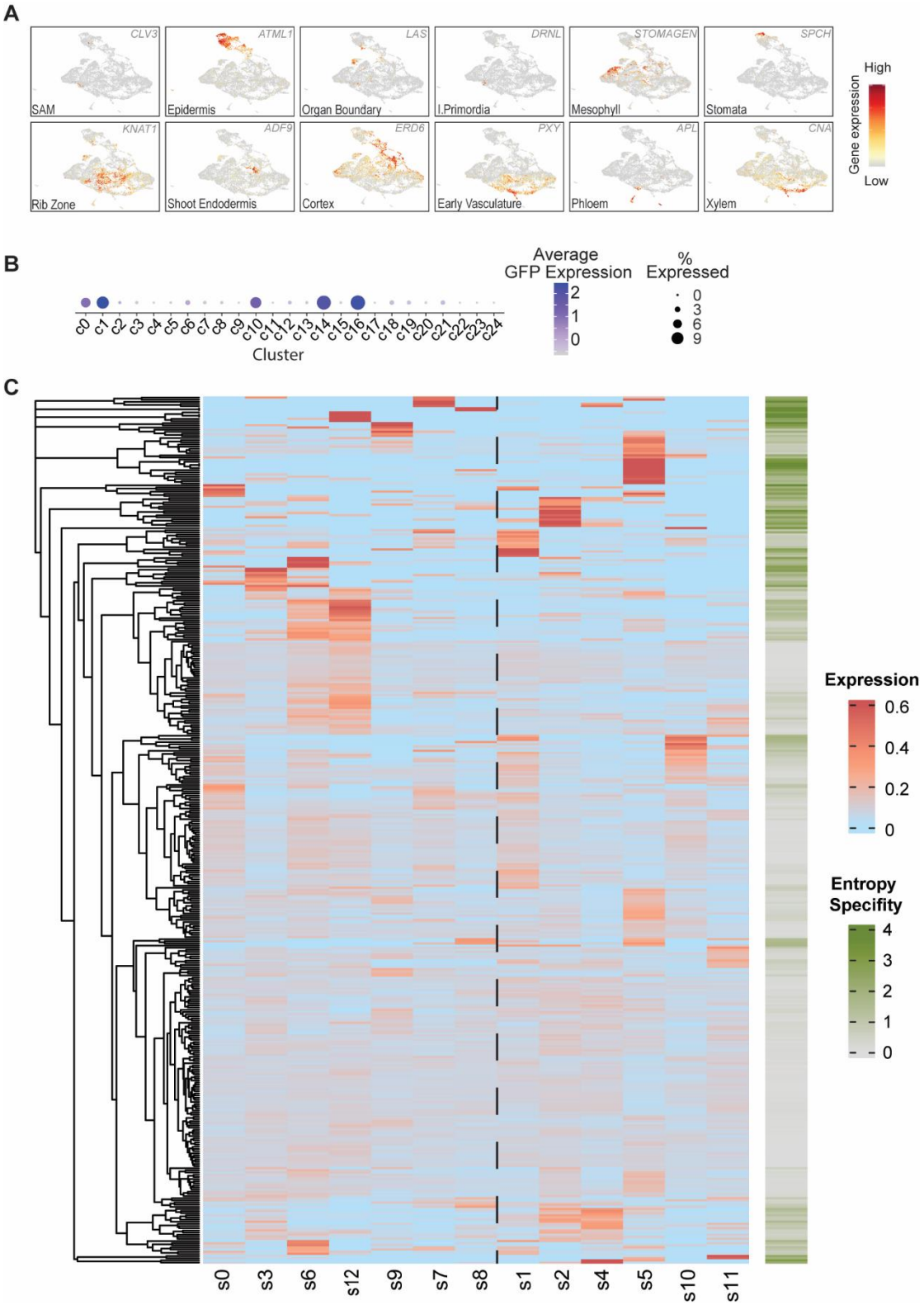

Sfig1: (A) UMAP plot of representative marker genes for different tissue types across the clusters. (B) Dot plot showing the expression of *MIR166A* (GFP) in clusters and identification of

MIR166A positive clusters. Dot diameter - the proportion of cluster cells expressing GFP; colour - mean expression across cells in that cluster. (C) Heatmap of all *MIR166A* regulators, belonging to 30 validated subtypes showing tissue-specific- and broad patterns of expression across *MIR166A* enriched and non-enriched subclusters. Colour, scaled mean expression across cells in that cluster. Heatmap (green) showing entropy specificity of the TFs across the sub-clusters.

Supplementary Tables:

All supplementary tables can be found in the attached compact disc.

General Conclusions and Perspectives

The development of flat leaves is a key evolutionary innovation to maximize the organ surface for efficient photosynthesis and gas exchange. Adaxial-abaxial (ad-ab) polarity specification is necessary to form such a flat leaf architecture and this polarity must be stably propagated across the length and width of the leaf, ensuring it remains flat throughout growth and development (Waites & Hudson, 1995). Indeed, perturbations to this polarity, as observed in multiple polarity determinant mutants, result in non-flat leaves (Eshed et al., 2001; McConnell & Barton, 1998; Waites & Hudson, 1995).

Chapters one and two, and a part of three of this thesis provide new insights into ad-ab polarity from inception to maintenance. A fundamental question in plant developmental biology is understanding the molecular mechanisms underlying ad/ab polarity establishment. In the last years, there has been much discussion concerning this, with various contradicting theories put forward (Caggiano et al., 2017; Qi et al., 2014). The involvement of auxin, during ad ab polarization, which is vital for leaf initiation and outgrowth is a major concern for these studies.

However, by combining time-lapse imaging, cell lineage tracing and molecular analyses that capture rapid spatiotemporal changes during primordium emergence at the shoot apex, we describe a model that provides new insights and ends the discrepancy (Chapter 1- (Burian et al., 2022)). Accordingly, Ad-Ab polarity is established by a uniform auxin maximum on a pre-pattern of *AS2* and *KAN1* expression at the meristem periphery. The pre-pattern converts this uniform auxin input into a polar auxin response via *ARF3* regulation in the *AS2* domain that differentiates the adaxial from abaxial founder cells (Chapter 1- (Burian et al., 2022)). Accordingly, auxin acts as a signal that coordinates the positioning, growth, and pattern of leaves. Going forward, it would be important to study the spatiotemporal regulation of ARF3 during this process in more detail, especially given that its initial adaxial expression during establishment, shifts abaxially in the growing primordium. In this regard, although we show that AS2 and KAN1 repress *ARF3* and that lower levels of AS2 at the meristem periphery during establishment promote ARF3 expression on the adaxial side, it is unclear which TFs activate its expression and how the position of the pre-pattern remains stable at the growing SAM. In the future, it would also be interesting to understand if activating TFs are indeed involved in ARF3 regulation, or if they follow a regulatory mechanism

such as class A ARFs, which are predominantly regulated by a network of repressor TFs (Truskina et al., 2021).

In Chapters Two and Three, we show that during ad-ab polarity establishment, *MIR165/166* is expressed at the meristem periphery, and represses HDZIPIII to restrict its activity to the Central Zone (CZ) of the meristem. As such miR165/166 may separate the function of HDZIPIII between the meristem and the leaf, to ensure proper spatiotemporal leaf emergence and ad-ab polarization. Our data shows that at the plant level, this is carried out in a threshold-based manner, whereby an optimal window exists for miR165/166 levels within which the plant has a normal SAM and develops flat leaves. If the level is altered on either side of the window, then phenotypic defects are present (Chapter 3). The thresholding behaviour of miR165/166 should be studied further by explicitly altering its level in an inducible manner at the meristem periphery to determine the qualitative and quantitative changes in HDZIPIII expression and study its effect on stem cell homeostasis and ad-ab polarity.

Following resolution, an intricate and redundant Gene Regulatory Network (GRN) of TFs and small RNAs maintains polarity. Here, antagonistic interactions between TFs promote adaxial- or abaxial cell fates (Husbands et al., 2009). However, the cells need to know their position relative to the tissue to determine their fate. miR165/166 and tasiARF, act as morphogens to provide the necessary positional information (Chitwood et al., 2009; Skopelitis et al., 2017). In addition, the polarity network must remain unperturbed in the face of environmental and genetic perturbations throughout growth. In Chapter Two, through in-depth theoretical and experimental analysis, we show that the GRN of leaf polarity follows the organizing principles of the Turing system, driven by the diffusible small RNAs. This self-organizing system, instructed by pre-patterned information dynamically adapts to ensure that the ad-ab pattern is robust. At the same time, it provides the flexibility needed for generating morphologically diverse leaf shapes. This leaf polarity GRN requires transient pre-patterned information to maintain a stable ad-ab polarity, but the mechanisms involved in transmitting this information remain to be studied. For example, miR165/166 polarizing HDZIPIII to the adaxial side of the primordia before the onset of the maintenance phase suggests that these small RNAs may play a role in this regard. However, the actual mechanisms are not fully understood.

In Chapters Three and Four, we provide new insights into the molecular underpinnings of critical concepts in developmental patterns such as how sensitive nodes within the network are governed to ensure the pattern is robust, and how tissue specificity of morphogens is regulated at spatiotemporal and quantitative levels. Within the leaf polarity network, miR165/166 is part of the most fragile node (Chapter 2- Scacchi et al.,2023). In Chapters Two and Three, through timelapse imaging and genetic analysis, we show the critical importance of correct spatiotemporal and quantitative levels for proper miR165/166 function at the shoot apex. We go on to show that plants have developed diverse mechanisms to cope with these sensitivities. In the scenario of miR165/166, genetic redundancy at the miRNA family level leads to excess miR165/166 production, which safeguards its activity and likely keeps it robust to perturbations. (Chapter 3). On an individual gene level, the presence of redundant CRMs within *pMIR166A* that are organized like "shadow enhancers" (Kvon et al., 2021) ensures robust gene expression which in turn leads to phenotypic robustness. Excess production of miR165/166 at the shoot apex could affect its diffusion distribution as well as the amplitude of the gradient, impacting the pattern (Skopelitis et al., 2017). It would be interesting to study further the mechanisms by which miR165/166 gradients are buffered to keep its function robust. Further, whether redundant *cis*-mechanism of *MIR166A* regulation is conserved in other members of the miR165/166 family is not known. Given that three CNSs of *pMIR166A* are also conserved in *MIR166B*, it strongly favours a similar regulatory mechanism, at least at the meristem periphery (Sfig 3B). This work further opens an exciting field of enhancer studies in small genome plants such as *Arabidopsis*, where it is plausible that enhancer elements are not always distant (Schmitz et al., 2021).

An intriguing question is how tissue specificity of morphogens is generated. In Chapter Four, using *MIR166A* as an example, the dominant contributor of miR165/166 at the shoot apex, we show that a complex network of TFs that are redundant and combinatorial generates tissue specificity. These TFs with multiple TFBS distributed across the promoter plausibly make the CRMs pleiotropic at the shoot apex, resulting in enhancer pleiotropy as observed in animals (Laiker & Frankel, 2022; Sabarís et al., 2019). Interestingly, preliminary analysis shows that the phylogenetically conserved CRMs of *pMIR166A* overlap with the Accessible Chromatin regions (ACR) of *pMIR166A,* obtained from root single cell ATAC seq data set in the root endodermis where *MIR166A* is expressed (Denyer & Parvanov, unpublished -not shown). Thus, the redundant *cis*-regulatory activity observed at the shoot apex may also be conserved in the root,

suggesting an additional layer of enhancer pleiotropy. However, this requires further analysis. Overall, the redundant regulatory architecture of both *cis*- and *trans* components ensures dynamic *MIR166A* expression on the abaxial side of the growing primordia and re-establishment of its expression at the meristem periphery. This study and other recent studies on comparable developmental programs show complex combinatorial TF-mediated gene regulation during development (Knauer et al., 2019; Sparks et al., 2016; Truskina et al., 2021). However, whether such regulation is reserved only for sensitive components of a developmental network like miR165/166 at the shoot apex, or crucial TFs like *SHORT ROOT* (*SHR*) in ground tissue development, remains to be explored (Sparks et al., 2016).

An immediate question for the future concerning the regulation of *MIR166A* is to understand how the combinatorial activity of TFs is integrated with CRMs. Our data suggests that distinct TF complexes, bind on *cis*-regions of *pMIR166A* to regulate its activity. Indeed, the type of TFs, their binding affinity and interactions, and the order, position, and spacing between the multiple TFBS are essential for the proper functioning of the enhancers. Based on these attributes, known as enhancer architecture, three different models are proposed and observed in animals. The first is a rigid model called the enhanceosome model, where all the TFs are co-operatively bound on the enhancer in a fixed motif order and orientation (motif grammar). More flexible are the billboard and TF collective models. In the billboard model, the motif grammar is flexible, involving both cooperativity as well as independent binding of TFs on the enhancer. In the TF collective model, the same TFs bind on multiple enhancers either directly via DNA binding or indirectly via protein-protein interactions, independent of the motif grammar (reviewed in (Long et al., 2016; Panigrahi & O'Malley, 2021; Ray-Jones & Spivakov, 2021; Spitz & Furlong, 2012)). Our data favours that the CRMs may follow a flexible model, whereby different combinations of TF complexes bind. Since multiple CRMs regulate, *pMIR166A*, it is also possible that a combination of both rigid and flexible models exists in *MIR166A* regulation, which remains to be explored. Going forward, it would also be important to understand the 3D spatial organization of these CRMs and how this selectively impacts TFs binding to modulate *MIR166A* expression at the shoot apex.

Although many questions regarding ad-ab polarity remain, this study provides significant insights into its establishment and maintenance. The observed dynamics in the system were

unexpected, especially given the robustness in leaf morphology displayed. The described complexity in gene regulatory mechanisms may begin to explain this seeming contradiction.

Material and Methods

(Chapter 3 and Chapter 4)

Plant Materials and Growth Conditions

All analyses were performed in the *Arabidopsis thaliana* Columbia (Col-0) ecotype. All *Arabidopsis* seeds were surface sterilized and plated on 0.5x MS plates supplemented with 0.7% Agar (hereby 0.5x MSA) without other supplements unless otherwise stipulated. The seeds were stratified at 4 °C for 3 days and then transferred to a growth chamber.

CRISPR knockout mutants of miR165/166 and *cis* mutants of *MIR166A* promoter (*pMIR166A*) were grown under long-day conditions (16h light, 8h darkness, at 22 °C).

Transgenic plants carrying wild-type *pMIR166A* (*pMIR166A^{WT}):miR166A* and *pMIR166A* variants with mutated TFBS *(pMIR166A^{mutTFBS}):miR166A* in *mir166a mir166b* background were germinated on 0.5x MSA supplemented with 1% sucrose and grown under long-day conditions. *pMIR166A^{WT}/pMIR166A^{mutTFBS}:3xVENUS_N7* in *Col-0* background for quantification experiments were selected on 0.5x MSA supplemented with phosphinothricin (PPT) under long-day conditions and harvested post 7 days of germination.

For light stress experiments, *pMIR166A cis* mutant seeds were germinated on 0.5x MSA and grown under long-day conditions but with different light intensities of 60- (low light), 120- (standard light), and 300 µmol/m2/s (UML) (high light). For continuous light experiments, plants were grown at a light intensity of 120 µmol/m2/s, with a 24-hour light cycle. For heat stress experiments, *pMIR166A* CRISPR *cis* mutants were grown on 0.5x MSA plates under long-day conditions at 28°C and 30°C.

Arabidopsis plants for imaging of the vegetative shoot apex were germinated on soil for 30-45 days under short-day conditions (8 h light, 22 °C and 16 h darkness, 20 °C) as previously described (Chapter 1 (Burian et al., 2022)). Here, *pMIR166A^{WT}/ pMIR166A^{mutTFBS}:3xVENUS_N7/Col-0* transgenics were first selected on 0.5x MSA

supplemented with phosphinothricin (PPT) germinated and then transferred to soil post 7 days under short-day conditions.

Plasmid Construction & Generation of Transgenic Lines

Generation of mir165/166 CRIPSR Knockouts.

Guide RNA (gRNA) design for all CRISPR experiments was based on the guidelines for on-target and off-target scores previously described (Doench et al., 2016; Hsu et al., 2013), using either the software CRISPR-P (http://cbi.hzau.edu.cn/CRISPR2/) or CRISPR/Cas9 tool from Benchling. When Benchling was used, gRNA with an on-target value of at least 50 (100 being optimal), was selected. Tables S8 and S9 summarise all gRNAs used in this study. Two gene-specific gRNAs were designed each for *MIR165A*, *MIR166A* and *MIR166B* loci, targeting the microRNA hairpin (pre-miRNA) in each case. For *MIR166A* and *MIR166B,* the gRNAs targeting its precursor were sequentially assembled into the entry plasmid (*pEn-2x-Chimera*) and cloned into *pDE_CAS9_OLE1* by a single site gateway LR reaction (Fauser et al., 2014). *pDE-Cas9* comprises a ubiquitin promoter, *PcUbi4-2*, driving CAS9, and a FAST-RED cassette (*pOLE1:OLE1_tagRFP),* active in the seed coat (to aid selection of transformants) (Fauser et al., 2014). These plasmids were transformed into Col-0 plants by floral dipping (Clough & Bent, 1998) and the transformed seeds were identified by screening red fluorescent seeds. For *MIR166B*, the transformed T1 plants were subjected to heat stress to maximize the CAS9 efficiency (LeBlanc et al., 2018) and screened for CRISPR edits in the next generation. Transformed seeds were screened for deletions spanning the hairpin of the microRNA by PCR and confirmed by sequencing.

Homozygous single mutants of *MIR166A* and *MIR166B* identified were crossed and subsequent F1 progeny selfed. The F2 generation was analyzed to obtain double homozygous *mir166a mir166b* mutant plants. In addition, CAS9-free plants were obtained in the same generation by analyzing non-fluorescent seeds devoid of the FAST-RED cassette. For *MIR165A*, entry plasmids carrying two sgRNAs were cloned by the gateway into both *pDE: CAS9* and *pEC: CAS9* (whereby CAS9 is driven by egg cell promoter combination *EC1.1*, *EC1.2*, (Doctoral thesis- (Klesen, 2020)) (Sprunck et al., 2012; Wang et al., 2015). These were transformed into a

subset of F2 progeny consisting of different allelic combinations of *mir166a* and *mir166b* mutants. The transformed seeds were then screened for deletions spanning the hairpin of microRNA to obtain all possible allelic combinations of *mir166a, mir166b,* and *mir165a,* along with single *mir165a* mutants.

Generation of *pMIR166A* CRISPR *cis* Mutants.

Multiple gRNAs targeting *pMIR166A* (2.435 kb) in the genome were designed as mentioned above. A multiplexing approach was used consisting of a modified CAS9 system that combines up to six guides into *pEC:CAS9* ((Decaestecker et al., 2019) (Doctoral thesis (Klesen, 2020)). This allowed the generation of diverse *cis*-regulatory alleles across *pMIR166A*. In brief, sgRNAs targeting different regions of *pMIR166A* were initially cloned downstream of the *U6* promoter in different entry clones (Decaestecker et al., 2019). These gRNAs in a combination of three to six were assembled into an intermediate vector by Green gate (golden gate) assembly (Doctoral thesis- (Klesen, 2020)). The intermediate vector carrying *attL1* and *attL2* sites, with the gRNAs was lastly cloned into *pEC: CAS9* by gateway reaction ((Doctoral thesis - (Klesen, 2020)). CRISPR/CAS9 expression vectors were transformed into *mir165a*$^{cr\text{-}1}$ *mir166b* mutants. Transformed T1 individuals, selected by red fluorescent seeds, were screened for genomic deletions across the targeted *pMIR166A* region by PCR. These plants were self-fertilized, and T2 seeds in a CAS9-free background (non-fluorescent seeds) were screened by PCR for the CRIPSR edits on *pMIR166A*. This was further confirmed by sequencing and subsequently assembled (Bachelor thesis- (Tauber, 2021)).

Generation of Transient Luciferase Assay Plasmids.

To generate the *pMIR166A: Luciferase*$_{firefly}$ reporter plasmids, *pMIR166A* (2.435kb) was amplified from genomic DNA of *Col-0* with *BamHI* and *SpeI* restriction sites flanking the 5' and 3' ends, respectively. This was cloned into a *pLucTraP* plasmid (Lau et al., 2011), upstream of the *Luciferase*$_{firefly}$. For all Transcription Factor (TF) effector plasmids, the coding sequence of each was amplified from Col-0 cDNA, flanking specific restriction sites on either side, and cloned ahead of the *2x 35S* promoter into *pJIT60* (Lau et al., 2011). Table S10 summarises the primers and restriction enzymes used.

Generation of Transcription Factor Binding Site (TFBS) Mutated Variants of *pMIR166A* Plants.

Position Weight Matrices (PWM) for TF binding sites were obtained from available data sets (Franco-Zorrilla et al., 2014; Mathelier et al., 2015; O'Malley et al., 2016). The occurrence of predicted TFBS for select TF subtypes on the *pMIR166A* was identified using FIMO software with a p-value cut off 10^{-3} (Table S3, https://meme-suite.org/meme/tools/fimo). *pMIR166A*, with mutated TF binding sites (*pMIR166A*^{mutTFBS}), were designed *in silico* by base substituting the core binding motif sequence. For predicted TFBS of the motif subtypes AP2/EREBP-2, AP2/EREBP-3, LOB/AS2-2, TCP-1, ZFHD-1, and ZFHD-2, all the predicted occurrences were mutated. For AP2/EREBP-1, MYB-1 and NAC-2 predicted TFBS specifically for ESE3, LOF1, and CUC3, were mutated respectively.These *in silico* designed *pMIR166A*^{mutTFBS} sequences were re-analyzed using FIMO to confirm the loss of all predicted TFBS of interest in *pMIR166A,* not generating new TF binding and leading to very minimal global changes. These *pMIR166A*^{mutTFBS} sequences were then *de novo* synthesized with flanking *KpnI* and *XmaI* restriction sites at 5' and 3' ends, respectively (Genscript).

For time-lapse imaging in the shoot apex, *pMIR166A*^{mutTFBS} variants were subcloned upstream of *3xVENUS_N7* and the OCS terminator in the *JM173* T DNA vector (a gift of Detlef Weigel, MPI, Tübingen), using *KpnI* and *XmaI* restriction sites to generate *pMIR166A*^{mutTFBS}*:3xVENUS_N7* plasmids (Table S11). As a positive control, wild-type *pMIR166A*^{WT}*:3xVENUS_N7* was cloned as described above. All were then transformed into Col-0 plants.

For complementation assays, *pMIR166A*^{mutTFBS} variants driving a 1080bp genomic fragment containing the *MIR166A* precursor and its downstream intergenic region (hereby *miR166A*) were generated. Using an overlap PCR approach, the *pMIR166A*^{mutTFBS} and miR166A amplicons flanking overlapping sequences at its 3' and 5' ends, respectively, were combined to generate *pMIR166A*^{mutTFBS}*:miR166A*. The combined PCR product thus generated flanked *KpnI* and *BamHI* restriction cut sites at their 5' and 3' ends, respectively (Table S11). These were subcloned into a binary vector carrying FAST RED cassette for plant selection (a gift from Marcella de Francisco Amorim, Universität Tübingen). As a positive control, wild type *pMIR166A*^{WT}*:miR166A* was analyzed (Bachelor thesis- (Tauber, 2021)). All

pMIR166A^{mutTFBS}:miR166A and *pMIR166A^{WT}:miR166A* plasmids were transformed into *miR166a miR166b* mutants for analysis.

Live Cell Imaging.

Vegetative Shoot apices (n>7) of transgenic reporter plants carrying *pMIR166A^{WT}:3xVENUS_N7*, *pMIR166A^{mutTFBS}:3xVENUS_N7*, *pMIR166A^{CNSE}:3xVENUS_N7* were dissected for imaging as previously described (Chapter- 1 (Burian et al., 2022). 0.1% Propidium Iodide stained apices were, imaged with an upright confocal laser-scanning microscope (Leica TCS SP8) with microscopic conditions set as previously described. (Chapter-1 (Burian et al., 2022)).

RNA Extraction & Quantification.

Vegetative shoot apices (n=10) of seven-day-old mir165/166 knockouts and *pMIR166A cis* mutants grown under long-day conditions were dissected, pooled, and processed for RNA extraction. To obtain adequate tissue, up to twenty apices of double- and triple *miR165/166* CRISPR knockouts were pooled. RNA was isolated using TRIzol reagent (Invitrogen) and treated with Turbo DNAse according to the manufacturer's recommended protocols (Invitrogen). cDNA was synthesized using LunaScript RT master mix according to the manufacturer's protocol (New England Biolabs) with the oligoDT and stem-loop reverse primers specific for miR166, and U6 sRNA (Table S12, (Varkonyi-Gasic et al., 2007)). miR166 small RNA levels were quantified using a Luna Universal qPCR master mix according to the manufacturer's protocol (New England Biolabs) and normalized to U6 small RNA as the internal control, while *PHB* transcripts were normalized to *PP2A* (Table S12). For *pMIR166A^{WT}:3xVENUS_N7* and *pMIR166A^{mutTFBS}: 3xVENUS_N7* seedlings, seven to ten shoot apices were pooled, RNA extracted and cDNA synthesized with oligoDT primers as described above. *Venus_N7* RNA levels were quantified and normalized to *PP2A* as an internal control. Up to ten biological replicates were used for analysis, with a minimum of three. For *pMIR166A,* CRISPR *cis* mutants, and miR165/166 CRISPR knockout three biological replicates were analyzed. *MIR165A, MIR166A and MIR166B* levels were quantified from Col-0 cDNA shoot apices and normalized to PP2A as internal control, from three biological replicates. Relative gene expression was

calculated using the Delta CT method. Statistical analysis was performed using a two-tailed student's t-test, and data were plotted using the ggplot2 package in R studio. Table S12 summarises all qPCR primers used.

Phylogenetic Footprinting of *MIR166A* Promoters Across *Brassicaceae.*

Genomic sequences 2.5 kb upstream of putative *MIR166A* orthologs (Chorostecki et al., 2017) of *Arabidopsis lyrata* (*A. lyrata*), *Capsella grandiflora* (*C. grandiflora*), *Capsella rubella* (*C. rubella*), *Boechera stricta* (*B. stricta*), *Brassica rapa FPsc* (*B. rapa*) and *Eutrema salsugineum* (*E. salsugineum*), were obtained from Phytozome database (https://phytozome-next.jgi.doe.gov/). For *pMIR166B*, a 2.5kb genomic region upstream of the precursor was used. These were analyzed for conserved noncoding sequences (CNS), identified by sequence homology using mVISTA with alignment windows of 100 bp at a similarity threshold of 70% (Frazer et al., 2004).

Enhanced Yeast1Hybrid (eY1H) Analysis.

Enhanced Yeast1Hybrid analysis was performed by the Yeast One-Hybrid Services Core Facility, University of California, Davis. In brief, the promoter fragment of *MIR166A* (2.435kb) was split into two fragments: *pMIR166A* fragment 1 (734bp): and *pMIR166A* fragment 2 (1906bp). These were cloned into *pMW2* and *pMW3* yeast reporter plasmids for HIS3, and LacZ selections, respectively, which were used as bait (Table S13). They were screened for TF-DNA interactions using a library of 2033 *Arabidopsis* TFs as prey. Positive interactions were identified by HIS3 and Lac Z reporters. All TFs obtained from the Y1H screen were grouped based on their binding motifs (Franco-Zorrilla et al., 2014; Mathelier et al., 2015; O'Malley et al., 2016) and phylogenetic analysis (http://planttfdb.gao-lab.org/). In addition, TFs within the whole genome belonging to a given subtype were similarly identified based on DNA binding motifs and phylogenetic analyses across TF families (http://planttfdb.gao-lab.org/). TFs and TF families with no motif or data were not considered.

DAP-seq Database Analysis.

We validated TF subtypes binding on *pMIR166A* by analysing the database of predicted DAP-Seq targets for TFs (O'Malley et al., 2016). Further, we manually analyzed DAP-Seq peaks for TF subtypes on *pMIR166A* (chromosome2, coordinates 19173645- 19176080) using Plant Cistrome Database (O'Malley et al., 2016).

Transient Luciferase Assay in *Arabidopsis* Protoplasts.

As previously described, the Luciferase assay was performed with cell culture protoplasts isolated from *Arabidopsis thaliana* (Burian et al., 2022; Lau et al., 2011; Mehlhorn et al., 2018). In brief, 2 µg each of *pMIR166A: Luciferase*$_{firefly}$, and *2x35s: TF* effector plasmids along with 2 µg of internal control plasmid *2x35S: renilla luciferase* (*pgl4.70*) were transfected into *Arabidopsis* cell culture protoplasts. Following overnight incubation, transfected protoplasts were analyzed and processed using the Dual Luciferase Assay System as described (Promega, (Burian et al., 2022)). Luciferase activity was measured using a TECAN's Infinite F-200 plate reader and relative activity was calculated as Firefly over Renilla. Three biological replicates for each TF-*pMIR166A* interaction were analyzed. Data were plotted using the ggplot2 package in R studio.

Single Cell RNA Sequencing (scRNA seq) of the Vegetative Shoot Apex.

Protoplast isolation, library preparation, and sequencing.

Vegetative shoot apices (n=100) of eight-day-old *pMIR166A: erGFP* (gift from Keiji Nakajima - Nara Institute of Science and Technology, Japan) seedlings grown under long-day conditions (23°C) were dissected for single-cell library preparation. Protoplasts were prepared in a protocol adapted from (Denyer et al., 2019) as previously described, with modifications. In brief, harvested apices were finely diced with a razor blade and digested in a cocktail of protoplast buffer solution (0.1 M KCl, 0.02 M MgCl2, 0.1 % BSA, 0.08 M MES, 0.6 M Mannitol, adjusted to pH 5.5 with 0.1M Tris HCl), supplemented with cell wall digestion enzymes (1.5 % Cellulase R-10, 1 % Pectolyase, and 1 % Hemicellulase). Digestion ran, for two hours on an orbital shaker (20°C, 200 revolutions/min). Samples were then filtered using a sieve (100 µm) and rinsed

thoroughly with the enzyme-free protoplast buffer. Cells were then washed by centrifugation (three minutes, 250g). The supernatant was gently removed, and the pellet was resuspended with 10 mL protoplast buffer. Protoplasts were washed twice again and filtered through a 40 μm sieve. The suspension was quantified using a hemocytometer, adjusting the concentration to 750 cells/μL. Single-cell libraries were prepared per the 10X Genomics 3' RNA-Seq Single Cell kit protocol (v2). Sequencing was performed by Novogene (Cambridge)- PE150 on the NovaSeq platform.

RNA expression analysis.

FastQC (v0.11.9) was used to validate the quality of the sequencing reads and aligned to the *Arabidopsis* TAIR10 reference genome and TAIR10.51 annotation with STAR (v2.7.9) software. For the detection of *MIR166A* expression (*GFP* transcript), the GFP sequence was added to the reference fasta and gtf files (Denyer et al., 2019). Low-quality cells with <3000 UMI(unique molecular identifier),> 5 % of mitochondrial and >10% of chloroplast reads were discarded for downstream analysis UMAP (Uniform Manifold Approximation and Projection) using Seurat (v4.0.5) (Hao et al., 2021). Cells were clustered using Louvain clustering with fifty principal components and a resolution parameter of 0.7. Clusters were annotated as specific tissue types based on known markers as previously reported (Burian et al., 2022; Byrne et al., 2000; Kim et al., 2021; Lopez-Anido et al., 2021; Shi et al., 2020; Tenorio Berrío et al., 2021; Tian et al., 2019; Yamada et al., 2010; Zhang et al., 2021). Average expressions of TFs across subclusters were calculated using the Seurat command AverageExpression. *MIR166A*-positive clusters were identified by analyzing the total proportion of GFP-positive cells (>2.4%) across each cluster (Table S4). These positive clusters were then subclustered to identify GFP-enriched subclusters by analyzing the proportion of GFP-positive cells across the subcluster (>7%. Table S5). Shannon entropy (entropy specificity) was computed with the BioQC package in R to identify tissue type-specific genes with entropy specificity score >1, while lower than 1 was considered to be expressed in multiple tissues (Ameri & Lewis, 2021). Expression data of TFs was visualized by heatmaps generated using the Complex Heatmap package in R.

Plant Phenotyping

MIR165/166 CRISPR KO Mutants.

Homozygous single-, double-, and triple mutant seedlings of *MIR166A*, *MIR166B,* and *MIR165A* were compared to wild type for phenotypic changes seven, sixteen, and twenty days after germination. Seedlings of each genotype were analyzed for changes in rosette and leaf development. *mir165a^{cr-1} mir166a mir166b,* triple homozygous mutants were selected from a segregating *mir166a*/+ *mir165a $^{cr-1}$* /- *mir166b*/- population. Similarly, the shoot apices (n≥5) of forty-day-old homozygous *mir165a $^{cr-2}$ mir166a, mir165a $^{cr-1}$ mir166b and mir166a mir166b* plants grown under short-day conditions were imaged and analyzed as previously described (Burian et al., 2022). For *mir165a^{cr-1} mir166a mir166b* mutants, shoot apices were analyzed in seven-day-old seedlings grown under short-day conditions.

pMIR166A CRISPR *Cis* mutants.

Forty to sixty T2 seeds of each *pMIR166A* CRISPR *cis* mutant (CAS9 free), either homozygous and heterozygous lines for the CRISPR edit/s, were analyzed for changes in rosette and leaf development at eight- and ten-days post-sowing (Bachelor thesis- (Tauber, 2021). In addition, for *cis* mutant allele variants lacking adequate seed numbers, fifty seeds of their T3 homozygous or heterozygous lines were analyzed for the phenotypic changes as described above. In addition, 18-day-old seedlings of select *pMIR166A* CRISPR *cis* mutant plants grown on 0.5x MSA plates were imaged using Zeiss axiocam.

Stress experiments.

Fifteen to thirty seeds of select homozygous *pMIR166A* CRISPR *cis* mutant plants were analyzed up to 18 days after sowing for changes in leaf development. Non-germinating plants were discarded from the analysis. Data were documented using a Cannon powershotX camera. In addition, representative images for each line were captured at 18 days using Zeiss axiocam. Stress experiments were performed twice for low light (60 UML), standard light (120 UML) and heat stress (28˚C,30˚ C) conditions and once for High light (300 UML) conditions.

Complementation Assays.

The rescue of the *mir166a mir166b* phenotype by plants carrying *pMIR166A^{WT}:miR166A* and *pMIR166A^{mutTFBS}: miR166A* was analyzed up to 12 days after sowing for phenotypic changes in comparison to *mir166a mir166b* phenotype. Based on observed rescued phenotypes, plants were grouped into complemented, non-complemented, and partially complemented phenotypic classes (the latter comprising developmentally delayed leaf growth and development). At least 45 independent T1 transformants were analyzed for each *pMIR166A^{mutTFBS}* variant (Bachelor thesis-(Tauber, 2021). For plants carrying *pMIR166A* (276 bp) comprising CNS E, 31 independent T1 transformants were analysed. Statistical significance was calculated using the Mann-Whitney U test. The phenotype of all the variants was imaged using Cannon powershotX.

Image Processing and Analysis.

Confocal images of the shoot apex (z-stacks) were processed and analyzed by MorphographX as previously described (Barbier de Reuille et al., 2015; Burian et al., 2022). All samples were processed equally within each experiment. Representative plant images from all phenotypic analysis experiments were captured using Zeis axiocam zoom. All samples within an experiment were treated equally.

References

Abley, K., Locke, J. C. W., & Leyser, H. M. O. (2016). Developmental mechanisms underlying variable, invariant and plastic phenotypes. *Annals of Botany*, *117*(5), 733-748. https://doi.org/10.1093/aob/mcw016

Aguilar Martinez, J., & Sinha, N. (2013). Analysis of the role of Arabidopsis class I TCP genes AtTCP7, AtTCP8, AtTCP22, and AtTCP23 in leaf development [Original Research]. *Frontiers in Plant Science*, *4*. https://doi.org/10.3389/fpls.2013.00406

Allen, E., & Howell, M. D. (2010). miRNAs in the biogenesis of trans-acting siRNAs in higher plants. *Semin Cell Dev Biol*, *21*(8), 798-804. https://doi.org/10.1016/j.semcdb.2010.03.008

Allen, E., Xie, Z., Gustafson, A. M., & Carrington, J. C. (2005). microRNA-directed phasing during trans-acting siRNA biogenesis in plants. *Cell*, *121*(2), 207-221. https://doi.org/10.1016/j.cell.2005.04.004

Allen, R. S., Li, J., Stahle, M. I., Dubroué, A., Gubler, F., & Millar, A. A. (2007). Genetic analysis reveals functional redundancy and the major target genes of the Arabidopsis miR159 family. *Proceedings of the National Academy of Sciences*, *104*(41), 16371-16376. https://doi.org/doi:10.1073/pnas.0707653104

Ameri, A. J., & Lewis, Z. A. (2021). Shannon entropy as a metric for conditional gene expression in Neurospora crassa. *G3 Genes|Genomes|Genetics*, *11*(4). https://doi.org/10.1093/g3journal/jkab055

Axtell, M. J., Jan, C., Rajagopalan, R., & Bartel, D. P. (2006). A two-hit trigger for siRNA biogenesis in plants. *Cell*, *127*(3), 565-577. https://doi.org/10.1016/j.cell.2006.09.032

Bar, M., & Ori, N. (2014). Leaf development and morphogenesis. *Development*, *141*(22), 4219-4230. https://doi.org/10.1242/dev.106195

Barbier de Reuille, P., Routier-Kierzkowska, A.-L., Kierzkowski, D., Bassel, G. W., Schüpbach, T., Tauriello, G., Bajpai, N., Strauss, S., Weber, A., Kiss, A., Burian, A., Hofhuis, H., Sapala, A., Lipowczan, M., Heimlicher, M. B., Robinson, S., Bayer, E. M., Basler, K., Koumoutsakos, P., . . . Smith, R. S. (2015). MorphoGraphX: A platform for quantifying morphogenesis in 4D. *Elife*, *4*, e05864. https://doi.org/10.7554/eLife.05864

Barkai, N., & Shilo, B.-Z. (2009). Robust Generation and Decoding of Morphogen Gradients. *Cold Spring Harbor Perspectives in Biology*, *1*(5). https://doi.org/10.1101/cshperspect.a001990

Bemer, M., van Dijk, A. D. J., Immink, R. G. H., & Angenent, G. C. (2017). Cross-Family Transcription Factor Interactions: An Additional Layer of Gene Regulation. *Trends in Plant Science*, *22*(1), 66-80. https://doi.org/10.1016/j.tplants.2016.10.007

Bhatia, N., Ahl, H., Jonsson, H., & Heisler, M. G. (2019). Quantitative analysis of auxin sensing in leaf primordia argues against proposed role in regulating leaf dorsoventrality. *Elife*, *8*. https://doi.org/10.7554/eLife.39298

Biłas, R., Szafran, K., Hnatuszko-Konka, K., & Kononowicz, A. K. (2016). Cis-regulatory elements used to control gene expression in plants. *Plant Cell, Tissue and Organ Culture (PCTOC)*, *127*(2), 269-287. https://doi.org/10.1007/s11240-016-1057-7

Birchler, J. A., & Yang, H. (2022). The multiple fates of gene duplications: Deletion, hypofunctionalization, subfunctionalization, neofunctionalization, dosage balance constraints, and neutral variation. *The Plant Cell*, *34*(7), 2466-2474. https://doi.org/10.1093/plcell/koac076

Bomblies, K., Dagenais, N., & Weigel, D. (1999). Redundant Enhancers Mediate Transcriptional Repression of AGAMOUS by APETALA2. *Developmental Biology*, *216*(1), 260-264. https://doi.org/https://doi.org/10.1006/dbio.1999.9504

Bowman, J. L., Smyth, D. R., & Meyerowitz, E. M. (1991). Genetic interactions among floral homeotic genes of Arabidopsis. *Development*, *112*(1), 1-20. https://doi.org/10.1242/dev.112.1.1

Braybrook, S. A., & Kuhlemeier, C. (2010). How a Plant Builds Leaves. *The Plant Cell*, *22*(4), 1006-1018. https://doi.org/10.1105/tpc.110.073924

Brunoud, G., Wells, D. M., Oliva, M., Larrieu, A., Mirabet, V., Burrow, A. H., Beeckman, T., Kepinski, S., Traas, J., Bennett, M. J., & Vernoux, T. (2012). A novel sensor to map auxin response and distribution at high spatio-temporal resolution. *Nature*, *482*(7383), 103-106. https://doi.org/10.1038/nature10791

Burian, A., Paszkiewicz, G., Nguyen, K. T., Meda, S., Raczyńska-Szajgin, M., & Timmermans, M. C. P. (2022). Specification of leaf dorsiventrality via a prepatterned binary readout of

a uniform auxin input. *Nature Plants*, *8*(3), 269-280. https://doi.org/10.1038/s41477-022-01111-3

Byrne, M. E., Barley, R., Curtis, M., Arroyo, J. M., Dunham, M., Hudson, A., & Martienssen, R. A. (2000). Asymmetric leaves1 mediates leaf patterning and stem cell function in Arabidopsis. *Nature*, *408*(6815), 967-971. https://doi.org/10.1038/35050091

Caggiano, M. P., Yu, X., Bhatia, N., Larsson, A., Ram, H., Ohno, C. K., Sappl, P., Meyerowitz, E. M., Jonsson, H., & Heisler, M. G. (2017). Cell type boundaries organize plant development. *Elife*, *6*. https://doi.org/10.7554/eLife.27421

Cannavò, E., Khoueiry, P., Garfield, David A., Geeleher, P., Zichner, T., Gustafson, E. H., Ciglar, L., Korbel, Jan O., & Furlong, Eileen E. M. (2016). Shadow Enhancers Are Pervasive Features of Developmental Regulatory Networks. *Current Biology*, *26*(1), 38-51. https://doi.org/https://doi.org/10.1016/j.cub.2015.11.034

Carles, C. C., & Fletcher, J. C. (2003). Shoot apical meristem maintenance: the art of a dynamic balance. *Trends in Plant Science*, *8*(8), 394-401. https://doi.org/https://doi.org/10.1016/S1360-1385(03)00164-X

Carlsbecker, A., Lee, J. Y., Roberts, C. J., Dettmer, J., Lehesranta, S., Zhou, J., Lindgren, O., Moreno-Risueno, M. A., Vaten, A., Thitamadee, S., Campilho, A., Sebastian, J., Bowman, J. L., Helariutta, Y., & Benfey, P. N. (2010). Cell signalling by microRNA165/6 directs gene dose-dependent root cell fate. *Nature*, *465*(7296), 316-321. https://doi.org/10.1038/nature08977

Chao, Q., Rothenberg, M., Solano, R., Roman, G., Terzaghi, W., & Ecker†, J. R. (1997). Activation of the Ethylene Gas Response Pathway in Arabidopsis by the Nuclear Protein ETHYLENE-INSENSITIVE3 and Related Proteins. *Cell*, *89*(7), 1133-1144. https://doi.org/10.1016/S0092-8674(00)80300-1

Chen, H., Bullock, D. A., Alonso, J. M., & Stepanova, A. N. (2022). To Fight or to Grow: The Balancing Role of Ethylene in Plant Abiotic Stress Responses. *Plants*, *11*(1), 33. https://www.mdpi.com/2223-7747/11/1/33

Chitwood, D. H., Nogueira, F. T., Howell, M. D., Montgomery, T. A., Carrington, J. C., & Timmermans, M. C. (2009). Pattern formation via small RNA mobility. *Genes Dev*, *23*(5), 549-554. https://doi.org/10.1101/gad.1770009

Chorostecki, U., Moro, B., Rojas, A. M. L., Debernardi, J. M., Schapire, A. L., Notredame, C., & Palatnik, J. F. (2017). Evolutionary Footprints Reveal Insights into Plant MicroRNA Biogenesis. *The Plant Cell*, *29*(6), 1248-1261. https://doi.org/10.1105/tpc.17.00272

Clough, S. J., & Bent, A. F. (1998). Floral dip: a simplified method for Agrobacterium -mediated transformation of Arabidopsis thaliana. *The Plant Journal*, *16*(6), 735-743. https://doi.org/https://doi.org/10.1046/j.1365-313x.1998.00343.x

D'Ario, M., Griffiths-Jones, S., & Kim, M. (2017). Small RNAs: Big Impact on Plant Development. *Trends Plant Sci*, *22*(12), 1056-1068. https://doi.org/10.1016/j.tplants.2017.09.009

Danisman, S., van der Wal, F., Dhondt, S., Waites, R., de Folter, S., Bimbo, A., van Dijk, A. D., Muino, J. M., Cutri, L., Dornelas, M. C., Angenent, G. C., & Immink, R. G. H. (2012). Arabidopsis Class I and Class II TCP Transcription Factors Regulate Jasmonic Acid Metabolism and Leaf Development Antagonistically *Plant Physiology*, *159*(4), 1511-1523. https://doi.org/10.1104/pp.112.200303

Decaestecker, W., Buono, R. A., Pfeiffer, M. L., Vangheluwe, N., Jourquin, J., Karimi, M., Van Isterdael, G., Beeckman, T., Nowack, M. K., & Jacobs, T. B. (2019). CRISPR-TSKO: A Technique for Efficient Mutagenesis in Specific Cell Types, Tissues, or Organs in Arabidopsis. *The Plant Cell*, *31*(12), 2868-2887. https://doi.org/10.1105/tpc.19.00454

Denyer, T., Ma, X., Klesen, S., Scacchi, E., Nieselt, K., & Timmermans, M. C. P. (2019). Spatiotemporal Developmental Trajectories in the Arabidopsis Root Revealed Using High-Throughput Single-Cell RNA Sequencing. *Developmental Cell*, *48*(6), 840-852.e845. https://doi.org/https://doi.org/10.1016/j.devcel.2019.02.022

Dhaka, N., Bhardwaj, V., Sharma, M. K., & Sharma, R. (2017). Evolving Tale of TCPs: New Paradigms and Old Lacunae [Mini Review]. *Frontiers in Plant Science*, *8*. https://doi.org/10.3389/fpls.2017.00479

Diss, G., Ascencio, D., DeLuna, A., & Landry, C. R. (2014). Molecular mechanisms of paralogous compensation and the robustness of cellular networks. *Journal of Experimental Zoology Part B: Molecular and Developmental Evolution*, *322*(7), 488-499. https://doi.org/https://doi.org/10.1002/jez.b.22555

Doench, J. G., Fusi, N., Sullender, M., Hegde, M., Vaimberg, E. W., Donovan, K. F., Smith, I., Tothova, Z., Wilen, C., Orchard, R., Virgin, H. W., Listgarten, J., & Root, D. E. (2016).

Optimized sgRNA design to maximize activity and minimize off-target effects of CRISPR-Cas9. *Nature Biotechnology*, *34*(2), 184-191. https://doi.org/10.1038/nbt.3437

Dolan, L., Janmaat, K., Willemsen, V., Linstead, P., Poethig, S., Roberts, K., & Scheres, B. (1993). Cellular organisation of the Arabidopsis thaliana root. *Development*, *119*(1), 71-84. https://doi.org/10.1242/dev.119.1.71

Driever, W., & Nüsslein-Volhard, C. (1988). The bicoid protein determines position in the Drosophila embryo in a concentration-dependent manner. *Cell*, *54*(1), 95-104. https://doi.org/https://doi.org/10.1016/0092-8674(88)90183-3

Duveau, F., Toubiana, W., & Wittkopp, P. J. (2017). Fitness Effects of Cis-Regulatory Variants in the Saccharomyces cerevisiae TDH3 Promoter. *Molecular Biology and Evolution*, *34*(11), 2908-2912. https://doi.org/10.1093/molbev/msx224

Eldar, A., Dorfman, R., Weiss, D., Ashe, H., Shilo, B.-Z., & Barkai, N. (2002). Robustness of the BMP morphogen gradient in Drosophila embryonic patterning. *Nature*, *419*(6904), 304-308. https://doi.org/10.1038/nature01061

Emery, J. F., Floyd, S. K., Alvarez, J., Eshed, Y., Hawker, N. P., Izhaki, A., Baum, S. F., & Bowman, J. L. (2003). Radial patterning of Arabidopsis shoots by class III HD-ZIP and KANADI genes. *Curr Biol*, *13*(20), 1768-1774. https://doi.org/10.1016/j.cub.2003.09.035

Eshed, Y., Baum, S. F., Perea, J. V., & Bowman, J. L. (2001). Establishment of polarity in lateral organs of plants. *Curr Biol*, *11*(16), 1251-1260. https://doi.org/10.1016/s0960-9822(01)00392-x

Fauser, F., Schiml, S., & Puchta, H. (2014). Both CRISPR/Cas-based nucleases and nickases can be used efficiently for genome engineering in Arabidopsis thaliana. *The Plant Journal*, *79*(2), 348-359. https://doi.org/https://doi.org/10.1111/tpj.12554

Ferguson, E. L., & Anderson, K. V. (1992). decapentaplegic acts as a morphogen to organize dorsal-ventral pattern in the Drosophila embryo. *Cell*, *71*(3), 451-461. https://doi.org/https://doi.org/10.1016/0092-8674(92)90514-D

Fletcher, J. C. (2002). Shoot and floral meristem maintenance in arabidopsis. *Annu Rev Plant Biol*, *53*, 45-66. https://doi.org/10.1146/annurev.arplant.53.092701.143332

Fletcher, J. C. (2018). The CLV-WUS Stem Cell Signaling Pathway: A Roadmap to Crop Yield Optimization. *Plants*, *7*(4), 87. https://www.mdpi.com/2223-7747/7/4/87

https://mdpi-res.com/d_attachment/plants/plants-07-00087/article_deploy/plants-07-00087.pdf?version=1539941165

Franco-Zorrilla, J. M., López-Vidriero, I., Carrasco, J. L., Godoy, M., Vera, P., & Solano, R. (2014). DNA-binding specificities of plant transcription factors and their potential to define target genes. *Proceedings of the National Academy of Sciences*, *111*(6), 2367-2372. https://doi.org/doi:10.1073/pnas.1316278111

Frankel, N., Davis, G. K., Vargas, D., Wang, S., Payre, F., & Stern, D. L. (2010). Phenotypic robustness conferred by apparently redundant transcriptional enhancers. *Nature*, *466*(7305), 490-493. https://doi.org/10.1038/nature09158

Frazer, K. A., Pachter, L., Poliakov, A., Rubin, E. M., & Dubchak, I. (2004). VISTA: computational tools for comparative genomics. *Nucleic Acids Research*, *32*(suppl_2), W273-W279. https://doi.org/10.1093/nar/gkh458

Gierer, A., & Meinhardt, H. (1972). A theory of biological pattern formation. *Kybernetik*, *12*(1), 30-39. https://doi.org/10.1007/BF00289234

Gomes, G. L. B., & Scortecci, K. C. (2021). Auxin and its role in plant development: structure, signalling, regulation and response mechanisms. *Plant Biology*, *23*(6), 894-904. https://doi.org/https://doi.org/10.1111/plb.13303

Guan, C., Wu, B., Yu, T., Wang, Q., Krogan, N. T., Liu, X., & Jiao, Y. (2017). Spatial Auxin Signaling Controls Leaf Flattening in Arabidopsis. *Curr Biol*, *27*(19), 2940-2950 e2944. https://doi.org/10.1016/j.cub.2017.08.042

Hao, Y., Hao, S., Andersen-Nissen, E., Mauck, W. M., Zheng, S., Butler, A., Lee, M. J., Wilk, A. J., Darby, C., Zager, M., Hoffman, P., Stoeckius, M., Papalexi, E., Mimitou, E. P., Jain, J., Srivastava, A., Stuart, T., Fleming, L. M., Yeung, B., . . . Satija, R. (2021). Integrated analysis of multimodal single-cell data. *Cell*, *184*(13), 3573-3587.e3529. https://doi.org/https://doi.org/10.1016/j.cell.2021.04.048

Hardtke, C. S., Ckurshumova, W., Vidaurre, D. P., Singh, S. A., Stamatiou, G., Tiwari, S. B., Hagen, G., Guilfoyle, T. J., & Berleth, T. (2004). Overlapping and non-redundant functions of the Arabidopsis auxin response factors MONOPTEROS and NONPHOTOTROPIC HYPOCOTYL 4. *Development*, *131*(5), 1089-1100. https://doi.org/10.1242/dev.00925

Hashimoto, K., Miyashima, S., Sato-Nara, K., Yamada, T., & Nakajima, K. (2018). Functionally Diversified Members of the MIR165/6 Gene Family Regulate Ovule Morphogenesis in Arabidopsis thaliana. *Plant and Cell Physiology*, *59*(5), 1017-1026. https://doi.org/10.1093/pcp/pcy042

Heisler, M. G., Ohno, C., Das, P., Sieber, P., Reddy, G. V., Long, J. A., & Meyerowitz, E. M. (2005). Patterns of auxin transport and gene expression during primordium development revealed by live imaging of the Arabidopsis inflorescence meristem. *Curr Biol*, *15*(21), 1899-1911. https://doi.org/10.1016/j.cub.2005.09.052

Hendelman, A., Zebell, S., Rodriguez-Leal, D., Dukler, N., Robitaille, G., Wu, X., Kostyun, J., Tal, L., Wang, P., Bartlett, M. E., Eshed, Y., Efroni, I., & Lippman, Z. B. (2021). Conserved pleiotropy of an ancient plant homeobox gene uncovered by cis-regulatory dissection. *Cell*, *184*(7), 1724-1739.e1716. https://doi.org/https://doi.org/10.1016/j.cell.2021.02.001

Hong, L., Rusnak, B., Ko, C. S., Xu, S., He, X., Qiu, D., Kang, S. E., Pruneda-Paz, J. L., & Roeder, A. H. K. (2023). Enhancer activation via TCP and HD-ZIP and repression by Dof transcription factors mediate giant cell-specific expression. *The Plant Cell*, *35*(6), 2349-2368. https://doi.org/10.1093/plcell/koad054

Hsu, P. D., Scott, D. A., Weinstein, J. A., Ran, F. A., Konermann, S., Agarwala, V., Li, Y., Fine, E. J., Wu, X., Shalem, O., Cradick, T. J., Marraffini, L. A., Bao, G., & Zhang, F. (2013). DNA targeting specificity of RNA-guided Cas9 nucleases. *Nature Biotechnology*, *31*(9), 827-832. https://doi.org/10.1038/nbt.2647

Hu, Y., Vandenbussche, F., & Van Der Straeten, D. (2017). Regulation of seedling growth by ethylene and the ethylene–auxin crosstalk. *Planta*, *245*(3), 467-489. https://doi.org/10.1007/s00425-017-2651-6

Huang, J., Yang, M., & Zhang, X. (2016). The function of small RNAs in plant biotic stress response. *J Integr Plant Biol*, *58*(4), 312-327. https://doi.org/10.1111/jipb.12463

Husbands, A. Y., Benkovics, A. H., Nogueira, F. T., Lodha, M., & Timmermans, M. C. (2015). The ASYMMETRIC LEAVES Complex Employs Multiple Modes of Regulation to Affect Adaxial-Abaxial Patterning and Leaf Complexity. *Plant Cell*, *27*(12), 3321-3335. https://doi.org/10.1105/tpc.15.00454

Husbands, A. Y., Chitwood, D. H., Plavskin, Y., & Timmermans, M. C. P. (2009). Signals and prepatterns: new insights into organ polarity in plants. *Genes & Development*, *23*(17), 1986-1997. https://doi.org/10.1101/gad.1819909

Ingham, P. W. (1988). The molecular genetics of embryonic pattern formation in Drosophila. *Nature*, *335*(6185), 25-34. https://doi.org/10.1038/335025a0

Iwakawa, H., Iwasaki, M., Kojima, S., Ueno, Y., Soma, T., Tanaka, H., Semiarti, E., Machida, Y., & Machida, C. (2007). Expression of the

gene in the adaxial domain of Arabidopsis leaves represses cell proliferation in this domain and is critical for the development of properly expanded leaves. *Plant Journal*, *51*(2), 173-184. https://doi.org/10.1111/j.1365-313X.2007.03132.x

Ju, C., & Chang, C. (2015). Mechanistic Insights in Ethylene Perception and Signal Transduction. *Plant Physiology*, *169*(1), 85-95. https://doi.org/10.1104/pp.15.00845

Juarez, M. T., Kui, J. S., Thomas, J., Heller, B. A., & Timmermans, M. C. (2004). microRNA-mediated repression of rolled leaf1 specifies maize leaf polarity. *Nature*, *428*(6978), 84-88. https://doi.org/10.1038/nature02363

Jung, J. H., & Park, C. M. (2007). MIR166/165 genes exhibit dynamic expression patterns in regulating shoot apical meristem and floral development in Arabidopsis. *Planta*, *225*(6), 1327-1338. https://doi.org/10.1007/s00425-006-0439-1

Jurgens, G. (2003). Growing up green: cellular basis of plant development. *Mech Dev*, *120*(11), 1395-1406. https://doi.org/10.1016/j.mod.2003.03.001

Kerstetter, R. A., Bollman, K., Taylor, R. A., Bomblies, K., & Poethig, R. S. (2001). KANADI regulates organ polarity in Arabidopsis. *Nature*, *411*(6838), 706-709. https://doi.org/10.1038/35079629

Kicheva, A., & Briscoe, J. (2023). Control of Tissue Development by Morphogens. *Annual Review of Cell and Developmental Biology*, *39*(1), 91-121. https://doi.org/10.1146/annurev-cellbio-020823-011522

Kieffer, M., Master, V., Waites, R., & Davies, B. (2011). TCP14 and TCP15 affect internode length and leaf shape in Arabidopsis. *The Plant Journal*, *68*(1), 147-158. https://doi.org/https://doi.org/10.1111/j.1365-313X.2011.04674.x

Kim, J.-Y., Symeonidi, E., Pang, T. Y., Denyer, T., Weidauer, D., Bezrutczyk, M., Miras, M., Zöllner, N., Hartwig, T., Wudick, M. M., Lercher, M., Chen, L.-Q., Timmermans, M. C.

P., & Frommer, W. B. (2021). Distinct identities of leaf phloem cells revealed by single cell transcriptomics. *The Plant Cell*, *33*(3), 511-530. https://doi.org/10.1093/plcell/koaa060

Kim, J., Jung, J.-H., Reyes, J. L., Kim, Y.-S., Kim, S.-Y., Chung, K.-S., Kim, J. A., Lee, M., Lee, Y., Narry Kim, V., Chua, N.-H., & Park, C.-M. (2005). microRNA-directed cleavage of ATHB15 mRNA regulates vascular development in Arabidopsis inflorescence stems. *The Plant Journal*, *42*(1), 84-94. https://doi.org/https://doi.org/10.1111/j.1365-313X.2005.02354.x

Kim, M., McCormick, S., Timmermans, M., & Sinha, N. (2003). The expression domain of PHANTASTICA determines leaflet placement in compound leaves. *Nature*, *424*(6947), 438-443. https://doi.org/10.1038/nature01820

Kitano, H. (2004). Biological robustness. *Nature Reviews Genetics*, *5*(11), 826-837. https://doi.org/10.1038/nrg1471

Klesen, S. (2020). *Gating of small RNA mobility in plant stem cell niches* Eberhard Karls University of Tübingen]. Tübingen.

Klesen, S., Hill, K., & Timmermans, M. C. P. (2020). Chapter Fifteen - Small RNAs as plant morphogens. In S. Small & J. Briscoe (Eds.), *Current Topics in Developmental Biology* (Vol. 137, pp. 455-480). Academic Press. https://doi.org/https://doi.org/10.1016/bs.ctdb.2019.11.001

Knauer, S., Javelle, M., Li, L., Li, X., Ma, X., Wimalanathan, K., Kumari, S., Johnston, R., Leiboff, S., Meeley, R., Schnable, P. S., Ware, D., Lawrence-Dill, C., Yu, J., Muehlbauer, G. J., Scanlon, M. J., & Timmermans, M. C. P. (2019). A high-resolution gene expression atlas links dedicated meristem genes to key architectural traits. *Genome Research*. https://doi.org/10.1101/gr.250878.119

Kosugi, S., & Ohashi, Y. (2002). DNA binding and dimerization specificity and potential targets for the TCP protein family. *The Plant Journal*, *30*(3), 337-348. https://doi.org/https://doi.org/10.1046/j.1365-313X.2002.01294.x

Koyama, T., Sato, F., & Ohme-Takagi, M. (2017). Roles of miR319 and TCP Transcription Factors in Leaf Development. *Plant Physiology*, *175*(2), 874-885. https://doi.org/10.1104/pp.17.00732

Krogan, N. T., & Berleth, T. (2012). A dominant mutation reveals asymmetry in MP/ARF5 function along the adaxial-abaxial axis of shoot lateral organs. *Plant Signal Behav*, *7*(8), 940-943. https://doi.org/10.4161/psb.20790

Kuhlemeier, C., & Timmermans, M. C. P. (2016). The Sussex signal: insights into leaf dorsiventrality. *Development*, *143*(18), 3230-3237. https://doi.org/10.1242/dev.131888

Kvon, E. Z., Waymack, R., Gad, M., & Wunderlich, Z. (2021). Enhancer redundancy in development and disease. *Nature Reviews Genetics*, *22*(5), 324-336. https://doi.org/10.1038/s41576-020-00311-x

Lachowiec, J., Queitsch, C., & Kliebenstein, D. J. (2015). Molecular mechanisms governing differential robustness of development and environmental responses in plants. *Annals of Botany*, *117*(5), 795-809. https://doi.org/10.1093/aob/mcv151

Laiker, I., & Frankel, N. (2022). Pleiotropic Enhancers are Ubiquitous Regulatory Elements in the Human Genome. *Genome Biology and Evolution*, *14*(6). https://doi.org/10.1093/gbe/evac071

Lau, S., Smet, I. D., Kolb, M., Meinhardt, H., & Jürgens, G. (2011). Auxin triggers a genetic switch. *Nature Cell Biology*, *13*(5), 611-615. https://doi.org/10.1038/ncb2212

LeBlanc, C., Zhang, F., Mendez, J., Lozano, Y., Chatpar, K., Irish, V. F., & Jacob, Y. (2018). Increased efficiency of targeted mutagenesis by CRISPR/Cas9 in plants using heat stress. *The Plant Journal*, *93*(2), 377-386. https://doi.org/https://doi.org/10.1111/tpj.13782

Lee, C., & Clark, S. E. (2015). A WUSCHEL-Independent Stem Cell Specification Pathway Is Repressed by PHB, PHV and CNA in Arabidopsis. *PLOS ONE*, *10*(5), e0126006. https://doi.org/10.1371/journal.pone.0126006

Lempe, J., Lachowiec, J., Sullivan, A. M., & Queitsch, C. (2013). Molecular mechanisms of robustness in plants. *Current Opinion in Plant Biology*, *16*(1), 62-69. https://doi.org/https://doi.org/10.1016/j.pbi.2012.12.002

Li, C., Potuschak, T., Colón-Carmona, A., Gutiérrez, R. A., & Doerner, P. (2005). Arabidopsis TCP20 links regulation of growth and cell division control pathways. *Proceedings of the National Academy of Sciences*, *102*(36), 12978-12983. https://doi.org/doi:10.1073/pnas.0504039102

Li, S. (2015). The Arabidopsis thaliana TCP transcription factors: A broadening horizon beyond development. *Plant Signaling & Behavior*, *10*(7), e1044192. https://doi.org/10.1080/15592324.2015.1044192

Li, X., Liang, T., & Liu, H. (2021). How plants coordinate their development in response to light and temperature signals. *The Plant Cell*, *34*(3), 955-966. https://doi.org/10.1093/plcell/koab302

Lian, H., Wang, L., Ma, N., Zhou, C.-M., Han, L., Zhang, T.-Q., & Wang, J.-W. (2021). Redundant and specific roles of individual MIR172 genes in plant development. *PLOS Biology*, *19*(2), e3001044. https://doi.org/10.1371/journal.pbio.3001044

Liao, C. Y., Smet, W., Brunoud, G., Yoshida, S., Vernoux, T., & Weijers, D. (2015). Reporters for sensitive and quantitative measurement of auxin response. *Nat Methods*, *12*(3), 207-210, 202 p following 210. https://doi.org/10.1038/nmeth.3279

Lin, W. C., Shuai, B., & Springer, P. S. (2003). The Arabidopsis LATERAL ORGAN BOUNDARIES-domain gene ASYMMETRIC LEAVES2 functions in the repression of KNOX gene expression and in adaxial-abaxial patterning. *Plant Cell*, *15*(10), 2241-2252. https://doi.org/10.1105/tpc.014969

Liu, L., Gallagher, J., Arevalo, E. D., Chen, R., Skopelitis, T., Wu, Q., Bartlett, M., & Jackson, D. (2021). Enhancing grain-yield-related traits by CRISPR–Cas9 promoter editing of maize CLE genes. *Nature Plants*, *7*(3), 287-294. https://doi.org/10.1038/s41477-021-00858-5

Long, H. K., Prescott, S. L., & Wysocka, J. (2016). Ever-Changing Landscapes: Transcriptional Enhancers in Development and Evolution. *Cell*, *167*(5), 1170-1187. https://doi.org/10.1016/j.cell.2016.09.018

Lopez-Anido, C. B., Vatén, A., Smoot, N. K., Sharma, N., Guo, V., Gong, Y., Anleu Gil, M. X., Weimer, A. K., & Bergmann, D. C. (2021). Single-cell resolution of lineage trajectories in the Arabidopsis stomatal lineage and developing leaf. *Developmental Cell*, *56*(7), 1043-1055.e1044. https://doi.org/https://doi.org/10.1016/j.devcel.2021.03.014

Lu, Z., Marand, A. P., Ricci, W. A., Ethridge, C. L., Zhang, X., & Schmitz, R. J. (2019). The prevalence, evolution and chromatin signatures of plant regulatory elements. *Nature Plants*, *5*(12), 1250-1259. https://doi.org/10.1038/s41477-019-0548-z

Ma, X., Denyer, T., Javelle, M., Feller, A., & Timmermans, M. C. P. (2021). Genome-wide analysis of plant miRNA action clarifies levels of regulatory dynamics across developmental contexts. *Genome Res*, *31*(5), 811-822. https://doi.org/10.1101/gr.270918.120

Maher, C., Stein, L., & Ware, D. (2006). Evolution of Arabidopsis microRNA families through duplication events. *Genome Research*, *16*(4), 510-519. https://doi.org/10.1101/gr.4680506

Marand, A. P., Eveland, A. L., Kaufmann, K., & Springer, N. M. (2023). cis-Regulatory Elements in Plant Development, Adaptation, and Evolution. *Annual Review of Plant Biology*, *74*(1), 111-137. https://doi.org/10.1146/annurev-arplant-070122-030236

Mathelier, A., Fornes, O., Arenillas, D. J., Chen, C.-y., Denay, G., Lee, J., Shi, W., Shyr, C., Tan, G., Worsley-Hunt, R., Zhang, A. W., Parcy, F., Lenhard, B., Sandelin, A., & Wasserman, W. W. (2015). JASPAR 2016: a major expansion and update of the open-access database of transcription factor binding profiles. *Nucleic Acids Research*, *44*(D1), D110-D115. https://doi.org/10.1093/nar/gkv1176

McConnell, J. R., & Barton, M. K. (1998). Leaf polarity and meristem formation in Arabidopsis. *Development*, *125*(15), 2935-2942. https://doi.org/10.1242/dev.125.15.2935

McConnell, J. R., Emery, J., Eshed, Y., Bao, N., Bowman, J., & Barton, M. K. (2001). Role of PHABULOSA and PHAVOLUTA in determining radial patterning in shoots. *Nature*, *411*(6838), 709-713. https://doi.org/10.1038/35079635

Mehlhorn, D. G., Wallmeroth, N., Berendzen, K. W., & Grefen, C. (2018). 2in1 Vectors Improve In Planta BiFC and FRET Analyses. In C. Hawes & V. Kriechbaumer (Eds.), *The Plant Endoplasmic Reticulum : Methods and Protocols* (pp. 139-158). Springer New York. https://doi.org/10.1007/978-1-4939-7389-7_11

Merelo, P., Ram, H., Pia Caggiano, M., Ohno, C., Ott, F., Straub, D., Graeff, M., Cho, S. K., Yang, S. W., Wenkel, S., & Heisler, M. G. (2016). Regulation of MIR165/166 by class II and class III homeodomain leucine zipper proteins establishes leaf polarity. *Proc Natl Acad Sci U S A*, *113*(42), 11973-11978. https://doi.org/10.1073/pnas.1516110113

Miyashima, S., Honda, M., Hashimoto, K., Tatematsu, K., Hashimoto, T., Sato-Nara, K., Okada, K., & Nakajima, K. (2013). A Comprehensive Expression Analysis of the Arabidopsis MICRORNA165/6 Gene Family during Embryogenesis Reveals a Conserved Role in

Meristem Specification and a Non-Cell-Autonomous Function. *Plant and Cell Physiology*, *54*(3), 375-384. https://doi.org/10.1093/pcp/pcs188

Montgomery, T. A., Howell, M. D., Cuperus, J. T., Li, D., Hansen, J. E., Alexander, A. L., Chapman, E. J., Fahlgren, N., Allen, E., & Carrington, J. C. (2008). Specificity of ARGONAUTE7-miR390 interaction and dual functionality in TAS3 trans-acting siRNA formation. *Cell*, *133*(1), 128-141. https://doi.org/10.1016/j.cell.2008.02.033

Nelson, A. C., & Wardle, F. C. (2013). Conserved non-coding elements and cis regulation: actions speak louder than words. *Development*, *140*(7), 1385-1395. https://doi.org/10.1242/dev.084459

Nogueira, F. T. S., Chitwood, D. H., Madi, S., Ohtsu, K., Schnable, P. S., Scanlon, M. J., & Timmermans, M. C. P. (2009). Regulation of Small RNA Accumulation in the Maize Shoot Apex. *PLOS Genetics*, *5*(1), e1000320. https://doi.org/10.1371/journal.pgen.1000320

O'Malley, Ronan C., Huang, S.-shan C., Song, L., Lewsey, Mathew G., Bartlett, A., Nery, Joseph R., Galli, M., Gallavotti, A., & Ecker, Joseph R. (2016). Cistrome and Epicistrome Features Shape the Regulatory DNA Landscape. *Cell*, *165*(5), 1280-1292. https://doi.org/https://doi.org/10.1016/j.cell.2016.04.038

Ó'Maoiléidigh, D. S., van Driel, A. D., Singh, A., Sang, Q., Le Bec, N., Vincent, C., de Olalla, E. B. G., Vayssières, A., Romera Branchat, M., Severing, E., Martinez Gallegos, R., & Coupland, G. (2021). Systematic analyses of the MIR172 family members of Arabidopsis define their distinct roles in regulation of APETALA2 during floral transition. *PLOS Biology*, *19*(2), e3001043. https://doi.org/10.1371/journal.pbio.3001043

Osterwalder, M., Barozzi, I., Tissières, V., Fukuda-Yuzawa, Y., Mannion, B. J., Afzal, S. Y., Lee, E. A., Zhu, Y., Plajzer-Frick, I., Pickle, C. S., Kato, M., Garvin, T. H., Pham, Q. T., Harrington, A. N., Akiyama, J. A., Afzal, V., Lopez-Rios, J., Dickel, D. E., Visel, A., & Pennacchio, L. A. (2018). Enhancer redundancy provides phenotypic robustness in mammalian development. *Nature*, *554*(7691), 239-243. https://doi.org/10.1038/nature25461

Palatnik, J. F., Allen, E., Wu, X., Schommer, C., Schwab, R., Carrington, J. C., & Weigel, D. (2003). Control of leaf morphogenesis by microRNAs. *Nature*, *425*(6955), 257-263. https://doi.org/10.1038/nature01958

Panigrahi, A., & O'Malley, B. W. (2021). Mechanisms of enhancer action: the known and the unknown. *Genome Biology*, *22*(1), 108. https://doi.org/10.1186/s13059-021-02322-1

Pekker, I., Alvarez, J. P., & Eshed, Y. (2005). Auxin response factors mediate Arabidopsis organ asymmetry via modulation of KANADI activity. *Plant Cell*, *17*(11), 2899-2910. https://doi.org/10.1105/tpc.105.034876

Perilli, S., Di Mambro, R., & Sabatini, S. (2012). Growth and development of the root apical meristem. *Current Opinion in Plant Biology*, *15*(1), 17-23. https://doi.org/https://doi.org/10.1016/j.pbi.2011.10.006

Perry, M. W., Boettiger, A. N., Bothma, J. P., & Levine, M. (2010). Shadow Enhancers Foster Robustness of Drosophila Gastrulation. *Current Biology*, *20*(17), 1562-1567. https://doi.org/https://doi.org/10.1016/j.cub.2010.07.043

Phelps-Durr, T. L., Thomas, J., Vahab, P., & Timmermans, M. C. P. (2005). Maize rough sheath2 and Its Arabidopsis Orthologue ASYMMETRIC LEAVES1 Interact with HIRA, a Predicted Histone Chaperone, to Maintain knox Gene Silencing and Determinacy during Organogenesis. *The Plant Cell*, *17*(11), 2886-2898. https://doi.org/10.1105/tpc.105.035477

Preger-Ben Noon, E., Sabarís, G., Ortiz, D. M., Sager, J., Liebowitz, A., Stern, D. L., & Frankel, N. (2018). Comprehensive Analysis of a cis-Regulatory Region Reveals Pleiotropy in Enhancer Function. *Cell Reports*, *22*(11), 3021-3031. https://doi.org/https://doi.org/10.1016/j.celrep.2018.02.073

Priest, H. D., Filichkin, S. A., & Mockler, T. C. (2009). cis-Regulatory elements in plant cell signaling. *Current Opinion in Plant Biology*, *12*(5), 643-649. https://doi.org/https://doi.org/10.1016/j.pbi.2009.07.016

Prigge, M. J., Otsuga, D., Alonso, J. M., Ecker, J. R., Drews, G. N., & Clark, S. E. (2005). Class III Homeodomain-Leucine Zipper Gene Family Members Have Overlapping, Antagonistic, and Distinct Roles in Arabidopsis Development. *The Plant Cell*, *17*(1), 61-76. https://doi.org/10.1105/tpc.104.026161

Qi, J., Wang, Y., Yu, T., Cunha, A., Wu, B., Vernoux, T., Meyerowitz, E., & Jiao, Y. (2014). Auxin depletion from leaf primordia contributes to organ patterning. *Proc Natl Acad Sci U S A*, *111*(52), 18769-18774. https://doi.org/10.1073/pnas.1421878112

Ray-Jones, H., & Spivakov, M. (2021). Transcriptional enhancers and their communication with gene promoters. *Cellular and Molecular Life Sciences*, *78*(19), 6453-6485. https://doi.org/10.1007/s00018-021-03903-w

Reinhardt, D., Frenz, M., Mandel, T., & Kuhlemeier, C. (2005). Microsurgical and laser ablation analysis of leaf positioning and dorsoventral patterning in tomato. *Development*, *132*(1), 15-26. https://doi.org/10.1242/dev.01544

Reinhardt, D., Mandel, T., & Kuhlemeier, C. (2000). Auxin Regulates the Initiation and Radial Position of Plant Lateral Organs. *The Plant Cell*, *12*(4), 507-518. https://doi.org/10.1105/tpc.12.4.507

Reinhardt, D., Pesce, E. R., Stieger, P., Mandel, T., Baltensperger, K., Bennett, M., Traas, J., Friml, J., & Kuhlemeier, C. (2003). Regulation of phyllotaxis by polar auxin transport. *Nature*, *426*(6964), 255-260. https://doi.org/10.1038/nature02081

Rhoades, M. W., Reinhart, B. J., Lim, L. P., Burge, C. B., Bartel, B., & Bartel, D. P. (2002). Prediction of plant microRNA targets. *Cell*, *110*(4), 513-520. https://doi.org/10.1016/s0092-8674(02)00863-2

Rodríguez-Leal, D., Lemmon, Z. H., Man, J., Bartlett, M. E., & Lippman, Z. B. (2017). Engineering Quantitative Trait Variation for Crop Improvement by Genome Editing. *Cell*, *171*(2), 470-480.e478. https://doi.org/https://doi.org/10.1016/j.cell.2017.08.030

Sabarís, G., Laiker, I., Preger-Ben Noon, E., & Frankel, N. (2019). Actors with Multiple Roles: Pleiotropic Enhancers and the Paradigm of Enhancer Modularity. *Trends in Genetics*, *35*(6), 423-433. https://doi.org/10.1016/j.tig.2019.03.006

Salazar-Ciudad, I. (2017). Mechanisms of Pattern Formation, Morphogenesis, and Evolution. In L. Nuno de la Rosa & G. Müller (Eds.), *Evolutionary Developmental Biology: A Reference Guide* (pp. 1-16). Springer International Publishing. https://doi.org/10.1007/978-3-319-33038-9_51-1

Salazar-Ciudad, I., Jernvall, J., & Newman, S. A. (2003). Mechanisms of pattern formation in development and evolution. *Development*, *130*(10), 2027-2037. https://doi.org/10.1242/dev.00425

Sanan-Mishra, N., Abdul Kader Jailani, A., Mandal, B., & Mukherjee, S. K. (2021). Secondary siRNAs in Plants: Biosynthesis, Various Functions, and Applications in Virology [Review]. *Frontiers in Plant Science*, *12*. https://doi.org/10.3389/fpls.2021.610283

Sarojam, R., Sappl, P. G., Goldshmidt, A., Efroni, I., Floyd, S. K., Eshed, Y., & Bowman, J. L. (2010). Differentiating Arabidopsis shoots from leaves by combined YABBY activities. *Plant Cell*, *22*(7), 2113-2130. https://doi.org/10.1105/tpc.110.075853

Schmid, M., Davison, T. S., Henz, S. R., Pape, U. J., Demar, M., Vingron, M., Schölkopf, B., Weigel, D., & Lohmann, J. U. (2005). A gene expression map of Arabidopsis thaliana development. *Nature Genetics*, *37*(5), 501-506. https://doi.org/10.1038/ng1543

Schmitz, R. J., Grotewold, E., & Stam, M. (2021). Cis-regulatory sequences in plants: Their importance, discovery, and future challenges. *The Plant Cell*, *34*(2), 718-741. https://doi.org/10.1093/plcell/koab281

Shi, D., Jouannet, V., Agustí, J., Kaul, V., Levitsky, V., Sanchez, P., Mironova, V. V., & Greb, T. (2020). Tissue-specific transcriptome profiling of the Arabidopsis inflorescence stem reveals local cellular signatures. *The Plant Cell*, *33*(2), 200-223. https://doi.org/10.1093/plcell/koaa019

Sieber, P., Wellmer, F., Gheyselinck, J., Riechmann, J. L., & Meyerowitz, E. M. (2007). Redundancy and specialization among plant microRNAs: role of the MIR164 family in developmental robustness. *Development*, *134*(6), 1051-1060. https://doi.org/10.1242/dev.02817

Siegfried, K. R., Eshed, Y., Baum, S. F., Otsuga, D., Drews, G. N., & Bowman, J. L. (1999). Members of the YABBY gene family specify abaxial cell fate in Arabidopsis. *Development*, *126*(18), 4117-4128. https://doi.org/10.1242/dev.126.18.4117

Simillion, C., Vandepoele, K., Van Montagu, M. C. E., Zabeau, M., & Van de Peer, Y. (2002). The hidden duplication past of Arabidopsis thaliana. *Proceedings of the National Academy of Sciences*, *99*(21), 13627-13632. https://doi.org/doi:10.1073/pnas.212522399

Skopelitis, D. S., Benkovics, A. H., Husbands, A. Y., & Timmermans, M. C. P. (2017). Boundary Formation through a Direct Threshold-Based Readout of Mobile Small RNA Gradients. *Developmental Cell*, *43*(3), 265-273.e266. https://doi.org/https://doi.org/10.1016/j.devcel.2017.10.003

Skopelitis, D. S., Hill, K., Klesen, S., Marco, C. F., von Born, P., Chitwood, D. H., & Timmermans, M. C. P. (2018). Gating of miRNA movement at defined cell-cell

interfaces governs their impact as positional signals. *Nature Communications*, *9*(1), 3107. https://doi.org/10.1038/s41467-018-05571-0

Sparks, Erin E., Drapek, C., Gaudinier, A., Li, S., Ansariola, M., Shen, N., Hennacy, Jessica H., Zhang, J., Turco, G., Petricka, Jalean J., Foret, J., Hartemink, Alexander J., Gordân, R., Megraw, M., Brady, Siobhan M., & Benfey, Philip N. (2016). Establishment of Expression in the SHORTROOT-SCARECROW Transcriptional Cascade through Opposing Activities of Both Activators and Repressors. *Developmental Cell*, *39*(5), 585-596. https://doi.org/https://doi.org/10.1016/j.devcel.2016.09.031

Spitz, F., & Furlong, E. E. M. (2012). Transcription factors: from enhancer binding to developmental control. *Nature Reviews Genetics*, *13*(9), 613-626. https://doi.org/10.1038/nrg3207

Sprunck, S., Rademacher, S., Vogler, F., Gheyselinck, J., Grossniklaus, U., & Dresselhaus, T. (2012). Egg Cell–Secreted EC1 Triggers Sperm Cell Activation During Double Fertilization. *Science*, *338*(6110), 1093-1097. https://doi.org/doi:10.1126/science.1223944

Stahl, Y., & Simon, R. (2010). Plant primary meristems: shared functions and regulatory mechanisms. *Current Opinion in Plant Biology*, *13*(1), 53-58. https://doi.org/https://doi.org/10.1016/j.pbi.2009.09.008

Stern, D. L., & Frankel, N. (2013). The structure and evolution of cis-regulatory regions: the shavenbaby story. *Philosophical Transactions of the Royal Society B: Biological Sciences*, *368*(1632), 20130028. https://doi.org/doi:10.1098/rstb.2013.0028

Strader, L., Weijers, D., & Wagner, D. (2022). Plant transcription factors — being in the right place with the right company. *Current Opinion in Plant Biology*, *65*, 102136. https://doi.org/https://doi.org/10.1016/j.pbi.2021.102136

Sun, X., Rikkerink, E. H. A., Jones, W. T., & Uversky, V. N. (2013). Multifarious Roles of Intrinsic Disorder in Proteins Illustrate Its Broad Impact on Plant Biology. *The Plant Cell*, *25*(1), 38-55. https://doi.org/10.1105/tpc.112.106062

Sussex, I. M. (1951). Experiments on the cause of dorsiventrality in leaves. *Nature*, *167*(4251), 651-652. https://doi.org/10.1038/167651a0

Sussex, I. M. (1954). Experiments on the Cause of Dorsiventrality in Leaves. *Nature*, *174*(4425), 351-352. https://doi.org/10.1038/174351a0

Tabata, T., & Takei, Y. (2004). Morphogens, their identification and regulation. *Development*, *131*(4), 703-712. https://doi.org/10.1242/dev.01043

Tauber, M. I. (2021). *Identification of CIS regulatory elements and various transcription factors regulating MIR166A expression during leaf polarity establishment in Arabidopsis thaliana* Eberhard Karls University of Tübingen].

Tenorio Berrío, R., Verstaen, K., Vandamme, N., Pevernagie, J., Achon, I., Van Duyse, J., Van Isterdael, G., Saeys, Y., De Veylder, L., Inzé, D., & Dubois, M. (2021). Single-cell transcriptomics sheds light on the identity and metabolism of developing leaf cells. *Plant Physiology*, *188*(2), 898-918. https://doi.org/10.1093/plphys/kiab489

Thomas, P. D., Ebert, D., Muruganujan, A., Mushayahama, T., Albou, L.-P., & Mi, H. (2022). PANTHER: Making genome-scale phylogenetics accessible to all. *Protein Science*, *31*(1), 8-22. https://doi.org/https://doi.org/10.1002/pro.4218

Tian, C., Wang, Y., Yu, H., He, J., Wang, J., Shi, B., Du, Q., Provart, N. J., Meyerowitz, E. M., & Jiao, Y. (2019). A gene expression map of shoot domains reveals regulatory mechanisms. *Nature Communications*, *10*(1), 141. https://doi.org/10.1038/s41467-018-08083-z

Truskina, J., Han, J., Chrysanthou, E., Galvan-Ampudia, C. S., Lainé, S., Brunoud, G., Macé, J., Bellows, S., Legrand, J., Bågman, A.-M., Smit, M. E., Smetana, O., Stigliani, A., Porco, S., Bennett, M. J., Mähönen, A. P., Parcy, F., Farcot, E., Roudier, F., . . . Vernoux, T. (2021). A network of transcriptional repressors modulates auxin responses. *Nature*, *589*(7840), 116-119. https://doi.org/10.1038/s41586-020-2940-2

Tsuzuki, M., Nishihama, R., Ishizaki, K., Kurihara, Y., Matsui, M., Bowman, J. L., Kohchi, T., Hamada, T., & Watanabe, Y. (2015). Profiling and Characterization of Small RNAs in the Liverwort, Marchantia polymorpha , Belonging to the First Diverged Land Plants. *Plant and Cell Physiology*, *57*(2), 359-372. https://doi.org/10.1093/pcp/pcv182

Turing, A. M. (1952). The chemical basis of morphogenesis. *Philosophical Transactions of the Royal Society of London. Series B, Biological Sciences*, *237*(641), 37-72. https://doi.org/doi:10.1098/rstb.1952.0012

Twell, D., Yamaguchi, J., Wing, R. A., Ushiba, J., & McCormick, S. (1991). Promoter analysis of genes that are coordinately expressed during pollen development reveals pollen-

specific enhancer sequences and shared regulatory elements. *Genes & Development*, *5*(3), 496-507. https://doi.org/10.1101/gad.5.3.496

Uberti-Manassero, N. G., Lucero, L. E., Viola, I. L., Vegetti, A. C., & Gonzalez, D. H. (2011). The class I protein AtTCP15 modulates plant development through a pathway that overlaps with the one affected by CIN-like TCP proteins. *Journal of Experimental Botany*, *63*(2), 809-823. https://doi.org/10.1093/jxb/err305

Valsecchi, I., Guittard-Crilat, E., Maldiney, R., Habricot, Y., Lignon, S., Lebrun, R., Miginiac, E., Ruelland, E., Jeannette, E., & Lebreton, S. (2013). The intrinsically disordered C-terminal region of Arabidopsis thaliana TCP8 transcription factor acts both as a transactivation and self-assembly domain. *Mol Biosyst*, *9*(9), 2282-2295. https://doi.org/10.1039/c3mb70128j

Varkonyi-Gasic, E., Wu, R., Wood, M., Walton, E. F., & Hellens, R. P. (2007). Protocol: a highly sensitive RT-PCR method for detection and quantification of microRNAs. *Plant Methods*, *3*(1), 12. https://doi.org/10.1186/1746-4811-3-12

Viola, I. L., Alem, A. L., Jure, R. M., & Gonzalez, D. H. (2023). Physiological Roles and Mechanisms of Action of Class I TCP Transcription Factors. *International Journal of Molecular Sciences*, *24*(6), 5437. https://www.mdpi.com/1422-0067/24/6/5437

https://mdpi-res.com/d_attachment/ijms/ijms-24-05437/article_deploy/ijms-24-05437-v2.pdf?version=1679372461

Wagner, A. (2008). Gene duplications, robustness and evolutionary innovations. *BioEssays*, *30*(4), 367-373. https://doi.org/https://doi.org/10.1002/bies.20728

Waites, R., & Hudson, A. (1995). phantastica: a gene required for dorsoventrality of leaves in Antirrhinum majus. *Development*, *121*(7), 2143-2154. https://doi.org/10.1242/dev.121.7.2143

Waites, R., Selvadurai, H. R. N., Oliver, I. R., & Hudson, A. (1998). The PHANTASTICA Gene Encodes a MYB Transcription Factor Involved in Growth and Dorsoventrality of Lateral Organs in Antirrhinum. *Cell*, *93*(5), 779-789. https://doi.org/https://doi.org/10.1016/S0092-8674(00)81439-7

Wang, J., Mei, J., & Ren, G. (2019). Plant microRNAs: Biogenesis, Homeostasis, and Degradation. *Front Plant Sci*, *10*, 360. https://doi.org/10.3389/fpls.2019.00360

Wang, X., Aguirre, L., Rodríguez-Leal, D., Hendelman, A., Benoit, M., & Lippman, Z. B. (2021). Dissecting cis-regulatory control of quantitative trait variation in a plant stem cell circuit. *Nature Plants*, *7*(4), 419-427. https://doi.org/10.1038/s41477-021-00898-x

Wang, Z.-P., Xing, H.-L., Dong, L., Zhang, H.-Y., Han, C.-Y., Wang, X.-C., & Chen, Q.-J. (2015). Egg cell-specific promoter-controlled CRISPR/Cas9 efficiently generates homozygous mutants for multiple target genes in Arabidopsis in a single generation. *Genome Biology*, *16*(1), 144. https://doi.org/10.1186/s13059-015-0715-0

Weber, B., Zicola, J., Oka, R., & Stam, M. (2016). Plant Enhancers: A Call for Discovery. *Trends in Plant Science*, *21*(11), 974-987. https://doi.org/https://doi.org/10.1016/j.tplants.2016.07.013

Whitacre, J. (2012). Biological Robustness: Paradigms, Mechanisms, and Systems Principles [Review]. *Frontiers in Genetics*, *3*. https://doi.org/10.3389/fgene.2012.00067

Whitewoods, C. D., Gonçalves, B., Cheng, J., Cui, M., Kennaway, R., Lee, K., Bushell, C., Yu, M., Piao, C., & Coen, E. (2020). Evolution of carnivorous traps from planar leaves through simple shifts in gene expression. *Science*, *367*(6473), 91-96. https://doi.org/doi:10.1126/science.aay5433

Willemsen, V., & Scheres, B. (2004). Mechanisms of pattern formation in plant embryogenesis. *Annu Rev Genet*, *38*, 587-614. https://doi.org/10.1146/annurev.genet.38.072902.092231

Williams, L., Grigg, S. P., Xie, M., Christensen, S., & Fletcher, J. C. (2005). Regulation of Arabidopsis shoot apical meristem and lateral organ formation by microRNA miR166g and its AtHD-ZIP target genes. *Development*, *132*(16), 3657-3668. https://doi.org/10.1242/dev.01942

Wolpert, L. (1969). Positional information and the spatial pattern of cellular differentiation. *J Theor Biol*, *25*(1), 1-47. https://doi.org/10.1016/s0022-5193(69)80016-0

Wolpert, L., Tickle, C., & Arias, A. M. (2015). *Principles of development*. Oxford University Press, USA.

Wu, G., Lin, W. C., Huang, T., Poethig, R. S., Springer, P. S., & Kerstetter, R. A. (2008). KANADI1 regulates adaxial-abaxial polarity in Arabidopsis by directly repressing the transcription of ASYMMETRIC LEAVES2. *Proc Natl Acad Sci U S A*, *105*(42), 16392-16397. https://doi.org/10.1073/pnas.0803997105

Xie, Z., Allen, E., Fahlgren, N., Calamar, A., Givan, S. A., & Carrington, J. C. (2005). Expression of Arabidopsis MIRNA genes. *Plant Physiol*, *138*(4), 2145-2154. https://doi.org/10.1104/pp.105.062943

Yadav, A., Kumar, S., Verma, R., Lata, C., Sanyal, I., & Rai, S. P. (2021). microRNA 166: an evolutionarily conserved stress biomarker in land plants targeting HD-ZIP family. *Physiol Mol Biol Plants*, *27*(11), 2471-2485. https://doi.org/10.1007/s12298-021-01096-x

Yamada, K., Osakabe, Y., Mizoi, J., Nakashima, K., Fujita, Y., Shinozaki, K., & Yamaguchi-Shinozaki, K. (2010). Functional Analysis of an Arabidopsis thaliana Abiotic Stress-inducible Facilitated Diffusion Transporter for Monosaccharides*. *Journal of Biological Chemistry*, *285*(2), 1138-1146. https://doi.org/https://doi.org/10.1074/jbc.M109.054288

Yan, J., Gu, Y., Jia, X., Kang, W., Pan, S., Tang, X., Chen, X., & Tang, G. (2012). Effective Small RNA Destruction by the Expression of a Short Tandem Target Mimic in Arabidopsis *The Plant Cell*, *24*(2), 415-427. https://doi.org/10.1105/tpc.111.094144

Yao, X., Wang, H., Li, H., Yuan, Z., Li, F., Yang, L., & Huang, H. (2009). Two types of cis-acting elements control the abaxial epidermis-specific transcription of the MIR165a and MIR166a genes. *FEBS Lett*, *583*(22), 3711-3717. https://doi.org/10.1016/j.febslet.2009.10.076

Zhan, J., & Meyers, B. C. (2023). Plant Small RNAs: Their Biogenesis, Regulatory Roles, and Functions. *Annual Review of Plant Biology*, *74*(1), 21-51. https://doi.org/10.1146/annurev-arplant-070122-035226

Zhang, C., Fan, L., Le, B. H., Ye, P., Mo, B., & Chen, X. (2020). Regulation of ARGONAUTE10 Expression Enables Temporal and Spatial Precision in Axillary Meristem Initiation in Arabidopsis. *Developmental Cell*, *55*(5), 603-616.e605. https://doi.org/https://doi.org/10.1016/j.devcel.2020.10.019

Zhang, T.-Q., Chen, Y., & Wang, J.-W. (2021). A single-cell analysis of the Arabidopsis vegetative shoot apex. *Developmental Cell*, *56*(7), 1056-1074.e1058. https://doi.org/https://doi.org/10.1016/j.devcel.2021.02.021

Zhao, F., & Traas, J. (2021). Stable establishment of organ polarity occurs several plastochrons before primordium outgrowth in Arabidopsis. *Development*, *148*(18). https://doi.org/10.1242/dev.198820

Zhou, J., Liu, G., Zhao, Y., Zhang, R., Tang, X., Li, L., Jia, X., Guo, Y., Wu, Y., Han, Y., Bao, Y., He, Y., Han, Q., Yang, H., Zheng, X., Qi, Y., Zhang, T., & Zhang, Y. (2023). An efficient CRISPR–Cas12a promoter editing system for crop improvement. *Nature Plants*, *9*(4), 588-604. https://doi.org/10.1038/s41477-023-01384-2

Zhu, H., Hu, F., Wang, R., Zhou, X., Sze, S.-H., Liou, Lisa W., Barefoot, A., Dickman, M., & Zhang, X. (2011). Arabidopsis Argonaute10 Specifically Sequesters miR166/165 to Regulate Shoot Apical Meristem Development. *Cell*, *145*(2), 242-256. https://doi.org/https://doi.org/10.1016/j.cell.2011.03.024

Zicola, J., Liu, L., Tänzler, P., & Turck, F. (2019). Targeted DNA methylation represses two enhancers of FLOWERING LOCUS T in Arabidopsis thaliana. *Nature Plants*, *5*(3), 300-307. https://doi.org/10.1038/s41477-019-0375-2

Appendix I

All supplementary data can be found in the attached compact disc.

nature plants

ARTICLES

https://doi.org/10.1038/s41477-022-01111-3

Check for updates

Specification of leaf dorsiventrality via a prepatterned binary readout of a uniform auxin input

Agata Burian[1,4], Gael Paszkiewicz[2,4], Khoa Thi Nguyen[2,3], Shreyas Meda[2], Magdalena Raczyńska-Szajgin[1] and Marja C. P. Timmermans[2]✉

Developmental boundaries play an important role in coordinating the growth and patterning of lateral organs. In plants, specification of dorsiventrality is critical to leaf morphogenesis. Despite its central importance, the mechanism by which leaf primordia acquire adaxial versus abaxial cell fates to establish dorsiventrality remains a topic of much debate. Here, by combining time-lapse confocal imaging, cell lineage tracing and molecular genetic analyses, we demonstrate that a stable boundary between adaxial and abaxial cell fates is specified several plastochrons before primordium emergence when high auxin levels accumulate on a meristem prepattern formed by the AS2 and KAN1 transcription factors. This occurrence triggers a transient induction of ARF3 and an auxin transcriptional response in AS2-marked progenitors that distinguishes adaxial from abaxial identity. As the primordium emerges, dynamic shifts in auxin distribution and auxin-related gene expression gradually resolve this initial polarity into the stable regulatory network known to maintain adaxial–abaxial polarity within the developing organ. Our data show that spatial information from an AS2–KAN1 meristem prepattern governs the conversion of a uniform auxin input into an ARF-dependent binary auxin response output to specify adaxial–abaxial polarity. Auxin thus serves as a single morphogenic signal that orchestrates distinct, spatially separated responses to coordinate the positioning and emergence of a new organ with its patterning.

Lateral organ formation is coordinated via the specification of developmental boundaries that provide spatial information to direct growth and regulate the acquisition of distinct cell fates. In plants, the elaboration of flat-leaf architecture requires a precisely positioned boundary between adaxial (top) and abaxial (bottom) cell fates that is stable despite prevalent cell proliferation[1,2]. The maintenance of adaxial–abaxial polarity within leaf primordia reflects the output of an intricate gene regulatory network in which mutually antagonistic interactions between transcription factors that promote either adaxial or abaxial identity reinforce initial cell fate decisions[3]. In addition, the mobile small RNAs miR166 and tasiARF, which target adaxial and abaxial determinants, respectively, provide positional information needed to maintain the proper separation of these cell fates at the domain level[4,5]. Reminiscent of classical morphogens, these small RNAs generate sharply defined domains of target gene expression through an intrinsic, threshold-based readout of the opposing mobility gradients.

Contrary to our understanding of the maintenance of adaxial and abaxial identities, the mechanism by which leaf primordia acquire adaxial–abaxial polarity remains a topic of much debate. A central reason for this is a lack of clarity on the contribution of auxin. This hormone provides spatial cues for the proper placing (phyllotaxy) and outgrowth of primordia at the meristem periphery[6,7]. However, there are opposing hypotheses on how auxin contributes to adaxial–abaxial patterning. One view argues that high auxin levels inhibit adaxial and/or promote abaxial identity[8]. In this scenario, a transient depletion of auxin from the leaf primordium to the meristem differentiates adaxial from abaxial cell fate. This view revisits a classical model for the origin of adaxial–abaxial polarity on the basis of microsurgical experiments performed on potato and tomato shoot apices that instead predicts that a mobile signal originating from the meristem centre promotes adaxial identity[9,10]. A further model poses that leaf primordia arise at a prepatterned middle domain characterized by high auxin signalling that promotes recruitment of adjacent adaxial and abaxial cells expressing Class III HD-ZIP (HD-ZIPIII) and KANADI (KAN) transcription factors, respectively[11]. Accordingly, the final domain organization of the leaf is already captured at the meristem. Thus, while there is agreement on how adaxial–abaxial polarity is maintained, the steps leading to the specification of this critical developmental axis remain unclear.

The challenge in understanding the origin of adaxial–abaxial leaf polarity is that the static view of development gained from mutant analyses and standard-imaging approaches is insufficient to capture the rapid, transient patterning events occurring at primordium inception. Moreover, reliable landmarks to identify the few leaf founder cells at the shoot apical meristem are lacking. Previous studies relied on auxin-related reporters[8,11,12]. However, local auxin response maxima move radially across the meristem periphery and are not strictly correlated with the positions of future leaves[13,14]. To overcome these challenges, we here used time-lapse confocal imaging with cell lineage tracing to accurately pinpoint the positions of incipient leaf primordia and to link dynamic behaviours in gene expression to the acquisition of cell fates. We show that adaxial–abaxial polarity is specified several plastochrons before primordium emergence not by an auxin gradient[8] or involving an auxin marked boundary domain[11] but instead via conversion of a uniform auxin

[1]Institute of Biology, Biotechnology and Environmental Protection, University of Silesia in Katowice, Katowice, Poland. [2]Center for Plant Molecular Biology, University of Tübingen, Tübingen, Germany. [3]NTT Hi-Tech Institute, Nguyen Tat Thanh University, Ho Chi Minh City, Vietnam. [4]These authors contributed equally: A. Burian, G. Paszkiewicz. ✉e-mail: marja.timmermans@zmbp.uni-tuebingen.de

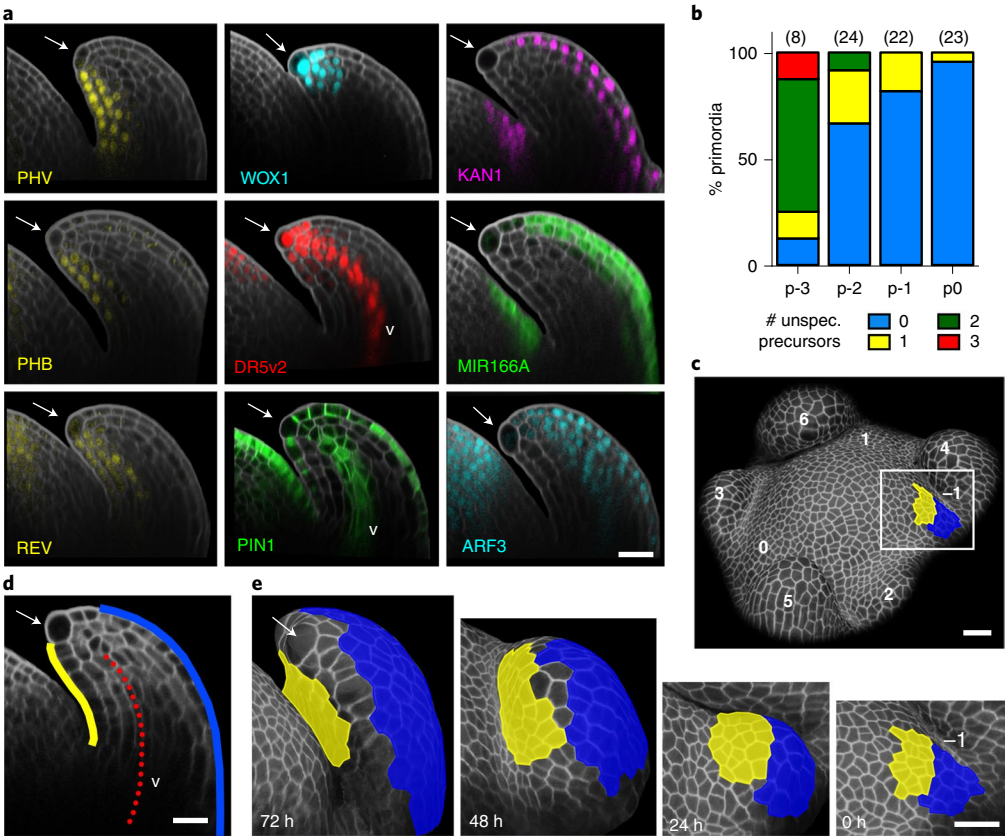

Fig. 1 | Adaxial–abaxial polarity is specified before primordium emergence. a, Patterns of gene expressions marking the adaxial (left), middle (middle) and abaxial (right) domains of a leaf primordium. Left: *pPHV:PHV-YPet, pPHB:PHB-YPet, pREV:REV-YPet*. Middle: *pWOX1:GFP, pDR5v2:GFP, pPIN1:PIN1-GFP*. Right: *pKAN1:KAN1-YPet, pMIR166A:erGFP, pARF3:ARF3-GFP*. **b**, Backward tracing of cell lineages from the adaxial, middle and abaxial domains of p6 primordia to their progenitors at p0 to p-3 reveals that the adaxial–abaxial boundary is specified before primordium emergence. At p-3 almost all leaf primordia contain multiple unspecified cells along the future boundary. The number of unspecified cells decreases sharply and at p-2, the adaxial–abaxial boundary for nearly all primordia analysed is stably defined or includes just a single undetermined cell (Extended Data Fig. 2c,d). Numbers in brackets represent the number of primordia analysed per stage. **c**, Top view of a shoot apex showing the position of the p-1 primordium at the meristem periphery (0 h). **d**, Optical longitudinal section of a p6 leaf primordium illustrating positions of the adaxial (yellow) and abaxial (blue) domains relative to the first forming trichome (arrow). **e**, Backward tracing of cell lineages from the adaxial (yellow), middle and abaxial (blue) domains of a p6 primordium (72 h) to their progenitors at p-1 (0 h), shows that while adaxial–abaxial polarity is specified before primordium emergence, the middle domain forms several plastochrons later from cells at the adaxial–abaxial boundary. Yellow, adaxial; blue, abaxial; red dotted line (v), midvein; arrow, the first forming trichome. Cell walls were stained by propidium iodide (PI). Scale bars, 20 µm. Representative examples from $n = 5$ (**a**) and $n = 22$ (**c**–**e**) primordia per line are shown.

input into an AUXIN RESPONSE FACTOR (ARF)-dependent binary auxin response output at an AS2–KAN1 meristem prepattern.

Results

Adaxial and abaxial fates are specified before primordium emergence. To discern how adaxial–abaxial leaf polarity arises and to resolve the contribution of auxin in this process, we used time-lapse confocal imaging of *Arabidopsis* plants grown on soil under short-day conditions. Plants grown under these more natural settings develop a larger shoot apical meristem with on average twice the number of visible leaf primordia (Extended Data Fig. 1), thus greatly improving the spatiotemporal resolution to capture rapid, transient changes in morphogenic processes. To then accurately pinpoint the positions of distinct leaf founder cells, we trace the lineages of cells in the adaxial, middle and abaxial domains of p6 primordia back to their progenitors at the meristem. At p6, cells of adaxial and abaxial identity are stably distinguished by expression of *PHV*, *PHB* and *REV*, versus *KAN1*, *MIR166A* and *ETTIN* (aka *ARF3*), respectively (Fig. 1a). Also, the middle domain, comprising the primordium tip, margins and inner provasculature, is clearly defined by expression of *WOX1*, *PIN1* and the DR5v2 synthetic auxin response marker. The position of the first trichome at the primordium tip, easily recognized by its increased cell size, delimits the border between the adaxial and middle domains. The first trichome therefore provides a morphological landmark and point of reference to trace the origin of adaxial, middle and abaxial identity during reverse cell lineage analysis used throughout this study (Fig. 1c–e and Extended Data Fig. 2a,b).

The backward tracing of cell lineages showed that adaxial and abaxial founder cells are distinctly defined as early as p-2. Whereas earlier progenitors typically contribute both adaxial and abaxial daughter cells, starting from p-2, the founder cells of the adaxial and abaxial sides form nonoverlapping domains, indicating the presence of an established adaxial–abaxial boundary (Fig. 1b and Extended Data Fig. 2). This boundary persists as the primordium develops. Adaxial–abaxial polarity thus is specified several plastochrons before primordium emergence. In contrast, the middle domain develops gradually from the adaxial–abaxial boundary after emergence of the primordium and this occurs via progressive recruitment of adaxial and abaxial daughter cells (Fig. 1d,e and Extended Data Fig. 3a,b) and the eventual onset of *WOX1* expression at p4 (ref.[15]) (Extended Data Fig. 3c,d).

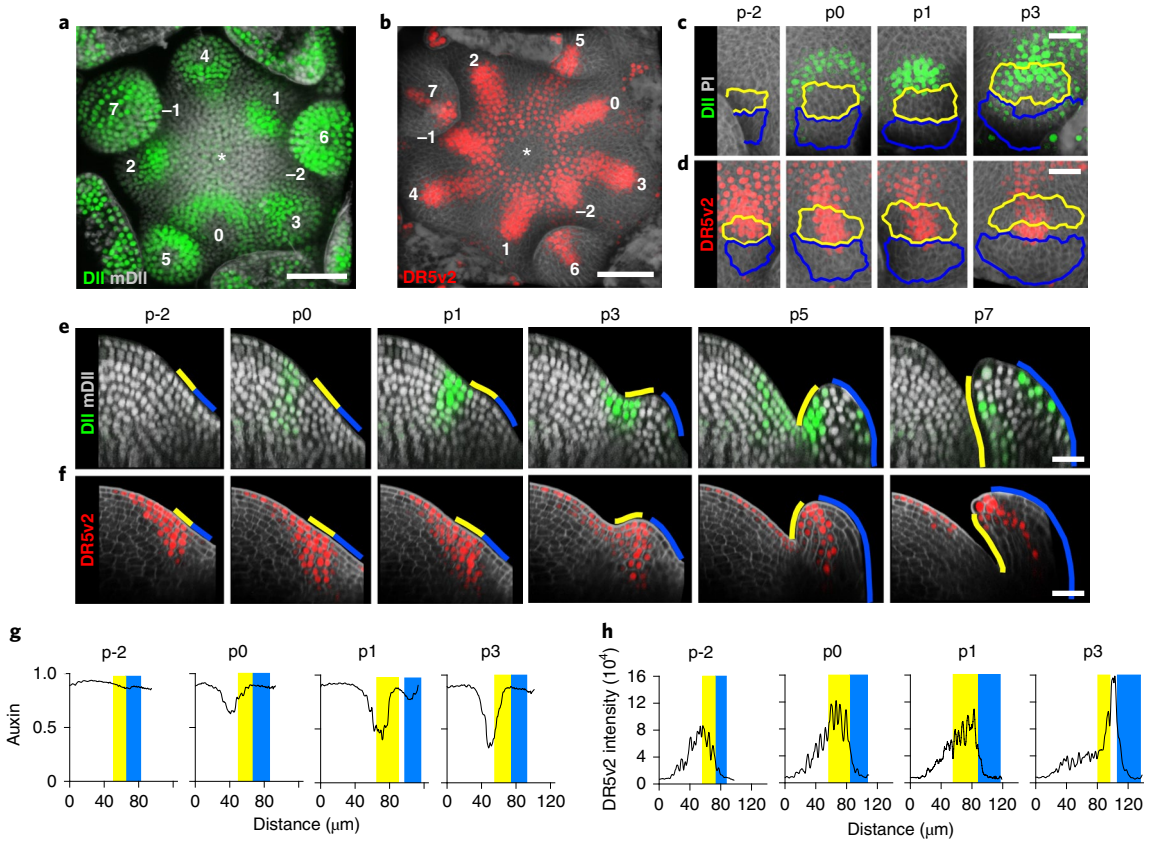

Fig. 2 | Conversion of a uniform auxin input into a binary auxin response output during the specification of adaxial–abaxial polarity. a–f, R2D2 (*DII-Venus* in green and *mDII-tdTomato* in grey) (**a**,**c**,**e**) and *pDR5v2:GFP* (**b**,**d**,**f**) expression patterns at the shoot apex show auxin levels are uniformly high at incipient primordia and are gradually depleted (increasing DII over mDII signal intensities) first from the adaxial and subsequently from the abaxial side after primordium emergence only. In contrast, a transcriptional auxin response output (DR5v2) distinguishes adaxial from abaxial identity starting from p-2. The auxin response output gradually shifts during primordium development to ultimately mark the middle domain. **a–d**, Top views of the meristem (**a**,**b**) and select leaf primordia (**c**,**d**). **e**,**f**, Optical longitudinal sections through select leaf primordia. **g**,**h**, Auxin levels, computed as 1-DII/mDII signal intensities (**g**) and *pDR5v2:GFP* signal intensities (**h**) measured along the apex radius (Extended Data Fig. 4c) at respective leaf primordium stages deviate, indicating a binary transcriptional auxin response output in adaxial versus abaxial progenitors. The distance 0 μm corresponds with the meristem centre (asterisks in **a** and **b**). Progenitors for the adaxial (yellow), abaxial (blue) and middle (not outlined) domains were discerned from backward lineage tracing. Cell walls (**a–d**,**f**) were stained by PI. Scale bars, 50 μm (**a**,**b**) and 20 μm (**c**,**f**). Representative examples from $n = 10$ apices (**a**,**b**) and $n = 6$ primordia per developmental stage (**c–h**) are shown.

A transient auxin response output distinguishes adaxial fate. Current models describing the acquisition of adaxial–abaxial polarity are contradictory with respect to the contribution of auxin to this process[8,11,12]. We addressed this controversy by examining the distribution of auxin at the apex in relation to the positions of adaxial and abaxial progenitors using reverse cell lineage analysis as above (Fig. 2 and Extended Data Fig. 4). The ratio-metric R2D2 reporter[16] reveals a dynamic pattern of DII/mDII expression associated with primordium development. Consistent with a role for auxin in driving organogenesis[6,7], incipient primordia fall within successive rays of decreased DII/mDII expression, indicating comparatively high auxin levels, at the meristem periphery (Fig. 2a,c,e,g and Extended Data Fig. 4). A DII/mDII expression maximum, indicating relatively low auxin levels, is first visible at the boundary between the p0 incipient primordium and the meristem but then gradually shifts position to coincide first with the adaxial side (p1–p4) and subsequently also with the abaxial side (p5–p7). Accordingly, the adaxial and abaxial sides of incipient leaf primordia experience similarly high auxin levels and only as the primordium emerges is auxin depleted from the adaxial side. As auxin is subsequently depleted also from the abaxial side, high auxin levels ultimately become focused on the then established middle domain.

To further assess a contribution of auxin to the establishment of adaxial–abaxial leaf polarity, we next determined its relationship to the nuclear transcriptional auxin response. The DR5v2 reporter[16] likewise shows rays of expression along the meristem periphery that extend from the central zone to sites of organogenesis (Fig. 2b). However, whereas high auxin levels are detected as early as p-4 (Extended Data Fig. 4), the onset of DR5v2 expression coincides with the first occurrence of a defined adaxial–abaxial boundary at p-2. Moreover, reverse lineage tracing shows that the DR5v2 expression front coincides with the position of this boundary (Fig. 2d,f), indicating that an asymmetric transcriptional auxin response output distinguishes adaxial from abaxial founder cells. While the DR5v2 expression maximum at p-2 centres around the meristem–primordium boundary, this maximum gradually shifts across the adaxial side reinforcing the polarized pattern of DR5v2 until primordium emergence (p1) (Fig. 2h). Subsequently, DR5v2 reporter activity gradually decreases on the adaxial side resulting in a DR5v2 expression maximum at the middle domain as this arises between the adaxial and abaxial sides (Fig. 2f,h).

Thus, while adaxial and abaxial founder cells experience near-equivalent auxin levels, this uniform signal input is converted into a highly polarized nuclear auxin response output that distin-

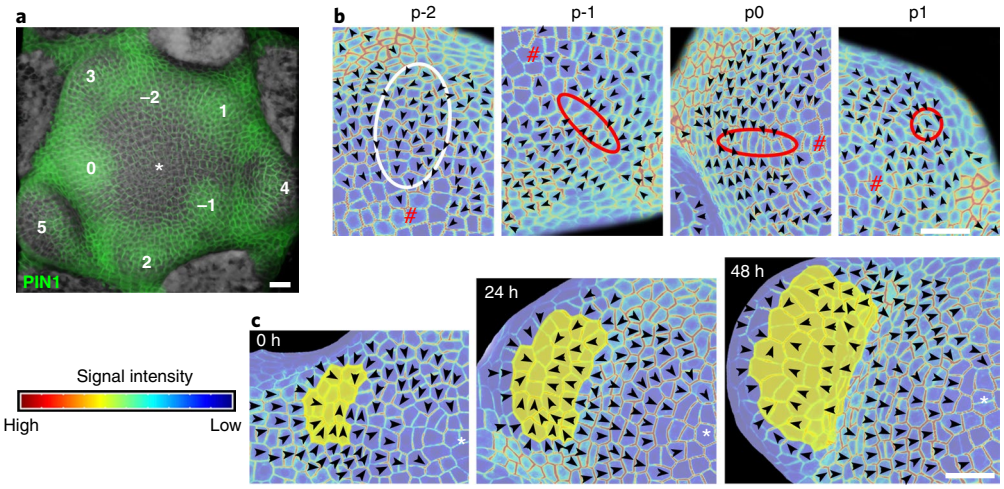

Fig. 3 | PIN1 convergence patterns orient towards the adaxial side of incipient leaf primordia. a, *pPIN1:PIN1-GFP* expression at the shoot apex shows that accumulation of this auxin efflux carrier overlaps broadly with positions of organogenesis and sites of auxin biosynthesis at the flanks of older leaf primordia (Extended Data Fig. 6). **b**, Patterns of PIN1–GFP polarity at the L1 are dynamic, generating transient PIN1 convergence domains at the adaxial side of incipient primordia (red ellipses) that subsequently become refined (red circle) to mark the primordium tip. White ellipse, pattern of PIN1–GFP polarity towards to meristem central zone near p-2. **c**, Time-lapse series of a representative p0 leaf primordium shows PIN1–GFP polarity first oriented toward the adaxial side (0 h), subsequently diverges towards the meristem central zone and primordium tip. Yellow highlight, adaxial cells discerned from backward lineage tracing (**c**); arrowheads, PIN1 polarity (**b**,**c**); asterisks, meristem centre (**a**,**c**); red hash, direction to the meristem centre (**b**). Cell walls were stained by PI. Scale bars, 20 μm. Representative data from $n = 6$ apices (**a**) and $n = 5$ primordia per developmental stage (**b**,**c**) are shown.

guishes adaxial from abaxial identity. As the primordium emerges (p1–p4), auxin depletion from the adaxial side prompts a transition from a high to low auxin state that is mirrored by a more gradual shift of the transcriptional response to the middle domain as this arises from the adaxial–abaxial boundary (evidenced by the temporary overlap in DR5v2 and DII expression, Fig. 2e,f). A subsequent (p5) depletion of auxin also from the abaxial side co-localizes an auxin maximum with the downstream transcriptional response at the middle domain. Thus, abaxial founder cells derive from a region of the meristem periphery where auxin-induced gene expression is constantly repressed, whereas adaxial founder cells are defined by rapid changes in auxin input and transcriptional output. Importantly, a polarized nuclear auxin response output is specific to organs of adaxial–abaxial polarity and is seen during the initiation of other leaf-like organs, such as cauline leaves, bracts and sepals but not at initiating axillary or floral meristems (Extended Data Fig. 5).

PIN1 polarization refines the auxin response pattern. Given the link between auxin responses and PIN1-based polar auxin transport[17–20], we next examined the patterns of PIN1 polarity using a functional *pPIN1:PIN1-GFP* reporter[21]. Strong PIN1 expression at the meristem is broadly associated with positions of organogenesis as well as sites of auxin biosynthesis at the flanks of older leaf primordia (Fig. 3a and Extended Data Fig. 6). At p-2, when the adaxial–abaxial boundary is specified and a DR5v2 auxin response is first detected, PIN1 polarity is primarily oriented from these sites of auxin synthesis towards the meristem central zone (Fig. 3b). This pattern is consistent with recent observations at the inflorescence meristem[14] and can explain the rays of high auxin levels visualized by R2D2 extending along the meristem periphery (Fig. 2a,g). At the onset of p-1, PIN1 shifts its polarity nearly orthogonally, resulting in a broad convergence domain (Fig. 3b). This domain traces to the adaxial side of the incipient primordium and adjacent future meristem–primordium boundary (Fig. 3c) and thus mirrors the nuclear response to auxin (Fig. 2d). In line with the observed auxin dynamics, the pattern of PIN1 polarity diverges again as the primordium emerges (p1), directing auxin from the meristem–primordium boundary towards the central zone and towards the primordium tip[18,22] (Fig. 3c).

Given that the onset in DR5v2 expression precedes the convergence of PIN1 polarities at incipient leaf primordia by approximately one plastochron, the binary readout of the uniform auxin input into a polarized transcriptional response output must involve PIN1-independent mechanisms. In addition, centring of the auxin response at the primordium middle domain cannot be explained solely by PIN1 activity. Although the change in PIN1 polarity at p1 presages the shift in auxin response to the middle domain, the latter transition is observed also in primordia grown in the presence of the polar auxin transport inhibitor NPA (Extended Data Fig. 7a–d). Instead, DR5v2 expression at the middle domain expands laterally in NPA-treated primordia. Thus, rather than triggering the observed auxin-induced expression dynamics[8], PIN1-mediated auxin transport probably reinforces and/or refines the initial auxin response and functions to constrain auxin-induced gene expression and other auxin-driven responses laterally. The observed lateral fusion of leaf primordia in the *pin1* mutant supports this idea (Extended Data Fig. 7e,f).

Rings of AS2 and KAN1 expression prepattern the meristem periphery. One of the current models to explain the acquisition of adaxial–abaxial polarity proposes that this is driven by a prepattern based in part on patterns of HD-ZIPIII and KAN expression at the meristem[11]. Consistent with a possible causal link to the binary transcriptional auxin response at leaf founder cells, KAN1 and the HD-ZIPIII transcription factor REV show opposing effects on expression of auxin-related genes. Whereas KAN1 acts as a repressor, REV promotes expression of multiple components involved in auxin biosynthesis, transport and signalling[23,24]. We, therefore, next traced the patterns of REV and KAN1 expression in relation to the specification of adaxial versus abaxial cell fates and the conversion of a symmetric auxin input at incipient primordia into an asymmetric nuclear auxin response output.

As reported previously[11,25], KAN1, imaged using a *pKAN1:KAN1-YPet* reporter, is expressed on the abaxial side of established

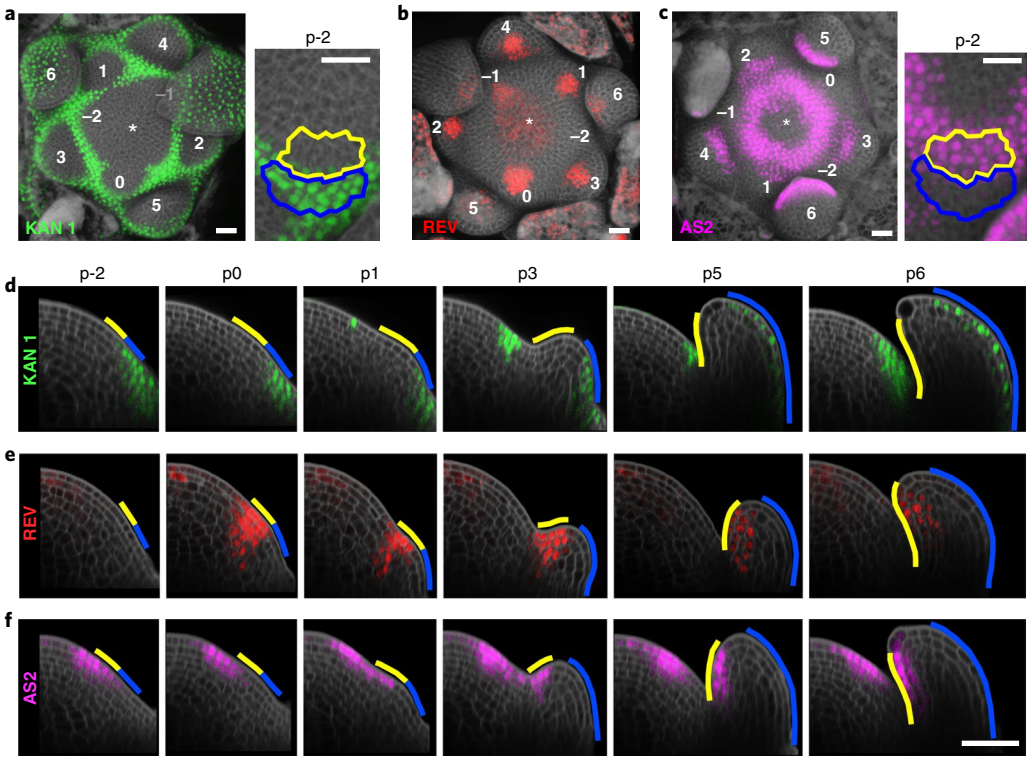

Fig. 4 | Concentric rings of AS2 and KAN1 expression prepattern adaxial–abaxial polarity at the shoot apical meristem. a–f, The patterns of *pKAN1:KAN1-YPet* (**a**,**d**), *pREV:REV-YPet* (**b**,**e**) and *pAS2:AS2-VENUS* (**c**,**f**) expression at the shoot apex show that accumulation of REV on the adaxial side of leaf primordia is delayed relative to the specification of adaxial–abaxial polarity at p-2. In contrast, KAN1 and AS2, which mark the abaxial and adaxial side of leaf primordia, respectively, also accumulate in a concentric pattern around the meristem periphery predetermining the position of the adaxial–abaxial boundary. **a**–**c**, Meristem top view with magnification of the p-2 primordium. **d**–**f**, Optical longitudinal sections through developing leaf primordia. Progenitors for the adaxial (yellow), abaxial (blue) and middle (not outlined) domains were discerned from backward lineage tracing. Asterisks (**a**–**c**), meristem centre. Cell walls were stained by PI. Scale bars, 20 µm (**a**–**c**) and 50 µm (**d**–**f**). Representative images of $n = 10$ (**a**), 7 (**b**) or 12 (**c**) apices and $n = 5$ primordia per developmental stage (**d**–**f**) are shown.

leaf primordia (Fig. 4a,d). In addition, KAN1 expression arises near the meristem–primordium boundary shortly following primordium outgrowth (p1), such that KAN1 also forms a narrow ring of expression at the meristem periphery (Fig. 4a). Lineage tracing confirms that this localization overlaps the abaxial founder cells at p-2 (Fig. 4a,d), thus supporting the idea that KAN1 activity prepatterns abaxial identity in incipient leaf primordia[11]. However, in contrast to KAN1, REV expression at the meristem periphery is restricted to sites of primordia and is delayed relative to the specification of adaxial–abaxial polarity and the first indication of an asymmetric transcriptional auxin response. A functional *pREV:REV-YPet* reporter shows that activity internal to the p-1 primordium (Extended Data Fig. 8), and only just before primordium emergence (p0), is expression detected across the adaxial side (Fig. 4b,e). The asymmetric nuclear auxin response and the specification of adaxial–abaxial polarity thus precede the accumulation of REV in adaxial cells, contradicting the proposed role for REV in prepatterning adaxial identity at incipient leaf primordia[11]. Instead, REV probably contributes to maintain adaxial–abaxial polarity on primordium emergence.

Given this outcome, we next focused our attention on AS2, which like REV, is an adaxial determinant and a core component in the adaxial–abaxial polarity network[3,26]. AS2 also acts in a mutually antagonistic manner to KAN1 and this is based, at least in part, on direct repressive interactions[27]. Accordingly, a *pAS2:AS2-VENUS* reporter shows expression on the adaxial side of established leaf primordia (Fig. 4c,f). However, strikingly, AS2 also accumulates at the meristem periphery in a ring of cells positioned just apical to the KAN1 expression domain. The concentric rings of AS2 and KAN1 form a prepattern that foreshadows the position of the adaxial–abaxial boundary. The unspecified progenitors at p-5 are positioned entirely within the AS2-expression domain but due to continued cell division and growth at the meristem, primordium founder cells at p-2 have centred on the AS2–KAN1 expression interface (Figs. 5a and 4a,c). At this stage, adaxial founder cells trace to the domain of AS2 expression (Fig. 4c,f). Further, whereas cells at the interface show occasional, weak co-expression of AS2 and KAN1, similar to the fate of precursor cells, expression of both transcription factors is fully resolved at p-2 (Figs. 1b and 5b,c). Interestingly, during subsequent stages of primordium development (p-1, p0), expression of both AS2 and KAN1 slightly recedes from the adaxial–abaxial boundary creating a small gap in expression that seems to presage the position of the future middle domain (Figs. 4d,f and 5b,c). Accordingly, the AS2–KAN1 prepattern may provide positional information to first fix the adaxial–abaxial boundary and subsequently, on dissipation of expression, to allow formation of the middle domain.

Taken together, our data link the specification of adaxial–abaxial polarity to a prepattern at the meristem periphery formed by concentric domains of AS2 and KAN1 expression. Considering that in this process a uniform auxin input is read out into a binary transcriptional auxin response output (Fig. 2), the prepatterning activities of AS2 and KAN1 may involve establishment of zones of distinct auxin responsiveness. Indeed, KAN1 acts as a direct repressor of auxin-induced gene expression[23,24,28]. However, in the

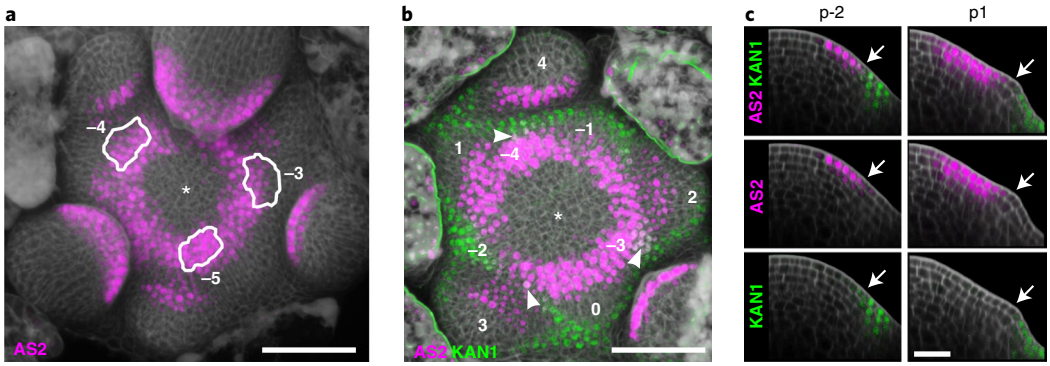

Fig. 5 | AS2 and KAN1 prepattern adaxial–abaxial polarity at the shoot apical meristem. a, Backward tracing of cell lineages at *pAS2:AS2-VENUS* shoot apices shows that the position of primordium precursors (outlined) changes relative to the AS2 prepattern. Precursors are gradually displaced through the AS2-expression domain towards the AS2–KAN1 prepattern interface. **b**,**c**, Image of a *pKAN1:KAN1-Turquoise pAS2:AS2-VENUS* shoot apex shows that AS2 and KAN1 form concentric rings of expression at the meristem periphery. Variable co-expression of AS2 and KAN1 at the prepattern interface (arrowheads, **b**) disappears with establishment of the adaxial–abaxial boundary at p-2 (arrows, **c**). A small gap in AS2 and KAN1 expression at the boundary at p1 presages the position of the future middle domain (arrows, **c**). **a**,**b**, Meristem top view. **c**, Optical longitudinal sections through p-2 and p1 primordia. Arrowheads, overlapping expression of AS2 and KAN1 (**b**); arrows, cell at the adaxial–abaxial boundary (**c**); asterisks, meristem centre (**a**,**b**). Cell walls were stained by PI. Scale bars, 50 µm (**a**,**b**) and 20 µm (**c**). Representative images of $n = 5$ (p-3, p-4) or $n = 3$ (p-5) primordia (**a**), $n = 4$ apices (**b**) and $n = 3$ primordia per developmental stage (**c**) are shown.

absence of an established link between AS2 and auxin signalling, the question as to how the adaxial transcriptional auxin response is realized remains.

ARF3 governs a local auxin response to distinguish adaxial fate. Localized accumulation of ARFs provides a likely scenario to generate the binary transcriptional auxin response output at incipient leaf primordia, especially if we consider the roles of ARF3 and ARF5/MP in promoting organogenesis at the inflorescence meristem[14,20,29,30]. Indeed, a functional *pMP:MP-GFP* reporter shows that this ARF is expressed at the meristem periphery in a pattern that predicts sites of future primordia starting from at least two plastochrons before the asymmetric nuclear auxin response reported by DR5v2 is visible (Fig. 6a). The distribution of MP at these early sites appears largely uniform (Extended Data Fig. 9), but starting from p-2, coincident with the specification of the adaxial–abaxial boundary, MP levels in the abaxial founder cells show a modest decline (Fig. 6c,e,g). Slightly higher MP levels thus become limited to cells positioned apical to the adaxial–abaxial boundary, where it overlaps with DR5v2 expression (Fig. 2b,d,f). An adaxially enriched pattern of MP expression is maintained until after primordia outgrowth (p1), when MP expression gradually centres on the emerging middle domain and adjacent adaxial layer (Fig. 6c,e,g).

The change in MP expression from a uniform into a slightly polarized pattern of accumulation during the p-3 to p-2 transition is intriguing, although this is unlikely to fully explain the binary auxin response output that distinguishes adaxial from abaxial fate. Unexpectedly, ARF3 activity instead may serve this function. Although known for its contributions to abaxial identity[4,5,26,31,32], ARF3 in fact marks the adaxial side of incipient leaf primordia (Fig. 6b,d,f,h). The functional *pARF3:ARF3-GFP* reporter[29] shows expression in the meristem central zone but, starting from p-2, expression extends into the incipient primordium where it overlaps with the AS2- but not the KAN1-marked founder cells. Indeed, consistent with the idea that KAN1 prepatterns a zone of low auxin responsiveness at the meristem periphery, KAN1 and ARF3 show complementary patterns of expression during the early stages of primordium development (Figs. 4a,d and 6b,d,f and Extended Data Fig. 10a). It is not until the primordium emerges (p1) that ARF3 expression shifts from the adaxial side to first cover the future middle domain and subsequently the abaxial side. It is thus comparatively late in primordium development that ARF3 fills its known function as abaxial determinant.

Overlay of high auxin levels on the AS2–KAN1 meristem prepattern at p-2 thus is paralleled by transient shifts in ARF3 and, to a lesser extent, MP expression. The resulting pattern of ARF3 localization at the meristem periphery matches the nuclear auxin response visualized by DR5v2 (Figs. 6d,f and 2df). In addition, the shift in this auxin response from the adaxial side to the middle domain following primordium emergence mirrors the spatial dynamics in auxin, ARF3 and MP accumulation. Our findings thus bring into play the local activation of ARF3 as a defining factor, possibly in conjunction with other ARFs, in generating the auxin transcriptional response and distinguishing adaxial and abaxial identities before primordium emergence. Substantiating this idea, DR5v2 reporter activity is dramatically reduced on *ARF3* mutation (ref. [14]; Fig. 6i,j).

AS2 and KAN1 repress *ARF3* to position the adaxial auxin response. The observed expression dynamics predict the presence of multiple repressive interactions between KAN1, AS2 and ARF3 to maintain the AS2–KAN1 meristem prepattern and to position the local induction of ARF3. Indeed, chromatin immunoprecipitation (ChIP) analyses showed that KAN1 is enriched at the *AS2* promoter and, vice versa, AS2 binds the promoter of *KAN1* (Fig. 7a–c). Transient luciferase reporter assays, which can discern effects of individual transcription factor–promoter interactions within complex gene regulatory networks, confirm that KAN1 acts as a strong repressor of *AS2* (ref. [27]; Fig. 7d). In addition, in a *kan1 kan2* background, AS2 expression extends basipetally along the meristem periphery into cells otherwise marked by KAN1 (Fig. 7e), thus identifying a critical role for KAN function in setting the basal limit of the AS2 prepattern. The KAN1 prepattern, on other hand, largely persists in *as2* (Fig. 7f), despite a significant repressive effect of AS2 on *KAN1* promoter activity in transient reporter assays (Fig. 7d). Similar to the observed redundancy between KAN1 and KAN2, this may signify involvement of yet unknown AS2-like or other transcription factors in delineating the KAN1 expression domain.

Both KAN1 and AS2 also bind the promoter of *ARF3* (Fig. 7a–c). KAN1 strongly represses *ARF3* promoter activity in transient

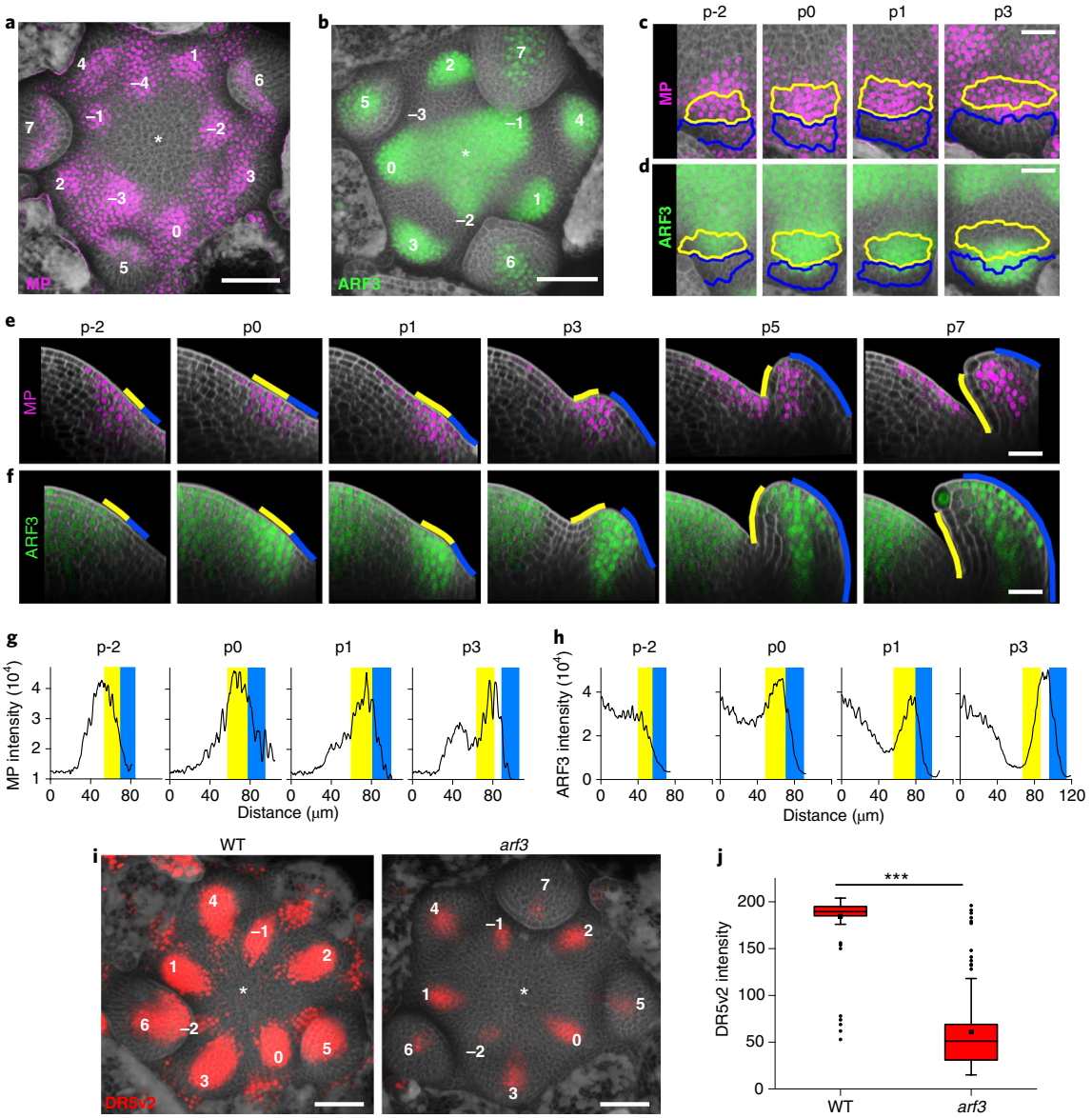

Fig. 6 | ARF3 expression distinguishes adaxial from abaxial founder cells. a–f, *pMP:GFP-MP* (**a**,**c**,**e**) and *pARF3:ARF3-GFP* (**b**,**d**,**f**) show dynamic patterns of expression at the shoot apex that starting from p-2 overlap the adaxial precursors and then gradually shift onto the middle domain. **a–d**, Top views of the meristem (**a**,**b**) and select leaf primordia (**c**,**d**). **e**,**f**, Optical longitudinal sections through developing leaf primordia. **g**,**h**, GFP-MP (**g**) and ARF3-GFP (**h**) signal intensities measured along the apex radius at respective leaf primordium stages illustrate the dynamic changes in expression. The distance 0 μm corresponds with the meristem centre. **i**, The patterns of *pDR5v2:Turquoise* expression at wild-type (WT, left) and *arf3* (right) shoot apices indicate a strongly reduced transcriptional auxin response in *arf3*, although a basal pattern persists. **j**, Box plot of *pDR5v2:Turquoise* signal intensity shows a significantly lower *pDR5v2* response in *arf3* compared to wild type (***$P = 5.53 \times 10^{-44}$ two-sided Kolmogorov–Smirnov test). Boxes, 25th to 75th percentile; whiskers, 5th to 95th percentile; black square, mean; black dots, outliers; asterisks, meristem centre. Progenitors for the adaxial (yellow), abaxial (blue) and middle (not outlined) domains were discerned from backward lineage tracing. Cell walls were stained by PI. Scale bars, 50 μm (**a**,**b**,**i**) and 20 μm (**c**–**f**). Representative data from $n = 10$ (**a**), 6 (**b**) or 8 (**i**) apices and $n = 5$ primordia per developmental stage (**c**–**h**) are shown. **j**, $n = 120$ cells from eight p-2, p-1 and p0 primordia per line.

assays (Fig. 7d) and, accordingly, ARF3 expression extends basipetally in *kan1 kan2* mutant meristems (Fig. 7g). A repressive interaction from KAN1 onto *ARF3* matches their complementary patterns of expression during the early stages of primordium development (Figs. 4a,d and 6b,d,f and Extended Data Fig. 10a). Further, considering the contribution of ARF3 to the nuclear auxin response (Fig. 6i,j), the finding that KAN1 suppresses ARF3 accumulation in abaxial founder cells identifies a direct mechanism for the binary readout of the uniform auxin input at p-2. Indeed, DR5v2 reporter activity in *kan1 kan2* likewise shows a basipetal shift and extends beyond sites of incipient and early primordia (Fig. 7h).

Interestingly, also AS2 represses *ARF3* promoter activity in transient assays (Fig. 7d) and the local ARF3 expression maxima at incipient primordia are less well defined in the *as2* mutant (Fig. 7g,i). Supporting a repressive interaction from AS2 onto *ARF3*, their respective patterns of expression during early primordium development are anticorrelated (Extended Data Fig. 10b). Induction of ARF3 at p-2 coincides with a slight local decrease in AS2 levels (Fig. 7j–l) and ARF3 levels adaxially further increase as growth at

the meristem displaces the primordium basipetal to the AS2 prepattern (p-1, p0) (Fig. 6b,d,f and Extended Data Fig. 10b). As ARF3 expression shifts from the adaxial side to the middle domain following primordium emergence (p1) (Fig. 6d,f), AS2 levels again increase in adaxial cells (Fig. 4c,f). As a result, cells expressing ARF3 span the small gap in AS2 and KAN1 expression that presages the arising middle domain (Extended Data Fig. 10a,b).

Thus, in addition to a mutually antagonistic interaction, KAN1 and AS2 act as direct repressors in the regulation of ARF3. AS2 refines the domain of ARF3 induction adaxially, whereas KAN1 prevents induction of ARF3 and the downstream transcriptional auxin response to distinguish abaxial fate. Given the established redundancies[3,26,27,31,32], AS2, KAN1 and ARF3 probably share these functions with other members in their transcription factor families.

Discussion

Through precise lineage tracing of adaxial and abaxial progenitors, we here show that a stable boundary between these fates is specified several plastochrons before primordium emergence. Adaxial–abaxial leaf polarity is triggered in response to high auxin levels superimposed on a prepattern of AS2 and KAN1 transcription factors at the meristem periphery. This occurrence is associated with induction of ARF3 and a downstream transcriptional auxin response in AS2-expressing founder cells that distinguishes adaxial from abaxial cell identity. Thus, spatial information provided by the AS2–KAN1 meristem prepattern triggers conversion of a uniform auxin input into an ARF-dependent binary nuclear auxin response output to specify adaxial–abaxial polarity (Fig. 8a).

This model, which is substantiated by molecular, genetic and microsurgical[33] experimentation, differs in significant ways from previous models on the origin of adaxial–abaxial polarity. At p-2, when a stable adaxial–abaxial boundary is specified, auxin is transported acropetally toward the central zone from a source of biosynthesis at the basal flanks of established primordia below (Fig. 8b). At this time, leaf founder cells experience equivalently high auxin levels, excluding the view that a local depletion of auxin specifies adaxial fate[8]. Likewise, adaxial identity is defined before the onset of REV expression and leaves are not initiated at a predefined middle domain of auxin responsive cells that recruits adjacent REV and KAN positive cells into the primordium[11]. Instead careful lineage analysis on key reporter lines shows that adaxial founder cells exhibit a strong nuclear auxin response and trace to a ring of cells first defined by AS2 expression (Fig. 8c). Thus, rather than being driven by an auxin gradient[8] or an auxin marked middle domain[11], our data show that adaxial–abaxial polarity is specified by a prepattern-driven binary readout of a uniformly high auxin input.

A critical amplifier of this binary readout is ARF3. That ARF3, an established abaxial determinant, is initially linked to adaxial identity is unexpected. ARF3 is a multifaceted transcriptional regulator with markedly different sets of gene targets distinguished via auxin-sensitive interactions with a range of additional transcriptional regulators[29,34]. Accordingly, ARF3 may initially activate an auxin response in adaxial founder cells, while subsequently promoting abaxial fate in cells of the primordium where auxin levels are low. The versatile contributions of ARF3 to adaxial–abaxial leaf polarity underscore the importance of lineage analysis and exemplify the dynamic nature of this patterning process. Governed by auxin-driven transcriptional shifts, the initial polarity established within the context of the meristem gradually resolves into the regulatory network within the developing organ that maintains polarity via opposing gradients of morphogen-like small RNAs[3,5]. The process of adaxial–abaxial patterning can thus be envisioned in three phases: establishment, resolution and maintenance (Fig. 8b–d).

Interestingly, the rapid shifts in gene expression observed explain the discrepancies between previous models[8,11,12,35]. Namely, REV becomes active adaxially in the primordium just before its emergence and this event is followed by a gradual depletion of auxin from adaxial cells. As also ARF3 expression progressively shifts from the adaxial to the abaxial side, the auxin response becomes centred on the middle domain (Fig. 8b–d). Importantly, this domain arises gradually following primordium emergence on a small gap between the AS2/REV and KAN domains. Middle domain identity thus follows from a respecification of cells at the adaxial–abaxial boundary, rather than being prepatterned at the meristem periphery[11]. On activation of WOX1 a stable configuration of adaxial, middle and abaxial domains results (Fig. 8b–d). Thus, the depletion of auxin from the adaxial side of leaf primordia, as well as adaxial REV expression and the occurrence of an auxin response marked middle domain are secondary events connected to the resolution and subsequent maintenance of adaxial–abaxial polarity in the developing primordium.

The interface between the concentric rings of AS2 and KAN1 expression at the meristem periphery predetermines the position of the adaxial–abaxial organ boundary. The AS2–KAN1 prepattern is formed independently of the auxin signal with which it interacts. Instead, an antagonistic relationship between KAN1 and AS2 guides its organization. The prepatterned boundary is also largely resilient to variations in auxin levels evident at the meristem. However, importantly, a transcriptional readout of the auxin input distinguishes

Fig. 7 | Antagonistic interactions between KAN1, AS2 and ARF3 positions the adaxial auxin response. a,**b**, Schematic representations of predicted KAN1 (**a**) or AS2 (**b**) binding sites in the promoters of *AS2*, *ARF3* or *KAN1*. **c**, ChIP analyses showing significant enrichment of KAN1 at specific regions of the *AS2* and *ARF3* promoters (left) or of AS2 at sites in the *KAN1* and *ARF3* promoters (right). Values (means ± s.e., $n = 3$ independents biological replicates) are relative to the enrichment of KAN1 or AS2 at the negative control gene *ACT2*. KAN1 occupancy at the *AS2* promoter was assessed at one previously reported binding site[27]. *$P < 0.05$ two-sided Student's *t*-test (see Supplementary Table 3 for individual *P* values). **d**, Box plot of relative luciferase activity, calculated as Firefly over *Renilla* Luciferase activity, shows significant repression of *pAS2:LUC* by KAN1 ($n = 15$; $P = 3.07 \times 10^{-14}$) (left), *pKAN1:LUC* by AS2 ($n = 13$; $P = 8.02 \times 10^{-4}$) (middle) and *pARF3:LUC* by AS2 ($n = 14$; $P = 4.60 \times 10^{-7}$) and KAN1 ($n = 14$; $P = 5.17 \times 10^{-12}$) (right) in *Arabidopsis* protoplast. *n*, independent biological replicates; boxes, 25th to 75th percentile; whiskers, 5th to 95th percentile; **$P < 0.01$ two-sided Student's *t*-test. **e**, Patterns of *pAS2:AS2-VENUS* expression at wild-type (left) and *kan1 kan2* (right) shoot apices show that AS2 expression in *kan1 kan2* extends basipetally along the meristem periphery (arrowheads) and is no longer polarized in the adaxialized leaf primordia. **f**, The patterns of *pKAN1:KAN1-Turquoise* expression at wild-type (left) and *as2* (right) apices are comparable. **g**,**h**, The patterns of *pARF3:ARF3-Ypet* and *pDR5v2:GFP* expression at wild-type (left) and *kan1 kan2* (right) shoot apices show that expression of both ARF3 and DR5v2 in *kan1 kan2* extends basipetally beyond sites of incipient and early primordia (arrowheads). **i**, The pattern of *pARF3:ARF3-Turquoise* at the *as2* shoot apex shows a broader pattern of ARF3 expression (arrowheads) at incipient primordia compared to wild type (**g**). **j**,**l**, *pAS2:AS2-VENUS* expression levels decrease quantitatively at p-2 compared to p-4. **j**, Top view of a *pAS2:AS2-VENUS* meristem. **k**, Standardized *pAS2:AS2-VENUS* signal intensity measured along the apex radius at p-2 and p-4. The distance 0 µm corresponds with the meristem centre. **l**, Box plot of *pAS2:AS2-VENUS* maximum signal intensity along the apex radius shows that AS2 levels are significantly lower at p-2 compared to p-4 (*$P = 0.00249$ two-sided Kolmogorov–Smirnov test). Boxes, 25th to 75th percentile; whiskers, 5th to 95th percentile; black square, mean. Asterisks, meristem centre; ip, incipient primordium; p, primordium. Cell walls were stained by PI. Scale bars, 50 µm. Representative data from $n = 8$ (**e**), $n = 6$ (**f**), $n = 5$ (**g**) and $n = 8$ (**h**–**l**) independent apices are shown.

adaxial cell fate. The KAN-directed repression of ARF3 at the meristem periphery identifies a mechanism to limit this response to cells in the AS2 domain. Conceptually, KAN1 and AS2 thus function in a manner analogous to selector genes in animal development[36], they promote distinct cell fate specific gene regulatory outputs in response to a common auxin input. Uncoupling the spatial arrangement of AS2 and KAN1 from their signal driven output permits a robust definition of the domain boundary without placing constraints on cell fate. This point is particularly critical to pattern formation in organs arising in an iterative manner from a stem cell niche where primordium progenitors "pass" through the prepattern.

The radial positional information that converges with the AS2–KAN1 meristem prepattern to locally induce ARF3 is presumably linked to the auxin-driven phyllotactic pattern[6,14]. As such, auxin may act both upstream and via ARF3; exposure to high auxin levels over time triggers ARF3 expression in the AS2 domain, where it then determines adaxial cell fate through induction of an auxin transcriptional response. AS2, which acts as a direct repressor of ARF3, may act in conjunction with auxin to refine the site of ARF3 induction. Interestingly, with auxin levels decreasing and AS2 expression increasing adaxially on primordium emergence, the same regulatory interactions also explain repositioning of the ARF3-dependent auxin response to delineate the emerging middle domain. Accordingly, the AS2–KAN1–ARF3 module first uses auxin cues to partition the p-2 primordium into adaxial and abaxial domains and then subsequently, in response to changes in auxin

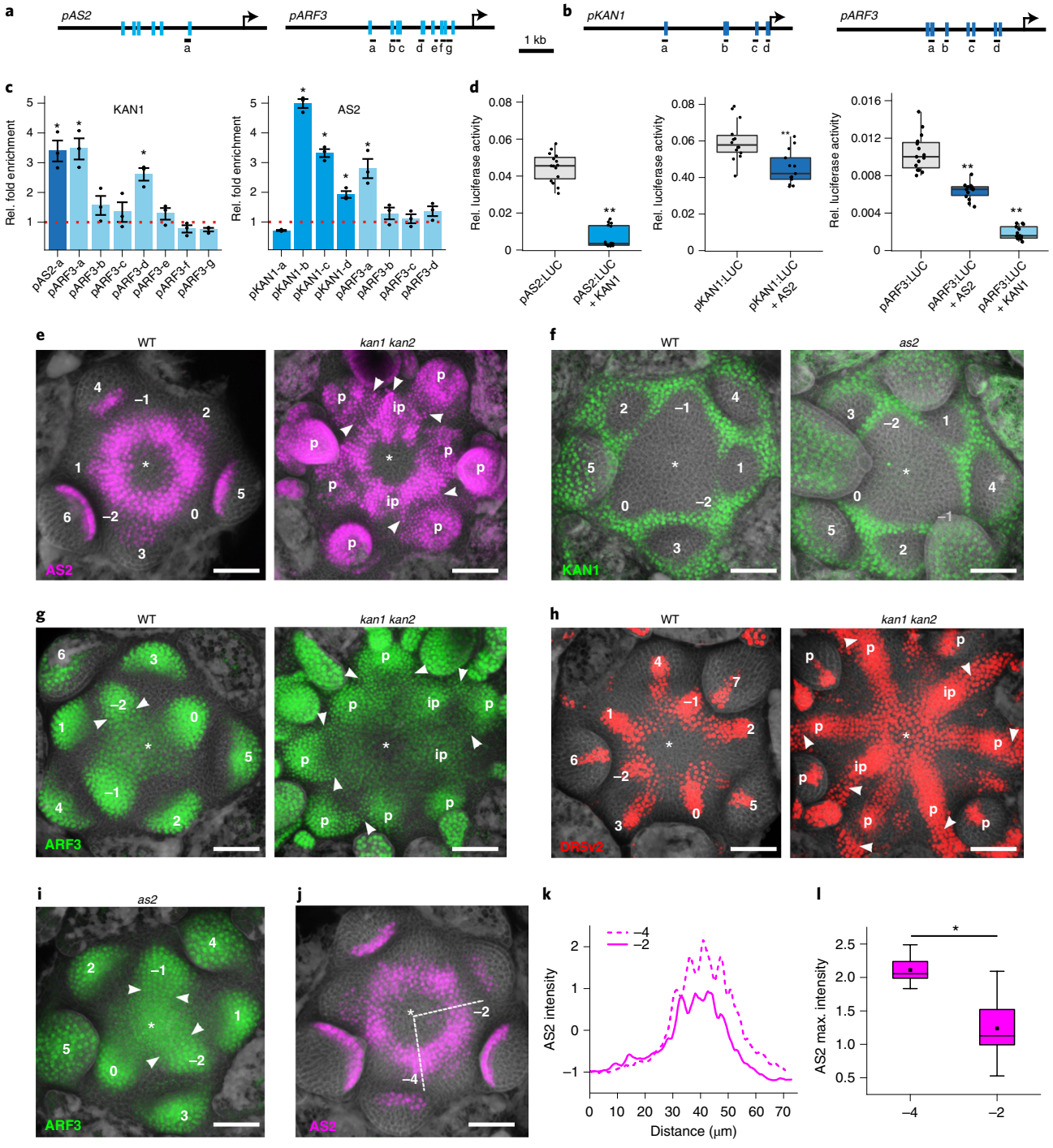

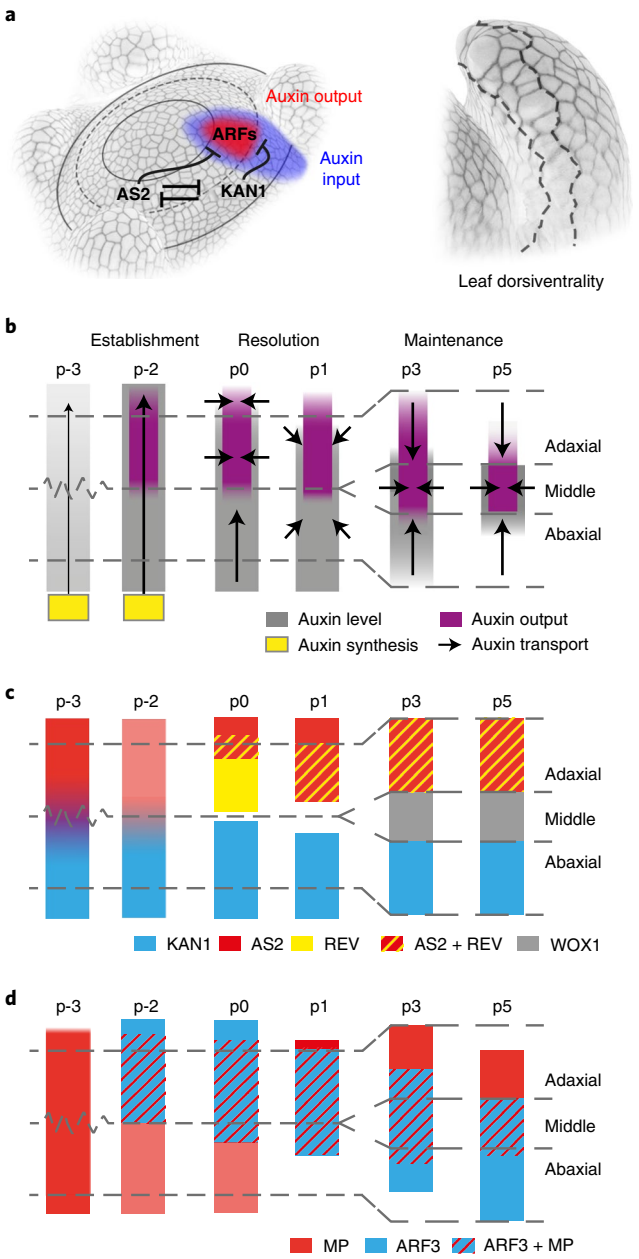

Fig. 8 | Spatial information from the AS2–KAN1 meristem prepattern triggers conversion of a uniform auxin input into an ARF-dependent binary nuclear auxin response output to specify adaxial–abaxial polarity. **a**, Model for the establishment of leaf dorsiventrality. This critical developmental axis is specified by the conversion of a uniform auxin input into an ARF-dependent binary transcriptional auxin response output. The polarized auxin response reflects a prepattern of the mutually antagonistic AS2 and KAN1 transcription factors at the meristem periphery that via direct repressive interactions positions a local induction of ARF3 activity. **b**, Diagram illustrating patterns of auxin input (grey), transcriptional auxin output (purple), PIN1 polarity (arrows) and auxin biosynthesis (yellow) during the establishment (p-2), resolution (p0, p1) and subsequent maintenance of adaxial–abaxial polarity. Please refer to the text, Figs. 2 and 3 and Extended Data Figs. 4 and 6 for more details. **c**, Diagram illustrating this information for the transcription factors AS2 (red), KAN1 (blue), REV (yellow) and WOX1 (grey). Please refer to the text, Figs. 4 and 5 and Extended Data Figs. 3, 8 and 10 for more details. **d**, Diagram illustrating this information for the transcription factors ARF3 (blue) and MP (red). Please refer to the text, Fig. 6 and Extended Data Figs. 9 and 10 for more details.

distribution, directs a switch from a two- into a three-domain configuration. Thus, while organization of the prepattern is uncoupled from auxin-driven dynamics at the meristem, it is the convergence of the latter dynamic signalling input onto the prepattern that coordinates lateral organ formation. This can allow for flexibility in organ initiation while ensuring robustness in subsequent morphogenesis. As auxin also drives growth, it serves as single morphogenic signal that orchestrates distinct, spatially separated responses to coordinate the positioning, emergence and, as shown here, also the patterning of a new organ.

Methods

Plant materials and growth conditions. *Arabidopsis* plants were grown on soil under short-day conditions (8 h light 22 °C and 16 h dark 20 °C) for 30–45 d to image the vegetative shoot apex or for ~60 d to image transition and reproductive stage apices. The following *Arabidopsis* lines were imaged in this study: *pDR5v2:GFP* (ref. [16]); R2D2 which combines *pRPS5a:DII-VENUS* and *pRPS5a:mDII-tdTomato* (ref. [16]); *pin1 pPIN1:PIN1-GFP* (ref. [21]), *ett-3 pARF3:ARF3-GFP* (ref. [34]), *pARF3:ARF3-Ypet* (this study), *pARF3:ARF3-Turquoise* (this study), *pPHV:PHV-YPet, pPHB:PHB-YPet and pREV:REV-YPet* (gifts from J. Long), *pMP:GFP-MP* (gift from B. Möller and D. Weijers), *pin1-7* (ref. [37]), *pYUC4:GFP* and *pYUC1:GFP* (ref. [38]), *pTAAp:GFP-TAA1* (ref. [39]), *pWOX1:GFP* (ref. [32]), *pKAN1:KAN1-YPet* (this study), *pAS2:AS2-VENUS* (this study), *pDR5v2:mTurquoise2* and *ett-22 pDR5v2:mTurquoise2* (this study), *kan1-11 kan2-5 pDR5v2:GFP* (this study), *kan1-11 kan2-5 pARF3:ARF3-Ypet* (this study), *kan1-11 kan2-5 pAS2:AS2-VENUS* (this study), *as2-1 pARF3:ARF3-Turquoise* (this study), *as2-1 pKAN1:KAN1-YPet* (this study) and the double-reporter lines *pKAN1:KAN1-Turquoise pAS2:AS2-VENUS* (this study), *pARF3:ARF3-Turquoise pKAN1:KAN1-YPet* (this study), *pARF3:ARF3-Turquoise pAS2:AS2-VENUS* (this study). All lines are in the Col-0 background, except for the HD-ZIPIII reporter lines, which are in the Ler (*pPHV:PHV-YPet, pPHB:PHB-YPet*) or No (*pREV:REV-YPet*) background.

Construction of transgenic lines. For construction of the *pAS2:AS2-VENUS* transgene, a 3,676 base pair (bp) fragment containing the *AS2* promoter and 5′ UTR was amplified from genomic DNA using primers AS2p_F and AS2p_R and inserted between KpnI and XmaI sites upstream of 3xVenus and OCS terminator in the JM173 T-DNA vector. The 3xVenus region was subsequently swapped using XmaI and BamHI sites for a de novo synthesized (Genscript) translational fusion of the 597 bp AS2 coding sequence to 1xVenus. Supplementary Table 1 gives primer details.

The KAN1 and ARF3 reporter transgenes were generated using GreenGate[40] from the following entry modules for *KAN1*—the *KAN1* promoter containing 4,552 bp upstream of the 5′ UTR (primers KAN1p_F and KAN1p_R), the *KAN1* gene containing the 674 bp 5′ UTR and the 3,725 bp gene body without stop codon (primers KAN1g_F and KAN1g_R) and the *KAN1* terminator containing the endogenous stop codon plus 503 bp downstream (primers KAN13U_F and KAN13U_R); or for *ARF3*—the *ARF3* promoter containing 4,621 bp upstream of the 5′ UTR and the 365 bp 5′ UTR (primers ARF3p_F and ARF3p_R), the *ARF3* gene containing the 3,167 bp gene body without stop codon (primers ARF3g_F and ARF3g_R) and the *ARF3* terminator containing the endogenous stop codon plus 288 bp downstream (primers ARF33U_F and ARF33U_R). Respective entry modules were assembled to generate translational fusions to a 4xGly-Ser and 9xAla linker followed by YPet or to a 9xAla linker and a tandem mTurquoise2 module into a pCAMBIA modified to be compatible with the GreenGate system. Only the *pKAN1:KAN1-YPet* construct was assembled in the pGGZ003 binary vector. To generate dual reporter lines, the *pKAN1:KAN1-Turquoise* transgene was transformed into multiple independent *pAS2:AS2-Venus* lines and, similarly, *pARF3:ARF3-Turquoise* was transformed into multiple independent *pKAN1:KAN1-YPet* and *pAS2:AS2-Venus* reporter lines. The *pDR5v2:GFP* was introduced into the *kan1-11 kan2-5* mutant via crossing. All other mutant reporter lines were generated via transformation.

The estradiol-inducible AS2-YFP line was described previously[26]. For construction of an estradiol-inducible KAN1-YFP line, the *KAN1* coding sequence fused to YFP was first cloned into pENTR/D-TOPO (Invitrogen) and subsequently transferred into pMDC7 using Gateway technologies. To generate the luciferase reporter plasmids, promoter fragments for *KAN1* (3,775 bp), *ARF3* (2,977 bp) and *AS2* (3,697 bp), defined relative to the start codon, were amplified from Col-0 genomic DNA and cloned into *pLucTraP* (ref. [41]) to drive expression of firefly LUCIFERASE. Effector plasmids expressing the KAN1 and AS2 transcription factors were generated by cloning coding sequences, amplified from Col-0 complementary DNA, behind the *2x35S* promoter in *pJIT60* (ref. [41]). Supplementary Table 1 gives primer details.

Live imaging. Plants were dissected and prepared for imaging according to ref. [42]. Dissected plants were grown in vitro in ref. [13], except that no extra cytokinins or IAA was added. Apices were imaged with an upright confocal laser-scanning

microscope (Leica TCS SP5 or SP8) using LAS X Life Science software (Leica) with ×63 or ×40, long working distance, water-immersion objectives. Cell walls were stained with 0.1% propidium iodide (PI; Sigma–Aldrich) for 3–5 min. The following excitation (ex) and emission (em) wavelengths were used: for Venus/YPets—488 nm or 514 nm (ex) and 505–545 nm or 519–545 nm (em); for GFP—488 nm (ex) and 500–540 nm (em); for PI—488 nm or 514 nm (ex) and 600–656 nm (em); for R2D2 in a sequential mode—514 nm (ex) and 524–540 nm (em) for DII-Venus and 552 nm (ex) and 571–700 nm (em) for mDII-tdTomato[16]; for R2D2 in a nonsequential mode—488 nm (ex) and 505–545 nm (em) for DII-Venus, 488 nm (ex) and 600–656 nm (em) for PI; for *pKAN1:KAN1-Turquoise pAS2:AS2-VENUS* lines in sequential mode—514 nm (ex) and 520–550 nm (em) for Venus, 514 nm (ex) and 600–665 nm (em) for PI, 448 nm (ex) and 450–490 nm (em) for *Turquoise*. Scanning speed was set at 200 or 400 Hz with 512 × 512 or 1,024 × 1,024 pixel^2 frames. The pinhole was set at 1AE. The step size in *z*-stacks was 0.08–0.5 µm. Images were collected at 12 or 16 bits. Shoot apices were imaged at approximately the same time of day either once (0 h) or over multiple consecutive days in a 24 h time-lapse series. Between imaging, dissected plants were kept under short-day conditions.

Cell fate tracking. To connect patterns of gene expression to cell fate decisions, cell lineages analysis was performed on all apices reported in this study. To this end, time-lapse confocal *z*-stacks of growing apices with PI-stained cell walls were processed using MorphoGraphX[19]. The PI signal from a depth of 1–6 µm, corresponding to the L1 cell layer, was projected onto the apex surface (for details see ref. [19]), to generate projections from which cell lineages were manually identified. Cells of adaxial, middle and abaxial identity were defined at the most advanced leaf primordium stage (p5–p7) using primordium geometry and the position of the first trichome as morphological landmarks. In agreement with genetic markers, the middle domain is two cells wide at the primordium margins and, depending on the primordium stage, two to three cells wide at the primordium tip where it includes the first trichome and one to two abaxially adjacent cells (Fig. 1a,d,e). The adaxial domain extends from the middle domain to the boundary between the primordium and the meristem, apparent as a sharp crease. The abaxial domain extends from the middle domain to the boundary between the primordium and the future suppressed stem internode. Progenitors of cells with adaxial, middle and abaxial identity at p5–p7 were manually traced backwards through earlier points in the time-lapse series. Progenitors at p-3, p-4 and p-5 in *pAS2:AS2-VENUS* lines were traced back from whole primordia at the p2 to p4 stage.

Analysis of gene expression patterns. Longitudinal median sections (~5 µm) through successive incipient and visible leaf primordia were generated optically using MorphoGraphX[19] from *z*-stacks containing either the PI signal alone or in combination with reporter gene expression. To associate patterns of gene expression with cell fates, individual cells recognized at top view were correlated to corresponding cells in sections. For all single reporter lines at least five leaf primordia of each stage were analysed from five to eight apices. For the dual reporter lines, apices from up to five independent T1 transformants were analysed. Data were reproducible across apices and representative examples are shown.

Signal intensities along the apex radius were obtained using ImageJ (https://imagej.nih.gov/ij/). First, original confocal *z*-stacks were converted into two-dimensional (2D) grey-scale *z*-projections (32 bits) by summing the signal from all slices in the stack. Next, using the Plot Profile tool, pixel intensity was measured along a slice 15 µm wide extending from the meristem centre across leaf primordia. Positions of adaxial and abaxial cells were identified by reverse lineage tracing and marked accordingly in the plots. *pDR5v2:Turquoise* signal intensities in wild type and *arf3* incipient primordia were quantified from 2D grey-scale *z*-projections. Signal at a depth of 0–5 µm below the surface, corresponding to the L1 layer, was projected onto the apex surface using MorphoGraphX[19] and signal intensity measured in ImageJ (https://imagej.nih.gov/ij/) with the Point tool in five random cells in p-2, p-1 and p0 primordia. Plots and statistical tests were generated in Origin (OriginLab Corporation).

PIN1 polarity and the resulting direction of polar auxin transport were defined from quantitative projections onto the apex surface of *pPIN1:PIN1-GFP* signal in the L1 cell layer across a depth of 5 µm below the surface using MorphoGraphX[19]. PIN1 polarity in each cell was manually recognized on a plane of view orthogonal to the respective analysed surface, on the basis of locally higher PIN1 signal intensity forming an arc around cell corners (Supplementary Fig. 1a–c; see also ref. [18]). For clarity, the quantitative projections in Fig. 3b,c are shown with 60–65% reduction of transparency (Adobe Photoshop).

NPA treatment. After obtaining the 0 h time point image, apices were treated with 100 µl of 100 µM NPA in 0.1% DMSO or mock (0.1% DMSO) for 24 h. The treatments were repeated after each round of imaging at 24 and 48 h. Two independent experiments were performed with similar results.

Chromatin immunoprecipitation. For chromatin immunoprecipitation (ChIP) analyses, 9-day-old estratradiol-inducible AS2-YFP or KAN1-YFP seedlings grown under long day conditions (16 h light/8 h dark) on ½ Murashige and Skoog media with 1% sucrose were submerged in a solution containing 20 µM ß-estratradiol and 0.01% Silwet for 10 min. At 24 h after inductions, whole seedlings were harvested and ChIP assays performed with anti-GFP (ab290, Abcam) as previously described[26]. ChIP (IP) and input (IN) DNA samples were quantified by quantitative PCR (qPCR) using Lunar qPCR mix (NEB). Relative enrichments were calculated as the ratio of % IP/IN at the promoter fragments of interest over % IP/IN at the *ACT2* negative control. All experiments were performed in three biological replicates and Student's *t*-test was used to calculate statistical significance. Promoter fragments assayed by ChIP were selected on the basis of the occurrence of predicted AS2 or KAN1 binding motifs identified using FIMO (https://meme-suite.org/meme/tools/fimo). Plots were generated using the ggplot2 package in Rstudio. See Supplementary Table 2 for primer details.

Transient luciferase assay in *Arabidopsis* protoplasts. Cell culture protoplasts from *Arabidopsis thaliana* were isolated and transfected as previously described[43]. The protoplasts were cotransfected with 2 µg each of reporter (*pLucTraP)* and effector (*pJIT60*) plasmid along with 2 µg of *pGL4.70* plasmid expressing *Renilla* Luciferase from the *2x35S* promoter as internal control. Transfected protoplasts were incubated overnight in the dark and then processed and analysed using the Dual-Luciferase Reporter Assay System (Promega) as previously described[41]. Luminescence was measured using the Tecan's Infinite F200 plate reader. Relative luciferase activity was calculated as Firefly over *Renilla* Luciferase activity. At least 13 biological replicates across three independent experiments were performed for each transcription factor–promoter interaction. Statistical significance was calculated using Student's *t*-test. Plots were generated using the ggplot2 package in Rstudio.

Reporting Summary. Further information on research design is available in the Nature Research Reporting Summary linked to this article.

Data availability

Data for the current study are available from the paper and its Supplementary Information or from the corresponding author on reasonable request.

Received: 19 March 2021; Accepted: 11 February 2022;
Published online: 22 March 2022

References

1. Waites, R. & Hudson, A. phantastica: a gene required for dorsoventrality of leaves in *Antirrhinum majus*. *Development* **121**, 2143–2154 (1995).
2. Whitewoods, C. D. et al. Evolution of carnivorous traps from planar leaves through simple shifts in gene expression. *Science* **367**, 91–96 (2020).
3. Kuhlemeier, C. & Timmermans, M. C. The Sussex signal: insights into leaf dorsiventrality. *Development* **143**, 3230–3237 (2016).
4. Chitwood, D. H. et al. Pattern formation via small RNA mobility. *Genes Dev.* **23**, 549–554 (2009).
5. Skopelitis, D. S., Benkovics, A. H., Husbands, A. Y. & Timmermans, M. C. P. Boundary formation through a direct threshold-based readout of mobile small RNA gradients. *Dev. Cell* **43**, 265–273 (2017).
6. Kuhlemeier, C. Phyllotaxis. *Trends Plant Sci.* **12**, 143–150 (2007).
7. Echevin, E. et al. Growth and biomechanics of shoot organs. *J. Exp. Bot.* **70**, 3573–3585 (2019).
8. Qi, J. et al. Auxin depletion from leaf primordia contributes to organ patterning. *Proc. Natl Acad. Sci. USA* **111**, 18769–18774 (2014).
9. Sussex, I. Experiments on the cause of dorsiventrality in leaves. *Nature* **167**, 651–652 (1951).
10. Reinhardt, D., Frenz, M., Mandel, T. & Kuhlemeier, C. Microsurgical and laser ablation analysis of leaf positioning and dorsoventral patterning in tomato. *Development* **132**, 15–26 (2005).
11. Caggiano, M. P. et al. Cell type boundaries organize plant development. *eLife* **6**, e27421 (2017).
12. Bhatia, N., Ahl, H., Jonsson, H. & Heisler, M. G. Quantitative analysis of auxin sensing in leaf primordia argues against proposed role in regulating leaf dorsoventrality. *eLife* **8**, e39298 (2019).
13. Burian, A., Barbier de Reuille, P. & Kuhlemeier, C. Patterns of stem cell divisions contribute to plant longevity. *Curr. Biol.* **26**, 1385–1394 (2016).
14. Galvan-Ampudia, C. S. et al. Temporal integration of auxin information for the regulation of patterning. *eLife* **9**, e55832 (2020).
15. Nakata, M. et al. Roles of the middle domain-specific WUSCHEL-RELATED HOMEOBOX genes in early development of leaves in *Arabidopsis*. *Plant Cell* **24**, 519–535 (2012).
16. Liao, C. Y. et al. Reporters for sensitive and quantitative measurement of auxin response. *Nat. Methods* **12**, 207–210 (2015).
17. Benková, E. et al. Local, efflux-dependent auxin gradients as a common module for plant organ formation. *Cell* **115**, 591–602 (2003).
18. Heisler, M. G. et al. Patterns of auxin transport and gene expression during primordium development revealed by live imaging of the *Arabidopsis* inflorescence meristem. *Curr. Biol.* **15**, 1899–1911 (2005).

19. Barbier de Reuille, P. et al. MorphoGraphX: a platform for quantifying morphogenesis in 4D. *eLife* **4**, 05864 (2015).
20. Bhatia, N. et al. Auxin acts through MONOPTEROS to regulate plant cell polarity and pattern phyllotaxis. *Curr. Biol.* **26**, 3202–3208 (2016).
21. Kierzkowski, D., Lenhard, M., Smith, R. & Kuhlemeier, C. Interaction between meristem tissue layers controls phyllotaxis. *Dev. Cell* **26**, 616–628 (2013).
22. Wang, Q., Kohlen, W., Rossmann, S., Vernoux, T. & Theres, K. Auxin depletion from the leaf axil conditions competence for axillary meristem formation in *Arabidopsis* and tomato. *Plant Cell* **26**, 2068–2079 (2014).
23. Huang, T. et al. *Arabidopsis* KANADI1 acts as a transcriptional repressor by interacting with a specific cis-element and regulates auxin biosynthesis, transport, and signaling in opposition to HD-ZIPIII factors. *Plant Cell* **26**, 246–262 (2014).
24. Merelo, P. et al. Genome-wide identification of KANADI1 target genes. *PLoS ONE* **8**, e77341 (2013).
25. Yu, T. et al. Dynamic patterns of gene expression during leaf initiation. *J. Genet. Genomics* **44**, 599–601 (2017).
26. Husbands, A. Y., Benkovics, A. H., Nogueira, F. T., Lodha, M. & Timmermans, M. C. The ASYMMETRIC LEAVES complex employs multiple modes of regulation to affect adaxial–abaxial patterning and leaf complexity. *Plant Cell* **27**, 3321–3335 (2015).
27. Wu et al. KANADI1 regulates adaxial–abaxial polarity in *Arabidopsis* by directly repressing the transcription of *ASYMMETRIC LEAVES2*. *Proc. Natl Acad. Sci. USA* **105**, 16392–16397 (2008).
28. Ram, H. et al. An integrated analysis of cell-type specific gene expression reveals genes regulated by REVOLUTA and KANADI1 in the *Arabidopsis* shoot apical meristem. *PLoS Genet.* **16**, e1008661 (2020).
29. Simonini, S., Bencivenga, S., Trick, M. & Ostergaard, L. Auxin-Induced modulation of ETTIN activity orchestrates gene expression in *Arabidopsis*. *Plant Cell* **29**, 1864–1882 (2017).
30. Chung, Y. et al. Auxin response factors promote organogenesis by chromatin-mediated repression of the pluripotency gene SHOOTMERISTEMLESS. *Nat. Commun.* **10**, 886 (2019).
31. Pekker, I., Alvarez, J. P. & Eshed, Y. Auxin response factors mediate *Arabidopsis* organ asymmetry via modulation of KANADI activity. *Plant Cell* **17**, 2899–2910 (2005).
32. Guan, C. et al. Spatial auxin signaling controls leaf flattening in *Arabidopsis*. *Curr. Biol.* **27**, 2940–2950 (2017).
33. Zhao, F. & Traas, J. Stable establishment of organ polarity occurs several plastochrons before primordium outgrowth in *Arabidopsis*. *Development* **148**, dev198820 (2021).
34. Simonini, S. et al. A noncanonical auxin-sensing mechanism is required for organ morphogenesis in *Arabidopsis*. *Genes Dev.* **30**, 2286–2296 (2016).
35. Guan, C., Du, F., Xiong, Y. & Jiao, Y. The 35S promoter-driven mDII auxin control sensor is uniformly distributed in leaf primordia. *J. Integr. Plant Biol.* **61**, 1114–1120 (2019).
36. Wolpert, L., Tickle, C. & Arias, A. M. *Principles of Development* (Oxford Univ. Press, 2015).
37. Smith, R. S. et al. A plausible model of phyllotaxis. *Proc. Natl Acad. Sci. USA* **103**, 1301–1306 (2006).
38. Robert, H. S. et al. Local auxin sources orient the apical–basal axis in *Arabidopsis* embryos. *Curr. Biol.* **23**, 2506–2512 (2013).
39. Stepanova, A. N. et al. TAA1-mediated auxin biosynthesis is essential for hormone crosstalk and plant development. *Cell* **133**, 177–191 (2008).
40. Lampropoulos, A. et al. GreenGate—a novel, versatile, and efficient cloning system for plant transgenesis. *PLoS ONE* **8**, e83043 (2013).
41. Lau, S., De Smet, I., Kolb, M., Meinhardt, H. & Jurgens, G. Auxin triggers a genetic switch. *Nat. Cell Biol.* **13**, 611–615 (2011).
42. Hamant, O., Das, P. & Burian, A. Time-lapse imaging of developing shoot meristems using a confocal laser scanning microscope. *Methods Mol. Biol.* **1992**, 257–268 (2019).
43. Mehlhorn, D. G., Wallmeroth, N., Berendzen, K. W. & Grefen, C. in *The Plant Endoplasmic Reticulum: Methods and Protocols* (eds Hawes, C. & Kriechbaumer, V.) 139–158 (Springer, 2018).

Acknowledgements

We thank our colleagues in Tübingen and Katowice who have contributed ideas and thoughtful comments to the manuscript. We also thank C. Kuhlemeier for constructive discussions, D. Vranjkovic and A. Feller for technical assistance, R. Smith and A.-L. Routier-Kierzkowska for their help with MorphoGraphX, C. Brancato and K. Berendzen for protoplast production, G. Jürgens for sharing the *pLucTraP* and *pJIT60* plasmids and C. Kuhlemeier, L. Ostergaard, Y. Jiao, J. Long, B. Möller and D. Weijers for sharing materials. A.B. and M.R-S are supported by a research grant SONATA BIS 6 (2016/22/E/NZ3/00342) from the National Science Centre, Poland. Work on leaf polarity in M.T.'s laboratory is supported through an Alexander von Humboldt Professorship.

Author contributions

A.B., G.P. and M.T. designed the project and experiments. K.N. performed the ChIP analyses and S.M. performed the transient expression assays. All other experiments and data analyses were performed by A.B. and G.P. with help from M.R.-S. The manuscript was written by A.B., G.P. and M.T.

Competing interests

The authors declare no competing interests.

Additional information

Extended data is available for this paper at https://doi.org/10.1038/s41477-022-01111-3.

Supplementary information The online version contains supplementary material available at https://doi.org/10.1038/s41477-022-01111-3.

Correspondence and requests for materials should be addressed to Marja C. P. Timmermans.

Peer review information *Nature Plants* thanks Lars Østergaard, Dolf Weijers, José Luis Micol and the other, anonymous, reviewer(s) for their contribution to the peer review of this work.

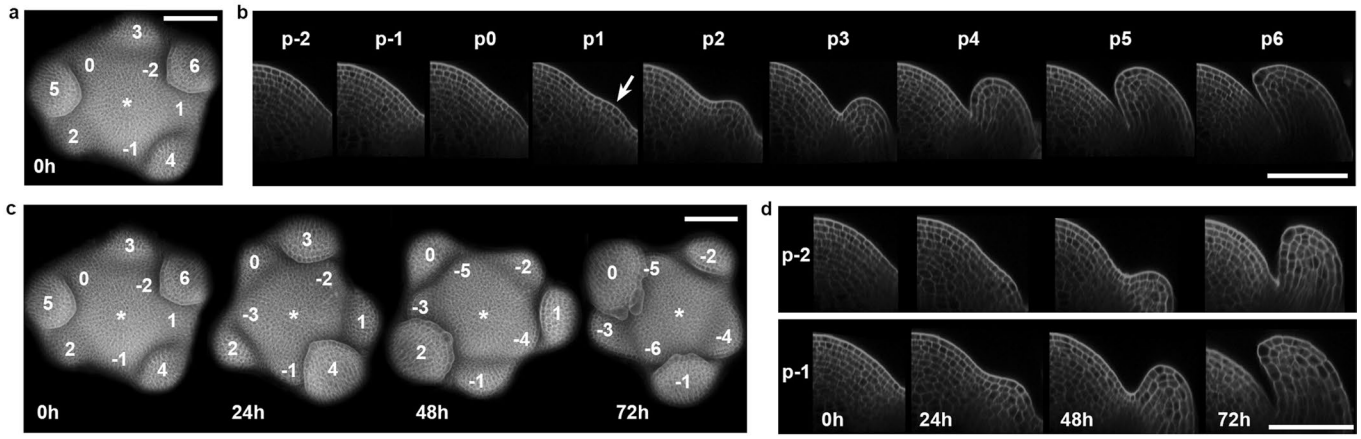

Extended Data Fig. 1 | The spatial sequence of leaf primordia at the shoot apex reflects primordium development in time. a-b, A representative sequence of leaf primordium stages (**b**) at the shoot apex (**a**). Leaf primordia are numbered relative to the first bulging primordium (p1), numbers <1 indicate incipient primordia. Arrow, the first bulging primordium. **c-d**, Time-lapse series of the shoot apex (**c**) showing a temporal sequence of leaf development. Development of p-2 and p-1 primordia over 3 days (**d**) mirrors consecutive leaf primordia at the meristem. The p-2 and p-1 incipient primordia after 24 h attain developmental stages corresponding to p1 and p2, respectively (**b**), indicating a plastochron under the growth conditions used is approximately 8 h. Primordium stage numbers are maintained from the first time point. (**a, c**) Top views of the meristems. (**b, d**) Optical longitudinal sections through leaf primordia. Cell walls were stained by PI. Scale bars, 50 μm. Representative images from n = 6 apices **(a, c**) and n = 6 primordia (**b, d**) are shown.

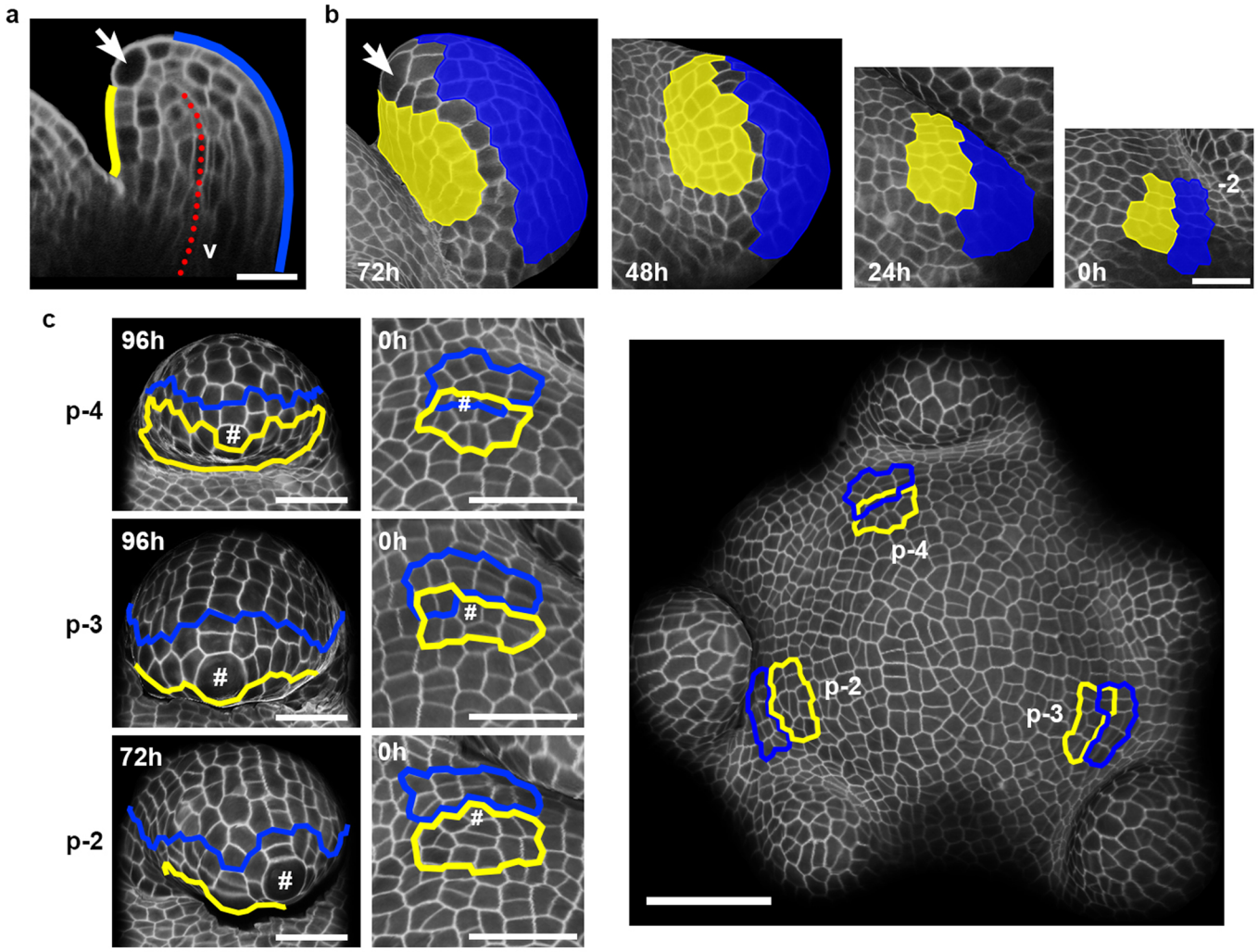

d

stage	adaxial	boundary	abaxial	n
p-3	10.6 ± 1.5	4.6 ± 0.5	12.4 ± 2.0	8
p-2	13.5 ± 2.0	5.2 ± 0.6	15.8 ± 2.9	20
p-1	15.5 ± 3.5	5.5 ± 0.8	16.5 ± 4.2	15
p0	20.2 ± 3.2	6.1 ± 0.8	19.9 ± 3.5	17
p1	23.3 ± 2.5	6.9 ± 0.8	22.5 ± 3.5	16

Extended Data Fig. 2 | The adaxial–abaxial boundary is specified prior to primordium emergence. a, Optical longitudinal section of a p5 leaf primordium illustrating positions of the adaxial (yellow) and abaxial (blue) domains relative to the first forming trichome (arrow). Domains were discerned based on patterns of reporter gene expression (Fig. 1a). **b**, Backward tracing of cell lineages from the adaxial (yellow), middle, and abaxial (blue) domains of a p5 primordium (72 h) to their progenitors at p-2 (0 h) shows the adaxial–abaxial boundary is specified prior to primordium emergence at p-2, while the middle domain forms several plastochrons later from cells at the adaxial–abaxial boundary. **c**, Backward tracing of cell lineages from the adaxial (yellow), middle, and abaxial (blue) domains of p5 (top), p6 (middle) (96 h), and p6 (bottom) (72 h) primordia to their progenitors at p-4, p-3, and p-2 (0 h), respectively, reveals that the adaxial–abaxial boundary is not defined at p-4 or p-3 when most progenitors along the future boundary contribute both adaxial and abaxial daughter cells (for quantification, see Fig. 1b). However, at p-2, the adaxial–abaxial boundary for nearly all primordia analysed is stably defined and undetermined cells giving rise to both adaxial and abaxial daughters are rarely observed. **d**, The number (mean ± SD) of cells corresponding to the adaxial and abaxial domain, as well as along the width of the (future) adaxial–abaxial boundary, at p-3 to p1; n, the number of primordia analysed. Yellow, adaxial; blue, abaxial; red dotted line (v), midvein; arrow or hash, the first forming trichome. Cell walls were stained by propidium iodide (PI). Scale bars, 20 μm (**a,b,c** left panels) and 50 μm (**c** right panel). Representative examples from n = 20 primordia (**a-b**), or n is as indicated in panel **d** (**c**), are shown.

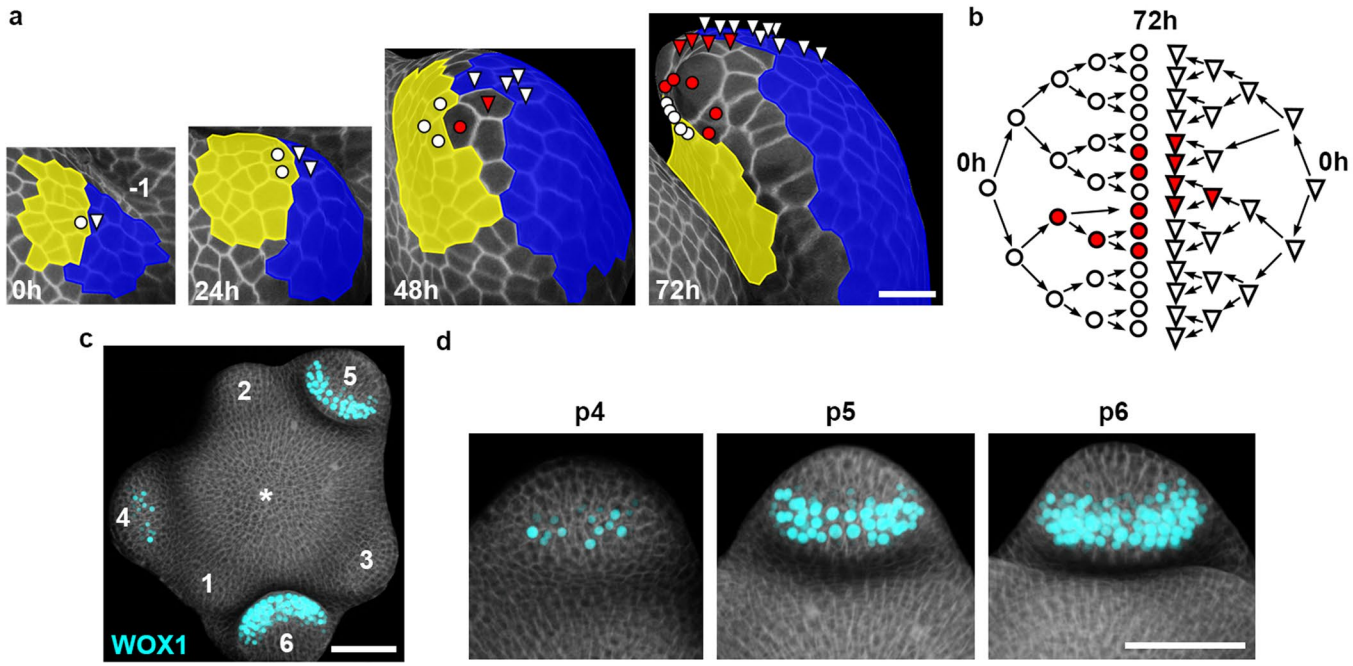

Extended Data Fig. 3 | The middle domain emerges gradually from the adaxial–abaxial boundary after primordium emergence. a-b, Cell lineage tracing of adaxial (circle) and abaxial (triangle) leaf founder cells from p-1 to p6 (**a**) and the resulting cell lineage graph (**b**) show that the middle domain derives from both adaxial and abaxial cells at the boundary that are respecified to middle domain identity (red) around p4 (48 h). The number of cells at the middle domain has increased at 72 h. White, adaxial or abaxial; red, middle identity; circle, adaxial and triangle, abaxial founder cells and their respective derivatives. **c-d**, The pattern of *pWOX1:GFP* expression at the shoot apex shows *WOX1* transcription marks the emerging middle domain. (**c**) Top view of the meristem. (**d**) Front view of select leaf primordia. Cell walls were stained by PI. Scale bars, 20 μm (**a**), 50 μm (**c-d**). Representative examples from n = 24 primordia (**a, b**), n = 5 apices (**c**), and n = 5 primordia per stage (**d**), are shown.

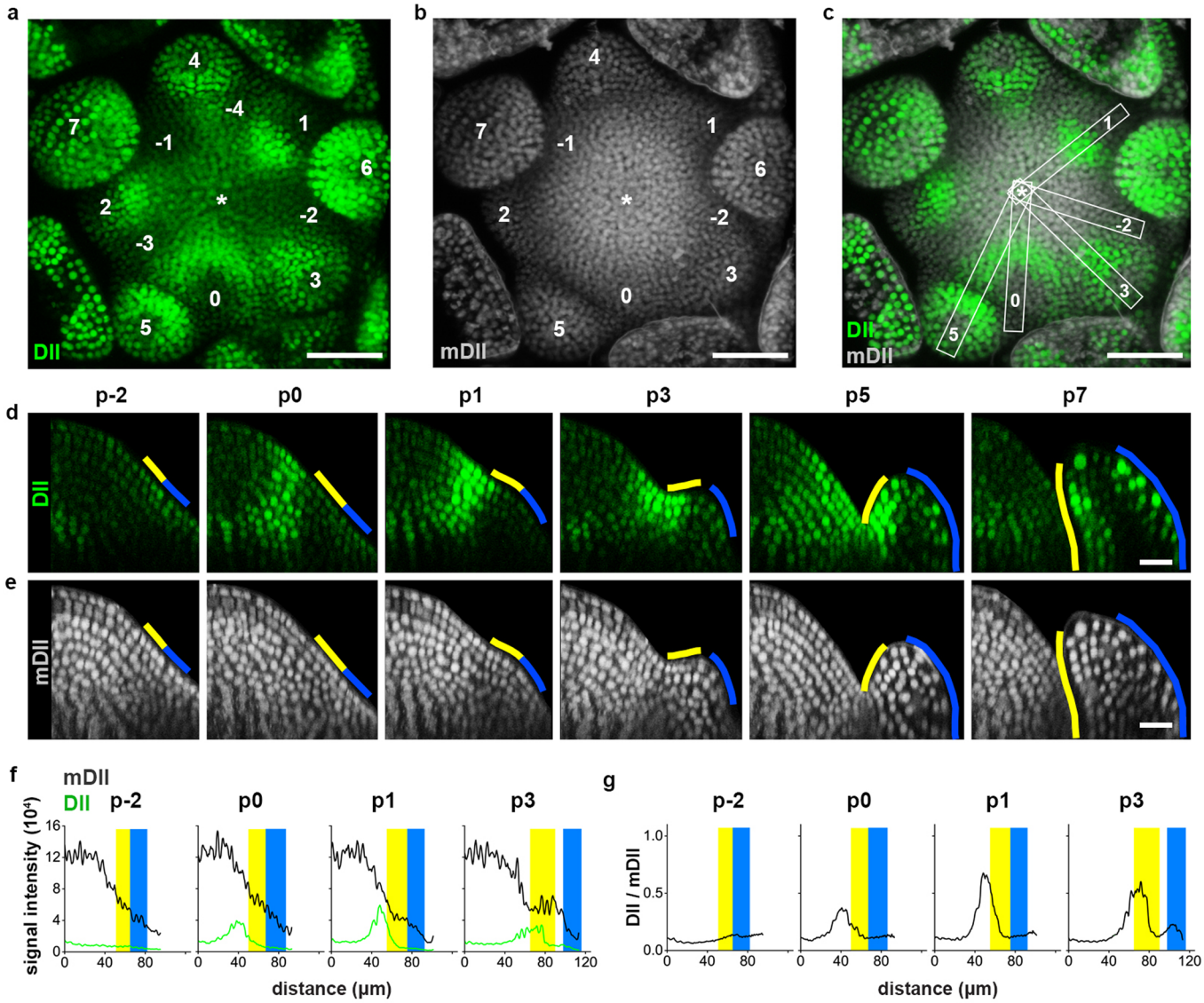

Extended Data Fig. 4 | Auxin input patterns change dynamically during primordium emergence. a-e, Expression patterns for *DII-Venus* (**a**), *mDII-tdTomato* (**b**), or both (**c**) at the shoot apex show auxin levels are uniformly high at p-2 incipient primordia but are gradually depleted (increasing DII relatively to mDII signal intensities) first from the adaxial and subsequently from the abaxial side following primordium emergence. (**a–c**) Top views of the meristem. (**d, e**) Optical longitudinal sections through leaf primordia. Yellow, adaxial; blue, abaxial; asterisks, meristem centre. The middle domain (not outlined) gradually emerges from the adaxial–abaxial boundary. **f-g**, Signal intensities of *DII-Venus* (green) and *mDII-tdTomato* (dark grey) (**f**) or the DII/mDII signal intensity ratio (**g**) measured along the apex radius at respective leaf primordium stages (**c**) illustrate the gradual quantitative depletion of auxin during primordium development. The distance 0 µm corresponds with the meristem centre. Positions of adaxial and abaxial identity discerned from backward lineage tracing are indicated by yellow and blue segments, respectively. Scale bars, 50 µm (**a–c**), 20 µm (**d, e**). Representative data from n = 12 apices (**a–c**), n = 6 primordia per developmental stage (**d-e**), and n = 5 primordia per developmental stage (**f,g**) is shown.

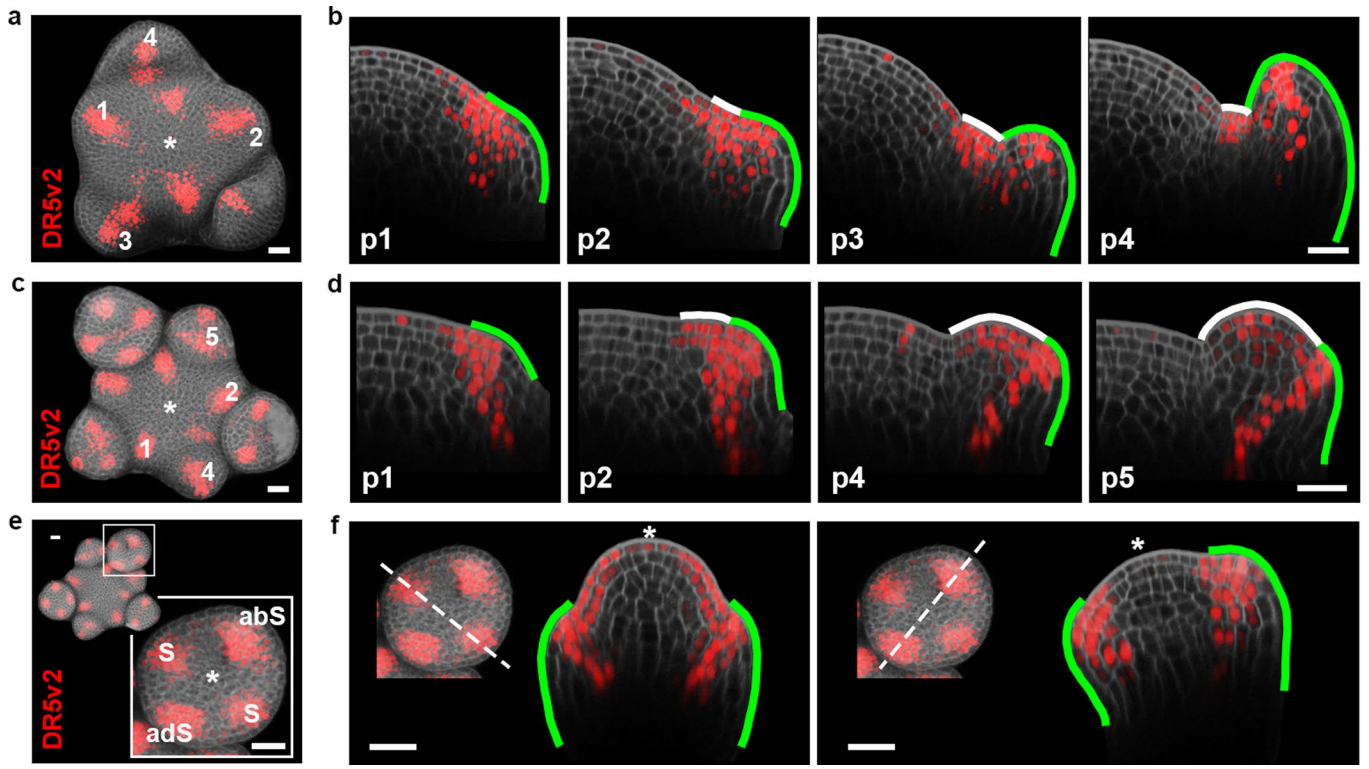

Extended Data Fig. 5 | An asymmetric auxin response output is specific for dorsiventral organs. a–f, The patterns of *pDR5v2:GFP* expression at the shoot apex during the transition to flowering (**a, b**) and at the reproductive phase (**c–f**) show dorsiventral organs (green) derive from meristem sites marked by a polarized transcriptional auxin response output. Early primordia of cauline leaves (**b**, p1, p2), bracts (**d**, p1, p2), and sepals (**f**). Subsequently, the auxin response output shifts to the middle domain and marks the primordium tip and underlying future midvein (**b**, p3, p4; **d**, p4, p5). In contrast, axillary (**b**) and floral (**d**) meristems (white), originate from sites marked by a uniform nuclear auxin response. (**a, c, e**) Meristem top views. (**b, d, f**) Optical longitudinal sections through primordia. Insets show the position of the optical section through the flower meristem (**f**). Green, dorsiventral leaf-like primordium; white, axillary or flower meristem; asterisks, shoot apical or flower meristem centre. Cell walls were stained by PI. Scale bars, 20 μm. Representative images from n = 5 (**a**) or n = 6 (**c, e**) meristems, and n = 5 (**b**) or n = 6 (**d, f**) primordia per developmental stage are shown.

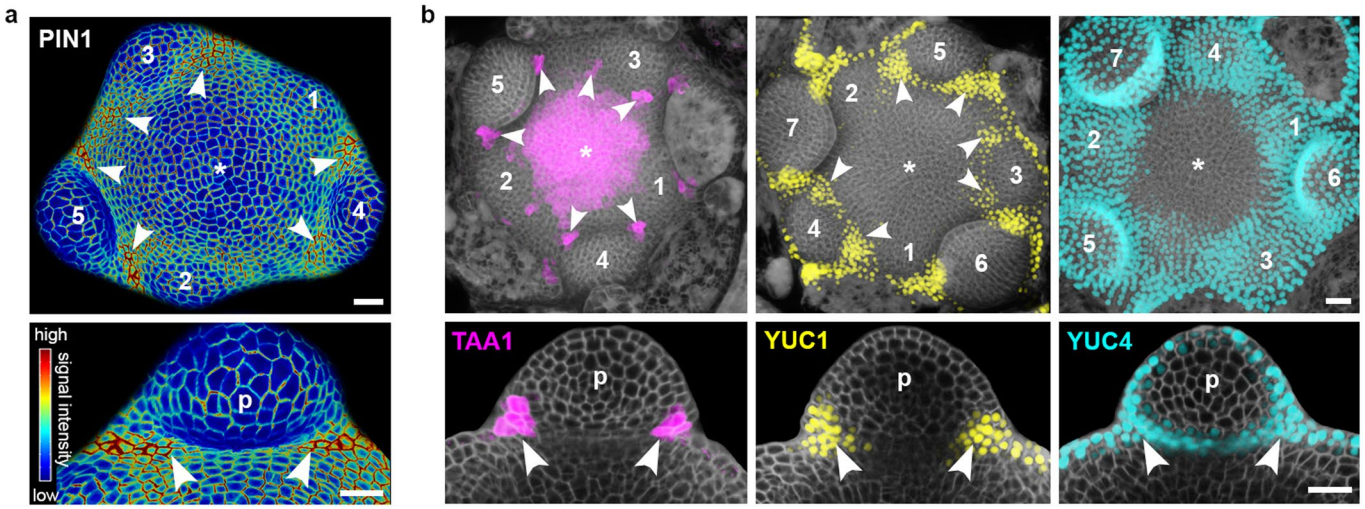

Extended Data Fig. 6 | Strong PIN1 expression is associated with sites of auxin biosynthesis. a-b, Quantitative projection of *pPIN1:PIN1-GFP* signal at the meristem L1 (**a**) and patterns of *pTAA1:TAA-GFP*, *pYUC1:GFP*, and *pYUC4:GFP* expression (**b**) at the shoot apex show PIN1 upregulation coincident with predicted sites of auxin biosynthesis (arrowheads). Top views of meristems (**a, b**, upper panels) or leaf primordium (**a**, lower panel), and optical transverse sections through select leaf primordia (**b**, lower panels). Arrowheads, flanks of primordium-meristem boundaries where local PIN1 upregulation coincides with sites of auxin biosynthesis deduced from co-expression of TAA1, YUC1, and YUC4. Cell walls were stained by PI. Asterisks, meristem centre; p, leaf primordium. Scale bars, 20 µm. Representative images from n = 6 apices (**a**), and n = 10 apices per line (**b**) are shown.

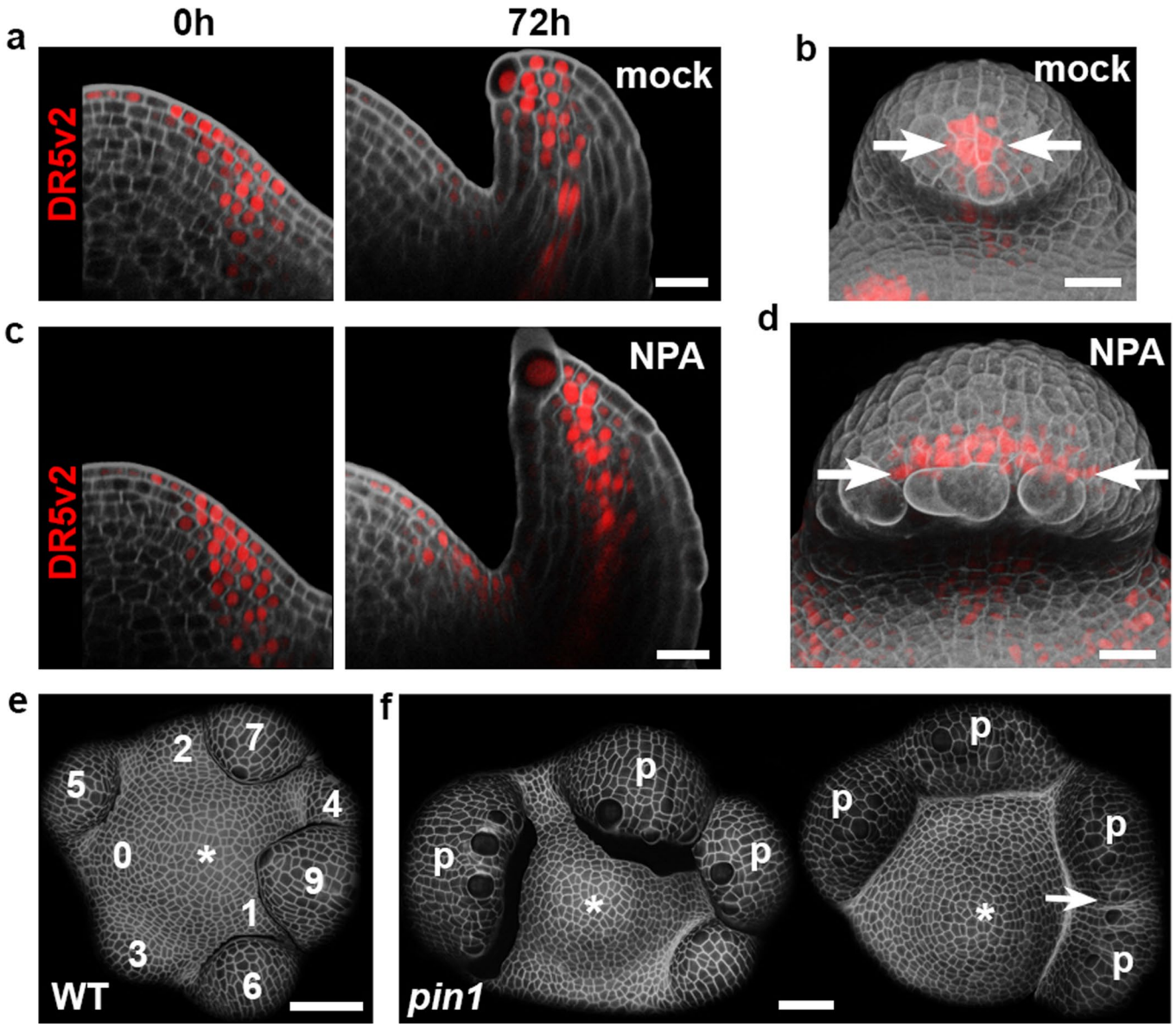

Extended Data Fig. 7 | PIN1-mediated polar auxin transport constrains auxin-induced gene expression laterally. a–d, Time-lapse series of representative p-1 leaf primordia without or with application of 100 µM NPA at 0 h (**a, c**) shows perturbation of PIN1-mediated polar auxin transport does not block the shift in auxin-induced gene expression (DR5v2) from the adaxial side at p-1 (0 h) to the middle domain 72 h later. Instead, in comparison to mock-treated primordia (**b**), NPA-treated primordia are wider and show a lateral expansion of the DR5v2 expression domain (arrows) (**d**). (**a, c**) Optical longitudinal sections and (**b, d**) top views of select leaf primordia. **e-f**, Wild type (**e**) and *pin1* mutant (**f**) shoot apices showing *pin1* leaf primordia are comparatively wider and occasionally laterally fused (arrow). Note also the irregular phyllotaxy of *pin1* apices (**f**). Cell walls were stained by PI. Asterisks, meristem centre; p, leaf primordium. Scale bars, 20 µm (**a–d**), 50 µm (**e-f**). Representative data from n = 6 primordia per treatment (**a–d**), and n = 12 apices per line (**e-f**) is shown.

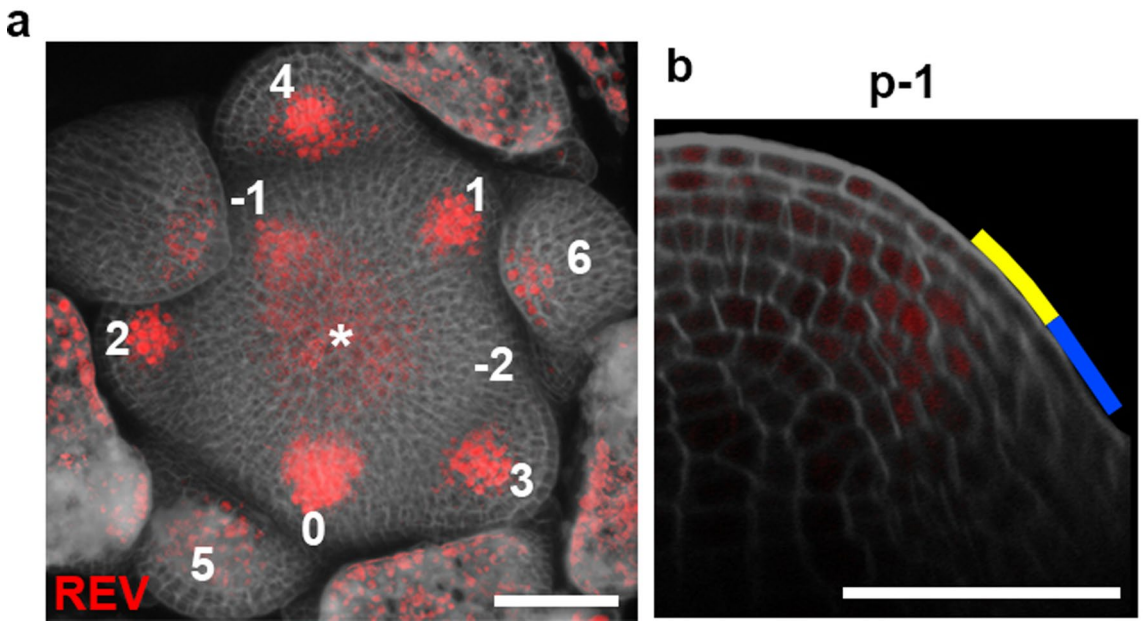

Extended Data Fig. 8 | REV expression before p0 is limited to inner tissues. The pattern of *pREV:REV-YPet* expression at the shoot apex showing weak internal REV accumulation just apical to p-1. Top view of the meristem (**a**) and optical longitudinal section at p-1 (**b**). Progenitors for the adaxial (yellow), abaxial (blue), and middle (not present at this developmental stage) domains were discerned by backward lineage tracing. Asterisks, meristem centre. Cell walls were stained by PI. Scale bars, 50 μm. Representative data from n = 7 apices (**a**), and n = 5 primordia (**b**) is shown.

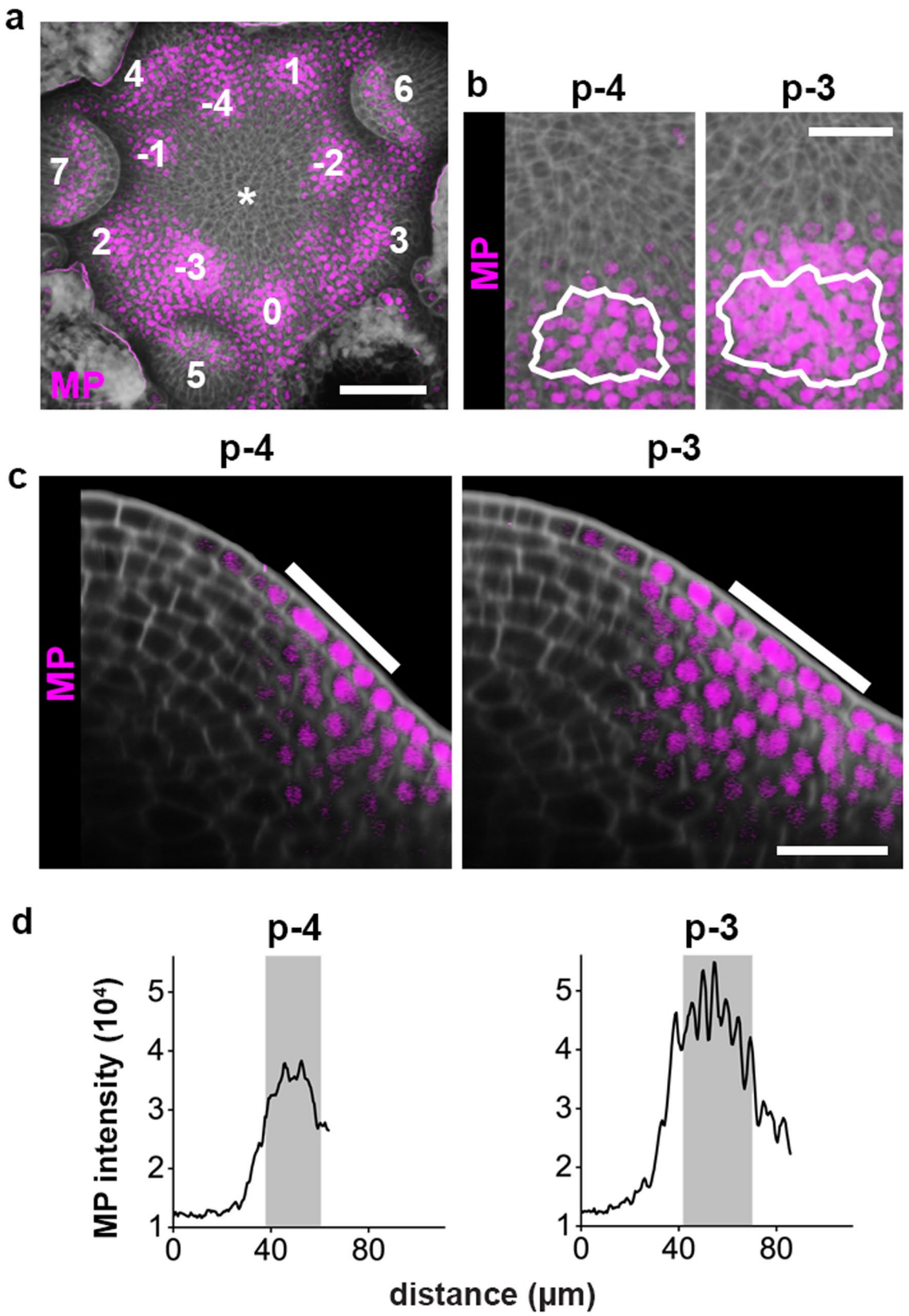

Extended Data Fig. 9 | Incipient leaf primordia up to p-2 show a near uniform level of MP expression. a–c, Representative pattern of *pMP:GFP-MP* expression at the shoot apex showing a mostly uniform accumulation of MP at p-4 and p-3 incipient primordia. (**a, b**) Top view of the meristem (**a**) and leaf primordia (**b**). (**c**) Optical longitudinal sections at p-4 and p-3 leaf primordia. White, incipient primordium; asterisks, meristem centre. Cell walls were stained by PI. Scale bars, 50 µm (**a**), 20 µm (**b, c**). **d**, GFP-MP signal intensities measured along the apex radius at indicated primordium stages illustrate the near uniform level of MP accumulation. The distance 0 µm corresponds with the meristem centre. Positions of incipient primordia discerned by lineage tracing are marked in grey. Representative data from n = 10 apices (**a**) and n = 5 primordia per developmental stage (**b-d**) is shown.

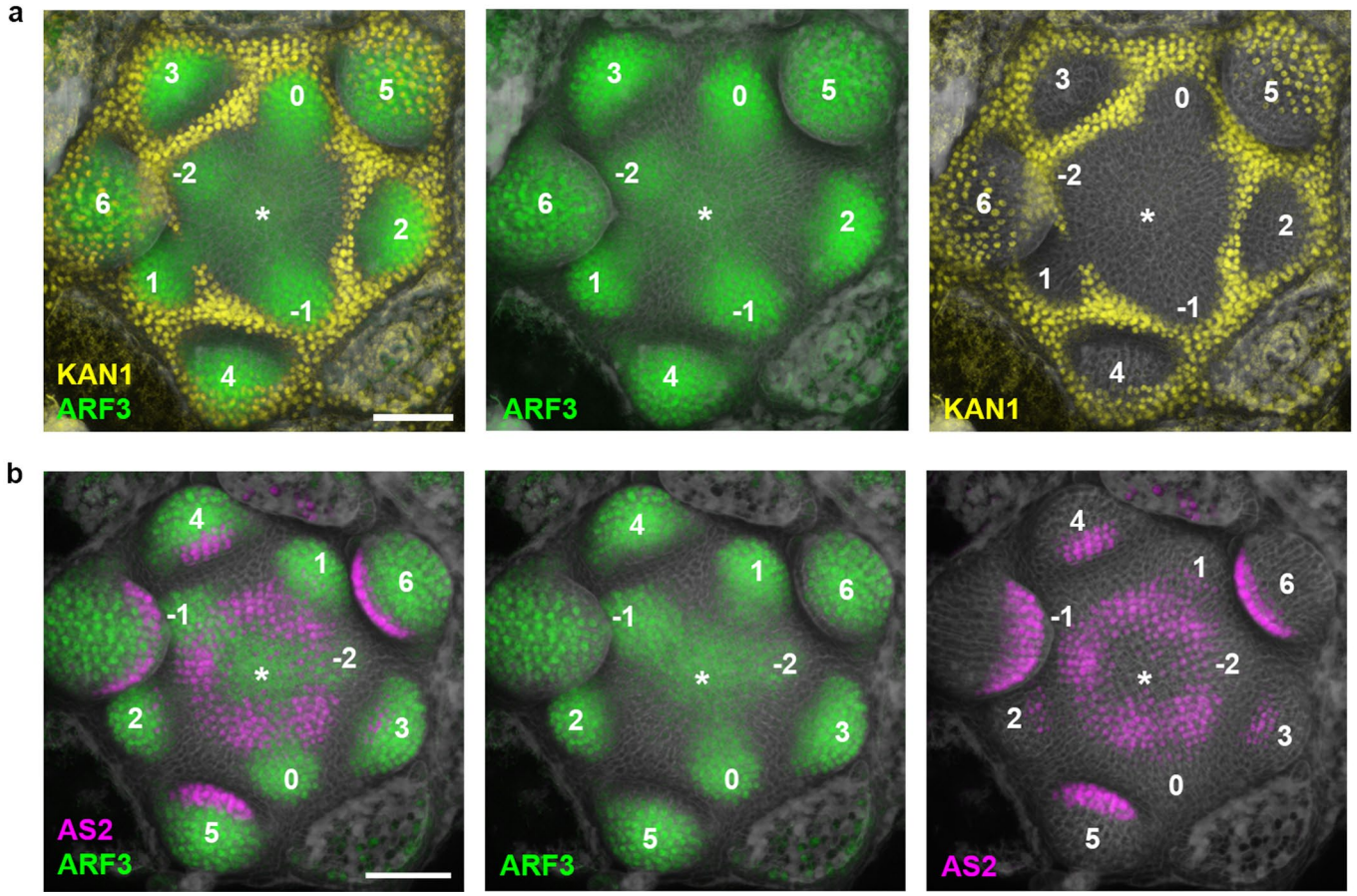

Extended Data Fig. 10 | Expression of KAN1, AS2, and ARF3 is anticorrelated during early primordium development. a, Dual *pARF3:ARF3-Turquoise* and *pKAN1:KAN1-YPet* reporter lines show a complementary pattern of KAN1 and ARF3 expression at the meristem from p-2 until primordium emergence at p1. Subsequently, ARF3 expression gradually shifts from the adaxial side of the primordium onto the emerging middle domain and then the abaxial side, where its expression then overlaps with that of KAN1. **b**, Dual *pARF3:ARF3-Turquoise* and *pAS2:AS2-VENUS* reporter lines show expression of AS2 and ARF3 is anticorrelated. Induction of ARF3 at p-2 correlates with a local decrease in AS2 expression, and ARF3 levels adaxially increase further as growth at the meristem displaces the primordium basipetal to the AS2 prepattern (p-1, p0). Subsequently, as the primordium emerges (p1) and ARF3 expression shifts towards the middle domain and abaxial side, AS2 levels again increase adaxially. Asterisks, meristem centre. Cell walls were stained by PI. Scale bars, 50 μm. Representative images from n = 5 (**a**) and n = 2 (**b**) independent apices are shown.

nature research

Corresponding author(s): Marja Timmermans

Last updated by author(s): Jan 27, 2022

Reporting Summary

Nature Research wishes to improve the reproducibility of the work that we publish. This form provides structure for consistency and transparency in reporting. For further information on Nature Research policies, see our Editorial Policies and the Editorial Policy Checklist.

Statistics

For all statistical analyses, confirm that the following items are present in the figure legend, table legend, main text, or Methods section.

n/a	Confirmed	
☐	☒	The exact sample size (*n*) for each experimental group/condition, given as a discrete number and unit of measurement
☐	☒	A statement on whether measurements were taken from distinct samples or whether the same sample was measured repeatedly
☐	☒	The statistical test(s) used AND whether they are one- or two-sided *Only common tests should be described solely by name; describe more complex techniques in the Methods section.*
☒	☐	A description of all covariates tested
☒	☐	A description of any assumptions or corrections, such as tests of normality and adjustment for multiple comparisons
☐	☒	A full description of the statistical parameters including central tendency (e.g. means) or other basic estimates (e.g. regression coefficient) AND variation (e.g. standard deviation) or associated estimates of uncertainty (e.g. confidence intervals)
☐	☒	For null hypothesis testing, the test statistic (e.g. *F*, *t*, *r*) with confidence intervals, effect sizes, degrees of freedom and *P* value noted *Give P values as exact values whenever suitable.*
☒	☐	For Bayesian analysis, information on the choice of priors and Markov chain Monte Carlo settings
☒	☐	For hierarchical and complex designs, identification of the appropriate level for tests and full reporting of outcomes
☒	☐	Estimates of effect sizes (e.g. Cohen's *d*, Pearson's *r*), indicating how they were calculated

Our web collection on statistics for biologists contains articles on many of the points above.

Software and code

Policy information about availability of computer code

Data collection	For confocal microscope imaging: LAS X Life Science software for SP5 and SP8 (Leica)
Data analysis	For image analysis: MorphoGraphX version 1.0 (https://www.mpipz.mpg.de/MorphoGraphX) Fiji version 1.51s (https://imagej.net/Fiji)) ImageJ version 1.53c (https://imagej.nih.gov/ij/) For preparing plots and statistical analyses: Origin version 9.85 (OriginLab Corporation, USA) Rstudio (https://www.rstudio.com/), using ggplot2 version 3.3.5 (https://cran.r-project.org/web/packages/ggplot2/index.html) For preparing figures: Adobe Photoshop CS6 Extended version 13.0 Adobe Illustrator CS6 version 6.2

For manuscripts utilizing custom algorithms or software that are central to the research but not yet described in published literature, software must be made available to editors and reviewers. We strongly encourage code deposition in a community repository (e.g. GitHub). See the Nature Research guidelines for submitting code & software for further information.

Data

Policy information about availability of data

All manuscripts must include a data availability statement. This statement should provide the following information, where applicable:

- Accession codes, unique identifiers, or web links for publicly available datasets
- A list of figures that have associated raw data
- A description of any restrictions on data availability

Data and recourses are available from the corresponding author on request.

Field-specific reporting

Please select the one below that is the best fit for your research. If you are not sure, read the appropriate sections before making your selection.

☒ Life sciences ☐ Behavioural & social sciences ☐ Ecological, evolutionary & environmental sciences

For a reference copy of the document with all sections, see nature.com/documents/nr-reporting-summary-flat.pdf

Life sciences study design

All studies must disclose on these points even when the disclosure is negative.

Sample size	Sample sizes were estimated based on similar previous studies (e.g. Caggiano et al. 2017; Bhatia et al. 2016; Galvan-Ampudia et al. 2020; Guan et al. 2017) and are mentioned in the text
Data exclusions	Only apices of similar size that enable a precise comparison across different transgenic lines were included. Expression patterns on younger, smaller apices are consistent.
Replication	Analyses in this study were performed on 5 or more independent biological replicates, with two exceptions as clearly indicated. In all instances was the data consistent across replicates
Randomization	Plants were analyzed from multiple independently grown biological replicates. Plant positions in the controlled growth conditions were random across replicates.
Blinding	Blinding is not possible given the distinctive expression patterns of the genes under analysis.

Reporting for specific materials, systems and methods

We require information from authors about some types of materials, experimental systems and methods used in many studies. Here, indicate whether each material, system or method listed is relevant to your study. If you are not sure if a list item applies to your research, read the appropriate section before selecting a response.

Materials & experimental systems

n/a	Involved in the study
☒	☐ Antibodies
☒	☐ Eukaryotic cell lines
☒	☐ Palaeontology and archaeology
☒	☐ Animals and other organisms
☒	☐ Human research participants
☒	☐ Clinical data
☒	☐ Dual use research of concern

Methods

n/a	Involved in the study
☒	☐ ChIP-seq
☒	☐ Flow cytometry
☒	☐ MRI-based neuroimaging

Appendix II

All Supplementary data, codes and movies can be found in the attached compact disc.

A Diffusible Small-RNA-based Turing System Dynamically Coordinates Organ Polarity

Emanuele Scacchi[1*#], Gael Paszkiewicz[1*], Khoa Thi Nguyen[1,2*], Shreyas Meda[1], Agata Burian[3], Walter de Back[4], and Marja C. P. Timmermans[1#]

[1]Center for Plant Molecular Biology, University of Tübingen, Tübingen, Germany.

[2]NTT Hi-Tech Institute, Nguyen Tat Thanh University, Ho Chi Minh City, Vietnam.

[3]Institute of Biology, Biotechnology and Environmental Protection, University of Silesia in Katowice, Katowice, Poland.

[4]Institute for Medical Informatics and Biometry, Faculty of Medicine Carl Gustav Carus, TU Dresden, Germany.

*These authors contributed equally: E. Scacchi, G. Paszkiewicz. K.T. Nguyen

[#]Authors for correspondence: marja.timmermans@zmbp.uni-tuebingen.de

emanuele.scacchi@zmbp.uni-tuebingen.de

SUMMARY

The formation of a flat and thin leaf presents a developmentally challenging problem, requiring intricate regulation of adaxial-abaxial (top-bottom) polarity. The patterning principles controlling the spatial arrangement of these domains during organ growth have remained unclear. Here, we show that this regulation is achieved by an organ-autonomous Turing reaction-diffusion system centered on mobile small RNAs. The data illustrates how Turing dynamics transiently instructed by pre-patterned information is sufficient to self-sustain properly oriented polarity in a dynamic, growing organ, presenting intriguing parallels to left-right patterning in the vertebrate embryo. Computational modelling demonstrates that this self-organising system continuously adapts to coordinate the robust planar polarity of a flat leaf while affording flexibility to generate the tissue patterns of evolutionarily diverse organ shapes. Our findings identify a small-RNA-based Turing network as a dynamic regulator of organ polarity that accounts for leaf shape diversity at the level of the individual organ, plant, or species.

ONE SENTENCE SUMMARY

A mobile small-RNA-based Turing system dynamically organises plant organ polarity, accommodating developmental diversity in leaf shape.

MAIN

As the principal photosynthetic organ, a leaf commonly develops as a thin, flat lamina optimised for light capture and gas exchange. The flattened architecture, while seemingly simple, presents a developmentally challenging problem. How can a microscopic bud acquire and retain a planar shape as it grows into a macroscopic structure? A key insight has been that flatness is intrinsically linked to adaxial-abaxial (ad-ab; top-bottom) polarity[1]. Formation of a flat leaf requires a planar polarity boundary, and any deviations from this ad-ab domain organisation during primordium growth lead to widely diverse leaf shapes[2–7]. Indeed, recent models illustrate how regional growth patterns guided by ad-ab gene expression can account for the emergence of diverse organ forms from an initially similar primordium[5,7]. However, what is currently missing is an understanding of the patterning principles controlling the arrangement of ad-ab domains.

The significant components promoting adaxial and abaxial identities are known (see[3,8]). In addition, the mechanism via which primordia first acquire ad-ab polarity has recently been established[9]. Leaves initiate at auxin maxima on an existing polarised field at the shoot apical meristem periphery

that creates a binary auxin readout to distinguish adaxial and abaxial domains in the incipient primordium (Fig. 1A). How the spatial arrangement of ad-ab domains is regulated after primordium emergence from the pre-patterned meristem environment is, however, less clear. The current consensus hypothesizes that leaf polarity is maintained by mutual antagonistic interactions between mobile adaxial and abaxial determinants[10,11]. Indeed, during leaf emergence, the initial asymmetry resolves into a new system of gene regulatory interactions[3,8] (Fig. 1B). Central to this network are opposing gradients of the mobile small RNAs, miR166 and tasiARF, which act as morphogens to govern the spatial separation of adaxial and abaxial determinants as the primordium grows[12].

The critical question thus arises how these gradients are organised and tuned during primordium growth to sustain formation of a planar leaf while allowing for developmental flexibility. Similar to the *Bicoid* and *Hunchback* morphogens in the early *Drosophila* embryo, miR166 and tasiARF could have a fixed source that is stably maintained in a manner independent of their downstream transcription factor targets (see [13]; Supplementary Fig. 1A). Alternatively, in the vertebrate embryo, *Nodal* and *Lefty* self-organise their gradient landscapes through a Turing reaction-diffusion system[14–16]. Such systems are capable of spontaneously generating periodic spatial patterns from an initial homogeneous state. Typically the repeated elements emerge as spots or labyrinthine stripes[17,18], but in the case of *Nodal* and *Lefty*, the pattern wavelength is significantly larger than the size of the tissue, thus creating a single gradient across the embryo[13,19]. By analogy, miR166 and tasiARF production could be integrated within a closed self-organising gene regulatory network (GRN) that dynamically controls ad-ab polarity by continuously coordinating both morphogen sources via their respective targets (Supplementary Fig. 1B).

Here, we harness the power of theoretical and computational models, molecular genetics, and live confocal imaging to demonstrate that an organ-autonomous small RNA-based Turing reaction-diffusion system coordinates the spatial organisation of adaxial and abaxial domains in developing leaves. Our integrated approach shows that the Turing dynamics when transiently guided by pre-patterned information from the meristem environment is sufficient to self-sustain a correctly oriented bipolar pattern during growth. The system displays a remarkable adaptability and robustness, explaining the propagation of a stable planar polarity boundary in flat leaves, while simultaneously affording flexibility to accommodate developmental and evolutionary diversity in organ form. Thus, our findings identify a unique small-RNA-based Turing network as a dynamic regulator of organ polarity that accounts for leaf shape diversity at the level of the individual organ, plant, or species.

A minimal theoretical network to self-organise the spatial distribution of polarity determinants

miR166 and tasiARF regulate ad-ab polarity by limiting expression of their respective Class III HOMEODOMAIN LEUCINE ZIPPER (HD-ZIPIII) and AUXIN RESPONSE FACTOR3/4 (ARF3/4) targets, which, in conjunction with ASYMMETRIC LEAVES1/2 (AS) and KANADI (KAN) transcription factors, distinguish adaxial versus abaxial cell fate via further antagonistic interactions[3,8] (Fig. 1B). The exact configuration of the ad-ab polarity network, however, remains unclear. Therefore, to gain insight into the patterning principles controlling ad-ab polarity during organ growth, we adopted a theoretical approach that considers all possible regulatory interactions, except those for miR166 and tasiARF, which only repress their specific targets (Supplementary Note 1.1-1.3). With the understanding that adaxial and abaxial cell fates are mutually exclusive, we first addressed the possibility that a Turing reaction-diffusion system governs their domain organisation. Such systems are mathematically deducible around a single steady-state[14,20,21]. Accordingly, we implemented a high-throughput theoretical pipeline through a computer algebra system[22] to identify all possible network topologies capable of spontaneously generating a Turing pattern with two out-of-phase diffusible morphogens, reflecting the contributions of miR166 and tasiARF[12] (Supplementary Note 1.1 and 1.2). The goal here was not to build a detailed quantitative biochemical gene regulatory model, but rather to arrive at minimal topological models. Although not every node or molecular interaction within the biological system may be explicitly represented in a minimal model, those interactions revealed are critical to the patterning process. Minimal network topologies can thus reveal the organizing principles hidden within the complexity of biological systems, and make specific predictions about critical network properties to test experimentally.

Using this approach, we identified 130 network topologies with 2- to 5-components theoretically capable of producing a Turing pattern with the desired self-organised spatial separation of morphogens (Supplementary Note 1.2). Then, imposing the specific repressive interactions for miR166 and tasiARF as a biological constraint, we identified a single 3-component network, referred to hereafter as the Leaf Polarity Model (LPM), as the minimal topological model. In this model, adaxial determinants represented by distinct HDZIPIII and AStasiARF nodes form a negative feedback loop, and act in mutual opposition to abaxial determinants, combined into a single miRKANARF node (Fig. 2A, and Supplementary Note 1.3-1.5).

Consistent with the theoretical analysis, the LPM, when simulated in 1-dimension with random initial conditions for one of its components, generates a stable periodic pattern in which miRKANARF is out-of-phase with both AStasiARF and HDZIPIII (Fig. 2B, and Supplementary Note 2.1). Still, although a plethora of Turing systems are theoretically plausible, only few are sufficiently robust to drive

biological processes[23]. The multi-dimensional parameter space inside which the LPM self-organises into a Turing pattern, known as the Turing space, accommodates a broad and continuous range of parameter values (Supplementary Note 1.5), indicating a robust network organisation[24]. As such, our theoretical analysis identified a single robust 3-component minimal network topology that enables the self-organised spatial separation of ad-ab polarity determinants.

The LPM self-organises a bipolar pattern in a growing cellular environment

Turing reaction-diffusion systems give rise to a multitude of periodic patterns, such as spots, labyrinths, and stripes[17,18,20]. To reproduce the ad-ab domain organisation of a planar organ, the LPM should resolve into a linearly-separated, bipolar pattern in a simulated cellular environment that resembles a mediolateral section through a developing leaf. For this, the wavelength of the periodic pattern generated (λ, Fig. 2B) must be significantly larger than the ad-ab dimension of the tissue template[13,25]. Sensitivity analyses show that the diffusion of AStasiARF plays a key role in scaling the LPM pattern wavelength (Supplementary Note 2.3). However, even with an appropriate diffusion rate for AStasiARF, the system produces a typical labyrinthine Turing pattern on a static cellular template in which each cell elaborates the LPM (Fig. 2C, and Supplementary Note 3.1).

Symmetry breaking in these simulations results from stochastic perturbations on homogenous initial conditions. However, in development, Turing systems often interact with pre-existing asymmetries that influence its outcome[13,25–28]. For example, pre-patterned maternal biases guide the *Nodal-Lefty* Turing system in the vertebrate embryo[19]. Considering the pre-patterned environment on which leaf primordia arise[9] (Fig. 1A), we next used such spatial information for miRKANARF in the abaxial epidermis as an initial condition (just t=0). This proved sufficient for the LPM components to resolve over time into two opposing domains separated by a linear boundary (Fig. 2D, and Supplementary Note 3.1). Moreover, with such an initial condition for any of the system components, the LPM generates and propagates a bipolar pattern in which HDZIPIII and AStasiARF mark the upper and miRKANARF the lower cell layers, also in a growing cellular environment resembling a young leaf (Fig. 2E, Supplementary Movies 1, 2, and Supplementary Note 3.2). Here, the system components can continuously adapt or maintain their distributions over time, as is characteristic of self-organising systems in a dynamic context[13,17,18,20,24,29].

Thus, in a model phenocopying the growing leaf, the LPM functioning in each cell orchestrates a collective cell behaviour that manifests as a single linear boundary between ad-ab domains at the "organ" level. This pattern emerges when parameter conditions generate a pattern wavelength significantly larger than the ad-ab axis and pre-patterned information, used as an initial condition,

instructs the network. The latter feature, for which there is experimental support[9], simultaneously ensures the formation of two bipolar domains and their proper orientation. This raises the intriguing possibility that, similar to the example of *Nodal* and *Lefty*[15,16,19], the opposing miR166 and tasiARF gradients are part of a self-organising Turing system that dynamically coordinates their distributions to support development of a planar leaf.

The LPM topology reflects molecular interactions between leaf polarity determinants

Notably, the LPM, although derived from few a-priori conditions connected to small RNA function, conforms with the previously established repressive interaction of HD-ZIPIII onto miR166[30], as well as with distinct diffusion rates for tasiARF and miR166[31] (Supplementary Note 1.5). The LPM topology further predicts a negative feedback loop between adaxial nodes and self-inhibition at the abaxial miRKANARF node as critical for generating the proper self-organised spatial separation of polarity determinants. To experimentally verify these predictions, we explored the landscape of direct regulatory interactions between network components. Given evidence for functional redundancy and conservation of DNA binding specificity[3,32], representative members from each core transcription factor family were tested by chromatin immunoprecipitation (ChIP) analysis for enrichment at promoters of key adaxial and abaxial identity genes (Fig. 3A, and Supplementary Figs. 2-3). This revealed a highly interconnected network with more extensive cross-connectivity between polarity determinants than previously anticipated (compare Figs. 1B and 3C). PHABULOSA (PHB), a representative HD-ZIPIII member, AS2, KAN1, and ARF3 each bind their own promoter and, in addition, connect to genes representing all other major nodes in the polarity network.

The transcriptional effects of these interactions were determined by qRT-PCR following short-term transcription factor induction, which due to the comparatively slow rates of protein production and turnover[33], define the output of direct regulatory interactions within the complex network. In line with the LPM, the experimentally defined ad-ab polarity GRN is characterised by inhibitory interactions (Fig. 3C). Both KAN1 and ARF3 act as repressors on their adaxial targets, as expected, but also down-regulate expression of abaxial determinants, including *KAN1*, *KAN2*, and *ARF4*, thus empirically validating self-inhibition of the abaxial miRKANARF node in the LPM (Fig. 3B, and Supplementary Fig. 4). Further, confirming the novel positive interaction in the LPM, PHB induction promotes expression of *AS2* and *TAS3A*, while decreasing transcript abundance for abaxial determinants (Fig. 3B, and Supplementary Fig. 4).

Induction of AS2, on the other hand, does not trigger the predicted downregulation in HD-ZIPIII expression. AS2 represses its abaxial targets and also inhibits activity at its own promoter and the

promoter of *TAS3A*, but HD-ZIPIII transcript levels increase upon AS2 induction (Supplementary Fig. 4B). According to the LPM, AS2 influences *PHB* expression via an incoherent feedback loop, by simultaneously repressing components in both the HDZIPIII and the antagonistic miRKANARF nodes. Because miRNAs often display an exceedingly short half-life, especially in comparison to proteins[33,34], we reasoned that miR166 levels may decrease comparatively rapidly upon AS2 induction, causing an indirect rise in *PHB* transcript levels. We, therefore, generated a transcriptional *pPHB:GFP* reporter fusion to distinguish the direct effect of AS2 on HD-ZIPIII promoter activity from any indirect effects on HD-ZIPIII levels via repression of miR166. GFP transcript levels decrease upon short-term AS2 induction, consistent with direct repressive feedback regulation from AS2 on HD-ZIPIII transcription, as in the LPM (Fig. 3B-C, and Supplementary Fig. 4E).

The experimentally defined GRN thus captures all interactions characterising the LPM, but perhaps not surprisingly, this biological network is far more complex (Fig. 3C). When simplified to a system of 3 components (HDZIPIII, AStasiARF, and miRKANARF), the resulting reduced biological network resembles the LPM with the addition of two further repressive interactions (Fig. 3D). However, the power of the theoretical and computational approach used here, lies in its ability to generate a minimal model that depicts only those interactions absolutely critical for the self-organised spatial separation of determinants. Additional regulatory interactions, while dispensable for Turing dynamics, may be allowed[21,22]. Indeed, theoretical analysis and numerical simulations indicate that the two additional regulatory interactions identified experimentally are fully compatible with the outcome of the LPM (Fig. 3E, and Supplementary Note 4.1), thus suggesting that the biological network and the LPM may share a common organising principle.

The leaf polarity network follows the organising principles of a Turing system

Elaborating on this finding, we next asked if the extended biological GRN satisfies the organising principles of a Turing system. To this end, we systematically resolved each node in the LPM into its sub-components, considering the regulatory interactions identified experimentally. Upon deconvolution of AStasiARF into distinct AS and tasiARF components (Fig. 4A), the system is unable to generate a Turing pattern (Fig. 4B). In the LPM, AStasiARF represses both the HDZIPIII and the miRKANARF node while it diffuses. Given that tasiARF selectively targets ARFs, we reasoned that the AS component requires diffusion to fully reproduce the critical properties of AStasiARF in the LPM. Indeed, when we assign the diffusivity of AStasiARF to both tasiARF and the AS node, the network self-organizes into a Turing pattern (Fig. 4C, and Supplementary Note 4.2.1). Confirming the predicted mobility, *AS2* promoter activity (*pAS2:3xVenus-NLS*) and accumulation of a non-mobile protein fusion of AS2 to 3xVenus[35] (*pAS2:AS2-3xVenus*) is limited to the adaxial epidermis, whereas

AS2-Venus protein (*pAS2:AS2-Venus*) is additionally detected in sub-epidermal layers of the leaf (Fig. 4D-F). Further, only expression of AS2-Venus, not AS2-3xVenus, from the *AS2* promoter can fully complement the *as2* leaf phenotype (Figs. 4G-J, and Supplementary Fig. 5). The AS2-3xVenus protein fusion is however fully functional in transient luciferase reporter assays, and represses *ARF3* promoter activity to a similar degree as AS2-Venus (Supplementary Fig. 5E). Therefore, in accordance with model predictions, AS2 is a mobile transcription factor, and its short-range movement from its site of synthesis in the adaxial epidermis contributes to normal leaf development.

In contrast to the AStasiARF node, deconvolution of miRKANARF into its constituents fails to generate a Turing pattern even if we confer the ability to move onto KAN and/or ARF (Supplementary Note 4.2.2). Instead, considering a relatively short half-life for miR166[33,34,36], which also emerged from the incoherent feedback regulation of AS2 onto HD-ZIPIII, we imposed a turnover parameter onto miR166 to reflect the essential self-inhibition of miRKANARF in the LPM. With this condition, the 5-component model self-organises into a Turing pattern (Supplementary Note 4.2.2). These findings substantiate the idea that the complex ad-ab polarity GRN defined experimentally follows the organising principles of a Turing reaction-diffusion system that dynamically organises the spatial distributions of its polarity determinants in the growing primordium.

KAN-ARF complex formation confers organ-autonomy onto the polarity network

The polarity GRN generates Turing dynamics without relying on explicit external activators that drive expression of its components in the leaf (Fig. 3C). As such, our work leaves open the specific molecular mechanisms through which each gene is activated. For example, the induction of both KAN and HD-ZIPIII expression by MONOPTEROS[11] is consistent with our model, but this activation is not essential for the actual self-organising patterning properties of the network. Nonetheless, activators internal to the system acting on miR166 and tasiARF could be significant for tuning their morphogenic gradients along the polarity axis. While the HD-ZIPIII transcription factors promote *TAS3A* expression on the adaxial side, an internal activator for miR166 was not identified (Fig. 3C).

The spatiotemporal expression patterns of the miR166 precursors at the vegetative apex predict early roles for *MIR166A* and *MIR166B* in ad-ab patterning (Supplementary Fig. 6). Similar to *KAN1*[9], both precursors are expressed on the abaxial side of established leaf primordia and within a ring of cells at the meristem periphery. Cell lineage tracing confirms that the ring of *MIR166A* expression marks the abaxial domain in incipient primordia along with KAN1[9] (Fig. 5A). Nonetheless, even though KAN1 binds the *MIR166A* and *MIR166B* promoters (Fig. 5B-C, and Supplementary Fig. 3),

transcript levels for both genes are unchanged upon KAN1 induction (Fig. 5D, and Supplementary Fig. 4, 7). Interestingly, ARF3 co-occupies a KAN1-binding element in the *MIR166A* promoter (Fig. 5B-C, and Supplementary Fig. 3), suggesting potential regulation by a KAN1-ARF3 complex[37,38]. Indeed, *MIR166A* transcript levels increase upon co-induction of KAN1 and ARF3 (Fig. 5D, and Supplementary Fig. 7). Computational modelling predicts that induction of miR166 by KAN-ARF inside this final 5-component GRN raises miR166 levels over other components in the system without altering its resolution into a periodic Turing pattern (Fig. 5E-G, and Supplementary Note 4.2.3). However, the wavelength of the resulting pattern increases, suggesting that regulation of *MIR166A* by a KAN-ARF complex could fine-tune miR166 morphogen levels and scale the wavelength of the Turing pattern relative to the number of cell layers within the primordium.

The above findings (Figs. 3B-C, 5D-E) further imply that individually, KAN1 and ARF3 primarily repress their targets, but when in complex, the two transcription factors promote expression of *MIR166A*. This distinction is intriguing, given the dynamic pattern of ARF3 expression. ARF3 initially marks adaxial cells, but its expression gradually shifts abaxially as the primordium emerges from the meristem environment[9]. Consequently, only after primordium emergence can a KAN1-ARF3 complex promote *MIR166A* expression. Indeed, abaxial *pMIR166A:erGFP* expression in early primordia persists in *kan1 kan2* and in lines expressing the synthetic miRNA *miRARF* (*p35S:miRARF*)[12], which targets transcripts for ARF3, as well as for its ARF2 and ARF4 homologs (Fig. 5H). In contrast, a drastic reduction in *pMIR166A:erGFP* expression in these backgrounds is evident in p3 and older leaf primordia. A comparable *pMIR166A:erGFP* expression phenotype is observed following the reduction of both KAN and ARF activities, providing also genetic evidence for *MIR166A* activation by a KAN-ARF complex.

The adaxial-to-abaxial shift in ARF3 localisation is linked, in part, to adaxial tasiARF production, as evidenced by the distinct expression patterns of *pARF3:ARF3-YPET* and its tasiARF resistant form. Notably, only expression of the latter persists in adaxial cells of p3 and older leaf primordia (Fig. S8). Accordingly, the ARF3 expression shift marks the time when the opposing miR166 and tasiARF gradients are integrated into a closed, self-organising Turing system. Given that this switch in expression occurs after primordium emergence from the meristem environment, this Turing system regulates the spatial arrangement of ad-ab domains in an organ-autonomous manner.

Turing dynamics generates ad-ab tissue patterns underlying evolutionarily diverse organ shapes.

As an important outcome, the ad-ab Turing network can organise the spatial arrangement of its components to coordinate the robust planar polarity of a flat leaf (Supplementary Note 3.2).

However, with deviations that vary the system wavelength relative to the tissue size, Turing systems will generate a range of distinct spatial patterns[25]. This point is of note, given that small shifts in ad-ab gene expression can translate into widely diverse leaf shapes[1–7]. To establish how variations in system wavelength might manifest at the organ level, we performed a morpho-sensitivity analysis of the LPM on the growing cellular template, using a parameter scale of k_2 and k_5 (Supplementary Note 4.3). The resulting morphospace demonstrates that on an equivalent leaf canvas, the LPM generates discrete patterns of ad-ab gene expression, dictated by specific thresholds of the system wavelength (Fig. 6A-F, Supplementary Movies 3-6, and Supplementary Note 4.3).

The bipolar expression pattern characteristic of planar leaves dominates the morphospace (Fig. 6A and D, and Supplementary Movie 3), indicating that this phenotype is stable across a range of wavelengths and thus robust to network perturbations. Nevertheless, a decrease in system wavelength outside this zone of robustness leads to a partial adaxialisation, seen as patches of adaxial identity within the abaxial domain or, as the wavelength shortens even further, to variable labyrinthine or spotty ad-ab patterns (Fig. 6E-F, and Supplementary Movies 4-5). In the opposite direction, increases in system wavelength ultimately result in a concentric arrangement of abaxial and adaxial components (Fig. 6B). Moreover, during the transition from a bipolar to a concentric pattern, the change in system wavelength restricts adaxial determinants to a central region on the top side of the growing leaf canvas (Fig. 6C, and Supplementary Movie 6).

The ability of the LPM to generate a broad repertoire of spatial patterns dictated by system wavelength has profound implications for understanding how small perturbations in the polarity GRN manifest at the organ level in vivo. Indeed, the repertoire closely resembles the highly variable and, at times, counterintuitive shifts in gene expression observed in polarity mutants[1,3,8]. For instance, *kan1 kan2* leaf primordia typically display a partial decrease in abaxial identity, as evidenced by a variable loss in *pFIL:3xVenus-NLS* and gain in *pAS2:AS2-Venus* expression (Fig. 6G-J and L). However, select primordia exhibit a counterintuitive gain in abaxial identity, apparent as an expanded labyrinthine or spotty *pFIL:3xVenus-NLS* pattern (Fig. 6K). Though previously observed[39], this phenotypic aspect remained unexplained. Its occurrence, however, aligns with Turing dynamics, further reinforcing the notion that the polarity GRN follows the organising principles of a Turing system.

Turing dynamics can also account for the occurrence of radialised (Fig. 6B and L) or cup-shaped leaves (Fig. 6C, and Supplementary Movie 6) in polarity mutants[1,3,6,8], even if the specific mutation is expected to reduce the system wavelength. The final shape of a Turing pattern reflects an interplay

between the wavelength of the system and the size of the tissue/organ in which this operates[25]. As a result, within a smaller mutant primordium, the effects of a shortened wavelength may manifest as a seemingly longer wavelength phenotype. Finally, Turing dynamics, as illustrated by the LPM's repertoire of spatial patterns, can account for the patterns of ad-ab gene expression observed in plant species exhibiting unifacial, peltate, or pitcher-shaped leaves[2,4,6,40]. Indeed, recent findings revealed that the formation of carnivorous traps in *Utricularia gibba* arises from a shift in ad-ab gene expression from a "bipolar linear" to a "polar shift up" pattern[5]. Consequently, Turing dynamics explains how polarity is robustly organised in a planar leaf, and how system variations can give rise to drastically different morphological phenotypes. Therefore, a Turing-based organisation of ad-ab polarity presents a mechanistic basis to account for variations in leaf shape within and across plant species.

Discussion

Our study clarifies how plants organise ad-ab polarity during primordium growth, elucidating a fundamental patterning process critical to morphogenesis. We show that this process is governed by a highly interconnected GRN that follows the organising principles of a Turing system. Through cell-cell communication and feedback regulation, the polarity GRN functioning in each cell orchestrates a collective cell behaviour that continuously organises the spatial arrangement of ad-ab domains at the organ level. As such, ad-ab gene expression can dynamically adapt to internal and external perturbations to sustain a robust polarity boundary in planar leaves while providing the flexibility needed to support morphological diversity.

Although Turing dynamics are often invoked in biology, examples where Turing systems have been convincingly demonstrated remain scarce[13,23,29]. Our conclusion is supported by experimental validation of essential theoretical constraints, including novel network interactions, differential mobility of miR166 and tasiARF[31], a relatively short half-life for miR166, and cell-to-cell movement of AS2. In addition, the variegated and often counterintuitive cell fate rearrangements in ad-ab polarity mutants align with Turing dynamics. Consequently, our findings uncover that mobile small RNAs directly interacting with transcription factors can generate Turing dynamics. Given the prevalence of small RNA-transcription factor modules in development[41,42], additional examples of this type of reaction-diffusion system may follow. Moreover, the system's simplicity, relative to receptor-ligand driven Turing networks, combined with the adaptability of small RNAs, offers exciting new perspectives in synthetic biology.

Turing systems have intrinsic symmetry-breaking properties, but in development, Turing dynamics often arise under the influence of pre-existing asymmetries rather than from random initial states[13,19,25–28]. As a prominent example, the Turing system underlying the periodic digit patterns in vertebrate appendages operates on independent morphogen gradients that modulate pattern shape, size and periodicity[13,21,27,43]. In the case of ad-ab polarity, the pre-patterned canvas at the meristem periphery initially guides the Turing dynamics to achieve a correctly oriented bipolar pattern. This suggests additional interesting parallels to the *Nodal-Lefty* system, in which Turing dynamics emerging from existing biases organise precisely oriented signal gradients over the vertebrate embryo[15,16,19]. Both Turing systems leverage the intrinsic adaptability and pattern maintenance properties provided by Turing dynamics to robustly propagate polarity in a dynamic, growing environment. Our work thus illustrates how Turing dynamics transiently instructed by pre-patterned information is sufficient to self-sustain stable, properly oriented polarity in an extensively growing structure.

The remarkable diversity of spatial patterns generated by Turing systems stems from their inherent flexibility. The ad-ab Turing network likely interacts with multiple additional regulatory pathways and may quantitatively vary from species to species[3,43]. Any deviations upon the conditions delineated by the LPM may tune the system, leading to shifts in ad-ab tissue organisation during primordium growth. Accordingly, a variety of organ shapes distinct from a planar leaf can emerge from the same pre-patterned meristem environment. Moreover, with the Turing system organising ad-ab polarity in an organ-autonomous manner, such deviations may explain heterophylly, the occurrence of differently shaped leaves within a single plant. For example, *Ranunculus trichophyllus* develop leaves with dramatically different flatness in air versus water[44]. Similarly, *Utricularia gibba* and *Cephalotus follicularis* develop carnivorous traps alongside radial or flat leaves within the same plant[4,5]. Thus, our findings identify a mobile small-RNA-based Turing network that dynamically regulates organ polarity, accounting for leaf shape diversity at the level of the individual organ, plant, or species.

MATERIALS AND METHODS

Plant materials and growth conditions

Plants were grown under long-day (16h light 22^{0}C and 8h dark 20^{0}C) or short-day (8h light 22^{0}C and 16h dark 20^{0}C) conditions as indicated. All lines are in the Col-0 background. The collection of *MIR165* and *MIR166* reporter lines[45] were a kind gift from Keiji Nakajima (Nara Institute of Science and Technology, Japan). The *pMIR166A:erGFP* reporter was crossed into the *kan1-11 kan2-5 (-/-, +/-)* background (NASC N67888). The artificial miRARF sequence targeting transcripts for ARF2/3/4 was

introduced into the pFK/390-B/c backbone as previously described[12]. This *p35S:miRARF* construct was transformed into the *pMIR166A:erGFP* and *pMIR166A:erGFP kan1-11 kan2-5* (-/-, +/-) backgrounds, and a minimum of six independent T2 lines were analysed.

For construction of the *pAS2:3xVenus-NLS* and *pFIL:3xVenus-NLS* reporters, a 3676 base pair (bp) fragment containing the *AS2* promoter and 3873 bp of the *FIL* promoter, each including the respective 5' UTR, were amplified from genomic DNA using primers AS2p_F and AS2p_R, or FILp_F and FILp_R respectively (See Supplementary Table 1 for primer details). The amplified fragments were inserted between *KpnI* and *XmaI* sites upstream of *3xVenus-N7* and the *OCS* terminator in the JM173 T-DNA vector, kindly provided by Detlef Weigel. To generate the *pAS2:AS2-Venus* and *pAS2:AS2-3xVenus* reporters, the *3xVenus* coding region in this construct was replaced using *XmaI* and *BamHI* cloning sites for *de novo* synthetized (Genscript) translational fusions of the 597 bp *AS2* coding sequence to either *Venus* or *3xVenus*. AS2 reporter constructs were transformed into Col-0, *kan1-11 kan2-5* (-/-, +/-) and *as2* for analysis. The *pFIL:3xVenus-NLS* reporter was transformed into Col-0 and *kan1-11 kan2-5* (-/-, +/-). A minimum of six independent T2 lines for each combination was analysed.

Construction of the estradiol-inducible AS2-YFP and KAN1-YFP lines has been described previously[9,46]. For construction of estradiol-inducible ARF3-YFP and PHB*-YFP lines, the coding sequences of *ARF3* or the miR166 resistant form of *PHB*[12] were fused to *YFP*, cloned into pENTR™/D-TOPO (Invitrogen) and subsequently transferred into pMDC7 using Gateway technologies. The *pPHB:erGFP* reporter has been described previously[47]. This was crossed to the estradiol-inducible AS2-YFP line and the F1 progeny used for analysis.

Construction of the *pARF3:ARF3-YPET* reporter has been described[9]. The *pARF3:ARF3*-YPET* reporter was generated similarly using GreenGate from entry modules for the *ARF3* promoter (4986 bp upstream of the start codon), terminator (endogenous stop codon plus 288 bp downstream), and 3725 bp gene body without stop codon (primer ARF3g_F and ARF3g_R). Mutations in the two tasiARF binding sites were introduced using overlapping PCR using primers ARF3*a_F, ARF3*a_R, ARF3*b_F, and ARF3*b_R. Entry modules were assembled to generate a translational fusion to a 4xGly-Ser-9xAla linker followed by a single Ypet into a modified pCAMBIA backbone[9]. See Supplementary Table 1 for primer details.

Chromatin Immunoprecipitation

For Chromatin immunoprecipitation (ChIP) analyses, 9-day-old estratradiol-inducible AS2-YFP, KAN1-YFP, ARF3-YFP, or PHB*-YFP seedlings grown under long day conditions on ½ Murashige and Skoog media supplemented with 1% sucrose, were submerged in a solution containing 20 µM ß-estratradiol and 0.01% Silwet for 10 min. 24h after induction, whole seedlings were harvested and ChIP assays performed with anti-GFP antibody (ab290, Abcam) as previously described[48]. ChIP (IP) and input (IN) DNA samples were quantified by qPCR using Lunar qPCR mix (NEB). Relative enrichments were calculated as the ratio of % IP/IN at the promoter fragments of interest over % IP/IN at the *ACT2* negative control. All experiments were performed in three biological replicates and Student's t test was used to calculate statistical significance. Promoter fragments assayed by ChIP were selected based on the occurrence of predicted transcription factor binding motifs identified using FIMO (https://meme-suite.org/meme/doc/fimo.html). See Supplementary Table 2 for primer details.

Quantitative RT-PCR analysis

Seedlings were grown under long-day conditions on ½ Murashige and Skoog medium supplemented with 1% sucrose. 9-day-old seedlings were submerged in a solution containing 20 µM ß-estradiol and 0.01% Silwet for 10 min. The first two true leaves were harvested 8h post-induction, except in the case of PHB*-YFP. Here, due to the much slower rate of protein accumulation[49], samples were harvested 16h post-induction. Total RNA was extracted using the Spectrum plant total RNA isolation kit (Sigma-Aldrich), and mRNA converted to cDNA using the IScript™ Select cDNA synthesis kit (Bio-Rad) according to the manufacturer's recommended protocols. Transcript levels were quantified by qPCR using Lunar qPCR mix (NEB). Relative expression values were calculated based on at least three biological replicates using the delta Ct method with *PP2A* as internal control and normalized to values in mock treatment. See Supplementary Table 3 for primer details.

Transient Luciferase assays

Protoplasts were isolated from *Arabidopsis* cell culture and transfected with 2ug each of reporter (pARF3:LucTraP), effector (p35S:AS2-3xVenus or p35S:AS2-Venus) and internal control (p2x35S:Renilla-Luc) plasmid, as previously described[9]. Transfected protoplasts were incubated overnight in the dark, and subsequently analysed using the Dual-Luciferase Reporter Assay System (Promega). Luminescence was measured using the Tecan's Infinite F200 plate reader, and relative Luciferase activity calculated as Firefly over Renilla luminescence from 5 biological replicates across 2 independent experiments. Statistical significance was calculated using Student's t test.

Live confocal imaging

Plants were grown on soil under short-day conditions for 30-50 days, and prepared for imaging according to[9]. Cell walls were stained with 0.1% propidium iodide (PI; Sigma-Aldrich) for 3-5 min. Apices were imaged with an upright confocal laser-scanning microscope (Leica TCS SP8) with 63x or 40x, long working distance, water-immersion objectives. The excitation wavelength was 488 nm for GFP-based reporters and 514 nm for Venus- and YPET-based reporters. Emission data was collected using a Hyd detector at 500-540 nm for GFP, and 519-545 nm for Venus and YPET. The excitation wavelength for PI was 488 nm or 514 nm, depending on the fluorescence reporter used, and emission was collected at 600-656 nm. Scanning was done using bidirectional mode at a speed of 200 Hz or 400 Hz and a frame resolution of 512x512 or 1024x1024 pixels. The pinhole was set at 1AE. The step size in z-stacks was 0.08-0.5 µm. Images were collected at 12 bits or 16 bits. Shoot apices were imaged at approximately the same time of day either once (0h), or over multiple consecutive days in a 24h time-lapse series.

Confocal microscopy of leaf sections

Plants were grown under short-day conditions on ½ Murashige and Skoog medium. 10-14 day-old seedlings were fixed in fresh 4% Paraformaldehyde in 1x PBS supplemented with 0.01% Triton X-100 under vacuum (550 mm Hg) for 45 min, washed 3 times (30 min per wash) in 1x PBS, and embedded in 6% low melting agarose (Sigma-Aldrich). 100 µm transverse sections were obtained using a VT1000S vibratome (Leica) and stained with 0.01% Fluorescent Brightener 28 (FB28; Sigma-Alrdich) dissolved in 1x PBS for at least 20 min. Transverse sections were imaged as above. The excitation wavelength for FB28 was 405 nm, and emission was collected at 410-475 nm. Scanning was done using sequential plus bidirectional mode at a speed of 400 Hz and a frame resolution of 512x512 or 1024x1024 pixels. The pinhole was set at 1AE. The step size in z-stacks was 0.9-0.75-0.47 µm. Images were collected at 16 bits.

Image processing and analysis

Optical sections through leaf primordia were generated using MorphographX[50] as previously described[9]. Cell lineage tracing was performed as previously described[9].

Computational modelling and theoretical analysis

Cellular modelling was performed using the open source software Morpheus 2.3.1[51], a modelling and simulation environment for the study of multi-scale and multicellular systems (https://morpheus.gitlab.io/). PDE and ODE simulations were implemented using Mathematica (Wolfram Research Inc, Version 13.1, https://www.wolfram.com/mathematica). Custom code was developed in Wolfram Mathematica to perform the theoretical analysis of Turing networks. The

open-source code RDNet[22] was used to study networks with more than three nodes. Statistical analyses were performed using R Statistics (https://www.r-project.org/).

Code and data accessibility

Supplementary Code 1-3 provides all code in XML format compatible with the Morpheus platform[51]. The cellular models are also available via the Git Morpheus open source repository at gitlab.com/morpheus.lab/model-repo. Details concerning the specific mathematical models are defined within Supplementary Note. Additional scripts and experimental data are available upon reasonable request from the authors.

REFERENCES

1. Waites, R. & Hudson, A. *phantastica*: a gene required for dorsoventrality of leaves in *Antirrhinum majus*. *Development* **121**, 2143–2154 (1995).
2. Kim, M., McCormick, S., Timmermans, M. & Sinha, N. The expression domain of PHANTASTICA determines leaflet placement in compound leaves. *Nature* **424**, 438–443 (2003).
3. Kuhlemeier, C. & Timmermans, M. C. P. The Sussex signal: insights into leaf dorsiventrality. *Development* **143**, 3230–3237 (2016).
4. Fukushima, K. *et al.* Genome of the pitcher plant *Cephalotus* reveals genetic changes associated with carnivory. *Nat Ecol Evol* **1**, 59 (2017).
5. Whitewoods, C. D. *et al.* Evolution of carnivorous traps from planar leaves through simple shifts in gene expression. *Science* **367**, 91–96 (2020).
6. Bhatia, N., Runions, A. & Tsiantis, M. Leaf shape diversity: From genetic modules to computational models. *Annu. Rev. Plant Biol.* **72**, 325–356 (2021).
7. Cheng, J. *et al.* Diversification of *ranunculaceous* petals in shape supports a generalized model for plant lateral organ morphogenesis and evolution. *Sci Adv* **9**, eadf8049 (2023).
8. Satterlee, J. W. & Scanlon, M. J. Coordination of leaf development across developmental axes. *Plants* **8**, (2019).
9. Burian, A. *et al.* Specification of leaf dorsiventrality via a prepatterned binary readout of a uniform auxin input. *Nat Plants* **8**, 269–280 (2022).
10. Husbands, A. Y., Chitwood, D. H., Plavskin, Y. & Timmermans, M. C. P. Signals and prepatterns: new insights into organ polarity in plants. *Genes Dev.* **23**, 1986–1997 (2009).
11. Guan, C., Qiao, L., Xiong, Y., Zhang, L. & Jiao, Y. Coactivation of antagonistic genes stabilizes polarity patterning during shoot organogenesis. *Sci Adv* **8**, eabn0368 (2022).

12. Skopelitis, D. S., Benkovics, A. H., Husbands, A. Y. & Timmermans, M. C. P. Boundary formation through a direct threshold-based readout of mobile small RNA gradients. *Dev. Cell* **43**, 265-273.e6 (2017).
13. Green, J. B. A. & Sharpe, J. Positional information and reaction-diffusion: two big ideas in developmental biology combine. *Development* **142**, 1203–1211 (2015).
14. Turing, A. M. The chemical basis of morphogenesis. *Philos. Trans. R. Soc. Lond. B Biol. Sci.* **237**, 37–72 (1952).
15. Nakamura, T. *et al.* Generation of robust left-right asymmetry in the mouse embryo requires a self-enhancement and lateral-inhibition system. *Dev. Cell* **11**, 495–504 (2006).
16. Müller, P. *et al.* Differential diffusivity of Nodal and Lefty underlies a reaction-diffusion patterning system. *Science* **336**, 721–724 (2012).
17. Meinhardt, H. *Models of Biological Pattern Formation (Academic Press, London, 1982)*. (Academic Press, 1982).
18. Kondo, S. & Miura, T. Reaction-diffusion model as a framework for understanding biological pattern formation. *Science* **329**, 1616–1620 (2010).
19. Rogers, K. W. & Müller, P. Nodal and BMP dispersal during early zebrafish development. *Dev. Biol.* **447**, 14–23 (2019).
20. Murray, J. D. *Mathematical Biology*. (Springer Berlin Heidelberg, 2014).
21. Raspopovic, J., Marcon, L., Russo, L. & Sharpe, J. Modeling digits. Digit patterning is controlled by a Bmp-Sox9-Wnt Turing network modulated by morphogen gradients. *Science* **345**, 566–570 (2014).
22. Marcon, L., Diego, X., Sharpe, J. & Müller, P. High-throughput mathematical analysis identifies Turing networks for patterning with equally diffusing signals. *Elife* **5**, e14022 (2016).
23. Scholes, N. S., Schnoerr, D., Isalan, M. & Stumpf, M. P. H. A Comprehensive network atlas reveals that turing patterns are common but not robust. *Cell systems* **9**, 243-257.e4 (2019).
24. Vittadello, S. T., Leyshon, T., Schnoerr, D. & Stumpf, M. P. H. Turing pattern design principles and their robustness. *Philos. Trans. A Math. Phys. Eng. Sci.* **379**, 20200272 (2021).
25. Murray, J. D. A Pre-pattern formation mechanism for animal coat markings. *J. Theor. Biol.* **88**, 161–199 (1981).
26. Gierer, A. & Meinhardt, H. A theory of biological pattern formation. *Kybernetik* **12**, 30–39 (1972).
27. Hiscock, T. W. & Megason, S. G. Orientation of Turing-like patterns by morphogen gradients and tissue anisotropies. *Cell Syst* **1**, 408–416 (2015).
28. Kondo, S. The present and future of Turing models in developmental biology. *Development* **149**, (2022).

29. Landge, A. N., Jordan, B. M., Diego, X. & Müller, P. Pattern formation mechanisms of self-organizing reaction-diffusion systems. *Dev. Biol.* **460**, 2–11 (2020).
30. Merelo, P. *et al.* Regulation of *MIR165/166* by class II and class III homeodomain leucine zipper proteins establishes leaf polarity. *Proc. Natl. Acad. Sci. U. S. A.* **113**, 11973–11978 (2016).
31. de Felippes, F. F., Ott, F. & Weigel, D. Comparative analysis of non-autonomous effects of tasiRNAs and miRNAs in *Arabidopsis thaliana*. *Nucleic Acids Res.* **39**, 2880–2889 (2011).
32. O'Malley, R. C. *et al.* Cistrome and epicistrome features shape the regulatory DNA landscape. *Cell* **165**, 1280–1292 (2016).
33. Li, J. *et al.* Proteome-wide mapping of short-lived proteins in human cells. *Mol. Cell* **81**, 4722-4735.e5 (2021).
34. Reichholf, B. *et al.* Time-resolved small RNA sequencing unravels the molecular principles of microRNA homeostasis. *Mol. Cell* **75**, 756-768.e7 (2019).
35. Schlereth, A. *et al.* MONOPTEROS controls embryonic root initiation by regulating a mobile transcription factor. **464**, 913–916 (2010).
36. Han, J. & Mendell, J. T. MicroRNA turnover: a tale of tailing, trimming, and targets. *Trends Biochem. Sci.* (2022).
37. Kelley, D. R., Arreola, A., Gallagher, T. L. & Gasser, C. S. ETTIN (ARF3) physically interacts with KANADI proteins to form a functional complex essential for integument development and polarity determination in Arabidopsis. *Development* **139**, 1105–1109 (2012).
38. Simonini, S. *et al.* A noncanonical auxin-sensing mechanism is required for organ morphogenesis in Arabidopsis. *Genes Dev.* **30**, 2286–2296 (2016).
39. Ha, C. M., Jun, J. H., Nam, H. G. & Fletcher, J. C. BLADE-ON-PETIOLE 1 and 2 control Arabidopsis lateral organ fate through regulation of LOB domain and adaxial-abaxial polarity genes. *Plant Cell* **19**, 1809–1825 (2007).
40. Yamaguchi, T., Yano, S. & Tsukaya, H. Genetic framework for flattened leaf blade formation in unifacial leaves of *Juncus prismatocarpus*. *Plant Cell* **22**, 2141–2155 (2010).
41. Jones-Rhoades, M. W., Bartel, D. P. & Bartel, B. MicroRNAS and their regulatory roles in plants. *Annu. Rev. Plant Biol.* **57**, 19–53 (2006).
42. Ma, X., Denyer, T., Javelle, M., Feller, A. & Timmermans, M. C. P. Genome-wide analysis of plant miRNA action clarifies levels of regulatory dynamics across developmental contexts. *Genome Res.* **31**, 811–822 (2021).
43. Onimaru, K., Marcon, L., Musy, M., Tanaka, M. & Sharpe, J. The fin-to-limb transition as the re-organization of a Turing pattern. *Nat. Commun.* **7**, 11582 (2016).
44. Kim, J. *et al.* A molecular basis behind heterophylly in an amphibious plant, *Ranunculus trichophyllus*. *PLoS Genet.* **14**, e1007208 (2018).

45. Hashimoto, K., Miyashima, S., Sato-Nara, K., Yamada, T. & Nakajima, K. Functionally diversified members of the *MIR165/6* gene family regulate ovule morphogenesis in *Arabidopsis thaliana*. *Plant Cell Physiol.* **59**, 1017–1026 (2018).
46. Husbands, A. Y., Benkovics, A. H., Nogueira, F. T. S., Lodha, M. & Timmermans, M. C. P. The ASYMMETRIC LEAVES complex employs multiple modes of regulation to affect adaxial-abaxial patterning and leaf complexity. *Plant Cell* **27**, 3321–3335 (2015).
47. Carlsbecker, A. *et al.* Cell signalling by microRNA165/6 directs gene dose-dependent root cell fate. *Nature* **465**, 316–321 (2010).
48. Lodha, M., Marco, C. F. & Timmermans, M. C. P. The ASYMMETRIC LEAVES complex maintains repression of KNOX homeobox genes via direct recruitment of Polycomb-repressive complex2. *Genes Dev.* **27**, 596–601 (2013).
49. Husbands, A. Y., Aggarwal, V., Ha, T. & Timmermans, M. C. P. In planta single-molecule pull-down reveals tetrameric stoichiometry of HD-ZIPIII:LITTLE ZIPPER complexes. *Plant Cell* **28**, 1783–1794 (2016).
50. Barbier de Reuille, P. *et al.* MorphoGraphX: A platform for quantifying morphogenesis in 4D. *Elife* **4**, 05864 (2015).
51. Starruß, J., de Back, W., Brusch, L. & Deutsch, A. Morpheus: a user-friendly modeling environment for multiscale and multicellular systems biology. *Bioinformatics* **30**, 1331–1332 (2014).

ACKNOWLEDGEMENTS

We are grateful to Cris Kuhlemeier, Michael Scanlon, Christian Hardtke, Aman Husbands, Raffaele Dello Ioio, and Laura Ragni for critical feedback on the manuscript. Support for this work came from the Alexander von Humboldt Professorship to MT.

AUTHOR CONTRIBUTIONS

ES, GP, KN, and MT conceived of the research direction and experiments; ES with support from WdB performed theoretical and computational analyses, GP and AB carried out the confocal imaging and image analysis, and KH and SM performed ChIP and other molecular biology work. ES and MT with input from all co-authors wrote the manuscript.

COMPETING INTERESTS

The authors declare that they have no competing interests.

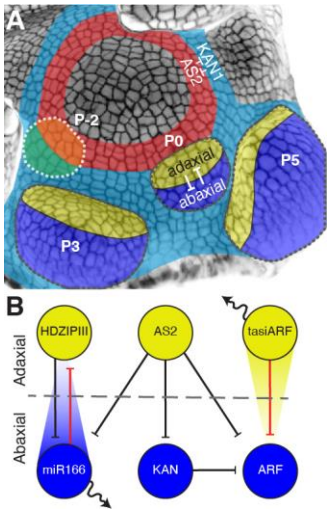

Fig. 1. A six-component GRN propagates ad-ab leaf polarity in the growing primordium. (A) Top view of a shoot apex illustrating the auxin-driven specification of adaxial (orange) and abaxial (green) polarity (p-2) on a pre-pattern at the meristem periphery defined by KAN1 (cyan) and AS2 (red) expression. Following primordium emergence from the pre-patterned meristem environment, adaxial (yellow) and abaxial (blue) domains are propagated by a GRN with six core components. **(B)** GRN proposed to propagate ad-ab polarity in the growing primordium, with previously established direct regulatory interactions indicated (for more details see[3,8]). Yellow nodes, adaxial determinants; blue nodes, abaxial determinants; red edges, interactions defined a priori in the theoretical analysis; serpentine arrows, mobility; dissolving triangles, miR166 and tasiARF gradients. Stages of primordium (P) development are indicated, numbers <1 indicate incipient primordia.

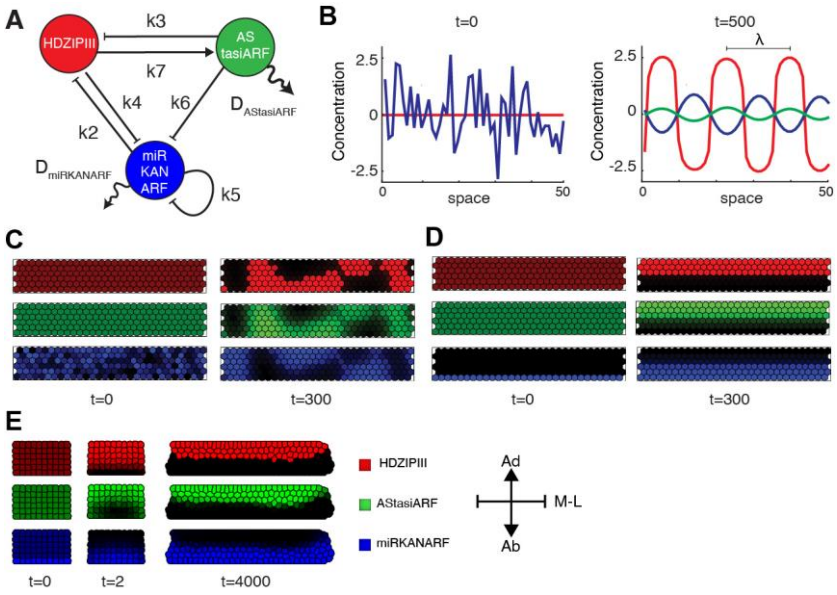

Figure. 2. A single three-component minimal network can self-organise a robust linear polarity boundary. (A) The Leaf Polarity Model (LPM) is the only 3-component network topology compatible with Turing dynamics and imposed biological constraints. Reaction parameters, k2..kn, and diffusion coefficients $D_{AStasiARF}$ and $D_{MIRKANARF}$ for the system of PDEs associated with the network are indicated (Supplementary Note 1). **(B)** Numerical simulation of the LPM on a 1-dimensional lattice of 50 unit cells with random initial conditions for miRKANARF (t=0), over time produces a stable spatial pattern with miRKANARF out-of-phase from HDZIPIII and AStasiARF (t=500). λ, system wavelength. **(C)** Numerical simulation of the LPM on a 2-dimensional static grid of cells with random initial conditions for miRKANARF (t=0) generates a variegated pattern (t=300). **(D)** With miRKANARF in the most abaxial cell layer as the initial condition (just t=0), the LPM self-organises into a bipolar pattern (t=300) reminiscent of ad-ab polarity in the planar leaf. **(E)** With this initial condition (t=0), the LPM dynamically adjust the distributions of its components over time to organise and propagate a linear bipolar pattern also in a growing cellular environment phenocopying the leaf (t=2; t=4000). M-L, Medio-Lateral axis. Note, the LPM operates in each cell and coordinates a spatial pattern at the organ level through cell-to-cell diffusion of mobile components.

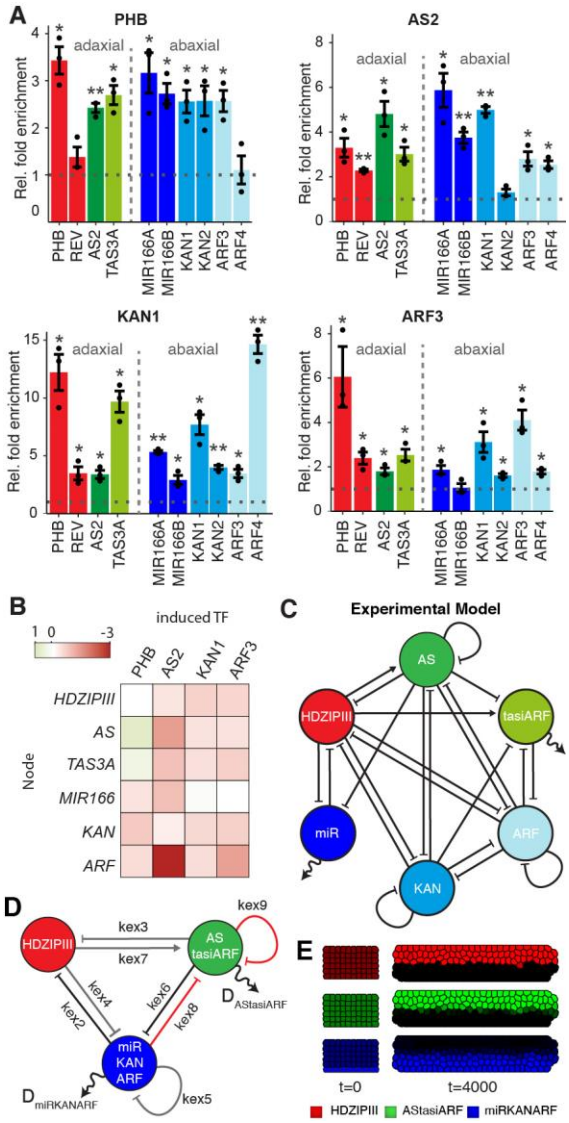

Figure. 3. The experimentally defined polarity GRN follows the LPM organising principles. (A) ChIP analyses show significant enrichments for PHB, AS2, KAN1 and ARF3 at select sites in the promoters of representative members for the HDZIPIII (red), AStasiARF (green), and miRKANARF (blue) nodes. Enrichment values ChIP/Input (means ± SE, n≥3) normalized to enrichment at the negative control locus *ACT2* are shown. Two-tailed Student's t-test: *p<0.05; **p<0.01. **(B)** Heatmap showing significant relative expression changes for representative targets in each node following short-term induction of PHB, AS2, KAN1, or ARF3 (Supplementary Fig. 4A-D). Note, the direct repressive effect of AS2 on *pPHB:GFP* expression (Supplementary Fig. 4E) is illustrated. **(C)** Network representation of all direct interactions between leaf polarity determinants discerned experimentally shows that most regulatory interactions in the polarity GRN are repressive. Noted exceptions are the induction of AS and tasiARF by HDZIPIII. **(D)** Simplified 3-component network of the polarity GRN in (C). Reaction parameters and diffusion coefficients for the associated system of PDEs (Supplementary Note 4.1) are indicated. Black edges, interactions defined a priori in the theoretical analysis; grey, LPM-predicted critical interactions; red, additional interactions discerned experimentally. **(E)** Numerical simulation of the 3-component network in (D) on the growing cellular template confirms that the additional interactions (red edges) are compatible with Turing dynamics and the self-organisation of a bipolar pattern that phenocopies ad-ab polarity in a planar leaf.

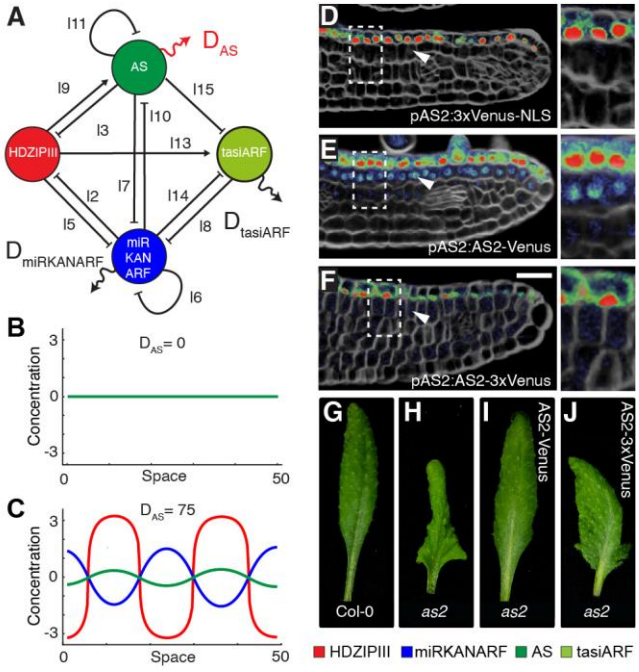

Figure. 4. AS2 mobility forms a critical factor in the self-organised regulation of ad-ab polarity. (A) Topology of the 4-component biological GRN with separate AS and tasiARF nodes. Reaction parameters and diffusion coefficients for the associated system of PDEs (Supplementary Note 4.2.1) are indicated. **(B-C)** Numerical simulations of the model in (A) fail to produce a Turing pattern in the absence of AS mobility (B, D_{AS}=0), but show Turing dynamics when AS diffuses (C, D_{AS}=75) (t=500). **(D-F)** Cross sections through young leaves show *AS2* promoter activity in the adaxial epidermis only (D), whereas AS2 protein accumulates also in the sub-epidermal layer (E). A non-mobile AS2 protein fusion is again detected in only the adaxial epidermis (F). Arrowheads mark the sub-epidermal cell layer. Fluorescence intensity, red - high to cyan - low. Scale bars, 20 µm. **(G-H)** Compared to wild-type Col-0 leaves (G), *as2* mutant leaves (H) are rumpled, asymmetric and lobed, at least in part resulting from defects in ad-ab polarity[46]. **(I-J)** The *as2* phenotype is rescued by expression of a mobile AS2 protein fusion (I, *pAS2:AS2-Venus*), but is only partially complemented upon expression of a non-mobile AS2 protein fusion (J, *pAS2:AS2-3xVenus*).

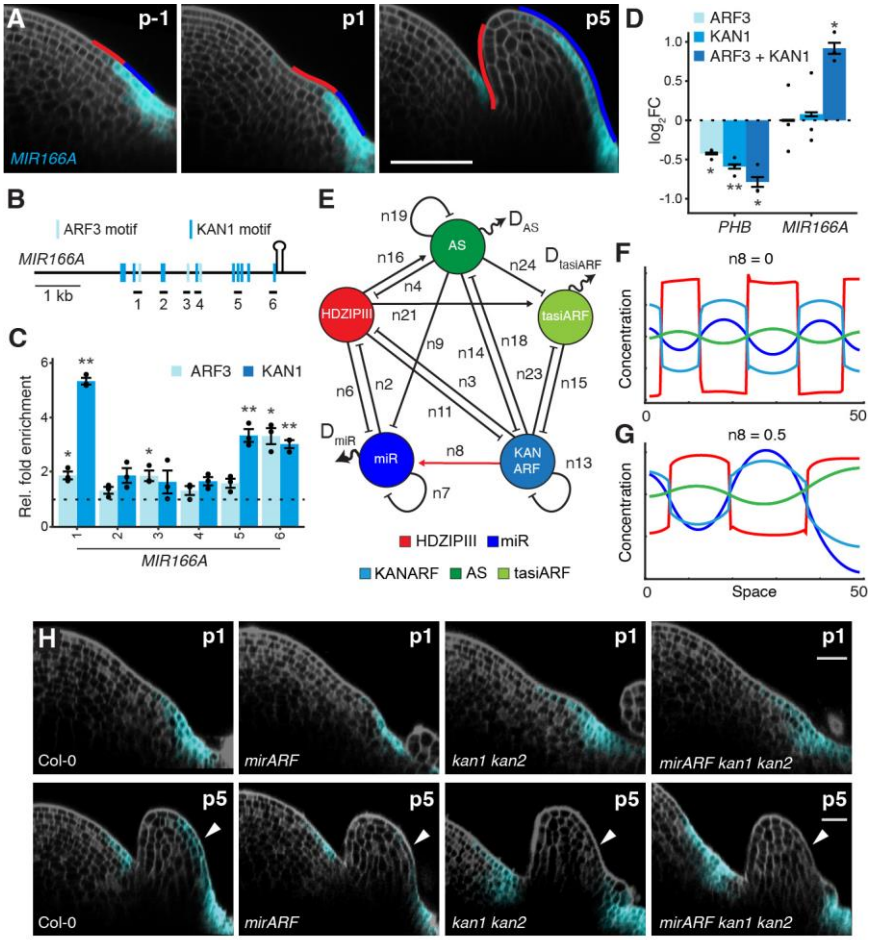

Figure. 5. A KAN-ARF complex induces *MIR166A* in an organ-autonomous leaf polarity network. (A) Optical longitudinal sections through young leaf primordia point to an early role for *MIR166A* in ad-ab patterning. Cells of the adaxial (red) and abaxial (blue) domains were discerned from backward lineage tracing. Scale bars, 50 µm. **(B)** Schematic representation of predicted KAN1 and ARF3 binding sites in the *MIR166A* promoter. **(C)** ChiP analysis showing significant enrichment of KAN1 and ARF3 at sites in the *MIR166A* promoter reveals that KAN1 and ARF3 co-occupy site 6 containing a predicted KAN1 binding motif. Values (means ± SE, n=3) are relative to the enrichment of KAN1 or ARF3 at the negative control *ACT2*. Two-tailed Student's t-test: *p<0.05, **p<0.01. **(D)** Relative transcript levels (mean ± SE, n=3) for *PHB* decrease upon induction of ARF3, KAN1, or ARF3 and KAN1 together, whereas *MIR166A* transcript levels increase only upon co-induction of both ARF3 and KAN1 (see also Supplementary Fig. 6). Two-tailed Student's t-test: *p<0.05, **p<0.01. **(E)** Topology of the final 5-component polarity GRN highlighting the induction of miR by KAN-ARF (red edge). Reaction parameters and diffusion coefficients for the associated system of PDEs (Supplementary Note 4.2.2) are indicated. **(F-G)** Numerical simulations of the model in (E) reveal that the induction of miR by the KAN-ARF complex increases the system wavelength (t=500). **(H)** Upon reduction of KAN and/or ARF activity, *MIR166A* expression is lost in the growing primordium (P5), but not in the primordium emerging at the meristem periphery (P1), indicating KAN and ARF together control the organ-autonomous expression of *MIR166A*. Arrowheads, abaxial side of the p5 primordium. Scale bars, 20 µm.

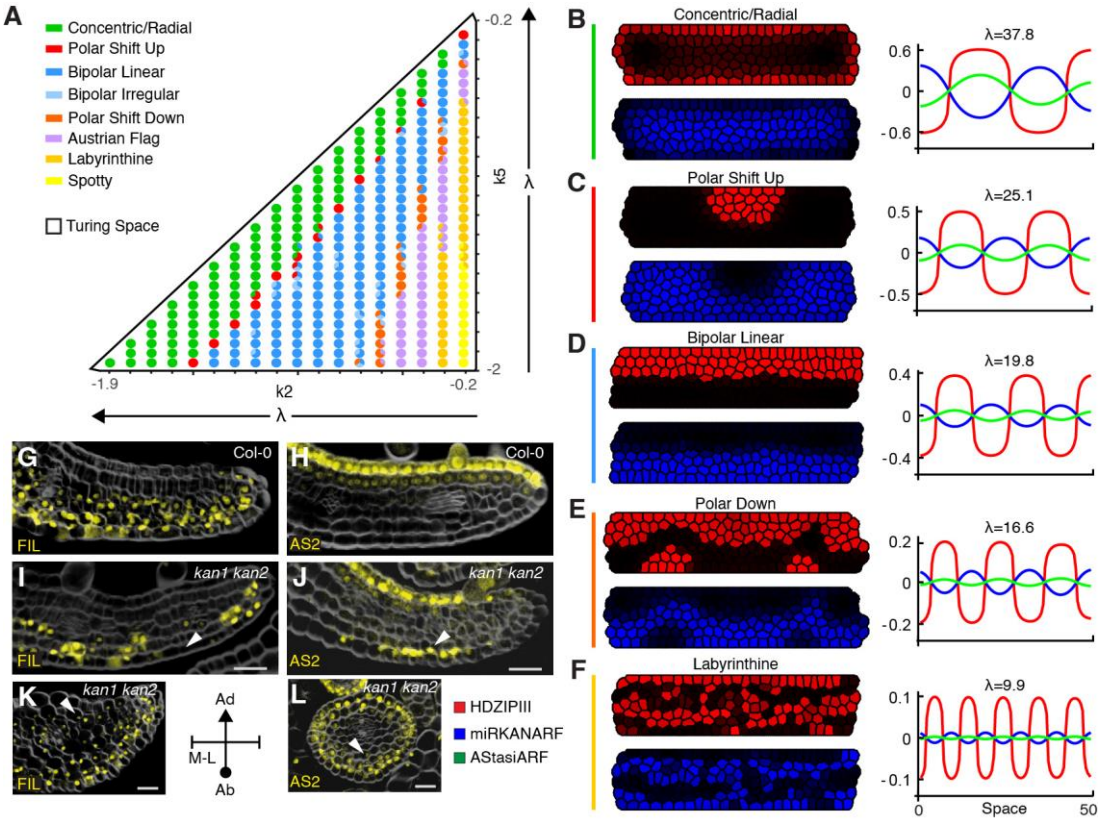

Figure. 6. Turing dynamics accounts for shifts in ad-ab gene expression underlying evolutionarily diverse organ shapes. (A) Morpho-sensitivity analysis of the LPM on the growing cellular template reveals it generates discrete spatial patterns of ad-ab identity at the organ level dictated by defined wavelength thresholds resulting from stepwise variations in k_2 and k_5. The scatter pie chart recapitulates simulation results (n=3) at t=5000. Colors define different phenotypic classes. Arrows marked λ indicate the direction in which parameter values lengthen the system wavelength. **(B-F)** Representative simulation outcomes for phenotypic classes in the morpho-sensitivity analysis in (A) alongside the corresponding 1-dimensional simulations illustrate the relationship between system wavelength and ad-ab tissue pattern. **(G-L)** In wild-type, *pFIL:3xVenus-NLS* (G) and *pAS2:AS2-Venus* (H) mark cells on the abaxial and adaxial side, respectively. In *kan1 kan2*, the patterns of *pFIL:3xVenus-NLS* (I, K) and *pAS2:AS2-Venus* (J, L) expression change, indicating a partial adaxialization (I, J), spotty abaxialization (K), or full adaxialization (L) coherent with phenotypic outcomes of the LPM in (E), (F) and (B), respectively. Arrowheads mark shifts in gene expression from the wild-type control.

Acknowledgements

I am extremely grateful to Prof. Dr Marja Timmermans for providing me with the wonderful opportunity to pursue my PhD in her research group. Words cannot describe my gratitude towards her. Throughout my time as a PhD student, she has been patient with me and, has guided and encouraged me to go above and beyond, which ultimately helped me advance my thinking in the field of developmental biology.

My sincere thanks to Prof. Dr Gerd Jurgens for agreeing to be my second supervisor as well as the reviewer of my thesis. I also would like to thank my thesis advisory committee members Dr. Martin Bayer and Dr. Laura Ragni for their constant guidance and encouragement throughout my time as a PhD student. In addition, discussions with all of them during progress reports and literature seminars helped me gain more confidence in putting forward my scientific thoughts.

I would like to thank all the current and former lab members who always supported me making each day in my lab worthwhile. Special thanks to Diana, Khoa, Holger, Simon, and Steffen for their support during the early days of my PhD. Thanks to Antje for constant support and for always being willing to help be it at work or outside. Special thanks to Gael who always encouraged me and for all the short scientific discussions we had on each other's work. Aleks, thank you for always being there and making me believe in myself every time. Pavel and Pin-Jou, heartfelt thanks for all the help with bioinformatics and statistics as well as for having an open ear for me on the days that I was down. Tom and Cecilia, I would like to sincerely thank you for proofreading my thesis, for providing your critical opinion on it, and for always encouraging me to be positive. I also extend my thanks to Emanuele, Marika, Richie, Wanyan and Qi for their constant support in the lab.

Finally, I would like to thank my family and friends. First, I would like to thank my father Ramesh Meda for his constant support throughout my life. A heartfelt gratitude to my wife Bhavishya for her positivity and constant encouragement. Thanks to these two amazing people who have seen me at my lowest but continue to motivate me every day to enjoy life and to strive towards my goals. I would also like to thank my friends, especially Bhargav, Praveen, Pooja, Saurabh, Shreya, Utkarsh, Indrani, Shruti, Yoga, Neelkant and Jaagni, for all the amazing experiences I have shared with them.